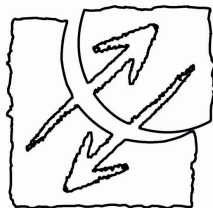# Bottom-up reconstitution using giant unilamellar vesicles as membrane compartments

Thomas Litschel

München 2021

LMU LUDWIG-
MAXIMILIANS-
UNIVERSITÄT
MÜNCHEN

MAX-PLANCK-INSTITUT
FÜR BIOCHEMIE

Bottom-up reconstitution using giant unilamellar vesicles as membrane compartments

Thomas Litschel

Dissertation
an der Fakultät für Physik
der Ludwig-Maximilians-Universität
München

vorgelegt von
Thomas Martin Litschel
aus Bietigheim-Bissingen

München, 7. April 2021

Erstgutachter/in: Prof. Dr. Petra Schwille
Zweitgutachter/in: PD Dr. Theobald Lohmüller
Tag der mündlichen Prüfung: 19. Mai 2021

Zusammenfassung

Eines der grundlegendsten Definitionsmerkmale einer lebenden biologischen Zelle ist ihre Fähigkeit, ihre molekularen Komponenten innerhalb einer isolierenden Barriere einzuschließen. In allen bis dato bekannten lebenden Zellen spielen Phospholipidmembranen diese zentrale Rolle, indem sie die zelluläre Maschinerie von der äußeren Umgebung abtrennen. Die Kompartmentalisierung durch Membranen ist ein Schlüsselprinzip des Lebens, nicht nur auf der Ebene der kompletten Zelle, sondern oft auch innerhalb von Zellen. Diese Einschließung und Isolierung wesentlicher Prozesse innerhalb einer einzigen, definierbaren Einheit hat Leben, wie wir es kennen, möglich gemacht. Damit stellt die Kompartimentierung eine wesentliche Aufgabe dar, die bei der Entstehung des Lebens realisiert werden musste, denn nur eine abgrenzende Barriere zur Umwelt ermöglicht die Unterscheidung einzelner Lebenseinheiten und damit die darwinistische Evolution. Eine weitere Kernaufgabe des Lebens, ist die Fähigkeit zur Vermehrung. Moderne Zellen sind in der Lage, sich durch Verformung ihrer kompartimentierenden Membranbarriere in zwei Tochterzellen zu teilen, und zwar mit einer Teilungsmaschinerie, die sich innerhalb dieser Barriere befindet - eine bemerkenswerte Leistung. In dieser Dissertation stelle ich meine Forschungsergebnisse vor, deren Ziel es war, diese Schlüsselmerkmale des Lebens durch Bottom-up-Rekonstruktionsansätze zu untersuchen. Die Bottom-up-Zellbiologie verwendet isolierte, gut charakterisierte Komponenten, wie gereinigte Proteine, und versucht, zelluläre Prozesse aus diesen einfachen Bausteinen zu rekonstruieren. Eine der Kernherausforderungen der klassischen Zellbiologie ist, wie man die intrinsische Komplexität biologischer Systeme mit einem analytischen Ansatz angehen kann. Komplexität ist eines der intrinsischen Merkmale des Lebens auf der Erde, das auf Milliarden von Jahren der Evolution zurückzuführen ist. Biologische Zellen sind nicht darauf ausgelegt, verstanden zu werden, und vielmehr trägt Komplexität zur Anpassungsfähigkeit und Robustheit biologischer Funktionsweisen bei. Durch die Rekonstruktion von biologischen Strukturen und Funktionen mit minimalen Komponenten können Wissenschaftler jedoch die Entstehung biologischer Komplexität beobachten und zu verstehen versuchen. Membranen spielen eine große Rolle in vielen zellulären Prozessen und tragen wesentlich zu dieser Komplexität bei. Sie können allerdings schwer in Bottom-up-Rekonstitutionsansätze zu integrieren sein, was die Möglichkeiten einschränken kann, einen vollständigen Blick auf solche Prozesse durch in vitro-Experimente zu erhalten. In dieser Arbeit stelle ich eine Reihe von Projekten vor, die riesige unilamellare Vesikel (GUVs) als Nachahmung der

kompartimentierenden Membranen von Zellen verwenden, um dabei grundlegende biologische Funktionen zu untersuchen. Dafür habe ich eine Vielzahl von biologischen Komponenten in GUVs eingekapselt, um biomimetisches Verhalten und Funktion zu erzielen. Dabei habe ich jeweils die einzigartigen Eigenschaften der GUVs genutzt, um Verhaltensweisen zu erreichen oder Beobachtungen zu machen, die mit anderen Ansätzen, einschließlich alternativer Modellmembransystemen, nicht möglich gewesen wären. Insgesamt stellt meine Arbeit einen Schritt vorwärts in Richtung der Rekonstruktion komplexer und dynamischer zellulärer Prozesse unter zellähnlichen Bedingungen dar.

Abstract

One of the most basic defining features of a living biological cell is its ability to confine its molecular components within an isolating boundary. In all living cells known to date, phospholipid membranes play this central role by separating cellular machinery from the outside environment. Compartmentalization by membranes is a key principle of life, not only on the scale of the cell as a whole, but, in many cases, within cells as well. This unification and isolation of essential processes within a single, definable unit has made life as we know it possible. As such, compartmentalization represents an essential task that had to be achieved in the emergence of life, as only a confining barrier to the environment allows for distinction of individual units of life and therefore for Darwinian evolution. Another core task of life, is the ability to reproduce. Modern cells are able to split into two daughter cells by deforming their compartmentalizing membrane barrier, all with a division machinery which is situated within this barrier itself – a quite remarkable feat. In this thesis, I present my doctoral work, which aimed to investigate these key features of life through bottom-up reconstitution approaches. Bottom-up cell biology uses isolated well-characterized components, like purified proteins, and tries to recreate cellular processes from these simple building blocks. One of the core challenges of classical cell biology is how to tackle the intrinsic complexity of biological systems with an analytical approach. Complexity is one of the most intrinsic features of life on earth, owing to billions of years of evolution. Biological cells are not designed to be understood and in fact, complexity itself contributes to the adaptability and robustness of biological function. However, by reconstitution of biological structure and function from the bottom-up with minimal components, scientists can observe and try to understand the emergence of biological complexity. Membranes, of course, play a great role in many cellular processes, and contribute significantly to this complexity. However, they can be difficult to incorporate into bottom-up reconstitution approaches, limiting our ability to get a complete view of such processes from in vitro experiments. In this thesis, I present a number of projects, which use giant unilamellar vesicles (GUVs) as mimicries of the compartmentalizing membranes of cells to investigate basic biological functions. I've encapsulated a diverse array of biological components in GUVs to achieve biomimetic behavior and function. In each case, I made use of the unique properties of the GUVs to achieve behaviors or make observations that would have not been possible with other approaches, including alternative model membrane systems. Overall, my work presents a step forward toward the reconstitution of complex and dynamic cellular processes under cell-like conditions.

List of publications

Publications that are part of this cumulative thesis

Litschel T, Schwille P
Protein Reconstitution Inside Giant Unilamellar Vesicles
Annu Rev Biophys **50** (2021) 525-548

Litschel T, Kelley CF, Holz D, Adeli Koudehi M, Vogel SK, Burbaum
L, Mizuno N, Vavylonis D, Schwille P
Reconstitution of contractile actomyosin rings in vesicles
Nat Commun **12** (2021) [no page number available yet]

Litschel T, Ramm B, Maas R, Heymann M, Schwille P
Beating vesicles: Encapsulated protein oscillations cause dynamic membrane
deformations
Angew Chem Int Ed **57** (2018) 16286–16290

Christ S, **Litschel T**, Schwille P, Lipowsky R
Active shape oscillations of giant vesicles with cyclic closure and opening of
membrane necks
Soft Matter **17** (2021) 319-330

Jia H, **Litschel T**, Heymann M, Eto H, Franquelim HG, Schwille P
Shaping Giant Membrane Vesicles in 3D-Printed Protein Hydrogel Cages
Small **16** (2020) 1906259

Ganzinger KA, Merino-Salomón A, García-Soriano DA, Butterfield
AN, **Litschel T**, Siedler F, Schwille P
FtsZ reorganisation facilitates deformation of giant vesicles in microfluidic
traps
Angew Chem Int Ed **59** (2020) 21372–21376

Litschel T, Ganzinger KA, Movinkel T, Heymann M, Robinson T,
Mutschler H, Schwille
Freeze-thaw cycles induce content exchange between cell-sized lipid vesicles
New J Phys **20** (2018) 055008

Other publications (not part of this thesis)

Kelley CF, **Litschel T**, Schumacher S, Dedden D, Schwille P, Mizuno N
Phosphoinositides regulate force-independent interactions between talin,
vinculin, and actin
eLife **9** (2020) e56110

Bashirzadeh Y, Redford SA, Lorpaiboon C, Groaz A, **Litschel T**, Schwille P,
Hocky GM, Dinner A, Liu AP

Actin crosslinker competition and sorting drive emergent GUV size-dependent actin network architecture
bioRxiv (2020) 2020.10.03.322354

Statement about contributions

All experiments in the publications with me as a first author were exclusively performed by me. All experimental data in the publications with me as a first author was exclusively acquired by me; one single exception is the electron micrograph in Figure 6C of Publication 2. I performed all data analysis and quantification for Publications 2 and 3. For Publication 2 I received help with developing computational analysis tools for this quantification. I performed only part of the data analysis for Publication 7. For all papers with me as a first author, I wrote the first draft of the manuscript and generally mostly received help from the corresponding authors of the respective publications in writing the publications. I created all figures of all publications with me as a first author. I did not perform any of the simulations or theoretical modeling in Publications 2 and 4. I performed the experimental work for Publication 4. I contributed with experiments to Publication 5. Contributions to Publication 6 were largely conceptual and with troubleshooting.

Table of contents

1. Introduction

1.1. Outline

In this thesis, I present my cumulative doctoral work in a comprehensive way. Each chapter contains either one publication or two thematically-related publications. The beginning of each chapter contains a one to two page description of how each publication relates to the thesis as a whole and to the other projects of this thesis. This is followed by a short section describing basic concepts related to the respective chapter, e.g. introductions to cytoskeletal proteins, the Min protein system, microfluidic systems and protocells in the origins of life. These basic concepts are only relevant to each individual topic, and are therefore not part of the current introductory chapter. The common thread between all projects is the use of GUVs for reconstitution studies, which is introduced in this chapter by a published literature review.

My doctoral work encompasses several projects that aimed to imitate properties of biological cells (or of collections thereof) through bottom-up in vitro reconstitution. In order to do so, I used giant unilamellar vesicles to encapsulate biological reactions and components. The second chapter concerns the encapsulation of actin, a protein that is the subject of many bottom-up biology studies. In the presented work we show how actin can assemble into rings within GUVs and even exert a contractile force onto the membrane. In the third chapter, the focus is on the Min protein system - a protein machinery that many people in the Schwille group have previously worked with. The system was first reconstituted in vitro by Loose et al. & Schwille in 2008[1] and since then was further characterized by other members of the group and led to many exciting discoveries. By encapsulating the proteins MinD and MinE we continue this list of exciting and unexpected discoveries made with this fascinating protein system. The fourth chapter concerns the manipulation of giant vesicles through microfabricated structures. I was involved in two projects that used two different approaches to achieve a common goal: the deformation of giant vesicles to investigate the effects of compartment geometry on the self-organization of encapsulated protein systems. Finally, the last chapter concerns a slightly different topic. Instead of focusing on what happens within individual vesicles, here we look at the exchange of content (i.e. the spread of genetic information) between populations of vesicles – all in the context of mechanisms that could have played a role in the emergence of life on early earth.

A recent literature review titled "Protein reconstitution in giant unilamellar vesicles" will introduce this thesis. This review not only describes the most important methods used during my doctoral work, but also discusses motivation, aim, and future outlook of the work in this thesis. While the very last chapter of this thesis does not concern the encapsulation of proteins, but rather the encapsulation of DNA fragments, the literature review also seems fitting as an introduction to this project, as the methods and motivations also heavily overlap with those of that project.

1.2. Publication 1: Protein reconstitution inside giant unilamellar vesicles

Literature review published in Annual Review of Biophysics.[2]

Litschel T, Schwille P. „Protein Reconstitution Inside Giant Unilamellar Vesicles". *Annu Rev Biophys* **50** (2021) 525-548

https://doi.org/10.1146/annurev-biophys-100620-114132

Reprinted with permission.

ANNUAL REVIEWS

Protein Reconstitution Inside Giant Unilamellar Vesicles

Thomas Litschel and Petra Schwille

Department of Cellular and Molecular Biophysics, Max Planck Institute of Biochemistry, Martinsried 82152, Germany; email: litschel@biochem.mpg.de, schwille@biochem.mpg.de

Keywords

model membranes, synthetic biology, bottom-up biology, in vitro reconstitution, liposomes, phospholipids

Abstract

Giant unilamellar vesicles (GUVs) have gained great popularity as mimicries for cellular membranes. As their sizes are comfortably above the optical resolution limit, and their lipid composition is easily controlled, they are ideal for quantitative light microscopic investigation of dynamic processes in and on membranes. However, reconstitution of functional proteins into the lumen or the GUV membrane itself has proven technically challenging. In recent years, a selection of techniques has been introduced that tremendously improve GUV-assay development and enable the precise investigation of protein–membrane interactions under well-controlled conditions. Moreover, due to these methodological advances, GUVs are considered important candidates as protocells in bottom-up synthetic biology. In this review, we discuss the state of the art of the most important vesicle production and protein encapsulation methods and highlight some key protein systems whose functional reconstitution has advanced the field.

Contents

1. INTRODUCTION

While biology has been an analytical science for most of its history, amazing progress in the life sciences within the past decades has triggered ambitions to use the knowledge and methodology acquired from dealing with living systems to actually build biological functionality from its elemental building blocks. Among these building blocks into which biological systems may be dissected, proteins are the most obvious. As the workhorses of the intricate chemical wiring of a cell, they are tasked with regulating or carrying out every major cellular function through specific interactions and enzymatic activities. In vitro protein reconstitution is a key practical challenge for protein biochemistry, which has long been concerned with the production, purification, and investigation of functional proteins under controlled settings.

Experiments with purified proteins have increased our understanding of life on the molecular scale, making it possible to characterize the biochemical and physical properties of isolated macromolecules. Through the combination of a limited number of components in simplified experimental systems, it has been possible to gain detailed insight into the biological processes and machines central to life. However, it has also become evident that purification and production of particular proteins in aqueous buffer solution fall short of recapitulating the function of many proteins, as proteins require specific geometries or biochemical environments to unfold their physiological functionality. Therefore, molecules and structures that mimic cellular environments are required for the functional reconstitution of purified proteins or protein systems. As these reconstituted biological systems grew ever more complex over recent years, the term bottom-up (synthetic) biology was coined, in contrast to the top-down approach applied to living cells, which is analytical in nature (82). This rapidly growing and multidisciplinary field combines molecular and cell biology, biophysics, and biochemistry, as well as engineering disciplines such as microfabrication and microfluidics. The term bottom-up suggests that the field aims to ascend from low to high complexity, toward the assembly of a—however rudimentary—living organism. Some researchers have taken on this challenge explicitly, with the daring goal of creating a functioning minimal cell from biological building blocks (119, 133). While still not entirely within reach, this goal will deepen our fundamental understanding of living organisms and the basic requirements of life while also having exciting potential applications for a new generation of bioeconomy. Being able to harness functional biological systems and subsystems with a modular synthetic approach

may yield benefits comparable to the ones that were provided by synthetic chemistry a century ago.

One key component at the center of many reconstitution experiments, and potentially essential in the pursuit of creating artificial cells, is the cell membrane. All living organisms known to date have a cell membrane made of lipid molecules. In addition to their roles as boundaries for cells and cell organelles, membranes are also home to approximately one-third of cellular proteins (6) and, thus, provide perhaps the most important reaction space in the cell. Crucial processes such as inter- and intracellular signaling, photosynthesis, respiration, adhesion, motility, and division are all centered around membranes.

The most obvious and fundamental feature of the cell membrane is still its compartment-forming role. In single-celled organisms—which are particularly important in the context of the origins of life—the function of membranes as confining boundaries enables the existence of individual entities whose personal genetic makeup is distinct from that of others and thereby forms the basis for Darwinian evolution (27, 145). As such, a selective barrier for the exchange of material and energy is one of the prerequisites for the emergence and existence of life as we know it (147). Furthermore, in eukaryotes, intracellular membranes are essential to allowing local up-concentration of proteins, metabolites and ions, and separate incompatible reactions in space to create optimized microenvironments and establish concentration gradients within the cell. In addition their action as selective boundaries, the facile deformability of cell membranes is another critical aspect, as membranes must support frequent division and subsequent growth, key prerequisites for the proliferation of organisms. Moreover, in most organisms, membranes are frequently required to adapt their shape to environmental cues and other structural components, including the internal cytoskeleton or an external cell wall. Not surprisingly, the lipid composition of higher organisms is very complex, often consisting of a large variety of amphiphilic phospholipids that readily form bilayers. From a physical perspective, membranes can be considered two-dimensional fluids for lipids and immersed molecules: easy to bend, yet hard to stretch.

Spatial confinement in cell-sized compartments is important for the kinetics of biochemical reactions (70, 159, 165) and the self-organization of structural elements and has thus been the subject of many biophysical studies. Processes like cytoskeletal assembly and biological pattern formation, which have been extensively studied in experiments and theory, heavily depend on 2D or 3D geometry. Many properties and functions of the cell membrane and the associated proteins can be studied independently, and in vitro reconstitution often calls for such reductionist approaches. Supported lipid bilayers or liposome assays of defined composition are frequently used to study protein–membrane interactions. In addition, water-in-oil emulsion microdroplets, which can be produced in large numbers by microfluidics, serve as excellent tools to investigate the effect of limited volumes on biochemical reactions (159, 164). They are often useful in the context of chemical evolution (63, 149). Furthermore, microfabricated structures coated by membrane are used to observe the effects of geometrical confinement on protein assembly of cytoskeletal structures or biological pattern formation (21, 31, 40, 91, 108, 138, 165), and free-standing bilayer structures, such as suspended membranes, have been used to investigate membrane deformations (59).

These widely used experimental model systems are each perfectly adapted to the study of one particular property of lipid membranes or membrane-associated proteins and have furthered our understanding of membrane protein function significantly in the past decades. However, considering each property in isolation does not yield a comprehensive picture of the complex and intertwined physiological roles of membranes in a living cell. A more generic model system, which reflects the fact that membranes serve as both containers and transformable spaces that respond to the reactions within, is based on the 3D encapsulation of functional biomolecules

within unilamellar vesicles, made of phospholipids that resemble the composition of cellular membranes. Until quite recently, systematic technical limitations hampered efficient membrane protein encapsulation in lipid vesicles. Specialized protocols and equipment were required to reconstitute proteins in these biomimetic compartments, and few labs with specific expertise have succeeded in their study. In the past few years, methodological developments and technical advancements in the field of bottom-up biology have made it easier to generate vesicles as cell-like compartments and opened up the field to a much broader community of researchers.

In this review, we discuss various ways in which encapsulation of functional proteins into synthetic lipid vesicles can be accomplished and demonstrate that this approach can be immensely useful to reach a new level of complexity in reconstitution experiments, potentially paving the way toward the creation of artificial cells. We introduce some of the most frequently used methods supporting the transfer of complex solutions into intact membranous vesicles and highlight relevant work that has led to new insights using these approaches to reconstitute a diverse array of proteins inside vesicles. **Figure 1** gives an overview of protein systems that are the subjects of these studies.
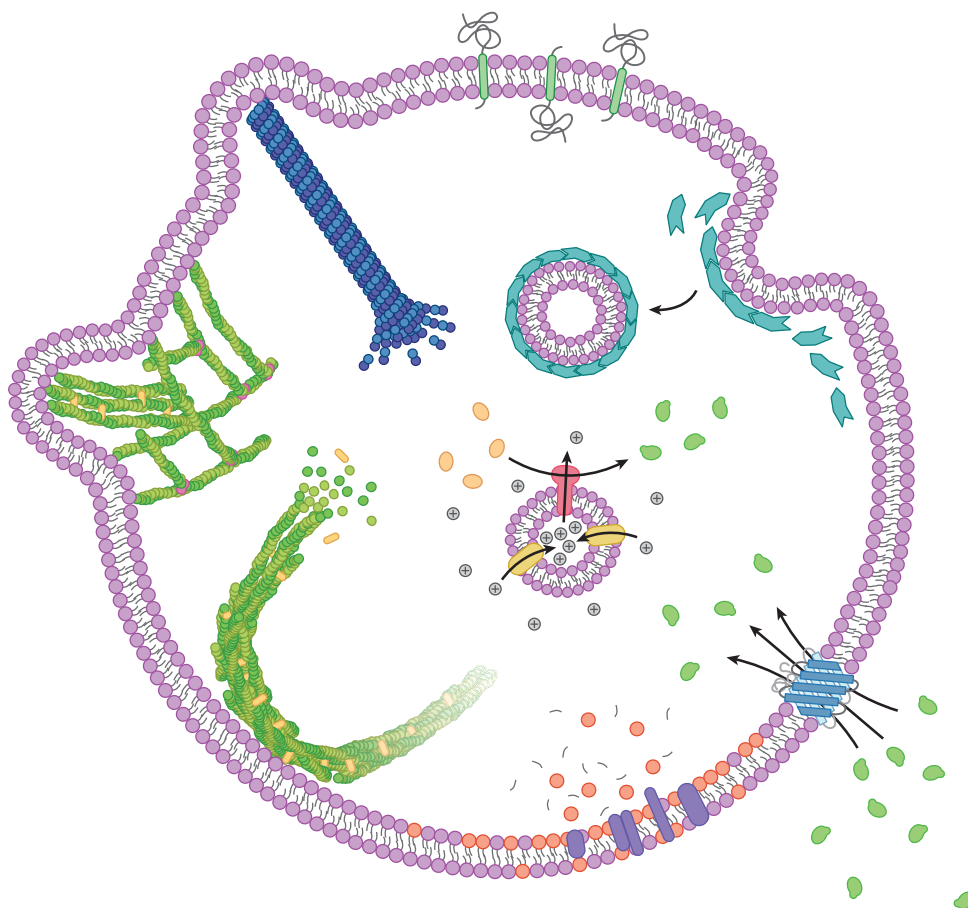
Figure 1

Hypothetical giant unilamellar vesicle containing protein systems that are of special interest to reconstitution studies.

2. METHODS OF PROTEIN ENCAPSULATION IN VESICLES

Giant unilamellar vesicles (GUVs) are made from amphiphilic molecules that form a single selective layer as an efficient boundary between an aqueous interior and an aqueous exterior. The most common type of vesicles are phospholipid vesicles, i.e., vesicles that consist of a bilayer of phospholipids and, therefore, best represent the cell membrane in structure and function. Phospholipids, such as phosphatidylcholines and phosphatidylethanolamines, are organic molecules that consist of a hydrophilic head group attached to two hydrophobic carbon chains. Above a certain concentration threshold (the so-called critical bilayer concentration) (99), phospholipids self-assemble into bilayers that spontaneously form spherical vesicles.

Such vesicles can be generated in a large range of sizes. Small unilamellar vesicles (SUVs) and large unilamellar vesicles (LUVs), which are both often referred to simply as liposomes, have long found applications as encapsulating compartments in areas such as pharmaceutics as drug delivery systems (5) or in cosmetics and other industries. These smaller vesicles are also useful in many ways in reconstitution experiments; for example, they can be used as intermediates when handling non-soluble membrane proteins or to investigate protein–membrane interactions with more analytical methods. GUVs are between 1 μm and 200 μm in size and thus roughly in the same size range as biological cells. Due to their size, GUVs are compatible with light microscopy assays, making them the preferred systems for biological reconstitution experiments using fluorescence imaging methods. The term unilamellar indicates that the membrane consists of a single bilayer. While the differentiation between unilamellar vesicles and the usually undesired multilamellar vesicles (MLVs) used to be critical with traditional methods for vesicle generation, modern encapsulation techniques generate unilamellar vesicles by default. A more desirable variant are multicompartment vesicles, either as vesicles that contain nested vesicles (vesosomes) (29) or with equally sized compartments that share a single outer membrane leaflet (28, 35).

The techniques used to generate lipid vesicles have evolved over the past decades, and recent advances have greatly improved reproducibility and potential applications. In this review, we give a brief overview of the most common techniques and discuss their suitability for encapsulating protein solutions within GUVs.
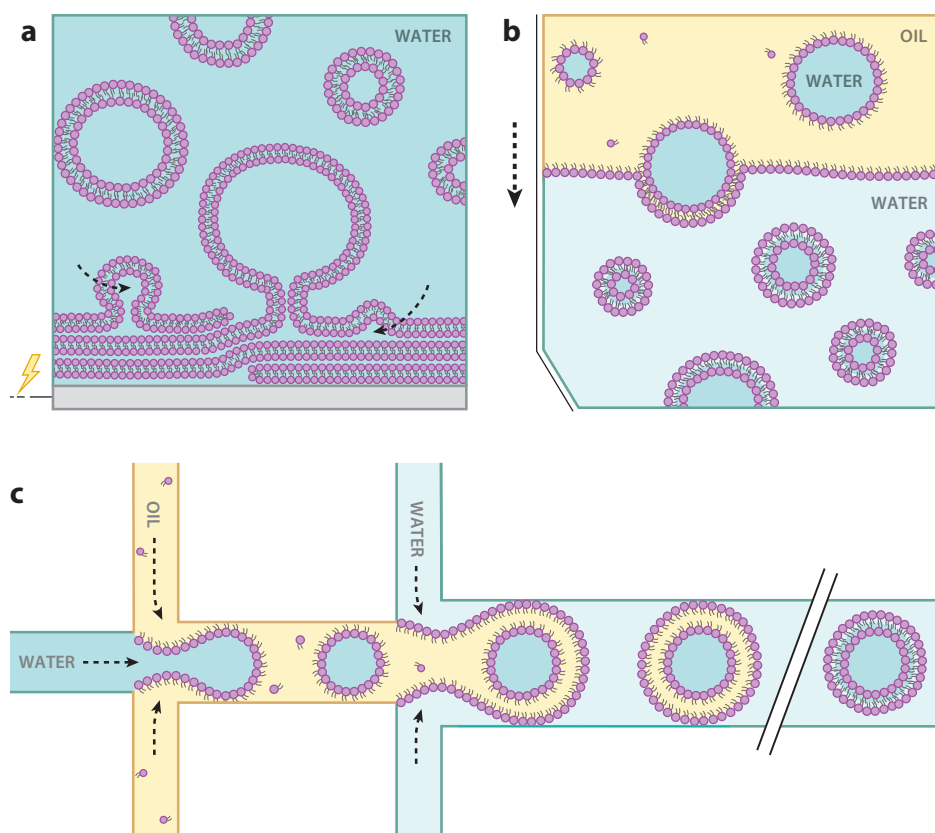
2.1. Lipid Film Hydration Methods

The formation of GUVs by hydration (also called swelling) is one of the earliest techniques for generating such vesicles (124). While some of the more recently developed methods discussed below facilitate the targeted encapsulation into GUVs, hydration methods are still the most frequently used techniques for the general preparation of GUVs as model membranes.

For the hydration method, phospholipids dissolved in chloroform are deposited as lipid films on a substrate such as glass. The lipid solution is then dried down to form lipid films. Subsequently, an aqueous solution is added, and the so-called swelling process starts. During this process, the aqueous solution penetrates the lipid film and forms membranous bubbles that eventually become vesicles (**Figure 2a**). This type of hydration has certain restrictions regarding the lipid compositions (ideally charged lipids) and requires low salt concentrations (3). For the standard gentle hydration method, the sample needs to be incubated above the phase transition temperature of the lipids, and the process takes an extended amount of time, usually overnight. Many variations have been developed that improve and extend the method according to various requirements (3, 61, 157), but each approach comes with its own drawbacks.

The most notable variant is the electroformation method. In this approach, swelling is assisted by an externally applied electric field (8). The lipid films are deposited on conductive surfaces

Figure 2

Giant unilamellar vesicle encapsulation methods. (*a*) Hydration method. Dried lipids form layered lipid films. Upon addition of water, lipid films hydrate, forming vesicular structures. If this process takes place on an electrode with an applied alternating electric current, then the process can be much more efficient. (*b*) Inverted emulsion transfer. A water-in-oil emulsion is prepared in which the lipid monolayer–lined aqueous droplets contain the protein solution. These droplets then pass through a second, planar water–oil interface where they become coated with the outer membrane leaflet. (*c*) Microfluidic method based on double emulsions. Water-in-oil-in-water double emulsions are generated using microfluidic polydimethylsiloxane (PDMS) chips (or with glass capillaries). The oil contains solubilized lipids, so that lipid monolayers assemble at the two interfaces of each droplet. In a second step (not shown), the oil phase has to be removed for a bilayer to form.

(usually indium tin oxide–coated glass or platinum wires). Because it uses the alternating electrical field as an additional driver of the spontaneous rehydration process, this method is much faster than the standard hydration (which is also called gentle hydration) and produces a higher yield of larger, more homogenous vesicles. While the electroformation method is preferred by many over gentle hydration, its major drawbacks come from being mostly incompatible with charged molecules. As such, this method is largely restricted to phospholipids with a neutral net charge and also requires solutions with low ionic strengths. Thus, the method is incompatible with most buffer conditions required for protein functionality (100). Over the years, improved protocols were proposed such that more complex solutions with physiologically relevant salt concentrations (100, 118, 135) and even charged lipids (143) could be employed. Nevertheless, the basic principles

of hydration methods render it difficult for large and complex molecules to penetrate the dried lipid films during the swelling step. This often results in a low encapsulation efficiency or overall failure to encapsulate these molecules. Following vesicle generation, the surrounding phase needs to be exchanged (i.e., highly diluted), and proteins that interact with membranes—which, naturally, are often the subject of reconstitution studies with vesicles—complicate the process even further. Other aspects, like the long incubation times or the low salt concentrations, might not be problematic if proteins are to be added to the outside solution after vesicle generation but render these methods problematic for encapsulation experiments.

2.2. Inverted Emulsion Transfer Methods

In recent years, inverted emulsion transfer methods (113) have proven to be among the most successful strategies for encapsulating complex solutions into vesicles. While this technique has its own challenges, many of the struggles that come with hydration methods are circumvented (encapsulation efficiency, multilamellarity) or far less critical (incubation times, charged molecules). Generally speaking, there are significantly fewer limitations to what can be encapsulated with emulsion transfer, as even large objects, close to the size of the final vesicle, can be encapsulated. Emulsion transfer methods, as well as the subsequent methods discussed in this review, are based on the ability of lipids to assemble into lipid monolayers at water–oil interfaces. This robust process can be used to convert lipid-layered water-in-oil droplets into lipid vesicles (**Figure 2*b***). Even asymmetric bilayers with leaflets of different lipid compositions can be produced, as the two monolayers that eventually form the vesicle membrane assemble independently (112). While there are fewer restrictions on the types of lipids that can be used, the final composition in the vesicle membrane can differ from the initial composition in the oil due to different interface adsorption kinetics, which depend on the lipid species.

While this is a very reliable method once established in a laboratory setting, some of the steps can initially be difficult to reproduce (152, 156). Details such as the composition of the (mineral) oil used or the humidity of the ambient air can be critical. (For the latter, it can be beneficial to use a humidity-controlled glove box.) If a simple procedure with little specialized equipment is desired, then the standard emulsion transfer technique developed by Pautot et al. (113) is an excellent choice, facilitating encapsulation drastically better than hydration methods and with only a few compromises compared to the methods discussed below, which allow for full or partial control over vesicle size and other parameters by employing microfluidics.

Some of these more sophisticated methods are directly based on the emulsion transfer principle but additionally utilize microfluidic components (90, 102). One such method that has gained popularity recently is the cDICE (continuous droplet interface crossing encapsulation) method developed by Massiera and coworkers (2). Particularly in combination with a novel protocol to prepare lipid-in-oil mixtures developed by the same group (22), this technique has proven successful in reconstituting several more complex protein–membrane systems and has been adapted by other groups (71, 79, 80, 84).

2.3. Microfluidic Methods

Another category of methods is based on the microfluidic generation of water-in-oil-in-water double emulsions (107) (**Figure 2*c***). Double emulsion droplets by default resemble vesicles in that they are aqueous compartments in a surrounding aqueous environment but with a compartmentalizing shell made from bulk liquid oil. Double emulsions can be stabilized by lining the two water–oil interfaces with lipid monolayers, in which case they only differ from vesicles due to the large quantities of oil trapped between the two leaflets of the bilayer. Various methods

were developed to remove the oil, either by solvent extraction (115, 150) or budding-off of the oil through interfacial forces (30). In a very similar way, double emulsions can be made in glass capillaries instead of silicone [polydimethylsiloxane (PDMS)] chips (153). The advantage of glass is that it is resistant to solvents like toluene or chloroform that are used for the oil extraction process (137). A method based on a different approach is the so-called jetting technique (42, 142), which under certain circumstances can also allow for the generation of quasi-oil-free bilayers (69). One strength shared by the microfluidic methods discussed above is that they allow for the generation of monodisperse vesicles.

The common thread between emulsion transfer and these microfluidic methods is the use of oil as a lipid solvent and water–oil interfaces as scaffolds for lipid monolayer assembly. Generally, these methods simplify the encapsulation of complex solution and allow flexibility regarding the choice of lipids. However, the mechanism is prone to producing membranes with trace amounts of oil between the bilayer leaflets. The amount of oil is small enough to not measurably alter the membrane thickness and does not affect most physiologically relevant properties (17, 98) and biocompatibility [e.g., transmembrane proteins are still readily incorporated into the membrane (2, 28, 30, 111)], but the minute presence of oil has been shown to result in vesicles with different dynamical properties in membrane nanotube experiments (17).

Recently, Weiss et al. (158) introduced a new microfluidic vesicle generation approach that is most likely unaffected by these uncertainties. This vesicle generation process relies on the charge-mediated fusion of SUVs inside a surfactant-stabilized droplet (55), a principle similar to techniques for generating planar supported lipid bilayers (SLBs). While a simplified version of the protocol was recently presented that does not require specialized equipment (52), the original method beautifully demonstrated some of the advantages that microfluidic techniques can offer: The technique allows for the sequential addition of several components through pico-injection (1) into a droplet-stabilized GUV. Weiss et al. showed that this temporal control can be crucial to reconstituting different features and cellular functionalities within one vesicle (158).

In summary, there are many different approaches for generating GUVs. In many cases, gentle hydration methods are still the standard for protein reconstitution experiments, in which free-standing model membranes are required, and addition of protein from the outside is sufficient. In particular, for quantitative membrane protein biochemistry and biophysics experiments, these assays guarantee that results are not affected by additional chemicals, such as trace amounts of oil in the bilayer. However, these methods often turn out to be incompatible with encapsulation of complex protein solutions. Therefore, it is very promising that, with emulsion transfer methods and microfluidic methods becoming more widespread, practical alternatives are available.

3. SUCCESSFULLY RECONSTITUTED PROTEINS AND PROTEIN MACHINERIES

3.1. Cytoskeletal Proteins

Phospholipids are not the only biomolecules that self-organize into large-scale assemblies. Cytoskeletal proteins polymerize into higher-order structures with emergent properties surpassing those of their individual units, forming elaborate networks that span the entire cell. These multipurpose structures are critical for myriad cellular processes, such as determining cell shape, regulating division and migration, and guiding intracellular transport, on scales several orders of magnitude larger than their building blocks. In this review, we focus on actin filaments and microtubules, which have been studied on and in model membranes for decades. Intermediate filaments and septins (now often referred to as the fourth type of eukaryotic cytoskeletal protein) have only

recently come into the spotlight, and in vitro studies are still limited in some respects. However, we also discuss work involving prokaryotic cytoskeletal proteins, most of which are homologs of eukaryotic proteins but can act in very different ways.

3.1.1. Actin. Actin not only was one of the first proteins to be subjected to in vitro experiments (146), but also remains one of the most prevalent candidates in current biophysical reconstitution experiments (47, 82). In fact, many of the methodological papers introduced in the previous section use actin as an example to demonstrate possible applications (2, 141, 157, 158). Thus, we also use actin reconstitution to exemplify the development of in vitro reconstitution and as a first example for protein encapsulation.

Many current actin reconstitution studies focus on actin–membrane interactions, as many actin-binding proteins are directly regulated via interactions with phospholipid bilayers (33). For these studies, SLBs can be the most straightforward model membrane system owing to their ease of preparation, stability, ability to form lipid patterns, and compatibility with most light microscopy methods (74). However, their physical properties, such as lipid diffusivity (121, 140) and deformability, drastically differ from cellular membranes and also from the free-standing bilayers of lipid vesicles, rendering the latter potentially more attractive to researchers in the field. While encapsulation of functional actin into vesicles is technically challenging, any of the methods discussed above can be used to generate vesicles as a membrane scaffold to bind proteins to their outside. Extensive experiments with actin on the outside of GUVs have been performed to investigate interactions between cytoskeletal proteins and membranes (18–20, 81, 83). The actin cytoskeleton has been a great system to study the role of compartmentalization and boundaries in the self-organization of biological systems. As mentioned above, microfluidic compartments (31, 138) or water-in-oil droplets (64, 65, 97) can also be used to study this aspect.

While work with proteins in vesicles has undergone a recent spike in popularity due to the prospect of creating artificial cells, encapsulation of actin in vesicles actually goes as far back as the late 1980s and early 1990s (23, 78, 95, 96). With emulsion transfer methods and microfluidics not yet existing, these studies used hydration methods, or even older techniques, to encapsulate actin inside vesicles. As described above, it can be challenging to encapsulate proteins such as actin under physiological conditions with these methods, not only because of electrostatic interactions, but also because polymerizing filaments are unlikely to penetrate the swelling membranes. To circumvent these issues, actin can initially be encapsulated under nonpolymerizing conditions with low salt concentrations. Polymerization is then induced by ion transport through the membrane, for example, through ion carriers like valinomycin or through electroporation. Actin in combination with bundling protein was reconstituted in GUVs by Honda et al. (60) and later systematically characterized by Tsai & Koenderink (151) (**Figure 4**), who observed that proteins like fascin, which cross-links actin into thick bundles, cause spike-like membrane protrusions or deform the entire vesicle into a rod-like shape, a process that is reversible when actin bundles are subsequently disassembled (12, 79). Limozin & Sackmann (79) observed that actin bundles can spontaneously form rings (and supercoiled rings) in vesicle confinement (**Figure 3b**), and recently, Litschel et al. (79) have come one step closer to reconstituting cell division by anchoring actin rings to the membrane and showing how this can lead to membrane deformations.

One frequently reconstituted physiological feature is the cell cortex, which in vivo primarily consists of cross-linked mesh-like actin networks. Early reports of a reconstituted actin cortex showed the formation of shell-like actin structures that form spontaneously without the addition of actin–membrane linkers (53, 76) (**Figure 3c**) and that have also been studied in detail for their mechanical properties (114, 130, 131, 163). The interactions between actin and the membrane in these vesicles are nonspecific and typically mediated by magnesium ions, a mechanism that has

Actin   Microtubules   Prokaryotic cytoskeleton
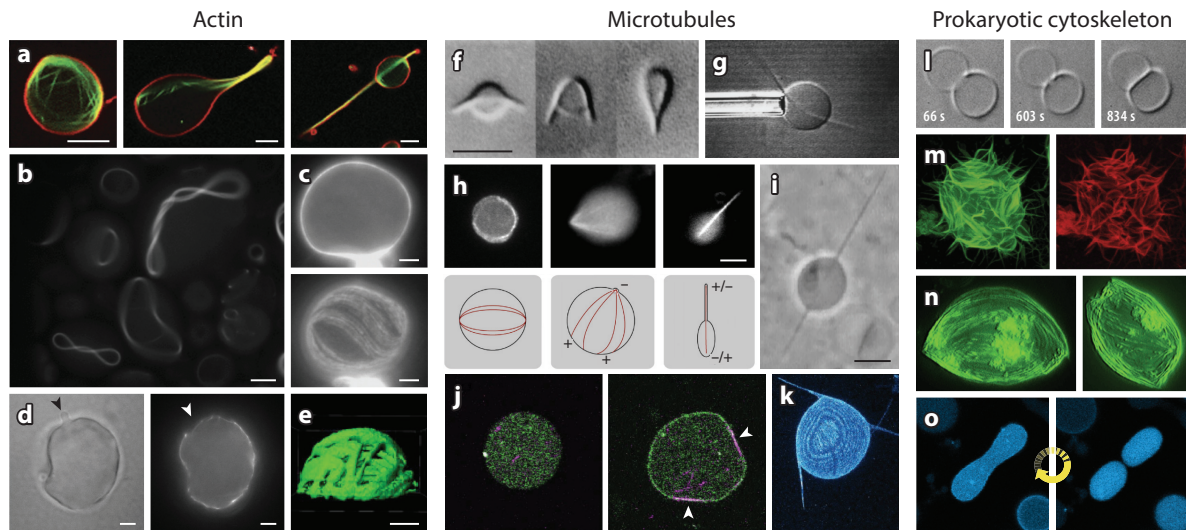
Figure 3

Giant unilamellar vesicles (GUVs) containing cytoskeletal assemblies. (*a*) Actin bundles in osmotically deflated vesicles can drastically determine vesicle shape. Panel adapted with permission from Reference 151. (*b*) Bundled actin can form rings or even supercoiled rings in vesicle confinement. Panel adapted with permission from Reference 77. (*c*) Membrane-bound actin bundles form a cortex and align in parallel. Panel adapted with permission from Reference 76. (*d*) Vesicle blebbing through contracting actomyosin cortex. Panel adapted with permission from Reference 84. (*e*) Deformed active actin cortex upon vesicle adhesion to a surface. Panel adapted with permission from Reference 86. (*f*) Membrane tension bends microtubule (MT) bundles in the vesicle. Panel adapted with permission from Reference 45. (*g*) MT bending can be controlled through micropipette aspiration. Despite the appearance, MTs are fully contained within the vesicle membrane. Panel adapted with permission from Reference 44. (*h*) Membrane stiffness determines organization of encapsulated MTs. Panel adapted with permission from Reference 116. (*i*) Long membrane protrusions in the MT-containing vesicle. Panel adapted with permission from Reference 38. (*j*) Light activation allows switching between different states of the MT-containing vesicle. Panel adapted with permission from Reference 129. (*k*) Dynamic vesicle containing MTs and motor proteins. Panel adapted with permission from Reference 71. (*l*) The FtsZ-ring divides the GUV. Panel adapted with permission from Reference 110. (*m*) Heavy deformation of a vesicle caused by membrane-bound FtsZ. Panel adapted with permission from Reference 66. (*n*) MreB controls vesicle shape. Panel adapted with permission from Reference 48. (*o*) Periodic vesicle deformations caused by Min protein oscillations. Panel adapted with permission from Reference 80. All scale bars are 5 μm.

not yet been shown to be relevant in vivo (132). Later work focused on reconstituting a thicker, mesh-like cortex by using actin cross-linkers, such as Arp2/3, and by binding actin through specific interactions to the vesicle membrane (93, 101, 117). Myosin activity in the cell cortex is crucial for dynamic remodeling and force exertion and has been the subject of several recent reconstitution approaches of actin cortices (20, 86, 152). Specifically, the Bausch group has been using actomyosin systems within vesicles to reconstitute features like blebbing of vesicles (84) (**Figure 3***d*), adhesion (86) (**Figure 3***e*), and cell protrusions (34) with physiologically relevant actin binding proteins.

3.1.2. Microtubules. While actin organization heavily depends on cross-linking proteins to achieve the various properties required for cell functions, single microtubules (MTs) are often spaced far apart and can act individually as transport tracks or structural elements (94). MTs are able to achieve this because they have a much greater bending stiffness (flexural rigidity) compared to actin, such that even single MTs are strong enough to resist compressive forces without buckling. When aligned into bundles, this rigidity naturally increases. Due to these mechanical properties, visible membrane deformations were observed in early encapsulation experiments with

534   Litschel • Schwille

dark-field microscopy (62), consistent with current studies. Specifically, the Libchaber group focused on the interplay between vesicles and microtubules, i.e., deformations of the membrane (45) (**Figure 3***f*) and buckling of the microtubules (37, 44) (**Figure 3***g*).

While actin encapsulation in vesicles has often been performed with the aim of reconstituting dynamic processes, such as membrane remodeling and motility-related functions, the motivation for encapsulating MTs is less obvious, as they play more indirect roles in concert with membranes in vivo. However, encapsulating dynamic MTs is nevertheless illuminating, particularly when aiming at a holistic model for artificial cells or more sturdy mimicries of living systems. Some groups have begun using the term molecular robots (54) for encapsulated dynamic MTs (58, 129) (**Figure 3***j*). Dogic and coworkers developed an active nematic system based on MTs with modified kinesin motors. Under confinement, not only did these components show nematic alignment on spherical surfaces, but the system was also shown to actively deform vesicles (71) (**Figure 3***k*) and autonomously move droplets through internal MT sliding (128).

3.1.3. Prokaryotic cytoskeleton.

While work with actin and MTs has been popular in reconstitution experiments for decades, prokaryotic cytoskeletal systems, although generally lower in complexity and thus simpler to recapitulate in vitro, can be more challenging, often due to the smaller scale of the cytoskeletal structures. While a contractile actomyosin ring in a eukaryotic cell is an easily discernible structure for contemporary fluorescence microscopes, a bacterial Z ring can be less than 1 micron in size and thus close to the microscope's diffraction limit. This factor also plays a role when attempting to reconstitute these protein systems within vesicles, and, in fact, vesicles the size of bacterial cells barely fall under common definitions of GUVs (1–200 μm). Nevertheless, exciting discoveries have been made through reconstitution of prokaryotic cytoskeleton proteins in GUVs, either by using sufficiently small vesicles or because the reconstituted features were scalable to larger sizes.

The most notable prokaryotic cytoskeletal protein might be the cell division protein FtsZ. FtsZ is a tubulin homolog found in almost all bacterial cells and even in chloroplasts and some mitochondria. The first reconstitution approaches of FtsZ in vesicles were performed by Erickson and colleagues, initially in tubular multilamellar vesicles (109) and later in more cell-like unilamellar vesicles (110). The major finding in these studies was that FtsZ assembles into rings in small GUVs and can constrict or even divide vesicles, similar to the proposed function in vivo (**Figure 3***l*). Later studies demonstrated that larger vesicles can also be useful to investigate aspects like FtsZ-mediated membrane deformation, even though FtsZ bundles are smaller than the size of the vesicles (16, 43, 46, 85, 122) (**Figure 3***m*).

Different bacteria make use of a variety of different actin homologs, which were found to fulfill a diverse array of functions. MreB is such a protein and has been used to demonstrate protein expression in vesicles (87, 89). Recent work showed that MreB bundles form a cortex and govern vesicle shape driven by membrane crowding (48, 49) (**Figure 3***n*).

3.2. Membrane Proteins

Membrane proteins have myriads of different functions and give each type of cell membrane its characteristic properties. They account for about half of the mass of a typical plasma membrane and even more in other types of membranes (4). Membrane proteins can be broadly classified into two categories based on whether they are transiently or permanently associated with the membrane: peripheral membrane proteins and intrinsic membrane proteins. The most common type of intrinsic membrane proteins are transmembrane proteins.

3.2.1. Peripheral membrane proteins. Peripheral membrane proteins bind to membranes transiently. They are cytosolic but can interact with or insert into a single leaflet of the bilayer. These proteins often alternate between membrane-bound and unbound states, which can correspond to physiologically active and inactive states of the protein. Peripheral membrane proteins play important regulatory roles in many processes, including signaling, channel regulation, and membrane remodeling.

The Min proteins from *Escherichia coli* are prime examples of transiently binding membrane proteins. Like FtsZ (see Section 3.1.3.), the Min protein system is part of the bacterial cell division machinery. In many bacteria, FtsZ is spatially positioned by the proteins MinD, MinE, and MinC in the process of cell division. In *E. coli*, the Min proteins oscillate between the two cell poles, based on a reaction–diffusion mechanism, and thereby direct the Z ring to the cell center. This impressive self-organization dynamics of Min proteins, which is only unfolded in the presence of membranes, makes them a highly attractive model system for studies with model membranes. By repeatedly binding and unbinding from the membrane in a coordinated fashion, Min proteins generate observable oscillatory reaction–diffusion patterns. Reaction–diffusion mechanisms are susceptible to their confinement geometry, and compartmentalization of the Min proteins leads to in vivo–like standing wave oscillation (21, 164, 165), different from the traveling waves observed in open systems. When reconstituted in GUVs, the membrane detachment and attachment of the proteins periodically deformed the vesicles, resembling vesicle division (51, 80) (**Figure 3o**). As such, encapsulating the Min system illustrates a great example of the benefits of encapsulation in lipid vesicles, both demonstrating an effect of limiting the reaction space by confinement and showing how protein–membrane interactions can lead to membrane deformations.

For Min proteins, the observation of membrane deformation came as an unexpected result, as these proteins are not thought to be directly responsible for membrane remodeling in vivo. However, many peripheral membrane proteins are primary players in such processes, and have therefore been studied in vitro, particularly in the context of membrane remodeling. **Figure 4b** shows different mechanisms through which peripheral membrane proteins can determine membrane shape: (*a*) insertion into the membrane, thereby inducing membrane bending; (*b*) imposition of their own shape onto the membrane; (*c*) scaffold assembly; and (*d*) steric hindrance, whereby crowding of membrane-bound proteins can cause the membrane to buckle. Oftentimes, peripheral membrane proteins use a combination of these mechanisms to deform lipid bilayers and regulate membrane shape.

GUVs, because they are deformable, free-standing membranes with negligible curvature on the molecular scale, are ideally suited to work with peripheral membrane-transforming proteins, as proteins can often just be added to the outside of vesicles. For example, vesicular trafficking proteins like clathrin and COPII were reconstituted on GUVs, leading to membrane budding and tubulation (10, 127). However, encapsulation inside vesicles has proven to be important to achieving certain cell-like membrane topologies. By combining protein encapsulation in vesicles with membrane nanotube pulling using optical tweezers and micropipettes, Bassereau and coworkers generated highly negative curvatures (120) and neck-like geometries (14, 26). These physiologically relevant topologies can be used to investigate curvature sensing and other properties of peripheral membrane proteins. With this technique, Prévost et al. (120) were recently able to show that the BAR domain protein IRSp53 preferentially binds to negatively curved membranes due to its intrinsic curvature.

In different work (14, 26), the same group encapsulated the ESCRT-III protein CHMP2B in GUVs. In this case, the protein bound preferentially to membrane topologies resembling dendritic spines. Interestingly, membrane-bound CHMP2B formed a diffusion barrier for lipids and other membrane-bound proteins. Additionally, in combination with other ESCRT-III complex
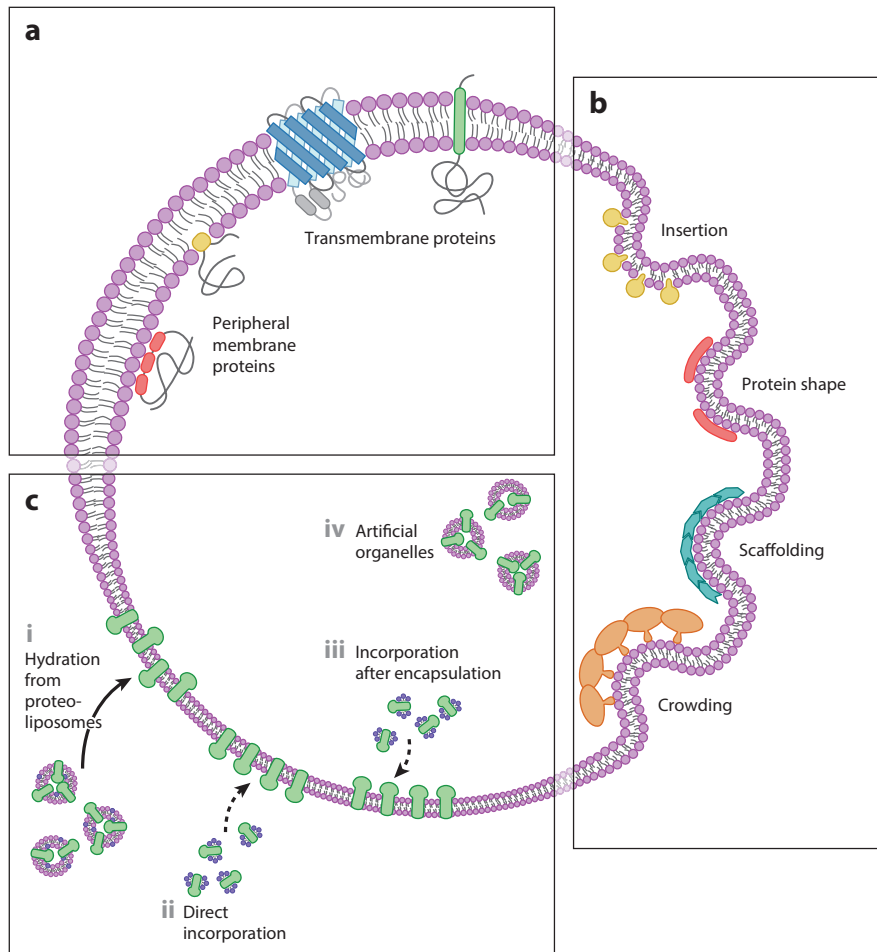
Figure 4

Graphical illustrations of membrane proteins. (*a*) Different types of membrane proteins. (*b*) Mechanisms of membrane remodeling by peripheral membrane proteins. Membrane curvature can be affected by insertion of hydrophobic protein motifs; by large proteins with several binding sites imposing their shape onto the membrane; through large-scale assemblies of proteins; or through protein crowding, where forces are exerted on the membrane due to steric collisions between proteins. For many membrane remodeling proteins, the exact mechanism is unknown and is likely a combination of some of the above. (*c*) Different methods for incorporating transmembrane proteins into giant unilamellar vesicles (GUVs) for in vitro reconstitution. From left to right: (*i*) GUVs can be generated from dried lipid films containing the proteins. By incorporating transmembrane proteins into pre-existing GUVs either (*ii*) from the outside or (*iii*) after encapsulation, the orientation of the transmembrane proteins can be controlled. (*iv*) Protein function can also be utilized by encapsulating transmembrane-containing small unilamellar vesicles (SUVs) as artificial organelles.

proteins, CHMP2B can deform pulled membrane nanotubes into corkscrew-like morphologies (14). In archaeal cells, homologs of these eukaryotic ESCRT proteins are responsible for cell division. Preliminary work with these archaeal homologs reconstituted inside GUVs showed invaginations of the vesicle membrane (56). These experiments demonstrate the potential for

using encapsulation to study the cellular membrane remodeling machinery, and reconstitution of such proteins offers another potential approach to achieving division of artificial vesicle compartments.

3.2.2. Transmembrane proteins.

While GUVs are an ideal model system for directly observing membrane remodeling and higher-order protein assemblies on membranes, most transmembrane proteins do not exhibit activities directly observable by light microscopy. Despite this, GUVs can be particularly valuable when studying transmembrane proteins, not only because freestanding bilayers are a prerequisite for unfolding most of their functions, but also because having compartmentalized volumes can be incredibly useful. Maintaining two separated aqueous phases is key to studying membrane potentials and concentration gradients created by channels, carriers, and pumps. Biophysicists have been studying membrane transport proteins for almost half a century—both in cells, using methods like patch clamp, and in vitro, using black lipid membranes or painted bilayers and smaller liposomes. Transmembrane proteins were incorporated into membranes of giant vesicles early on using hydration methods and even older techniques (24, 67). While some channel proteins are easily reconstituted, studies of other proteins have only been possible owing to recent methodological advances.

Figure 4c illustrates different methods to incorporate transmembrane proteins into GUVs. The first step for the reconstitution of transmembrane proteins in GUVs is usually the formation of SUVs or LUVs with incorporated proteins, which we refer to as proteoliposomes. As transmembrane proteins have large hydrophobic regions, they typically need to be solubilized using detergents during protein purification. Proteoliposomes are formed by mixing solubilized protein with lipid-detergent micelles and subsequently removing the detergent. When dried down into lipid films, these proteoliposomes can be used to form GUVs with straightforward hydration methods (25, 50). However, the drying step can be harmful to some membrane proteins. To reconstitute more delicate proteins, incorporation into preformed GUVs can be beneficial by allowing one to avoid the dehydration step. This is possible either by fusion of proteoliposomes with preformed GUVs (32, 68) or by omitting the step of proteoliposome formation altogether and directly incorporating detergent-solubilized proteins into GUVs (32).

Reconstitution of transmembrane channels into GUV membranes has a long history (67) and can only be touched upon, as we predominantly focus on GUVs as containers. However, below, we quickly highlight some examples that have proven useful as tools in contemporary in vitro reconstitution studies. As mentioned above, ion carriers can be used to create physiological salt concentrations within vesicles post–vesicle formation, which is especially useful when vesicles are formed in low-salt conditions in hydration methods. Ion carriers do not have to be proteins, but can instead be peptides (or even smaller molecules), such as the potassium carrier valinomycin, which has often been used for these applications (23, 32, 95). Another commonly used channel protein is the cytotoxic protein α-hemolysin, which, as a heptamer, forms large water-filled pores that allow even small biomolecules to pass through the membrane. α-Hemolysin is a popular tool in many reconstitution experiments. It can even be used to introduce ATP into vesicles, thereby triggering biological reactions (155) such as actin polymerization. Often, α-hemolysin is used to introduce a fluorescent dye into the vesicle lumen as a control to demonstrate membrane functionality (2, 28, 30, 35, 98, 103, 111, 142). Microfluidic chips with vesicle traps can be particularly useful for these kinds of assays, as they hold the vesicle in place while exchanging the surrounding solution (to incorporate α-hemolysin or add a fluorescent dye), so that the same vesicle can be imaged over the course of the experiment (126). Recently, transmembrane pores and channels have again come into focus in the context of creating artificial cells, as groups are trying to engineer primitive means of communication between these compartments (9, 123).

Membrane proteins are generally asymmetric, possessing two hydrophilic parts with very different properties, sizes, and function. Even large pores like α-hemolysin transport asymmetrically (92). Therefore, the orientation of the incorporated transmembrane proteins generally matters for their functionality. The methods described above for membrane protein incorporation involving the use of proteoliposomes typically result in more or less randomly oriented transmembrane proteins, which in most cases is a satisfactory outcome. Often, the wrongly incorporated proteins are simply rendered dysfunctional due to their orientation and have a negligible effect on the outcome of the experiment, leaving the membrane with sufficient amounts of functional proteins. For example, even highly asymmetric transmembrane proteins, like the focal adhesion protein integrin (41, 144) or the SNARE protein synaptobrevin (11, 148), have been reconstituted using such approaches. For both of these examples, the physiologically accurate orientation has the larger hydrophilic part outside of the vesicle; however, outside-in coincorporated proteins do not affect these reconstitution experiments negatively.

For certain proteins, controlling orientation can be important—for example, for proton pumps like bacteriorhodopsin, where a pH gradient will be generated across the vesicle membrane only with a preferential asymmetric incorporation (32, 50, 68). This can be achieved with direct incorporation of detergent-solubilized transmembrane proteins into preformed vesicles (32). If membrane proteins are incorporated from the outside solution into the vesicle membrane, then proteins are inserted with their most hydrophilic domain pointing outward. In the case of bacteriorhodopsin, this results in cytoplasmic regions that face outward (inside-out orientation) but that also create a proton surplus within the vesicles, as is potentially desired (32).

In cells, the more hydrophilic regions of transmembrane proteins usually face the cytosol [to be more precise, generally, the more positively charged part faces inward (57)]. To preferentially reconstitute this opposing orientation, encapsulation methods are used (7, 125, 160). Via encapsulation of solubilized membrane proteins, proteins can be directed to orient their most hydrophilic part toward the vesicle center. Using this approach, physiologically oriented incorporation of proteins has been demonstrated for potassium channels (160); for photosynthetic reaction centers (7); and, with a comparable approach, for SNARE proteins (125).

ATP synthases make up an important class of transmembrane proteins that use proton gradients to produce ATP; as such, researchers have long attempted to coreconstitute these proteins with bacteriorhodopsin. With the goal of establishing photosynthesis of ATP, this system has been of special interest in the context of synthetic cells. Again, asymmetric incorporation is crucial, as a proton gradient is required to successfully generate ATP inside the vesicle. Interestingly, photosynthetic ATP generation has been achieved not by incorporating the proteins into the GUV membrane itself, but by encapsulating proteoliposomes (SUVs) containing both proteins into the GUVs without merging them with the GUV membrane (13, 75). The proteins are incorporated inside-out into the SUVs, such that protons are pumped into the SUVs, and ATP is generated in the GUV lumen. Remarkably, these synthetic organelles have been demonstrated to produce sufficient ATP to power actin assembly (75) and synthesis of GFP (13).

3.3. Enzymes

Enzymes are biological catalysts that guide networks of chemical transformations in cells. Acting in organized sequences, enzymes coordinate the many stepwise reactions in metabolic pathways by which nutrients are degraded, chemical energy is transformed and stored, and larger molecules are synthesized from simple precursors. As many cellular reactions would not be possible or would take years without catalysis, enzymes are ubiquitously required but, at the same time, highly spatially targeted. Through spatially and temporally regulated expression of enzymes, the cell can control which of the many possible chemical reactions actually take place.

3.3.1. Metabolic reactions.

For biological reactions, spatial confinement can be a defining factor. While the effect of space and scale is especially pronounced for reaction–diffusion mechanisms like the Min system (see above), metabolic reactions are affected as well. Virk et al. (154) found that, when encapsulated inside GUVs, an alcohol oxidase enzyme was 3.5 times more active and 20 times more stable than in bulk. They argued that encapsulation of enzymes in vesicles can protect the enzyme from proteases or self-denaturation. Nonspecific interactions with the encapsulating membrane have also been thought to have stabilizing effects on enzymes (161).

Generally, GUVs are relatively large compared to the molecular scale, and effects of confinement are much more pronounced in smaller vesicle compartments like SUVs, where stochastic effects come into play (72). However, for some complex biochemical reactions, GUV confinement can be a determining factor for reaction dynamics. This is particularly the case for reaction–diffusion systems, like the above-mentioned Min protein system (80), where biochemical reactions are spatially coupled. Traveling waves can thus form with wavelengths on the scale of the GUVs themselves. In this case, the presence of a confining membrane is of great relevance, as it induces a symmetry break with respect to free 3D diffusion.

Membranes, as confining boundaries, further enable intracellular compartmentalization, a key feature of all eukaryotic life forms. The separation of the intracellular space into membrane-bound compartments allows crucial biochemical reactions to take place in optimized microenvironments. Therefore, imitating cell organelles has been the subject of several in vitro studies in the recent years (29, 52, 75). Elani et al. (35, 36) achieved remarkably complex spatial organization of enzymatic reactions within vesicles by creating multicompartment supergiant vesicles with multistep enzymatic cascades. In this case, the different steps of the reaction pathway are isolated by bilayers in equally sized vesicle compartments but connected via membrane channels, allowing the products of each step to traverse between the compartments (35). Elani et al. demonstrated the conversion of lactose into the fluorescent molecule resorufin in a three-step signaling cascade, with each of the steps taking place in a separate compartment. In another study, they encapsulated eukaryotic cells in GUVs, which contribute, as organelle-like modules, to a similar metabolic pathway (36). While the engineered eukaryotic cells only carry out the first step by converting lactose into glucose, a synthetic enzymatic cascade then processes glucose into the fluorescent product. Elani et al. also showed that the vesicle membrane can even help protect the encapsulated cells from a surrounding toxic solution.

3.3.2. Transcription–translation systems.

From the point of view of creating synthetic cells, protein synthesis in artificial lipid vesicles has been considered one of the greatest milestones. The first attempts at vesicle-encapsulated transcription were reported by the Luisi group, who synthesized short polypeptides with essential transcription components in small vesicles (105). Shortly after, Yu et al. (162) reported the first full protein synthesis inside giant vesicles. By encapsulating cell extract with nucleotides, amino acids, T7 RNA polymerase, and plasmids, they reconstituted both transcription and translation inside GUVs and were able to observe the synthesis of green fluorescent protein (GFP) by fluorescence microscopy (104, 162). An impressive demonstration of the forthcoming advances in the field was given by Noireaux & Libchaber (103), who fused the genes of eGFP and α-hemolysin and showed the successful synthesis and incorporation of the labeled transmembrane complex into the membrane from within the vesicle.

In the past few years, in vitro transcription and translation (TXTL) has developed into a powerful tool. This method provides a viable, convenient alternative to the traditional approach of generating pure proteins via expression in cells and is thus often referred to as cell-free protein synthesis. This success is the result of continuous improvements of the systems that are used. Modern cell-free protein synthesis allows for the production of large quantities of protein in just

a few hours. One milestone in the field was the development of the PURE (protein synthesis using recombinant elements) system, which is a protein expression system completely reconstituted from purified proteins without the use of cell extract (136). New commercial TXTL kits (such as new versions of the PURE system) are constantly being developed with improved efficiency and variability for cell-free protein expression.

The convenience and protein yield of these systems have improved greatly within the past few years, and TXTL has become a true alternative to traditional protein expression and purification for reconstitution experiments, even within GUVs. In fact, some of the above-mentioned examples of reconstitution within vesicles were conducted using TXTL in vesicles, rather than by encapsulating purified proteins (43, 48, 49, 51, 87, 89). Since the same encapsulation procedure can be used for the production of very different proteins, this could allow for streamlined protocols for the reconstitution of proteins in vesicles. In the case of transmembrane proteins, TXTL in vesicles can even simplify reconstitution experiments (88, 139). For example, expression of the bacterial transporter protein EmrE has shown that some of the technical challenges that come with the reconstitution of purified transmembrane proteins (see above) can be circumvented by synthesizing transmembrane proteins directly inside GUVs (139). Although the mechanism of the protein insertion is not fully understood (and must be different from both in vivo and conventional transmembrane reconstitution), more than 20% of the synthesized proteins can be incorporated into the vesicle membrane (139). A more cell-like approach is also being pursued by reconstituting translocons entirely through in vitro TXTL in GUVs (106).

One of the greatest challenges of the field of synthetic biology is lipid synthesis, as it provides the basis for vesicle surface growth (39). Kuruma et al. (73) have taken on this task, demonstrating an enzymatic cascade linking the synthesis of membrane proteins to synthesis and incorporation of lipids into the membrane. Using in vitro TXTL, two acyltransferases are synthesized inside small liposomes, which in turn produce phosphatic acids (the simplest forms of phospholipids) and incorporate them into the liposome membrane (73, 134). So far, these experiments have only been performed in SUVs; even if they are reproduced in GUVs, the yield of the reactions in the current form would be too low to result in observable changes in membrane area (15). However, reconstituting these two features—protein and membrane synthesis—within GUVs would be a great leap toward achieving replication of synthetic vesicles, and thus toward creating life-like artificial cells (39).

4. CONCLUSIONS AND OUTLOOK

GUVs have long been a popular model system to study the functionality of membrane-attached and transmembrane proteins in defined membrane environments. Through varying the membrane composition of GUVs, specific protein–protein and protein–lipid interactions could be reproducibly studied in great detail, in particular by fluorescence microscopy and spectroscopy. GUVs were also considered ideal starting points for a potential bottom-up assembly of functional biological modules into minimal protocells. However, many traditional GUV production methods make the incorporation of functional proteins into the membrane or the lumen of vesicles during their production extremely difficult, which has hampered the progress of many studies and restricted the use of the GUV model membrane system to a limited number of expert labs in the biomembrane field. However, recent breakthroughs, mainly from microsystems technology, have given us several simple and versatile methods that drastically simplify the production of large membrane-enclosed protein reaction systems. The development toward GUV-based protocells with complex functionalities will likely dramatically benefit from these technical breakthroughs,

promising an enormous acceleration of work with the aim to construct a minimal living cell—a goal that only recently seemed decades away but may actually be closer than we think.

DISCLOSURE STATEMENT

The authors are not aware of any affiliations, memberships, funding, or financial holdings that might be perceived as affecting the objectivity of this review.

ACKNOWLEDGMENTS

LITERATURE CITED

1. Abate AR, Hung T, Mary P, Agresti JJ, Weitz DA. 2010. High-throughput injection with microfluidics using picoinjectors. *PNAS* 107:19163–66

2. Abkarian M, Loiseau E, Massiera G. 2011. Continuous droplet interface crossing encapsulation (cDICE) for high throughput monodisperse vesicle design. *Soft Matter* 7:4610–14

3. Akashi K, Miyata H, Itoh H, Kinosita K. 1996. Preparation of giant liposomes in physiological conditions and their characterization under an optical microscope. *Biophys. J.* 71:3242–50

4. Alberts B, Johnson A, Lewis J, Raff M, Roberts K, et al. 2002. *Molecular Biology of the Cell.* New York: Garland Sci. 4th ed.

5. Allen TM, Cullis PR. 2004. Drug delivery systems: entering the mainstream. *Science* 303:1818–22

6. Almén MS, Nordström KJV, Fredriksson R, Schiöth HB. 2009. Mapping the human membrane proteome: A majority of the human membrane proteins can be classified according to function and evolutionary origin. *BMC Biol.* 7:50

7. Altamura E, Milano F, Tangorra RR, Trotta M, Omar OH, et al. 2017. Highly oriented photosynthetic reaction centers generate a proton gradient in synthetic protocells. *PNAS* 114:3837–42

8. Angelova MI, Dimitrov DS. 1986. Liposome electroformation. *Faraday Discuss. Chem. Soc.* 81:303–11

9. Aufinger L, Simmel FC. 2019. Establishing communication between artificial cells. *Chemistry* 25:12659–70

10. Bacia K, Futai E, Prinz S, Meister A, Daum S, et al. 2011. Multibudded tubules formed by COPII on artificial liposomes. *Sci. Rep.* 1:17

11. Bacia K, Schuette CG, Kahya N, Jahn R, Schwille P. 2004. SNAREs prefer liquid-disordered over "raft" (liquid-ordered) domains when reconstituted into giant unilamellar vesicles. *J. Biol. Chem.* 279:37951–55

12. Bashirzadeh Y, Wubshet NH, Liu AP. 2020. Confinement geometry tunes fascin-actin bundle structures and consequently the shape of a lipid bilayer vesicle. *Front. Mol. Biosci.* 7:337

13. Berhanu S, Ueda T, Kuruma Y. 2019. Artificial photosynthetic cell producing energy for protein synthesis. *Nat. Commun.* 10:1325

14. Bertin A, de Franceschi N, de la Mora E, Maiti S, Alqabandi M, et al. 2020. Human ESCRT-III polymers assemble on positively curved membranes and induce helical membrane tube formation. *Nat. Commun.* 11:2663

15. Blanken D, Foschepoth D, Serrão AC, Danelon C. 2020. Genetically controlled membrane synthesis in liposomes. *Nat. Commun.* 11:4317

16. Cabre EJ, Sanchez-Gorostiaga A, Carrara P, Ropero N, Casanova M, et al. 2013. Bacterial division proteins FtsZ and ZipA induce vesicle shrinkage and cell membrane invagination. *J. Biol. Chem.* 288:26625–34

17. Campillo C, Sens P, Köster D, Pontani L-L, Lévy D, et al. 2013. Unexpected membrane dynamics unveiled by membrane nanotube extrusion. *Biophys. J.* 104:1248–56

18. Caorsi V, Lemière J, Campillo C, Bussonnier M, Manzi J, et al. 2016. Cell-sized liposome doublets reveal active tension build-up driven by acto-myosin dynamics. *Soft Matter* 12:6223–31

19. Carvalho K, Lemiere J, Faqir F, Manzi J, Blanchoin L, et al. 2013. Actin polymerization or myosin contraction: two ways to build up cortical tension for symmetry breaking. *Philos. Trans. R. Soc. Lond. B* 368:20130005

20. Carvalho K, Tsai FC, Lees E, Voituriez R, Koenderink GH, Sykes C. 2013. Cell-sized liposomes reveal how actomyosin cortical tension drives shape change. *PNAS* 110:16456–61

21. Caspi Y, Dekker C. 2016. Mapping out Min protein patterns in fully confined fluidic chambers. *eLife* 5:e19271

22. Claudet C, In M, Massiera G. 2016. Method to disperse lipids as aggregates in oil for bilayers production. *Eur. Phys. J. E* 39:9

23. Cortese JD, Schwab B 3rd, Frieden C, Elson EL. 1989. Actin polymerization induces a shape change in actin-containing vesicles. *PNAS* 86:5773–77

24. Criado M, Keller BU. 1987. A membrane fusion strategy for single-channel recordings of membranes usually non-accessible to patch-clamp pipette electrodes. *FEBS Lett.* 224:172–76

25. Darszon A, Vandenberg CA, Schönfeld M, Ellisman MH, Spitzer NC, Montal M. 1980. Reassembly of protein-lipid complexes into large bilayer vesicles: perspectives for membrane reconstitution. *PNAS* 77:239–43

26. De Franceschi N, Alqabandi M, Miguet N, Caillat C, Mangenot S, et al. 2019. The ESCRT protein CHMP2B acts as a diffusion barrier on reconstituted membrane necks. *J. Cell Sci.* 132:jcs217968

27. Deamer D, Dworkin JP, Sandford SA, Bernstein MP, Allamandola LJ. 2002. The first cell membranes. *Astrobiology* 2:371–81

28. Deng N-N, Yelleswarapu M, Huck WTS. 2016. Monodisperse uni- and multicompartment liposomes. *J. Am. Chem. Soc.* 138:7584–91

29. Deng N-N, Yelleswarapu M, Zheng L, Huck WTS. 2017. Microfluidic assembly of monodisperse veso-somes as artificial cell models. *J. Am. Chem. Soc.* 139:587–90

30. Deshpande S, Caspi Y, Meijering AEC, Dekker C. 2016. Octanol-assisted liposome assembly on chip. *Nat. Commun.* 7:10447

31. Deshpande S, Pfohl T. 2015. Real-time dynamics of emerging actin networks in cell-mimicking compartments. *PLOS ONE* 10:e0116521

32. Dezi M, Di Cicco A, Bassereau P, Lévy D. 2013. Detergent-mediated incorporation of transmembrane proteins in giant unilamellar vesicles with controlled physiological contents. *PNAS* 110:7276–81

33. Doherty GJ, McMahon HT. 2008. Mediation, modulation, and consequences of membrane-cytoskeleton interactions. *Annu. Rev. Biophys.* 37:65–95

34. Dürre K, Keber FC, Bleicher P, Brauns F, Cyron CJ, et al. 2018. Capping protein-controlled actin polymerization shapes lipid membranes. *Nat. Commun.* 9:1630

35. Elani Y, Gee A, Law RV, Ces O. 2013. Engineering multi-compartment vesicle networks. *Chem. Sci.* 4:3332–38

36. Elani Y, Trantidou T, Wylie D, Dekker L, Polizzi K, et al. 2018. Constructing vesicle-based artificial cells with embedded living cells as organelle-like modules. *Sci. Rep.* 8:4564

37. Elbaum M, Fygenson DK, Libchaber A. 1996. Buckling microtubules in vesicles. *Phys. Rev. Lett.* 76:4078–81

38. Emsellem V, Cardoso O, Tabeling P. 1998. Vesicle deformation by microtubules: a phase diagram. *Phys. Rev. E* 58:4807–10

39. Exterkate M, Driessen AJM. 2019. Synthetic minimal cell: self-reproduction of the boundary layer. *ACS Omega* 4:5293–303

40. Faivre-Moskalenko C, Dogterom M. 2002. Dynamics of microtubule asters in microfabricated chambers: the role of catastrophes. *PNAS* 99:16788–93

41. Frohnmayer JP, Brüggemann D, Eberhard C, Neubauer S, Mollenhauer C, et al. 2015. Minimal synthetic cells to study integrin-mediated adhesion. *Angew. Chem. Int. Ed.* 54:12472–78

42. Funakoshi K, Suzuki H, Takeuchi S. 2007. Formation of giant lipid vesiclelike compartments from a planar lipid membrane by a pulsed jet flow. *J. Am. Chem. Soc.* 129:12608–9

43. Furusato T, Horie F, Matsubayashi HT, Amikura K, Kuruma Y, Ueda T. 2018. De novo synthesis of basal bacterial cell division proteins FtsZ, FtsA, and ZipA inside giant vesicles. *ACS Synth. Biol.* 7:953–61

44. Fygenson DK, Elbaum M, Shraiman B, Libchaber A. 1997. Microtubules and vesicles under controlled tension. *Phys. Rev. E* 55:850–59

45. Fygenson DK, Marko JF, Libchaber A. 1997. Mechanics of microtubule-based membrane extension. *Phys. Rev. Lett.* 79:4497–500

46. Ganzinger KA, Merino-Salomón A, García-Soriano DA, Butterfield AN, Litschel T, et al. 2020. FtsZ reorganization facilitates deformation of giant vesicles in microfluidic traps. *Angew. Chem. Int. Ed.* 59:21372–76

47. Ganzinger KA, Schwille P. 2019. More from less—bottom-up reconstitution of cell biology. *J. Cell Sci.* 132:jcs227488

48. Garenne D, Libchaber A, Noireaux V. 2020. Membrane molecular crowding enhances MreB polymerization to shape synthetic cells from spheres to rods. *PNAS* 117:1902–9

49. Garenne D, Noireaux V. 2020. Analysis of cytoplasmic and membrane molecular crowding in genetically programmed synthetic cells. *Biomacromolecules* 21:2808–17

50. Girard P, Pécréaux J, Lenoir G, Falson P, Rigaud J-L, Bassereau P. 2004. A new method for the reconstitution of membrane proteins into giant unilamellar vesicles. *Biophys. J.* 87:419–29

51. Godino E, López JN, Foschepoth D, Cleij C, Doerr A, et al. 2019. De novo synthesized Min proteins drive oscillatory liposome deformation and regulate FtsA-FtsZ cytoskeletal patterns. *Nat. Commun.* 10:4969

52. Göpfrich K, Haller B, Staufer O, Dreher Y, Mersdorf U, et al. 2019. One-pot assembly of complex giant unilamellar vesicle-based synthetic cells. *ACS Synth. Biol.* 8:937–47

53. Häckl W, Bärmann M, Sackmann E. 1998. Shape changes of self-assembled actin bilayer composite membranes. *Phys. Rev. Lett.* 80:1786–89

54. Hagiya M, Konagaya A, Kobayashi S, Saito H, Murata S. 2014. Molecular robots with sensors and intelligence. *Acc. Chem. Res.* 47:1681–90

55. Haller B, Göpfrich K, Schröter M, Janiesch J-W, Platzman I, Spatz JP. 2018. Charge-controlled microfluidic formation of lipid-based single- and multicompartment systems. *Lab Chip* 18:2665–74

56. Härtel T, Schwille P. 2014. ESCRT-III mediated cell division in *Sulfolobus acidocaldarius*—a reconstitution perspective. *Front. Microbiol.* 5:257

57. Hartmann E, Rapoport TA, Lodish HF. 1989. Predicting the orientation of eukaryotic membrane-spanning proteins. *PNAS* 86:5786–90

58. Hayashi M, Nishiyama M, Kazayama Y, Toyota T, Harada Y, Takiguchi K. 2016. Reversible morphological control of tubulin-encapsulating giant liposomes by hydrostatic pressure. *Langmuir* 32:3794–802

59. Heinemann F, Vogel SK, Schwille P. 2013. Lateral membrane diffusion modulated by a minimal actin cortex. *Biophys. J.* 104:1465–75

60. Honda M, Takiguchi K, Ishikawa S, Hotani H. 1999. Morphogenesis of liposomes encapsulating actin depends on the type of actin-crosslinking. *J. Mol. Biol.* 287:293–300

61. Horger KS, Estes DJ, Capone R, Mayer M. 2009. Films of agarose enable rapid formation of giant liposomes in solutions of physiologic ionic strength. *J. Am. Chem. Soc.* 131:1810–19

62. Hotani H, Miyamoto H. 1990. Dynamic features of microtubules as visualized by dark-field microscopy. *Adv. Biophys.* 26:135–56

63. Ichihashi N, Usui K, Kazuta Y, Sunami T, Matsuura T, Yomo T. 2013. Darwinian evolution in a translation-coupled RNA replication system within a cell-like compartment. *Nat. Commun.* 4:2494

64. Ierushalmi N, Malik-Garbi M, Manhart A, Abu-Shah E, Goode BL, et al. 2019. Centering and symmetry breaking in confined contracting actomyosin networks. arXiv:1907.10642 [physics.bio-ph]

65. Ito H, Nishigami Y, Sonobe S, Ichikawa M. 2015. Wrinkling of a spherical lipid interface induced by actomyosin cortex. *Phys. Rev. E* 92:062711

66. Jiménez M, Martos A, Cabré EJ, Raso A, Rivas G. 2013. Giant vesicles: a powerful tool to reconstruct bacterial division assemblies in cell-like compartments. *Environ. Microbiol.* 15:3158–68

67. Jørgensen IL, Kemmer GC, Pomorski TG. 2017. Membrane protein reconstitution into giant unilamellar vesicles: a review on current techniques. *Eur. Biophys. J.* 46:103–19

68. Kahya N, Pécheur E-I, de Boeij WP, Wiersma DA, Hoekstra D. 2001. Reconstitution of membrane proteins into giant unilamellar vesicles via peptide-induced fusion. *Biophys. J.* 81:1464–74

69. Kamiya K, Kawano R, Osaki T, Akiyoshi K, Takeuchi S. 2016. Cell-sized asymmetric lipid vesicles facilitate the investigation of asymmetric membranes. *Nat. Chem.* 8:881–89

70. Kato A, Yanagisawa M, Sato YT, Fujiwara K, Yoshikawa K. 2012. Cell-sized confinement in microspheres accelerates the reaction of gene expression. *Sci. Rep.* 2:283

71. Keber FC, Loiseau E, Sanchez T, DeCamp SJ, Giomi L, et al. 2014. Topology and dynamics of active nematic vesicles. *Science* 345:1135–39

72. Küchler A, Yoshimoto M, Luginbühl S, Mavelli F, Walde P. 2016. Enzymatic reactions in confined environments. *Nat. Nanotechnol.* 11:409–20

73. Kuruma Y, Stano P, Ueda T, Luisi PL. 2009. A synthetic biology approach to the construction of membrane proteins in semi-synthetic minimal cells. *Biochim. Biophys. Acta Biomembr.* 1788:567–74

74. Lagny TJ, Bassereau P. 2015. Bioinspired membrane-based systems for a physical approach of cell organization and dynamics: usefulness and limitations. *Interface Focus* 5:20150038

75. Lee KY, Park S-J, Lee KA, Kim S-H, Kim H, et al. 2018. Photosynthetic artificial organelles sustain and control ATP-dependent reactions in a protocellular system. *Nat. Biotechnol.* 36:530–35

76. Limozin L, Bärmann M, Sackmann E. 2003. On the organization of self-assembled actin networks in giant vesicles. *Eur. Phys. J. E* 10:319–30

77. Limozin L, Sackmann E. 2002. Polymorphism of cross-linked actin networks in giant vesicles. *Phys. Rev. Lett.* 89:168103

78. Lipowsky R, Richter D, Kremer K. 1992. The structure and conformation of amphiphilic membranes: overview. In *The Structure and Conformation of Amphiphilic Membranes: Proceedings of the International Workshop on Amphiphilic Membranes, Jülich, Germany, September 16–18, 1991*, pp. 1–6. Berlin: Springer

79. Litschel T, Kelley CF, Holz D, Koudehi MA, Vogel SK, et al. 2020. Reconstitution of contractile actomyosin rings in vesicles. bioRxiv **https://doi.org/10.1101/2020.06.30.180901**

80. Litschel T, Ramm B, Maas R, Heymann M, Schwille P. 2018. Beating vesicles: encapsulated protein oscillations cause dynamic membrane deformations. *Angew. Chem. Int. Ed.* 57:16286–90

81. Liu AP, Fletcher DA. 2006. Actin polymerization serves as a membrane domain switch in model lipid bilayers. *Biophys. J.* 91:4064–70

82. Liu AP, Fletcher DA. 2009. Biology under construction: in vitro reconstitution of cellular function. *Nat. Rev. Mol. Cell Biol.* 10:644–50

83. Liu AP, Richmond DL, Maibaum L, Pronk S, Geissler PL, Fletcher DA. 2008. Membrane-induced bundling of actin filaments. *Nat. Phys.* 4:789–93

84. Loiseau E, Schneider JA, Keber FC, Pelzl C, Massiera G, et al. 2016. Shape remodeling and blebbing of active cytoskeletal vesicles. *Sci. Adv.* 2:e1500465

85. López-Montero I, López-Navajas P, Mingorance J, Vélez M, Vicente M, Monroy F. 2013. Membrane reconstitution of FtsZ-ZipA complex inside giant spherical vesicles made of *E. coli* lipids: large membrane dilation and analysis of membrane plasticity. *Biochim. Biophys. Acta Biomembr.* 1828:687–98

86. Maan R, Loiseau E, Bausch AR. 2018. Adhesion of active cytoskeletal vesicles. *Biophys. J.* 115:2395–402

87. Maeda YT, Nakadai T, Shin J, Uryu K, Noireaux V, Libchaber A. 2012. Assembly of MreB filaments on liposome membranes: a synthetic biology approach. *ACS Synth. Biol.* 1:53–59

88. Majumder S, Garamella J, Wang Y-L, DeNies M, Noireaux V, Liu AP. 2017. Cell-sized mechanosensitive and biosensing compartment programmed with DNA. *Chem. Commun.* 53:7349–52

89. Martino C, Kim S-H, Horsfall L, Abbaspourrad A, Rosser SJ, et al. 2012. Protein expression, aggregation, and triggered release from polymersomes as artificial cell-like structures. *Angew. Chem. Int. Ed.* 51:6416–20

90. Matosevic S, Paegel BM. 2013. Layer-by-layer cell membrane assembly. *Nat. Chem.* 5:958–63

91. Mellouli S, Monterroso B, Vutukuri HR, te Brinke E, Chokkalingam V, et al. 2013. Self-organization of the bacterial cell-division protein FtsZ in confined environments. *Soft Matter* 9:10493–500

92. Menestrina G. 1986. Ionic channels formed by *Staphylococcus aureus* alpha-toxin: voltage-dependent inhibition by divalent and trivalent cations. *J. Membr. Biol.* 90:177–90

93. Merkle D, Kahya N, Schwille P. 2008. Reconstitution and anchoring of cytoskeleton inside giant unilamellar vesicles. *ChemBioChem* 9:2673–81

94. Mitchison TJ. 1992. Compare and contrast actin filaments and microtubules. *Mol. Biol. Cell* 3:1309–15

95. Miyata H, Hotani H. 1992. Morphological changes in liposomes caused by polymerization of encapsulated actin and spontaneous formation of actin bundles. *PNAS* 89:11547–51

96. Miyata H, Nishiyama S, Akashi K, Kinosita K. 1999. Protrusive growth from giant liposomes driven by actin polymerization. *PNAS* 96:2048–53

97. Miyazaki M, Chiba M, Eguchi H, Ohki T, Ishiwata S. 2015. Cell-sized spherical confinement induces the spontaneous formation of contractile actomyosin rings in vitro. *Nat. Cell Biol.* 17:480–89

98. Moga A, Yandrapalli N, Dimova R, Robinson T. 2019. Optimization of the inverted emulsion method for high-yield production of biomimetic giant unilamellar vesicles. *ChemBioChem* 20:2674–82

99. Monnard P-A, Deamer DW. 2002. Membrane self-assembly processes: steps toward the first cellular life. *Anat. Rec.* 268:196–207

100. Montes LR, Alonso A, Goñi FM, Bagatolli LA. 2007. Giant unilamellar vesicles electroformed from native membranes and organic lipid mixtures under physiological conditions. *Biophys. J.* 93:3548–54

101. Murrell M, Pontani L-L, Guevorkian K, Cuvelier D, Nassoy P, Sykes C. 2011. Spreading dynamics of biomimetic actin cortices. *Biophys. J.* 100:1400–9

102. Nishimura K, Suzuki H, Toyota T, Yomo T. 2012. Size control of giant unilamellar vesicles prepared from inverted emulsion droplets. *J. Colloid Interface Sci.* 376:119–25

103. Noireaux V, Libchaber A. 2004. A vesicle bioreactor as a step toward and artificial cell assembly. *PNAS* 101:17669–74

104. Nomura SM, Tsumoto K, Hamada T, Akiyoshi K, Nakatani Y, Yoshikawa K. 2003. Gene expression within cell-sized lipid vesicles. *ChemBioChem* 4:1172–75

105. Oberholzer T, Nierhaus KH, Luisi PL. 1999. Protein expression in liposomes. *Biochem. Biophys. Res. Commun.* 261:238–41

106. Ohta N, Kato Y, Watanabe H, Mori H, Matsuura T. 2016. In vitro membrane protein synthesis inside Sec translocon-reconstituted cell-sized liposomes. *Sci. Rep.* 6:36466

107. Okushima S, Nisisako T, Torii T, Higuchi T. 2004. Controlled production of monodisperse double emulsions by two-step droplet breakup in microfluidic devices. *Langmuir* 20:9905–8

108. Opathalage A, Norton MM, Juniper MPN, Langeslay B, Aghvami SA, et al. 2019. Self-organized dynamics and the transition to turbulence of confined active nematics. *PNAS* 116:4788–97

109. Osawa M, Anderson DE, Erickson HP. 2008. Reconstitution of contractile FtsZ rings in liposomes. *Science* 320:792–94

110. Osawa M, Erickson HP. 2013. Liposome division by a simple bacterial division machinery. *PNAS* 110:11000–4

111. Ota S, Yoshizawa S, Takeuchi S. 2009. Microfluidic formation of monodisperse, cell-sized, and unilamellar vesicles. *Angew. Chem. Int. Ed.* 48:6533–37

112. Pautot S, Frisken BJ, Weitz DA. 2003. Engineering asymmetric vesicles. *PNAS* 100:10718–21

113. Pautot S, Frisken BJ, Weitz DA. 2003. Production of unilamellar vesicles using an inverted emulsion. *Langmuir* 19:2870–79

114. Perrier DL, Vahid A, Kathavi V, Stam L, Rems L, et al. 2019. Response of an actin network in vesicles under electric pulses. *Sci. Rep.* 9:8151

115. Petit J, Polenz I, Baret J-C, Herminghaus S, Bäumchen O. 2016. Vesicles-on-a-chip: a universal microfluidic platform for the assembly of liposomes and polyersomes. *Eur. Phys. J. E* 39:59

116. Pinot M, Chesnel F, Kubiak JZ, Arnal I, Nedelec FJ, Gueroui Z. 2009. Effects of confinement on the self-organization of microtubules and motors. *Curr. Biol.* 19:954–60

117. Pontani L-L, van der Gucht J, Salbreux G, Heuvingh J, Joanny J-F, Sykes C. 2009. Reconstitution of an actin cortex inside a liposome. *Biophys. J.* 96:192–98

118. Pott T, Bouvrais H, Méléard P. 2008. Giant unilamellar vesicle formation under physiologically relevant conditions. *Chem. Phys. Lipids* 154:115–19

119. Powell K. 2018. How biologists are creating life-like cells from scratch. *Nature* 563:172–75

120. Prévost C, Zhao H, Manzi J, Lemichez E, Lappalainen P, et al. 2015. IRSp53 senses negative membrane curvature and phase separates along membrane tubules. *Nat. Commun.* 6:8529

121. Przybylo M, Sýkora J, Humpolíčková J, Benda A, Zan A, Hof M. 2006. Lipid diffusion in giant unilamellar vesicles is more than 2 times faster than in supported phospholipid bilayers under identical conditions. *Langmuir* 22:9096–99

122. Ramirez-Diaz DA, Merino-Salomon A, Heymann M, Schwille P. 2019. Bidirectional FtsZ filament treadmilling promotes membrane constriction via torsional stress. bioRxiv 587790. **https://doi.org/10.1101/587790**

123. Rampioni G, D'Angelo F, Leoni L, Stano P. 2019. Gene-expressing liposomes as synthetic cells for molecular communication studies. *Front. Bioeng. Biotechnol.* 7:1

124. Reeves JP, Dowben RM. 1969. Formation and properties of thin-walled phospholipid vesicles. *J. Cell Physiol.* 73:49–60

125. Richmond DL, Schmid EM, Martens S, Stachowiak JC, Liska N, Fletcher DA. 2011. Forming giant vesicles with controlled membrane composition, asymmetry, and contents. *PNAS* 108:9431–36

126. Robinson T, Kuhn P, Eyer K, Dittrich PS. 2013. Microfluidic trapping of giant unilamellar vesicles to study transport through a membrane pore. *Biomicrofluidics* 7:044105

127. Saleem M, Morlot S, Hohendahl A, Manzi J, Lenz M, Roux A. 2015. A balance between membrane elasticity and polymerization energy sets the shape of spherical clathrin coats. *Nat. Commun.* 6:6249

128. Sanchez T, Chen DTN, DeCamp SJ, Heymann M, Dogic Z. 2012. Spontaneous motion in hierarchically assembled active matter. *Nature* 491:431–34

129. Sato Y, Hiratsuka Y, Kawamata I, Murata S, Nomura SM. 2017. Micrometer-sized molecular robot changes its shape in response to signal molecules. *Sci. Robot.* 2:eaal3735

130. Schäfer E, Kliesch T-T, Janshoff A. 2013. Mechanical properties of giant liposomes compressed between two parallel plates: impact of artificial actin shells. *Langmuir* 29:10463–74

131. Schäfer E, Vache M, Kliesch TT, Janshoff A. 2015. Mechanical response of adherent giant liposomes to indentation with a conical AFM-tip. *Soft Matter* 11:4487–95

132. Schroer FEC, Baldauf L, Buren L, Wassenaar TA, Melo MN, et al. 2020. Charge-dependent interactions of monomeric and filamentous actin with lipid bilayers. *PNAS* 117:5861–72

133. Schwille P, Spatz J, Landfester K, Bodenschatz E, Herminghaus S, et al. 2018. MaxSynBio: avenues towards creating cells from the bottom up. *Angew. Chem. Int. Ed.* 57:13382–92

134. Scott A, Noga MJ, de Graaf P, Westerlaken I, Yildirim E, Danelon C. 2016. Cell-free phospholipid biosynthesis by gene-encoded enzymes reconstituted in liposomes. *PLOS ONE* 11:e0163058

135. Shaklee PM, Semrau S, Malkus M, Kubick S, Dogterom M, Schmidt T. 2010. Protein incorporation in giant lipid vesicles under physiological conditions. *ChemBioChem* 11:175–79

136. Shimizu Y, Inoue A, Tomari Y, Suzuki T, Yokogawa T, et al. 2001. Cell-free translation reconstituted with purified components. *Nat. Biotechnol.* 19:751–55

137. Shum HC, Lee D, Yoon I, Kodger T, Weitz DA. 2008. Double emulsion template monodisperse phospholipid vesicles. *Langmuir* 24:7651–53

138. Soares e Silva M, Alvarado J, Nguyen J, Georgoulia N, Mulder BM, Koenderink GH. 2011. Self-organized patterns of actin filaments in cell-sized confinement. *Soft Matter* 7

139. Soga H, Fujii S, Yomo T, Kato Y, Watanabe H, Matsuura T. 2014. In vitro membrane protein synthesis inside cell-sized vesicles reveals the dependence of membrane protein integration on vesicle volume. *ACS Synth. Biol.* 3:372–79

140. Sonnleitner A, Schütz GJ, Schmidt T. 1999. Free Brownian motion of individual lipid molecules in biomembranes. *Biophys. J.* 77:2638–42

141. Stachowiak JC, Richmond DL, Li TH, Brochard-Wyart F, Fletcher DA. 2009. Inkjet formation of unilamellar lipid vesicles for cell-like encapsulation. *Lab Chip* 9:2003–9

142. Stachowiak JC, Richmond DL, Li TH, Liu AP, Parekh SH, Fletcher DA. 2008. Unilamellar vesicle formation and encapsulation by microfluidic jetting. *PNAS* 105:4697–702

143. Steinkühler J, De Tillieux P, Knorr RL, Lipowsky R, Dimova R. 2018. Charged giant unilamellar vesicles prepared by electroformation exhibit nanotubes and transbilayer lipid asymmetry. *Sci. Rep.* 8:11838

144. Streicher P, Nassoy P, Bärmann M, Dif A, Marchi-Artzner V, et al. 2009. Integrin reconstituted in GUVs: a biomimetic system to study initial steps of cell spreading. *Biochim. Biophys. Acta Biomembr.* 1788:2291–300

145. Szathmáry E, Santos M, Fernando C. 2005. Evolutionary potential and requirements for minimal pro-
     tocells. In *Prebiotic Chemistry*, ed. P Walde, pp. 167–211. Berlin: Springer

146. Szent-Györgyi AG. 2004. The early history of the biochemistry of muscle contraction. *J. Gen. Physiol.*
     123:631–41

147. Szostak JW, Bartel DP, Luisi PL. 2001. Synthesizing life. *Nature* 409:387–90

148. Tareste D, Shen J, Melia TJ, Rothman JE. 2008. SNAREpin/Munc18 promotes adhesion and fusion of
     large vesicles to giant membranes. *PNAS* 105:2380–85

149. Tawfik DS, Griffiths AD. 1998. Man-made cell-like compartments for molecular evolution. *Nat. Biotech-
     nol.* 16:652–56

150. Teh S-Y, Khnouf R, Fan H, Lee AP. 2011. Stable, biocompatible lipid vesicle generation by solvent
     extraction-based droplet microfluidics. *Biomicrofluidics* 5:044113

151. Tsai FC, Koenderink GH. 2015. Shape control of lipid bilayer membranes by confined actin bundles.
     Soft Matter 11:8834–47

152. Tsai F-C, Stuhrmann B, Koenderink GH. 2011. Encapsulation of active cytoskeletal protein networks
     in cell-sized liposomes. *Langmuir* 27:10061–71

153. Utada AS, Lorenceau E, Link DR, Kaplan PD, Stone HA, Weitz DA. 2005. Monodisperse double emul-
     sions generated from a microcapillary device. *Science* 308:537–41

154. Virk SS, Baruah VJ, Goswami P. 2013. Giant vesicles as encapsulating matrix for stabilizing alcohol
     oxidase and as container for coupled enzymatic reactions. *Artif. Cells Nanomed. Biotechnol.* 41:255–58

155. Visco I, Hoege C, Hyman AA, Schwille P. 2016. In vitro reconstitution of a membrane switch mechanism
     for the polarity protein LGL. *J. Mol. Biol.* 428:4828–42

156. Walde P, Cosentino K, Engel H, Stano P. 2010. Giant vesicles: preparations and applications.
     ChemBioChem 11:848–65

157. Weinberger A, Tsai F-C, Koenderink GH, Schmidt TF, Itri R, et al. 2013. Gel-assisted formation of
     giant unilamellar vesicles. *Biophys. J.* 105:154–64

158. Weiss M, Frohnmayer JP, Benk LT, Haller B, Janiesch J-W, et al. 2018. Sequential bottom-up assembly
     of mechanically stabilized synthetic cells by microfluidics. *Nat. Mater.* 17:89–96

159. Weitz M, Kim J, Kapsner K, Winfree E, Franco E, Simmel FC. 2014. Diversity in the dynamical behavior
     of a compartmentalized programmable biochemical oscillator. *Nat. Chem.* 6:295–302

160. Yanagisawa M, Iwamoto M, Kato A, Yoshikawa K, Oiki S. 2011. Oriented reconstitution of a membrane
     protein in a giant unilamellar vesicle: experimental verification with the potassium channel KcsA. *J. Am.
     Chem. Soc.* 133:11774–79

161. Yoshimoto M. 2011. Stabilization of enzymes through encapsulation in liposomes. In *Enzyme Stabiliza-
     tion and Immobilization: Methods and Protocols*, ed. SD Minteer, pp. 9–18. Totowa, NJ: Humana Press

162. Yu W, Sato K, Wakabayashi M, Nakaishi T, Ko-Mitamura EP, et al. 2001. Synthesis of functional protein
     in liposome. *J. Biosci. Bioeng.* 92:590–93

163. Zhang Y, Cheng C, Cusick B, LeDuc PR. 2007. Chemically encapsulated structural elements for probing
     the mechanical responses of biologically inspired systems. *Langmuir* 23:8129–34

164. Zieske K, Chwastek G, Schwille P. 2016. Protein patterns and oscillations on lipid monolayers and in
     microdroplets. *Angew. Chem. Int. Ed.* 55:13455–59

165. Zieske K, Schwille P. 2013. Reconstitution of pole-to-pole oscillations of min proteins in microengi-
     neered polydimethylsiloxane compartments. *Angew. Chem. Int. Ed.* 52:459–62

2. Actin reconstitution in GUVs

2.1. Introduction and context

In living cells, biomolecules self-assemble into ordered structures with emergent properties surpassing those of their individual units. Aside from lipids, which form the membranes so central to this thesis, cytoskeletal proteins are one of the few other components able to assemble into structures that span the entire cell. Thereby, they determine cell shape and guide intercellular transport on scales several orders of magnitude larger than their building blocks. In minimal systems with purified proteins, a handful of components can drive the formation of complex and diverse cytoskeletal morphologies, providing insight into the many varied roles these proteins fill within cells. However, while bottom-up biology has been an invaluable approach to investigate molecular interactions between cytoskeletal proteins and their regulators, relatively little is understood about self-organization of cytoskeletal components on the scale of an entire cell.

Membrane shape and cytoskeletal dynamics are undeniably linked. While membrane compartments physically confine and thereby shape cytoskeletal networks, so too can lipid compartments be shaped by the cytoskeletal network within. The work presented in this chapter allows direct observation of both these processes: We observe how the vesicle shapes the encapsulated actin network into both cortices and rings, and that actin can both exert extensile forces by protruding the membrane with stiff bundles, or constrict the vesicle through actomyosin forces.

2.2. The actin cytoskeleton

Actin is the most abundant cytoskeletal protein in eukaryotic cells, as well as one of the most abundant proteins in cells in general, making up about 15% of the total protein mass in some cell types.[3] In cells, actin filaments are organized into mesh-like networks through branching and cross-linking, or packed into tight bundles. These different architectures appear in a variety of different cellular structures and are responsible for essential processes like cell migration, cell division, phagocytosis, axonal growth and organelle transport. To fulfill these roles, actin structures are constantly changing. Despite the name cyto-"skeleton", these structures are highly dynamic and are constantly being reorganized.

Actin filaments (also called F-actin) are polymers composed of actin subunits. Actin monomers (also called G-actin, for globular actin) can bind ATP. When in its ATP-bound form, monomeric G-actin can polymerize into chains of F-actin. The resulting filament is composed of two chains of polymerized actin monomers that wind helically around each other. Actin monomers in filaments are oriented, as such actin filaments have two distinct ends: a barbed (plus) and a pointed (minus) end. In respect to the polarity of the filaments, polymerization behavior is not symmetric, with different on-off rates at each end, and unique sets of binding partners.

Actin dynamics and organization is highly regulated in the cell, allowing actin filaments to form everything from stable to highly dynamic, transient structures, and to play countless, highly specific roles in different processes. Cells contain hundreds of actin binding proteins that regulate actin nucleation, polymerization, and depolymerization, determine actin cross linking, stabilize or sever actin filaments, or mediate actin-membrane interactions. The functions of the cytoskeleton depend on the fine tuning of these accessory proteins with each actin-related cell function having their own set of crucial actin-binding proteins. These actin regulatory proteins turn actin into perhaps the most versatile protein in any given cell.

2.3. Actin in reconstitution studies

In vitro reconstitution of actin filaments is a large and broad field within the reconstitution community[4,5], with a long history. In fact, some of the earliest in vitro experiments with purified protein were performed with actomyosin – long before the time of PCR and genetic manipulation.[6,7]

Since these early days, the focus of actin related work has shifted from simply identifying the components responsible for muscle contraction,[8] to investigating more detailed aspects of the cytoskeleton[5,9], such as the kinetics of actin assembly[10,11] or the cross-talk with other cytoskeletal elements like microtubules.[12] These experiments have extended to the many actin binding proteins[13], including the oft-studied motor protein myosin. Contractile actomyosin networks were investigated (1) in a gel-like bulk state[14-16], (2) by restricting the actomyosin network to a quasi 2D layer through crowding agents[17,18], (3) immobilizing myosin motors on a static surface[19] and (4) anchoring actin to supported lipid bilayers (SLBs). In the latter case, the actin network assembles into a membrane-bound actomyosin cortex. Binding to the membrane has been achieved by various means, e.g. through biotin-

neutravidin bonds[20], by connecting actin to nickel-conjugated lipids through His-tagged actin binding proteins[21,22].

Many studies look at actin-membrane interactions, as many actin binding proteins are directly regulated via interactions with phospholipid bilayers.[23] For these studies, supported lipid bilayers (SLBs) can offer a great model membrane system owing to their ease of preparation, stability, ability to form lipid patterns, and their compatibility with most light microscopy methods.[24] On the other hand, their physical properties can differ from free-standing membranes: As the name itself implies, these SLBs are structurally supported and thus don't offer the deformability of biological membranes. Further SLBs differ in terms of their lipid diffusivity[25,26]. For these reasons, GUVs can be a popular model membrane system, not necessarily using them as an compartment for encapsulation, but simply as a free standing model membrane to which proteins can be added from the outside. However, by encapsulation into the GUVs, a new level of protein reconstitution can be achieved - generating individual units of cell-like membrane compartments that can perform simple protein functions within.

While work with proteins in vesicles has had a recent spike in popularity due to the prospect of creating artificial cells, encapsulation of actin in vesicles actually goes as far back as the late 1980s and early 1990s.[27-30] Early studies focused on shape deformations and described that polymerizing actin can quite drastically alter the shape of the encapsulating vesicles. It is likely, however, that these observations might have been the result of the formation of crystalline actin structures (liquid crystals) due to the high concentrations of actin used in these studies[30-32]. With a growing field of in vitro reconstitution and technical advances in microscopy, including the rise of confocal fluorescence microscopy, the field expanded and experiments became more biomimetic. As actin research developed, cross-linking proteins came into focus. While single actin filaments are very flexible structures with a rather small bending stiffness, cross-linked actin can have much more significant mechanical effects on, for example, membranes. Cross-linking proteins can form parallel bundles or a mesh-like network. Actin in combination with bundling protein was reconstituted in GUVs by Honda et al. [33] and later systematically characterized by Tsai et al.[34], who saw that proteins like fascin, which cross-links actin into thick bundles, cause spike-like membrane protrusions or deform the entire vesicle into a rod-like shape. Limozin & Sackmann observed that less rigid actin bundles can robustly self-organize into rings in vesicles.[35]

With the work shown in this chapter, we combined actin bundling and actin–membrane linkage to obtain results more closely resembling in vivo morphologies than previously achieved. We further not only achieve the formation of membrane-attached actin rings within lipid vesicles, but also observe large-scale membrane deformation when including myosin in the system.

2.4. Publication 2: Reconstitution of contractile actomyosin rings in vesicles

Research paper in press at Nature Communications.[36]

Litschel T, Kelley CF, Holz D, Adeli Koudehi M, Vogel SK, Burbaum L, Mizuno N, Vavylonis D, Schwille P. "Reconstitution of contractile actomyosin rings in vesicles". *Nat Commun* **12** (2021) [no page number available yet]

https://doi.org/10.1038/s41467-021-22422-7

Reconstitution of contractile actomyosin rings in vesicles

Thomas Litschel [1], Charlotte F. Kelley [1,2], Danielle Holz[3], Maral Adeli Koudehi[3], Sven K. Vogel[1], Laura Burbaum[1], Naoko Mizuno [2], Dimitrios Vavylonis[3] & Petra Schwille [1✉]

One of the grand challenges of bottom-up synthetic biology is the development of minimal machineries for cell division. The mechanical transformation of large-scale compartments, such as Giant Unilamellar Vesicles (GUVs), requires the geometry-specific coordination of active elements, several orders of magnitude larger than the molecular scale. Of all cytoskeletal structures, large-scale actomyosin rings appear to be the most promising cellular elements to accomplish this task. Here, we have adopted advanced encapsulation methods to study bundled actin filaments in GUVs and compare our results with theoretical modeling. By changing few key parameters, actin polymerization can be differentiated to resemble various types of networks in living cells. Importantly, we find membrane binding to be crucial for the robust condensation into a single actin ring in spherical vesicles, as predicted by theoretical considerations. Upon force generation by ATP-driven myosin motors, these ring-like actin structures contract and locally constrict the vesicle, forming furrow-like deformations. On the other hand, cortex-like actin networks are shown to induce and stabilize deformations from spherical shapes.

[1] Department of Cellular and Molecular Biophysics, Max Planck Institute of Biochemistry, Martinsried, Germany. [2] Department of Structural Cell Biology, Max Planck Institute of Biochemistry, Martinsried, Germany. [3] Department of Physics, Lehigh University, Bethlehem, PA, USA. ✉email: schwille@biochem.mpg.de

In cells, actin filaments are organized into cross-linked, branched, and bundled networks. These different architectures appear in structures, such as filopodia, stress fibers, the cell cortex, and contractile actomyosin rings; each has unique physical properties and fulfills different roles in important cellular processes[1]. These different structures must be actively assembled and maintained by cellular factors, such as the many actin cross-linking proteins. By mediating higher-order actin organization, cross-linkers allow actin filaments to fill a diverse array of structural and functional roles within cells[2,3].

In many cases, actin networks are linked to, or organized around, cellular membranes. Actin polymerization is a driving force behind many examples of membrane dynamics, including cell motility, membrane trafficking, and cell division[1]. Many of the actin-binding proteins involved in these processes are directly regulated via interactions with phospholipid bilayers[4,5] and membrane interactions have, in turn, been shown to physically guide actin assembly[6]. While the link between the actin cytoskeleton and phospholipid bilayers is clear, how these connections affect the large-scale organization of complex actin networks remains an open question.

Actin is not only one of the most prevalent proteins in current reconstitution experiments[7,8], but also was one of the first proteins to be explored in such approaches[9,10]. The focus of actin-related work has since shifted from identifying the components responsible for muscle contraction[11], to investigating more detailed aspects of the cytoskeleton[8,12], such as the dynamics of actin assembly[13,14] or the cross-talk with other cytoskeletal elements[15]. These experiments have extended to actin–membrane interactions, including reconstitution of actin cortices on the outside of giant unilamellar vesicles (GUVs)[16–18], and contractile actomyosin networks associated with supported membranes[19–21]. Recently, creating a synthetic cell with minimal components recapitulating crucial life processes, such as self-organization, homeostasis, and replication, has become an attractive goal[22,23]. As such, there is increased interest in work with actin in confinement and specifically within GUVs[24,25], in order to mimic cellular mechanics, by encapsulating actin and actin-binding proteins in vesicles[26–29]. However, the investigation of higher-order actin structures or networks has been the subject of few studies thus far[29–32].

Particularly, interesting for the reconstitution of actin-related cell processes is the co-encapsulation of myosin with actin, in order to form contractile actomyosin structures. While Tsai et al. showed the reconstitution of a contractile network in vesicles[26], and others have reconstituted actomyosin networks in vesicles that imitate actin cortices[27,29], contractile actomyosin rings have proven difficult to achieve. A true milestone toward the reconstitution of a division ring is the work of Miyazaki and coworkers, who encapsulated actomyosin with a depletant in water-in-oil droplets[33]. They showed not only that the formation of equatorial rings from actin bundles is a spontaneous process that occurs in spherical confinement, in order to minimize the elastic energy of the bundles, but also demonstrate the controlled constriction of these actomyosin rings.

Due to the difficulty of encapsulating functional proteins within membrane vesicles, much of the past work has been limited to water-in-oil emulsions and adding proteins to the outside of vesicles or onto supported lipid membrane systems. However, novel encapsulation methods such as continuous droplet interface crossing encapsulation (cDICE), as used here, have enabled the efficient transfer of proteins and other biomolecules into cell-sized phospholipid vesicles, as an ideal setting to study complex cellular processes involving membranes[34–37]. The challenges and applications of protein encapsulation in GUVs are summarized in a current review article[38]. Here, we optimized

actin encapsulation for a high degree of reproducibility and precision. This allowed us to reconstitute novel cell-like cytoskeletal features, as well as compare our experimental results with numerical simulations of confined interacting actin filaments. The development of experimentally testable predictive theoretical models is central for the future design of complex experiments that approach the functional complexity of biological systems.

We combined actin bundling and actin–membrane linkage to obtain results more closely resembling in vivo morphologies than previously achieved in vitro. Specifically, we induced the formation of membrane-bound single actin rings, which imitate the contractile division rings observed in many cells. In agreement with our numerical simulations, we show that membrane anchoring significantly promotes the formation of actin rings inside vesicles. We achieved close to 100% probability of ring formation in vesicles, when using the focal adhesion proteins talin and vinculin, which we recently identified as effective actin bundlers[39]. With the inclusion of motor proteins, these actomyosin rings contract similar to those observed in yeast protoplasts[40].

Thus, in this study, we not only achieve the formation of membrane-attached actin rings within lipid vesicles, but also observe large-scale membrane deformation when including myosin in the system. Although aspects of our study were previously addressed individually, such as encapsulation of actin bundles, actin binding to the inner membrane of a vesicle, or encapsulation of contractile actomyosin networks in vesicles, until now it proved too experimentally challenging to reproducibly combine these within one experimental system. Our results provide a high-yield approach, returning reproducible and quantifiable results, that brings us that much closer to the ultimate goal of being able to quantitatively design and experimentally achieve full division of a synthetic membrane compartment, and thus, to the self-reproduction of artificial cells, a persistent goal in bottom-up biology[41–44].

Results

Experimental system. In order to investigate the interplay between actin cross-linking and membrane binding, we used a modified cDICE method[45,46] to encapsulate G-actin with associated proteins and generate cytoskeletal GUVs made from the lipid POPC (Fig. 1a). Since components cannot be added once the reaction mix is encapsulated, the precise composition of the initial reaction mix is crucial. By tuning concentrations of the polymerization buffer, bundling proteins, membrane anchors, and motor proteins, we manipulated the final morphology of the actin network.

By co-encapsulating actin with known actin cross-linking proteins, we achieved large-scale networks with clearly discernible actin structures, similar to earlier studies with cytoskeletal GUVs[30]. We tested four different types of actin bundling proteins: fascin, α-actinin, vasodilator-stimulated phosphoprotein (VASP), and a combination of the focal adhesion proteins talin and vinculin. Each case represents a slightly different mechanism of actin binding. Fascin, a 55 kDa protein, binds to actin through two distinct actin-binding sites, thereby inducing filament cross-links as a monomer[47]. α-Actinin, 110 kDa, forms a dimer which bridges two filaments[30,48]. Talin (272 kDa) and vinculin (116 kDa) both dimerize, and also require interactions with each other in order to bind and bundle actin filaments[39]. Here we use a deregulated vinculin mutant (see Supplementary Information). VASP (50 kDa) forms a tetramer, which can link up to four filaments together[49]. Under all four conditions, the formation of thick filament bundles was observed (Fig. 1b, c). Interestingly, while α-actinin, talin/vinculin, and VASP all produced similar
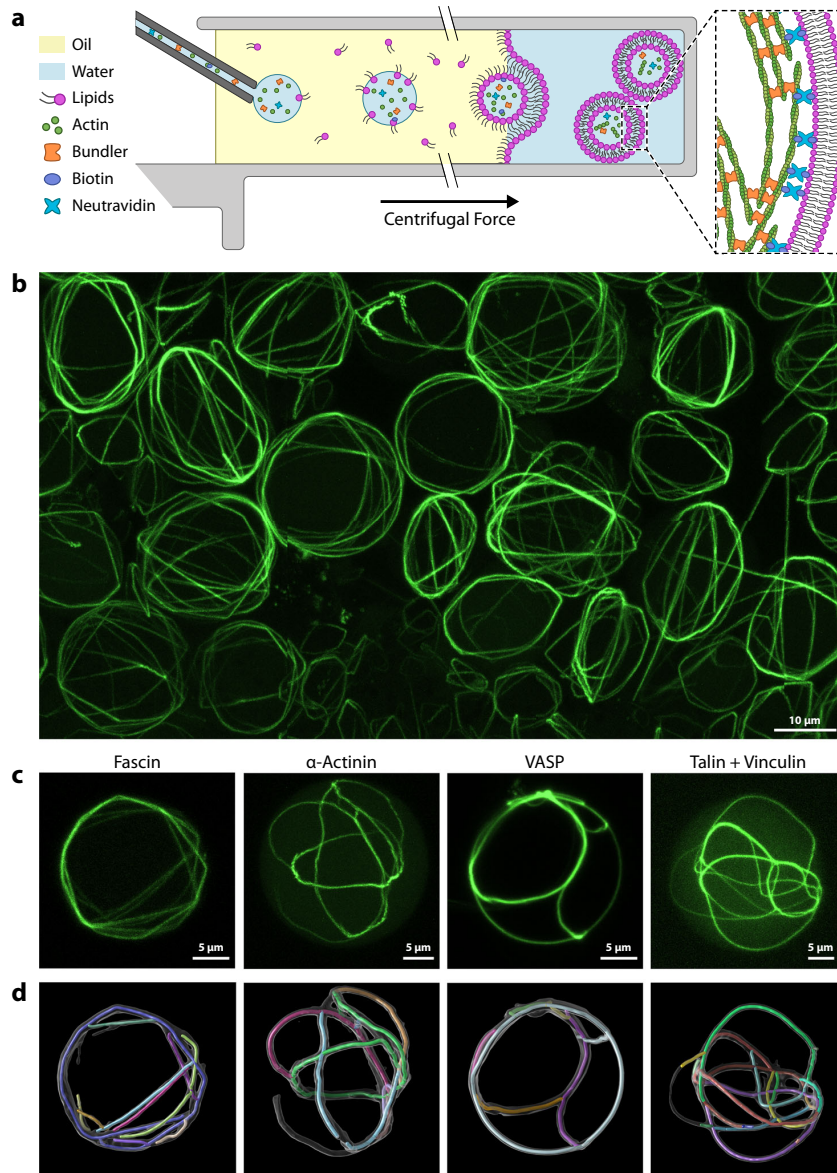
Fig. 1 Encapsulation of bundled actin in giant unilamellar vesicles. a Schematic depiction of the vesicle generation process. The aqueous protein solution is injected into a rotating chamber through a glass capillary. Droplets form at the capillary tip in the oil phase, which contains lipids. The droplets then pass through a water–oil interphase lined with a second lipid monolayer, forming the giant unilamellar vesicles (GUVs). **b** Field of view image (Z-projections of confocal stacks) with many cytoskeletal vesicles. Actin in green. See Supplementary Movie 1 for 3D effect. **c** Comparison of cytoskeletal vesicles with actin bundled by four different types of bundling proteins. We used 2 µM actin in all cases, but due to differences in bundling activity, different concentrations of bundling protein: 0.3 µM fascin, 0.9 µM VASP, 1 µM α-actinin, 2 µM talin, and 2 µM vinculin. **d** Automated tracing of bundles by analysis script. Confocal z-stacks are converted into a three-dimensional "skeleton" model. Supplementary Movie 2 shows a 3D view of both representations of these vesicles.

morphologies, fascin bundles take on the most unique appearance. These bundles often bend in kinks when their path is obstructed by the membrane, while the other proteins form smoothly curved bundles that can follow the curvature of the encapsulating membrane (Fig. 1c, d). While similar observation

have been made in the past, generally, bulk assays will be better suited for quantifying these bundle parameters[30,50–53].

After establishing successful encapsulation of actin and its bundling proteins, we modified the approach and linked the actin filaments to the phospholipid bilayer via biotin–neutravidin bonds, similar to previous work on planar supported lipid

bilayers[19]. This requires the incorporation of biotinylated lipids in the vesicle membranes and the addition of both, biotinylated g-actin and neutravidin in the encapsulated reaction mix. We tested different fractions of biotinylated lipids, as well as biotinylated actin (Supplementary Figs. 2 and 3) and identified 1% biotinylated lipids and 4% biotinylated actin as suitable amounts, which we used in the following experiments.

Numerical simulations. Theoretical predictions by Adeli Kou-dehi et al. have suggested that actin organization depends cru-cially on confinement and surface attachment[54]. In order to explore the agreement of our experimental results with these simulations, we adopted their theoretical model. As such, we performed numerical simulations of interacting actin filaments under spherical confinement using Brownian dynamics (see Supplementary Methods)[54]. Semiflexible actin filaments were modeled as beads connected by springs, with cross-linking represented by a short-range attraction with spring constant k_{atr}. Polymerization from an initial number of filament seeds was simulated by addition of beads at one of the filament ends (representing the barbed end). The number of seeds was changed to achieve different final filament lengths. Boundary attraction was simulated as short-range attraction to the confining bound-ary. Simulated maximum intensity projections were performed as in Bidone et al.[55].

Membrane attachment shapes actin organization by curvature induction. We performed a series of experiments with the sim-plest bundling protein fascin to investigate the effects of mem-brane binding on bundle morphology. We notice that membrane-binding primarily affects the curvature of these bundles: while actin with fascin forms very straight bundles that are just gen-erally confined by the membrane, we see that membrane-bound fascin bundles often adopt the exact curvature of the membrane (Fig. 2a). Figure 2b shows a histogram for the distribution of bundle curvatures in these vesicles. The histogram shows a much broader distribution for unbound bundles, with a maximum at low curvatures, while the maximum for membrane-bound actin bundles is centered around the curvature of the membrane (relative curvature = 1.0).

Despite this difference on a small scale, the general distribution of bundles within the vesicles seems to be largely independent on the presence of actin–membrane linkers. Figure 3a shows a set of conditions with and without membrane binding. We quantified the average actin distribution for each condition and find that

(with some exceptions) actin is consistently positioned in close proximity to the membrane, with only minor differences between conditions with and without membrane linkers (Fig. 3c, d). While in previous work even unbundled actin has been seen to be more concentrated at the membrane[32], our results indicate that bundles need to be sufficiently long, so that confinement by the vesicle boundary forces them to bend and concentrate at the inner surface. We note that for 2 μM actin (Fig. 3a, top row) even low concentrations of fascin are sufficient to cause this effect, while we do observe that the thickness of the bundles increases with higher concentrations (Supplementary Fig. 5).

At higher actin concentrations (6 μM) and low fascin to actin ratios (3.3 and 6.7%), bundles were shorter and thus more homogeneously distributed in the vesicles when not bound to the membrane (Fig. 3d). Interestingly, we note that membrane-binding affects the threshold at which long actin bundles form: we observe long bundles at a fascin to actin ratio of 6.7%, when we include membrane linkers (see also Supplementary Fig. 6). These observations agree with corresponding simulations (Fig. 3b).

In our experiments, ring-like structures consistently form at 2 μM actin, while at 6 μM actin, multiple bundles usually arrange themselves into cortex-like structures that do not condense into single rings. In our simulations, we see similar cortex-like morphologies in the early stages, but at longer times these condense into rings, both for low and high actin concentrations (Supplementary Fig. 7). As discussed below, the smaller confinement size we chose due to computation limitations favors ring formation. Another ring promoting factor could be the absence of a simulated maximum bundle thickness, unlike in experiments[56].

Ring formation. Excitingly, and in accordance with theoretical predictions, the most noticeable effect of membrane attachment was an increase in the formation of single actin rings. Although ring formation could still be observed without membrane–actin links, the introduction of membrane binding greatly enhances the probability of actin condensation into one single clearly dis-cernible ring in vesicles. Membrane-bound actin rings have so far not been reported within synthetic vesicles.

Figure 4 highlights this effect of membrane attachment on the formation of actin rings. Figure 4a summarizes ring formation probabilities for three different bundlers, comparing conditions with and without membrane binding. We chose actin and bundler concentrations for which the formation of single rings is
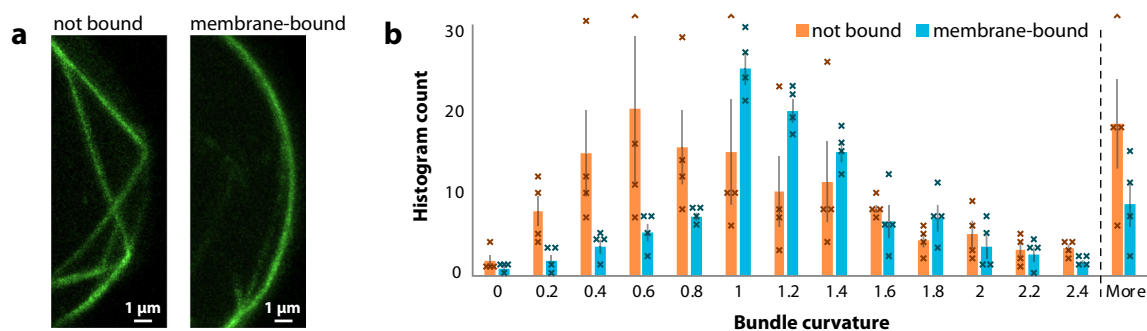
Fig. 2 Membrane attachment affects curvature of actin bundles. a Each image shows a section of the membrane of a GUV with actin bundles bundled by fascin (2 μM actin and 0.2 μM fascin). Actin is in green. Unattached bundles have long sections with zero curvature, while membrane-bound bundles follow the curvature of the membrane. **b** Distribution of curvatures for actin bundles in vesicles with and without membrane binding. $n = 4$ GUVs for each condition. Confocal z-stacks were converted into 3D information (see Fig. 1d). Bundles were then divided into small segments and their curvature was measured. Curvature is normalized by membrane curvature, so that a curvature of 1.0 equals the curvature of the membrane. Data are shown as mean values with individual histogram counts and SEM. More details about the analysis can be found in the Supplementary Method.
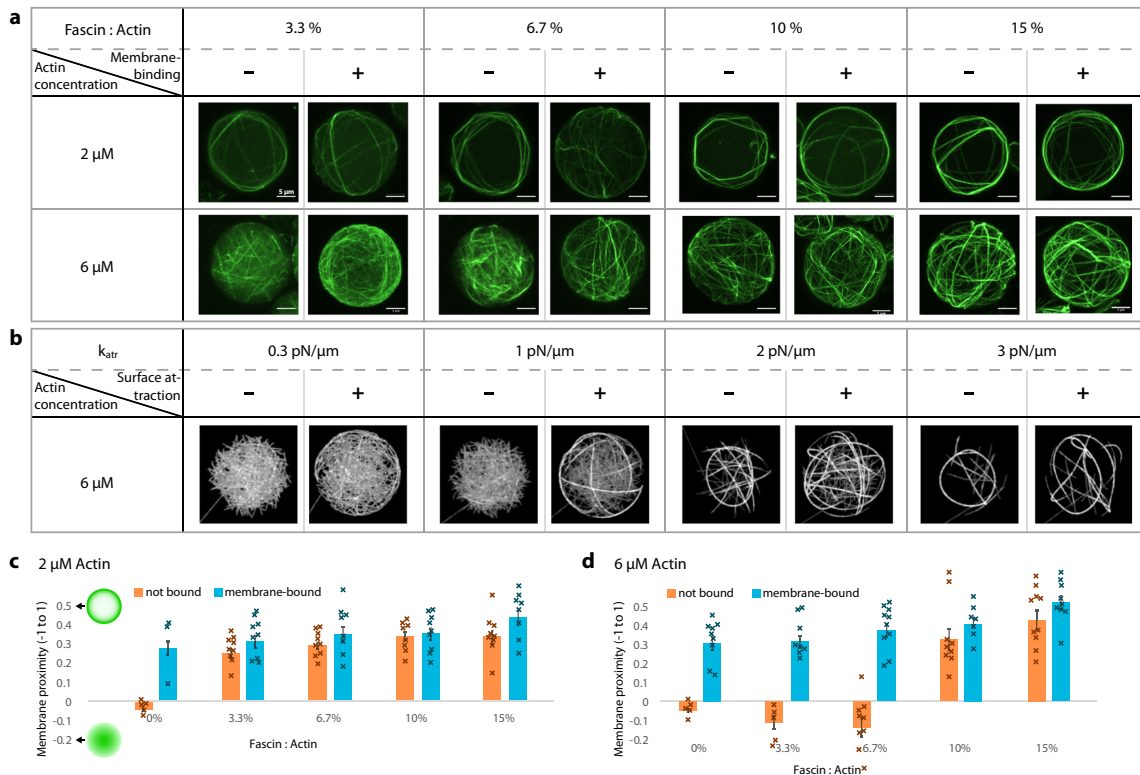
Fig. 3 Actin organization in dependence on bundler to actin ratio and membrane binding. Actin is positioned close to the membrane regardless of membrane-anchoring. **a** Overview of conditions with varying actin concentration (2 µM and 6 µM), fascin to actin ratios (3.3:100–15:100) and with and without actin–membrane binding. Supplementary Movie 3 shows a 3D version of this figure panel. **b** Simulations for similar conditions as 6 µM conditions in **a** using radius = 6 µm. **c** Average membrane proximity of actin signal for vesicles with 2 µM actin. Normalized range from −1 (all actin in the center of the vesicle) to +1 (all actin on the membrane). **d** Membrane proximity of actin signal for vesicles with 6 µM actin. Data in **c** and **d** are presented as mean values with individual datapoints and SEM. $n = 10$ vesicles for each condition (except $n \geq 3$ for controls with 0% fascin).

already relatively likely (12–35%) even without membrane attachment. In vesicles with membrane-attached actin, probability of ring formation roughly doubles for all bundlers, and reaches up to 80% for actin bundled by vinculin and talin (fluorescence image in Fig. 4c).

In simulations, Adeli Koudehi et al. found that boundary attraction in the case of spherical confinement enhances the probability of ring formation from bundled filaments[54]. However, the effect of boundary attraction in their work was studied for filament lengths larger than the confining diameter, whereas in experiments, we observed increased ring formation for vesicles and actin concentrations where the opposite should be true. We thus performed new simulations of actin filaments for concentrations chosen as in our experiments ($c = 2$ µM), and varied their lengths and confinement sizes (Fig. 4b, Supplementary Fig. 11, and Supplementary Movie 5). We selected filament cross-linking simulation parameters that lead to bundle formation without filament sliding and associated bundle compaction $k_{atr} = 2$ pN/µm. Including surface attraction greatly enhanced ring and ring-like structure formation for short filaments (length $L = 1.2$ µm) in small spheres (radius $R = 2.5$ µm). We also observed an enhancement of ring formation for filament lengths and sphere sizes comparable to that of our experiments ($L = 6$ µm as estimated from prior studies[33,57,58], $R = 5$ µm), including when we increased the persistence length of individual actin filaments to simulate cross-linking induced bundle stiffening (Supplementary Fig. 11). Inspired by modeling results implying that the probability of ring

formation depends on compartment size[54], we analyzed our experimental data to confirm that rings preferably form in smaller vesicles (Supplementary Fig. 12).

Actomyosin contraction. The rings observed here can be assumed to mimic reorganization of actin that occurs during the last stages of cell division. In order to take this analogy one step further, we included muscle myosin II with the ultimate goal of forming a contractile actomyosin ring. Constriction of non-anchored actin rings was shown by Miyazaki et al., who demonstrated myosin-mediated contraction in a less cell-like system. They used actin bundled by depletion forces in water-in-oil droplets and showed that the behavior reproduced by this system has a striking resemblance to constricting cell division rings[33].

In our vesicles, the addition of myosin complicated the formation of single actin bundle rings. We used low concentrations of myosin II, such that the effect of myosin activity on bundling was minimized and motor-induced constriction slow enough to be observed while imaging. Although it appeared that the appropriate assay conditions for homogeneously contracting single rings have not yet been met in our giant vesicles, we recorded the constriction of a membrane-anchored ring-like structure along with membrane deformations. Figure 5a and Supplementary Movie 6 show this example over the course of 2 h. In accordance with our expectations, in this minimal system without further ring-stabilizing components, the constricting
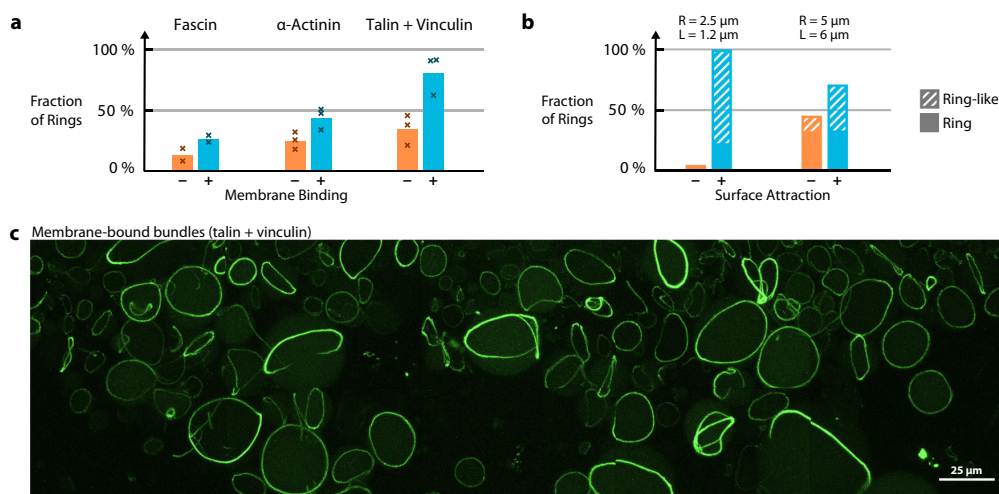
Fig. 4 Formation of membrane-anchored actin rings. a Membrane-binding promotes ring formation. Shown is the probability of the formation of single actin rings in GUVs (i.e., GUVs with one single unbranched actin bundle connected into a ring) in the absence and presence of membrane-anchoring. Data are shown as mean values with individual fractions of experimental runs. Three hundered ninety two vesicles between 15 and 20 µm were analyzed in $n = 2$ (fascin) or $n = 3$ experimental runs per condition. We use 2 µM actin in all cases, but due to differences in bundling activity different concentrations of bundling protein: 0.3 µM fascin, 1 µM α-actinin, 2 µM talin, and 2 µM vinculin. **b** Probability of ring formation for simulations with different initial parameters (R: vesicle radius, L: filament lengths). In simulations, we classified rings with small gaps or closed rings with additional side branches as "ring like" (see Supplementary Method). Snapshots from all simulation shown in Supplementary Fig. 11. **c** Condition with particularly robust ring formation: actin bundled by talin with vinculin and bound to the membrane. Supplementary Movie 4 shows a 3D view of this image. Supplementary Figure 8 shows a DIC image of this field of view, and Supplementary Figs. 9 and 10 show rings formed by other bundling proteins.

actomyosin ring eventually slides along the membrane and collapses into a single condensate on one side of the vesicle, a behavior that has been seen in yeast cells lacking cell walls[40]. Such an arbitrary local collapse is not too surprising, as coordinated ring constriction in the cell is a highly spatially regulated process involving hundreds of proteins. Clearly, additional cellular machinery is required to stabilize the position of the ring, and membrane geometry and fluidity likely play additional roles. Figure 5a shows how the actomyosin ring initially deforms the vesicle membrane (orange arrows), leading to a furrow-like indentation. The entire time series without overlays is shown in Supplementary Movie 6. Our experiments clearly show that the actin bundles are firmly attached to the inner leaflet of the vesicle membrane and that active forces are exerted by the motor proteins, capable of deforming the vesicle. Figure 5b shows another instance of actomyosin contractions leading to deformations of the vesice membrane. Unfortunately the above mentioned complications in assay design hampered consistent observations of these membrane deformations.

An additional effect of the contraction of membrane-bound actomyosin is a change in the x–y cross section area of the vesicle after contraction. This effect also appears for vesicles without initial furrow constriction. This is likely due to crumpling of the membrane into the actomyosin contraction point, which decreases membrane area (while vesicle volume is largely preserved) and increases membrane tension. As a result, vesicles that are initially slightly deflated become more spherical as a result of actomyosin contraction. Supplementary Figure 14a shows a differential interference contrast (DIC) image of the actomyosin contraction point in Fig. 5a, and more examples of vesicles with shrinking x–y cross section.

Shaping the membrane compartment. Lipid membranes are highly flexible, and the shape of GUVs is mostly determined by the osmotic pressure inside the vesicle with respect to its

environment. If this pressure is low, i.e., vesicles are osmotically deflated, strong deviations from the spherical shape are possible, and additional mechanical determinants, such as external forces or an encapsulated cytoskeleton induce arbitrary shapes of the vesicles[32], as can be seen in Fig. 6a. The experiment we performed in Fig. 6b confirms the role of an artifcial cytoskeleton in determining vesicle shape, i.e., stabilizing the shapes of membrane compartments: by imaging deformed cytoskeletal vesicles with increased laser power on our confocal microscope, the actin filaments depolymerize after some time due to photodamage[59], relaxing the cytoskeleton-inferred shape determinants and leaving the deflated vesicles without internal support. This leads to dramatic changes in their shape, usually by taking on a spheroid (oblate) shape.

These stabilizing cortices of actin bundles can even protect the vesicles, e.g., against the unfavorable conditions of sample preparation for cryo-electron microscopy, specifically the drying of the sample (removal of the surrounding aqueous phase): Fig. 6c shows a cryo scanning electron microscopy image of frozen cytoskeletal vesicles. When trying to freeze and image vesicles without an encapsulated actin cortex or with actin bundles that are not attached to the membrane, vesicles rarely survive the process (Supplementary Fig. 15). Although a thorough quantitative assessment of this effect is not within the scope of this study, it confirms previous work that GUVs can be stabilized through a shell of cross-linked material on the membrane of GUVs, not only with unbundled actin[60], but also with other proteins[61], as well as DNA origami[62]. Here, we show that heterogeneously distributed, higher-order structures can potentially achieve a similar mechanical effect.

Discussion

In this work, we succeeded in reconstituting ring-like actomyosin structures in GUVs. With respect to a suitable protein machinery that may serve as a minimal divisome for protocells, this

Myosin II-induced contraction of membrane-bound bundles (talin + vinculin)
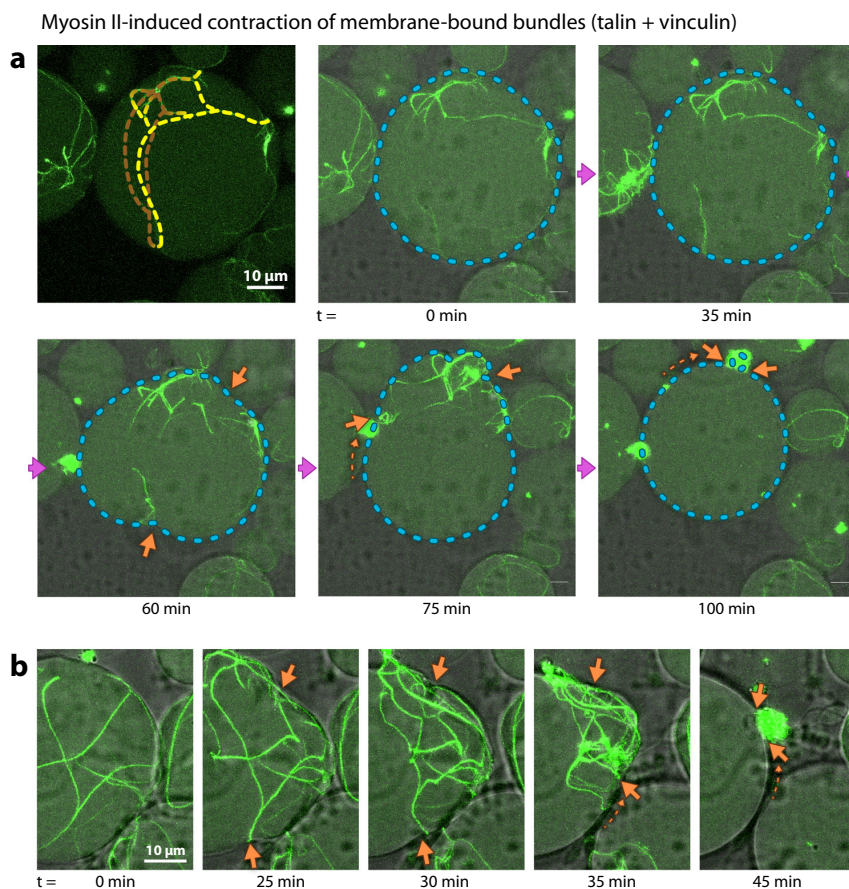
Fig. 5 Actomyosin contraction leads to membrane deformations. a Time series of a contracting ring-like structure in a GUV. Same conditions as in Fig. 4c but with 0.1 μM myosin II. Only the midsection of the vesicle is shown, top and bottom are missing, but the yellow dotted lines in the first frame show the approximate position of the bundles (see also Supplementary Fig. 13). Cyan dotted lines in the following frames indicate the outline of the vesicle. Orange arrows indicate membrane deformations (vesicle constriction). The partially visible vesicle on the left can be seen to undergo a similar transition from a large actin network ($t = 0$) to myosin-constricted cluster ($t = 60$ min). Supplementary Movie 6 shows the same field of view. **b** Additional example of large-scale vesicle deformation through actomyosin contraction. Even though no furrow-like deformation was observed, the contraction of actin bundles still causes large-scale vesicle deformations (orange arrows).

constitutes the first important step toward assembling contractile rings of sufficiently large sizes. To this end, we encapsulated a reaction mix into the vesicles that causes actin to polymerize, bundle, bind to the vesicle membrane, and even contract. We show that the bundle networks can be highly organized and, under many conditions, reproducibly cross-linked into single rings.

Clearly discernible ring formation has been previously shown by Miyazaki et al., who utilized depletion forces through the crowding agent methylcellulose, while confining actin polymers in small water-in-oil droplets[33]. These rings were shown to contract, but due to the lack of surface attachment in this system, unable to transmit contractile forces to the compartment interface. The formation of rings from biopolymer bundles in confinement due to a minimization of bending energy is known from both, theory[54,63] and other experimental systems[31,64,65]. Here, we achieved similar actin rings bundled by various physiological factors. However, encapsulation in lipid vesicles allowed us to go an important step further and explore the effect of attaching these rings to the compartmentalizing lipid bilayer. In this scenario, ring contraction may be able to transmit a contractile force

directly to the membrane, resulting in dramatic shape transformation of the respective compartment, induced by energy dissipation within.

We have thus shown, as a proof of principle, that noneequilibrium myosin-mediated constriction of such ring-like membrane-bound actin structures can be induced in lipid membrane vesicles. These vesicle deformations (Fig. 5a) demonstrate the strength of the membrane anchoring. The final contracted state reveals myosin-induced symmetry breaking, as observed in other actomyosin in vitro systems under confinement[18,26,27,66]. For example, Tsai et al. encapsulated a contractile actomyosin system in vesicles that condensed into dense clusters[26].

Unless membrane area can be expanded at the same time, the osmotic pressure inside a spherical vesicle complicates a cell division-like symmetric constriction in the center of the vesicle, and in the absence of other geometric regulators, the fluidity of the membrane causes the ring-like bundles to "slip" and contract into a cluster in one location. Our experiments indicate, that in order to achieve a binary fission through contraction of a single ring, more spatial determinants are required.
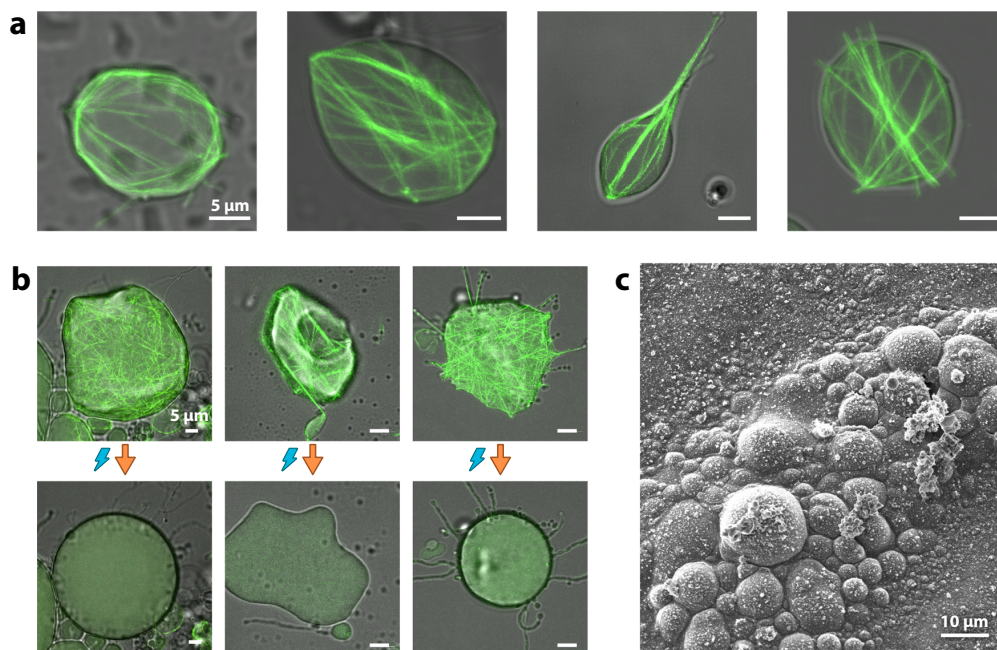
Fig. 6 Actin network governs vesicle shape in osmotically deflated vesicles. a Variety of vesicle shapes produced by different morphologies of encapsulated actin networks, some with stabilizing cortices and others with filopodia-like membrane protrusions. **b** Upon exposure to photodamage through increased laser power, cytoskeletal vesicles lose their stabilizing actin cortex, and often take on a flat and round shape. All three examples are shown in Supplementary Movie 7. **c** Vesicles with a stabilizing artificial actin cortex can be dried, frozen, and imaged using cryo scanning electron microscopy.

A behavior similar to what we observe can be seen in vivo for the contraction of actomyosin rings in yeast protoplasts (yeast cells that have been stripped of their cell walls)[40]. Stachowiak et al. beautifully demonstrated that in these spherical cells without cell walls, the contractile actomyosin ring slides along the cell membrane, collapsing into one point at the side of the cells. The absence of a cell wall in fission yeast results in both a loss of their elongated shape and a lack of stabilizing the actomyosin ring in the cell center[40].

We conclude that further assay improvement and, very likely, additional functional components will be necessary to accomplish a complete division of a cell-sized vesicle compartment in vitro. Functional studies will allow us to identify a machinery that ensures the placement of a contractile actomyosin ring at a defined site, while envoking other spatial cues to prevent the deflection of the induced contractile forces by surface slipping. The MinDE system, which has previously been shown to target FtsZ rings to the middle of compartments[67], and extend this potential of positioning even to functionally unrelated membrane-binding particles[68], may be an attractive candidate. Moreover, ring constriction could be more successful in a non-spherical, elongated vesicle; such a confinement shape, however, will likely prevent initial ring formation along the desired constriction site. Further requirements may include mechanisms to generate actin filament bundles of mixed polarity, and to sustain such distribution throughout the constriction process, possibly through turnover of components[69].

To summarize, by reconstituting a contractile actomyosin ring-like structure in GUVs, we have made one essential step forward with regard to establishing a minimal system for active membrane vesicle division from the bottom up. Using this protein machinery from eukaryotes, large-size contractile ring structures could be generated and attached to vesicle membranes from the inside to transmit their contractile forces. Our experiments suggest that ring formation, membrane attachment, and contraction are not sufficient for division of these cell-like compartments, as long as the positional stability of the force-inducing machinery on the compartment surface cannot be ensured. However, toward the bottom-up design of a minimal division machinery, this system is an ideal starting point for identifying the additional parameters and components required. Furthermore, the robust and reproducible in vitro assembly methods used here provide a reliable platform for further reconstitution of the key processes of life beyond cell division.

Methods

Proteins. The proteins fascin (human, recombinant), α-actinin (turkey gizzard smooth muscle), myosin II (rabbit, m. psoas), actin (alpha-actin skeletal muscle, rabbit), ATTO488-actin (alpha-actin skeletal muscle, rabbit), and biotin-actin (alpha-actin, rabbit skeletal muscle) were purchased from HYPERMOL (www. hypermol.com). VASP was expressed in *Drosophila* S2 cells, and purified using Ni-NTA affinity purification followed by gel filtration. We use the mutant vincu-lin[N773A,E775A] (vinculin2A), which has reduced autoinhibitory interactions[70]. Purification of talin and vinculin2A was performed as described in detail in our previous publication[39]. In brief, the His-tagged proteins were expressed in *Escherichia coli* BL21 (DE3) and purified via Ni-NTA affinity purification. Talin was further purified using ion exchange purification and gel filtration chromatography on a Superdex 200 16/600 column (GE Healthcare) or Superose 6 10/300 column (GE Healthcare) in storage buffer (50 mM HEPES, pH 7.8, 150 mM KCl, 10% glycerol, and 0.1 mM EDTA). Protein purity was assessed via SDS–PAGE and gel filtration. Proteins were quick frozen and stored in aliquots at −80 °C until further use.

Reaction mix preparation. In all experiments, we used 10% labeled actin (ATTO488-actin). In conditions with membrane-attached actin bundles we used 4% biotinylated actin and 0.17 μM neutravidin. In all cases, actin, labeled actin, and biotinylated actin were resuspended in deionized water and pre-spun at $15,000 \times g$ for 10 min at 7 °C in a tabletop microcentrifuge. The top 75% of the actin solution was then transferred to a new Eppendorf tube and kept on ice for the duration of the experiment.

Publication 2   **Page 40 of 210**

The actin concentrations we used are within the typical range used in in vitro experiments. However, it should be noted that these concentrations are much lower than the concentrations present in living cells, where a complex regulatory system controls the amount of polymerizable actin.

The reaction mix contained 10 mM imidazole, 50 mM KCl, 1 mM MgCl₂, 1 mM EGTA, 0.2 mM ATP, pH 7.5, and 15% iodixanol (from OptiPrep™, Sigma Aldrich). For the experiments shown in all figures and movies except Fig. 6 and Supplementary Movie 7, the solution surrounding the GUVs contained 10 mM imidazole, 50 mM KCl, 1 mM MgCl₂, 1 mM EGTA, 0.2 mM ATP, pH 7.5, and 200 mM glucose. For the deflated GUVs in Fig. 6 and Supplementary Movie 7 the outer solution contained a higher glucose concentration (300 mM).

For the experiment in Fig. 5, we used 0.1 μM myosin II.

Lipids. The preparation of the lipid-in-oil mixture is based on published protocols[27,71]. We use DOPC (1,2-dioleoyl-sn-glycero-3-phosphocholine, Avanti Polar Lipids, Inc.) with 1% DSPE-PEG(2000) biotin (1,2-distearoyl-sn-glycero-3-phosphoethanolamine-N-[biotinyl(polyethyleneglycol)-2000], Avanti Polar Lipids, Inc.; both 25 mg/ml in chloroform) and give 77 μl thereof in a 10 ml vial with 600 μl chloroform. In experiments with labeled membranes, 3 μl DOPE-ATTO655 (0.1 mg/ml in chloroform) is added. While being mixed on a vortex mixer, 10 ml of a silicon oil and mineral oil (Sigma Aldrich, M5904) mix (4:1 ratio) is slowly added to the lipid solution. Since the lipids are not soluble in this mix of silicon oil, mineral oil, and chloroform, the resulting liquid is cloudy.

Vesicle generation. Vesicles were produced using the cDICE method as described by Abkarian et al.[45] with modifications we described in a previous publication[46]: instead of utilizing petri dishes, we 3D printed the rotating chamber, in which the vesicles are generated. Inner diameter of chamber: 7 cm, diameter top opening: 3 cm, height of chamber: 2 mm. (CAD file available at https://doi.org/10.5281/zenodo.4555840.) Printed with Clear Resin on Formlabs Form 2. A magnetic stirring device (outdated IKA-COMBIMAG RCH) served as a motor, after the heating unit was removed to expose the motor shaft.

The inner solution is loaded into a syringe (BD Luer-Lock™ 1-ml syringe), which is then placed into a syringe pump system (neMESYS base 120 with neMESYS 290 N) and connected through tubing to a glass capillary (100 μm inner diameter).

A total of 700 μl of the outer solution is pipetted into the rotating chamber, followed by ~5 ml of the lipid-in-oil mixture. The capillary tip is then immersed in the oil phase and the inner phase injected at a flow rate of 50 μl/h for 10 min. The vesicles are withdrawn from the cDICE chamber with a micropipette.

The concentration of the encapsulated protein varies within a certain range. In experiments in which we encapsulated a simple soluble fluorescent dye, we found that the concentrations within the vesicle population follows a log normal distribution (Supplementary Fig. 4b). We assume that this effect is reduced for a reaction mix containing actin in the process of polymerizing and bundling. During vesicle generation, this vesicle content is much less diffusive and therefore less likely to leave the vesicles.

Imaging. The vesicles are pipetted into a microtiter plate for imaging (Greiner Bio-One, 384-well glass bottom SensoPlate™), each well passivated beforehand with 50 μl of 5 mg/ml β-casein (Sigma Aldrich) for 20 min.

Imaging is then performed with an LSM 780/CC3 confocal microscope (Carl Zeiss, Germany) equipped with a C-Apochromat, 40×/1.2 W objective. We use PMT detectors (integration mode) to detect fluorescence emission (excitation at 488 nm for ATTO488) and record confocal images.

Z-stack datasets of vesicles contain between 40 and 65 confocal slices (depending on vesicle size) with a slice interval of 0.5 μm with the exception of time series (Figs. 5 and 6b, and Supplementary Figs. 13 and 14), which contain less slices with a larger z interval.

Image analysis. Image processing and analysis is mostly performed using the software ImageJ/Fiji[72,73] and SOAX[74,75]. All images shown in the manuscript are maximum projections of z-stacks of confocal images (see Supplementary Fig. 1). Only exceptions are the images in Supplementary Figs. 2 and 3, which show single confocal images in order to highlight membrane binding. The three-dimensional representations in Supplementary Movies 1–4 are created with the Fiji command "3D Project".

For the computational, three-dimensional characterization of the actin networks, we generate skeletonized models from selected vesicles in our confocal z-stacks. The networks are identified and extracted with SOAX by active contour methods. In order to optimize the images for the identification of the filaments, the stacks are first deconvolved using the software Huygens (Scientific Volume Imaging) and then further preprocessed using Fiji. Bundle curvature (Fig. 2b) is estimated with SOAX. Membrane proximity (Fig. 3c, d) is calculated with a custom ImageJ script, which is available at https://doi.org/10.5281/zenodo.4555840.

Visualizations of the skeletonized models of actin networks by SOAX, as shown in Fig. 1d and Supplementary Movie 2, are generated in UCSF Chimera[76].

Vesicle sizes were manually measured using a MATLAB (MathWorks) script.

For more details regarding image processing and analysis see Supplementary Method.

Statistics and reproducability. Most of the images show particular features that were not reproduced with identical protein concentrations, however, were reproduced under similar conditions and in sum reflect on robust underlying mechanisms. In total, we performed ≥30 independent experiments with fascin, ≥15 independent experiments with α-actinin, ≥10 independent experiments with talin + vinculin and three independent experiments with VASP that all showed similar actin morphologies, as evidenced by the respective images. All images in Fig. 1 were reproduced at least three times with similar concentrations. Results in Fig. 2 were obtained on four different vesicles for each condition within two experimental runs. Conditions as in Fig. 3 were varied once with a total of 20 conditions and incremental differences between the parameters, indicates a high degree of reproducibility. Experiments in Fig. 4 were performed two (fascin) or three (α-actinin and talin + vinculin) times. Reproducibility of experiments with myosin was poor, as described in the paper. Figure 5a shows the most "furrow-like" membrane deformation we observed. We captured time series of membrane deformation in four additional cases. Membrane deformations as shown in Fig. 6a were observed on many occasions in ≥5 experimental runs. Result shown in Fig. 6b was repeated many times within ≥3 experimental runs. Cryo-EM shown in Fig. 6c was repeated once with similar results. Experiments shown in Supplementary Figs. 1–4 were performed once. Images in Supplementary Fig. 6 are from three different experimental runs per condition. Images shown in Supplementary Figs. 8–10 were reproduced at least once with similar concentrations. Images in Supplementary Figs. 13–15 were not reproduced.

Data availability
Data supporting the findings of this manuscript are available from the corresponding author upon reasonable request. A reporting summary for this article is available as a Supplementary Information file. Source data are provided with this paper.

Code availability
The custom ImageJ for the membrane proximity analysis (Fig. 3c, d) is provided at https://doi.org/10.5281/zenodo.4555840.

References
1. Rottner, K., Faix, J., Bogdan, S., Linder, S. & Kerkhoff, E. Actin assembly mechanisms at a glance. *J. Cell Sci.* **130**, 3427–3435 (2017).
2. Blanchoin, L., Boujemaa-Paterski, R., Sykes, C. & Plastino, J. Actin dynamics, architecture, and mechanics in cell motility. *Physiol. Rev.* **94**, 235–263 (2014).
3. Schwayer, C., Sikora, M., Slovakova, J., Kardos, R. & Heisenberg, C. P. Actin rings of power. *Dev. Cell* **37**, 493–506 (2016).
4. Doherty, G. J. & McMahon, H. T. Mediation, modulation, and consequences of membrane-cytoskeleton interactions. *Annu. Rev. Biophys.* **37**, 65–95 (2008).
5. Bezanilla, M., Gladfelter, A. S., Kovar, D. R. & Lee, W.-L. Cytoskeletal dynamics: a view from the membrane. *J. Cell Biol.* **209**, 329–337 (2015).
6. Liu, A. P. et al. Membrane-induced bundling of actin filaments. *Nat. Phys.* **4**, 789–793 (2008).
7. Ganzinger, K. A. & Schwille, P. More from less - bottom-up reconstitution of cell biology. *J. Cell Sci.* **132**, jcs227488 (2019).
8. Liu, A. P. & Fletcher, D. A. Biology under construction: in vitro reconstitution of cellular function. *Nat. Rev. Mol. Cell Biol.* **10**, 644–650 (2009).
9. Kuhne, W. *Untersuchungen uber das Protoplasma und die Contractilitat*. (W. Engelmann, 1864).
10. Straub, F. Studies from the Institute of Medical Chemistry, University of Szeged, Vol. II, 3 (ed. Szent-Györgyi, A.) (S. Karger, 1942).
11. Szent-Györgyi, A. G. The early history of the biochemistry of muscle contraction. *J. Gen. Physiol.* **123**, 631–641 (2004).
12. Mullins, R. D. & Hansen, S. D. In vitro studies of actin filament and network dynamics. *Curr. Opin. Cell Biol.* **25**, 6–13 (2013).
13. Smith, B. A., Gelles, J. & Goode, B. L. Single-molecule studies of actin assembly and disassembly factors. *Methods Enzymol.* **540**, 95–117 (2014).
14. Pollard, T. D. Actin and actin-binding proteins. *Cold Spring Harb. Perspect. Biol.* **8**, a018226 (2016).
15. Dogterom, M. & Koenderink, G. H. Actin-microtubule crosstalk in cell biology. *Nat. Rev. Mol. Cell Biol.* **20**, 38–54 (2019).
16. Carvalho, K. et al. Cell-sized liposomes reveal how actomyosin cortical tension drives shape change. *Proc. Natl Acad. Sci. USA* **110**, 16456–16461 (2013).

Page 41 of 210   **Publication 2**

17. Caorsi, V. et al. Cell-sized liposome doublets reveal active tension build-up driven by acto-myosin dynamics. *Soft Matter* **12**, 6223–6231 (2016).

18. Carvalho, K. et al. Actin polymerization or myosin contraction: two ways to build up cortical tension for symmetry breaking. *Philos. Trans. R. Soc. Lond. B Biol. Sci.* **368**, 20130005 (2013).

19. Vogel, S. K., Petrasek, Z., Heinemann, F. & Schwille, P. Myosin motors fragment and compact membrane-bound actin filaments. *Elife* **2**, e00116 (2013).

20. Sonal, et al. Myosin-II activity generates a dynamic steady state with continuous actin turnover in a minimal actin cortex. *J. Cell Sci.* **132**, jcs219899 (2018).

21. Murrell, M. & Gardel, M. L. Actomyosin sliding is attenuated in contractile biomimetic cortices. *Mol. Biol. Cell* **25**, 1845–1853 (2014).

22. Gopfrich, K., Platzman, I. & Spatz, J. P. Mastering complexity: towards bottom-up construction of multifunctional eukaryotic synthetic cells. *Trends Biotechnol.* **36**, 938–951 (2018).

23. Schwille, P. et al. MaxSynBio: avenues towards creating cells from the bottom up. *Angew. Chem. Int. Ed. Engl.* **57**, 13382–13392 (2018).

24. Mulla, Y., Aufderhorst-Roberts, A. & Koenderink, G. H. Shaping up synthetic cells. *Phys. Biol.* **15**, 041001 (2018).

25. Bashirzadeh, Y. & Liu, A. P. Encapsulation of the cytoskeleton: towards mimicking the mechanics of a cell. *Soft Matter* **15**, 8425–8436 (2019).

26. Tsai, F.-C., Stuhrmann, B. & Koenderink, G. H. Encapsulation of Active cytoskeletal protein networks in cell-sized liposomes. *Langmuir* **27**, 10061–10071 (2011).

27. Loiseau, E. et al. Shape remodeling and blebbing of active cytoskeletal vesicles. *Sci. Adv.* **2**, e1500465 (2016).

28. Durre, K. et al. Capping protein-controlled actin polymerization shapes lipid membranes. *Nat. Commun.* **9**, 1630 (2018).

29. Maan, R., Loiseau, E. & Bausch, A. R. Adhesion of active cytoskeletal vesicles. *Biophys. J.* **115**, 2395–2402 (2018).

30. Honda, M., Takiguchi, K., Ishikawa, S. & Hotani, H. Morphogenesis of liposomes encapsulating actin depends on the type of actin-crosslinking. *J. Mol. Biol.* **287**, 293–300 (1999).

31. Limozin, L. & Sackmann, E. Polymorphism of cross-linked actin networks in giant vesicles. *Phys. Rev. Lett.* **89**, 168103 (2002).

32. Tsai, F. C. & Koenderink, G. H. Shape control of lipid bilayer membranes by confined actin bundles. *Soft Matter* **11**, 8834–8847 (2015).

33. Miyazaki, M., Chiba, M., Eguchi, H., Ohki, T. & Ishiwata, S. Cell-sized spherical confinement induces the spontaneous formation of contractile actomyosin rings in vitro. *Nat. Cell Biol.* **17**, 480–489 (2015).

34. Majumder, S., Wubshet, N. & Liu, A. P. Encapsulation of complex solutions using droplet microfluidics towards the synthesis of artificial cells. *J. Micromech. Microeng.* **29**, 083001 (2019).

35. Sato, Y. & Takinoue, M. Creation of artificial cell-like structures promoted by microfluidics technologies. *Micromachines* **10**, 216 (2019).

36. Supramaniam, P., Ces, O. & Salehi-Reyhani, A. Microfluidics for artificial life: techniques for bottom-up synthetic biology. *Micromachines* **10**, 299 (2019).

37. Robinson, T. Microfluidic handling and analysis of giant vesicles for use as artificial cells: a review. *Adv. Biosyst.* **3**, e1800318 (2019).

38. Litschel, T. & Schwille, P. Protein reconstitution inside giant unilamellar vesicles. *Annu. Rev. Biophys.* **50**, 525–548 (2021).

39. Kelley, C. F. et al. Phosphoinositides regulate force-independent interactions between talin, vinculin, and actin. *eLife* **9**, e56110 (2020).

40. Stachowiak, M. R. et al. Mechanism of cytokinetic contractile ring constriction in fission yeast. *Dev. Cell* **29**, 547–561 (2014).

41. Hürtgen, D., Härtel, T., Murray, S. M., Sourjik, V. & Schwille, P. Functional modules of minimal cell division for synthetic biology. *Adv. Biosyst.* **3**, 1800315 (2019).

42. Kretschmer, S., Ganzinger, K. A., Franquelim, H. G. & Schwille, P. Synthetic cell division via membrane-transforming molecular assemblies. *BMC Biol.* **17**, 43 (2019).

43. Exterkate, M. & Driessen, A. J. M. Synthetic minimal cell: self-reproduction of the boundary layer. *ACS Omega* **4**, 5293–5303 (2019).

44. Schwille, P. Division in synthetic cells. *Emerging Top. Life Sci.* **3**, 551–558 (2019).

45. Abkarian, M., Loiseau, E. & Massiera, G. Continuous droplet interface crossing encapsulation (cDICE) for high throughput monodisperse vesicle design. *Soft Matter* **7**, 4610–4614 (2011).

46. Litschel, T., Ramm, B., Maas, R., Heymann, M. & Schwille, P. Beating vesicles: encapsulated protein oscillations cause dynamic membrane deformations. *Angew. Chem. Int Ed. Engl.* **57**, 16286–16290 (2018).

47. Jansen, S. et al. Mechanism of actin filament bundling by fascin. *J. Biol. Chem.* **286**, 30087–30096 (2011).

48. Winkelman, J. D. et al. Fascin- and alpha-actinin-bundled networks contain intrinsic structural features that drive protein sorting. *Curr. Biol.* **26**, 2697–2706 (2016).

49. Hüttelmaier, S. et al. Characterization of the actin binding properties of the vasodilator-stimulated phosphoprotein VASP. *FEBS Lett.* **451**, 68–74 (1999).

50. Gittes, F., Mickey, B., Nettleton, J. & Howard, J. Flexural rigidity of microtubules and actin filaments measured from thermal fluctuations in shape. *J. Cell Biol.* **120**, 923–934 (1993).

51. Ott, A., Magnasco, M., Simon, A. & Libchaber, A. Measurement of the persistence length of polymerized actin using fluorescence microscopy. *Phys. Rev. E* **48**, R1642–R1645 (1993).

52. Claessens, M. M. A. E., Bathe, M., Frey, E. & Bausch, A. R. Actin-binding proteins sensitively mediate F-actin bundle stiffness. *Nat. Mater.* **5**, 748–753 (2006).

53. Takatsuki, H., Bengtsson, E. & Månsson, A. Persistence length of fascin-cross-linked actin filament bundles in solution and the in vitro motility assay. *Biochim. Biophys. Acta* **1840**, 1933–1942 (2014).

54. Adeli Koudehi, M., Rutkowski, D. M. & Vavylonis, D. Organization of associating or crosslinked actin filaments in confinement. *Cytoskeleton* **76**, 532–548 (2019).

55. Bidone, T. C., Tang, H. & Vavylonis, D. Dynamic network morphology and tension buildup in a 3D model of cytokinetic ring assembly. *Biophys. J.* **107**, 2618–2628 (2014).

56. Claessens, M. M., Semmrich, C., Ramos, L. & Bausch, A. R. Helical twist controls the thickness of F-actin bundles. *Proc. Natl Acad. Sci. USA* **105**, 8819–8822 (2008).

57. Sept, D., Xu, J., Pollard, T. D. & Andrew McCammon, J. Annealing accounts for the length of actin filaments formed by spontaneous polymerization. *Biophysical J.* **77**, 2911–2919 (1999).

58. Limozin, L., Bärmann, M. & Sackmann, E. On the organization of self-assembled actin networks in giant vesicles. *Eur. Phys. J. E* **10**, 319–330 (2003).

59. van der Gucht, J., Paluch, E., Plastino, J. & Sykes, C. Stress release drives symmetry breaking for actin-based movement. *Proc. Natl Acad. Sci. USA* **102**, 7847–7852 (2005).

60. Schafer, E., Vache, M., Kliesch, T. T. & Janshoff, A. Mechanical response of adherent giant liposomes to indentation with a conical AFM-tip. *Soft Matter* **11**, 4487–4495 (2015).

61. Dieluweit, S. et al. Mechanical properties of bare and protein-coated giant unilamellar phospholipid vesicles. A comparative study of micropipet aspiration and atomic force microscopy. *Langmuir* **26**, 11041–11049 (2010).

62. Kurokawa, C. et al. DNA cytoskeleton for stabilizing artificial cells. *Proc. Natl Acad. Sci. USA* **114**, 7228–7233 (2017).

63. Vetter, R., Wittel, F. K. & Herrmann, H. J. Morphogenesis of filaments growing in flexible confinements. *Nat. Commun.* **5**, 4437 (2014).

64. Keber, F. C. et al. Topology and dynamics of active nematic vesicles. *Science* **345**, 1135–1139 (2014).

65. Baumann, H. & Surrey, T. Motor-mediated cortical versus astral microtubule organization in lipid-monolayered droplets. *J. Biol. Chem.* **289**, 22524–22535 (2014).

66. Ierushalmi, N. et al. Centering and symmetry breaking in confined contracting actomyosin networks. *eLife* **9**, e55368 (2020).

67. Zieske, K. & Schwille, P. Reconstitution of pole-to-pole oscillations of min proteins in microengineered polydimethylsiloxane compartments. *Angew. Chem. Int. Ed. Engl.* **52**, 459–462 (2013).

68. Ramm, B. et al. The MinDE system is a generic spatial cue for membrane protein distribution in vitro. *Nat. Commun.* **9**, 3942 (2018).

69. Pollard, T. D. & O'Shaughnessy, B. Molecular mechanism of cytokinesis. *Annu. Rev. Biochem.* **88**, 661–689 (2019).

70. Cohen, D. M., Chen, H., Johnson, R. P., Choudhury, B. & Craig, S. W. Two distinct head-tail interfaces cooperate to suppress activation of vinculin by talin. *J. Biol. Chem.* **280**, 17109–17117 (2005).

71. Claudet, C., In, M. & Massiera, G. Method to disperse lipids as aggregates in oil for bilayers production. *Eur. Phys. J. E Soft Matter* **39**, 9 (2016).

72. Schneider, C. A., Rasband, W. S. & Eliceiri, K. W. NIH Image to ImageJ: 25 years of image analysis. *Nat. Methods* **9**, 671–675 (2012).

73. Schindelin, J. et al. Fiji: an open-source platform for biological-image analysis. *Nat. Methods* **9**, 676–682 (2012).

74. Xu, T., Vavylonis, D. & Huang, X. 3D actin network centerline extraction with multiple active contours. *Med. Image Anal.* **18**, 272–284 (2014).

75. Xu, T. et al. SOAX: A software for quantification of 3D biopolymer networks. *Sci. Rep.* **5**, 9081 (2015).

76. Pettersen, E. F. et al. UCSF Chimera—a visualization system for exploratory research and analysis. *J. Comput. Chem.* **25**, 1605–1612 (2004).

Acknowledgements

Publication 2   **Page 42 of 210**

Author contributions

T.L. and P.S. designed the experiments. T.L. performed experiments and analyzed the results. D.H. and M.A.K. performed computer simulations. L.B. generated electron micrographs. C.F.K. purified proteins. C.F.K. and S.K.V. performed preliminary experiments. T.L. wrote the manuscript. P.S., C.F.K., and D.V. edited the manuscript. P.S., D.V., and N.M. provided resources.

Funding

Competing interests

The authors declare no competing interests.

Additional information

Supplementary information The online version contains supplementary material available at https://doi.org/10.1038/s41467-021-22422-7.

Correspondence and requests for materials should be addressed to P.S.

Peer review information *Nature Communications* thanks Kerstin Göpfrich, Glen Hocky and the other, anonymous, reviewer(s) for their contribution to the peer review of this work. Peer reviewer reports are available.

Reprints and permission information is available at http://www.nature.com/reprints

Publisher's note Springer Nature remains neutral with regard to jurisdictional claims in published maps and institutional affiliations.

Supplementary Information for

"Reconstitution of contractile actomyosin rings in vesicles"

Thomas Litschel, Charlotte F. Kelley, Danielle Holz, Maral Adeli Koudehi, Sven K. Vogel,
Laura Burbaum, Naoko Mizuno, Dimitrios Vavylonis and Petra Schwille

Supplementary Method

Details regarding theoretical modeling
Simulations are based on the Brownian dynamics model of Adeli-Koudehi et al.[1], as summarized below.

Filament representation
Filaments are represented as series of beads separated by $l_0 = 0.1\ \mu m$, representing 37 actin subunits, connected by springs. Bead motion is governed by forces from the spring and bending forces, rigid confining boundary, crosslinking and stochastic forces. The 3D positions, $\mathbf{r}_i$ of the i bead is evolved in time according to:

$$\mathbf{F}_i^{spring} + \mathbf{F}_i^{bend} + \mathbf{F}_i^{stoch} + \mathbf{F}_i^{boundary} + \mathbf{F}_i^{atr} = \zeta_b \frac{d\mathbf{r}_i}{dt}, \qquad (1)$$

where ζ_b = 0.108 pN s/µm is an effective drag coefficient, which corresponds to a viscosity 350 times higher than water (lower viscosity values become computationally costly to simulate). The spring, bending and stochastic forces are as follows:

$$\mathbf{F}_i^{spring} = -\frac{k}{2} \sum_{j=1}^{N-1} \frac{\partial \left(\left|\mathbf{r}_{j+1} - \mathbf{r}_j\right| - l_0\right)^2}{\partial \mathbf{r}_i}, \qquad (2)$$

$$\mathbf{F}_i^{bend} = \frac{\kappa}{l_0} \sum_{j=2}^{N-1} \frac{\partial \left(\mathbf{t}_j \cdot \mathbf{t}_{j-1}\right)}{\partial \mathbf{r}_i}, \qquad (3)$$

$$\langle \mathbf{F}_i^{stoch}(t)\mathbf{F}_i^{stoch}(t')\rangle_{\alpha,\beta} = 2k_B T \zeta_b \delta(t - t')\hat{I}_{\alpha\beta}, \qquad (4)$$

where N is the number of beads per filament, $\mathbf{t}_j = \left(\mathbf{r}_{j+1} - \mathbf{r}_j\right)/\left|\mathbf{r}_{j+1} - \mathbf{r}_j\right|$ is the local unit tangent vector, $\kappa = k_B T l_p$ is the flexural rigidity, k_B is Boltzmann's constant, T is temperature, l_p is the persistence length of the filament, k = 100 pN/µm is the spring constant between filament beads (stiff enough to prevent significant filament extension or compression) and $\hat{I}_{\alpha\beta}$ is the second-order unit tensor (α and β labeling the x, y or z directions).

Attraction force between actin filaments
Crosslinking between filaments is due to a short-range, isotropic attractive potential between filament beads. If bead i is within the distance r_{atr} to bead j, then the force on bead i due to bead j is:

$$\mathbf{F}_i^{atr} = -\frac{k_{atr}}{2} \frac{\partial \left(\left|\mathbf{r}_j - \mathbf{r}_i\right| - r_0\right)^2}{\partial r_i} \quad \left(\left|\mathbf{r}_j - \mathbf{r}_i\right| < r_0\right), \qquad (5)$$

where the spring constant is k_{atr} and the crosslink equilibrium length is r_0 = 0.012 µm. The parameters k_{atr} and r_{atr} characterize the effective stiffness and range of interaction between filament beads due to cross-linking. For the simulations in this study we used r_{atr}= 0.06 µm, a value that allows bundle formation without significant filament sliding along the bundle.

Boundary conditions and interactions

Filaments are in a spherical confinement with a repulsive hard wall, which was represented by a constant force of magnitude 1 pN normal to the cell boundary exerted on every bead crossing it. In simulations where filaments were attracted to the boundary, a short-range attraction near the spherical hard wall was implemented by the following short-range surface force to each bead: (6)

$$\mathbf{F}_i^{srf} = -\frac{k_{srf}}{2}\frac{\partial\big(|\mathbf{R}_{conf} - \mathbf{r}_i| - r_0\big)^2}{\partial\mathbf{r}_i} \qquad \big(|\mathbf{R}_{conf} - \mathbf{r}_i| < r_{srf}\big),$$

where k_{srf} = 3 pN/μm is the corresponding spring constant and r_{srf} = 0.06 μm is the distance from the confinement surface where beads can feel the force. Here $\mathbf{R}_{conf}$ points to the confining sphere boundary in the direction of $\mathbf{r}_i$.

Simulation of polymerization

We start with a fixed number of filament nuclei which elongate over time by addition of beads at one end of the filament. The elongation rate is proportional to the concentration of the remaining bulk monomers, $C(t)$ and the barbed end polymerization rate, $k_+ = 10$ μM/s. For a fixed filament concentration $C(t)$ decays according to:

$$C(t) = C_{actin}e^{-k_+F_0 t} \qquad (7)$$

where F_0 is the initial filament nuclei concentration and C_{actin} is the initial bulk actin monomer concentration. In these simulations, all filaments are the same length and we tuned F_0 to get the desired final filament length, taking into consideration that the higher spontaneous nucleation rate of higher actin concentrations leads to shorter filaments, as in Adeli-Koudehi et al.

Implementation of the simulation

We used a $dt = 1.5 \times 10^{-4}$ s for Supplementary Fig. 7a, b and Supplementary Fig. 11a, b. We used a smaller value of $dt = 0.5 \times 10^{-4}$ s for Fig. 3b, Supplementary Fig. 7c and Supplementary Fig. 11c that have higher persistence length and require a smaller value for numerical stability. The code of Adeli-Koudehi et al. was modified by adding a list of nearest neighbors to check interactions every timestep. The nearest neighbors list was updated ever 50 dt to speed up the runtime.

Classification of ring (R) and ring-like (RL) structures in simulations.
In the simulations of ring formation as function of confining diameter for c = 2 μM and final filament length L = 6 μm (Fig. 3, Supplementary Fig. 11b, c, Supplementary Fig. 12c), we see formations that are close to what could be considered a ring, but have some imperfections such as forking small bundles that stick out of the main ring. Such structures are not as frequently observed in experiments. We anticipate that simulations with longer run-times that also allow filament breakage for filaments with high curvature at intersection points would allow a clean single ring to eventually form. We thus labeled such structures as RL. In the simulations with short filaments for c = 2 μM and final filament length L = 1.2 μm (Fig. 3, Supplementary Fig. 11a), we also labeled as RL structures with small gaps (less the 20% of the circumference) that could also be filled by

diffusion of bundle segments to the main ring over longer simulation times. Explicit examples are shown in Supplementary Fig. 11.

Details regarding experimental analysis

Image processing and analysis of the Z-stack confocal datasets of actin-labelled vesicles was mostly performed using the software ImageJ/Fiji[2,3], complemented with the plugins Image Stabilizer[4] and Squassh[5] (from the MOSAIC ToolSuite update site). The organization of the actin networks in vesicles under the different experimental conditions was characterized using ImageJ/Fiji in combination with SOAX[6,7]. Specifically, the workflow to derive a skeleton model from the confocal volumes was implemented as a combination of a series of ImageJ scripts, each one performing a processing step on all the images acquired. Some parts of analysis required manual intervention, as below outlined. After making the images conform to its input specifications, the software SOAX was launched and controlled through Fiji to determine a model of the filaments in batch mode.

When characterizing actin bundle morphologies, we analyzed vesicles regardless of their content with exception of clear outliers, such as deformed vesicles and vesicles that did not contain any discernable actin bundles.

Image processing for 3D analysis (Fig. 1d and for Fig. 2b)

The confocal z-stacks were deconvolved using the software Huygens Essential (Scientific Volume Imaging), by means of the Classic Maximum Likelihood Estimation algorithm with a theoretical Point Spread Function. In some stacks a drift between planes of either the actin network within the vesicles or the vesicles themselves was compensated with the Image Stabilizer plugin[4]. All the vesicles in each stack were manually selected and then cropped to generate subvolumes, each containing only one vesicle. The subvolumes were filtered and the filaments segmented from them with the Squassh algorithm as implemented in Fiji[5]. The structures were detected using the following options: background removal with a window of 1 μm size; regularization parameter: 0.075; removal of background intensity with threshold determined by the Triangle method; removal of segmented regions smaller than 1 μm linear size; automatic local intensity estimation; Poisson noise model; soft mask applied to final segmentation. Finally the subvolumes were scaled along the z axis to make the voxels isotropic, as required by SOAX, and a mild 3D Gaussian Blur filter (1 pixel sigma) was applied to reduce any artefact from the scaling procedure.

Generation of 3D actin filament network models (Fig. 1d and for Fig. 2b)

A model for the filament network in each vesicle was determined using the software SOAX[7] on the subvolumes of the segmented filaments. The software implements a Stretching Open Active Contours method to compute a centerline (called 'snake' in the software) from each filament, which can be used for quantitative analysis. The batch processing procedure to extract the

centerlines was launched from Fiji, after setting the parameters that controls the algorithm (see SOAX documentation for their definitions) as follows: Intensity Scaling: 0; Gaussian std: 1.2 pixels; Ridge Threshold: 0.007; Minimum Foreground: 1 sigma level; Maximum Foreground: maximum bit depth of the data; Snake Point Spacing: 2 pixel; Init z: True; Minimum Snake Length: 7 µm; Maximum Iterations: 10000; Check Period: 100; Change Threshold: 0.1 pixels; Alpha: 0.03; Beta: 0.5; Gamma: 2; External Factor: 1; Stretch Factor: 0.2; Number of Background Radial Sectors: 8; Radial Near: 0.35 µm; Radial Far: 0.525 µm; Background Z/XY Ratio: 3; Delta: 0.25 µm; Overlap Threshold: 0.313 µm; Grouping Distance Threshold: 0.5 µm; Grouping Delta: 0.813 µm; Minimum Angle for SOAC Linking: 100 degrees; Damp z: True. The batch procedure generated a file for each vesicle, containing the coordinates of the centerlines modeling the actin network, which were then converted to marker model for visualization in UCSF Chimera[8].

Curvature Analysis (Fig. 2b)

The filament models generated by batch processing were then analyzed from the SOAX GUI, using the Filament Curvature Analysis option. This tool divides the models into equally sized segments and then determines a curvature value for each of the segments. The curvature values (in μm^{-1}) from each vesicle were then normalized with respect to the curvature of the respective vesicle membranes, and the values from all the vesicles under the same experimental condition were finally aggregated to generate the bundle curvature distribution. Curvature values less than 1 corresponds to regions where the filaments are flatter than the membrane, and vice versa.

Membrane Proximity Analysis (Fig. 3c, d)

The quantification of the distribution of the actin networks inside the vesicles was performed on the radial intensity profile. The center and the radius of the vesicle was determined semi automatically, starting from two opposite points on the membrane marked manually in Fiji on a maximum intensity projection of the volume (script provided at https://doi.org/10.5281/zenodo.4555840). The radial profile was used to compute the membrane proximity metric, defined as the weighted average of the radii, with the weights given by the intensity at each radius, and the average normalized by the vesicle radius. Values close to one indicate that most of the intensity is found close to the membrane, while a uniform distribution of the intensity within the vesicle gives a membrane proximity value of 0. Smaller values indicate that the intensity is condensed at the vesicle center.
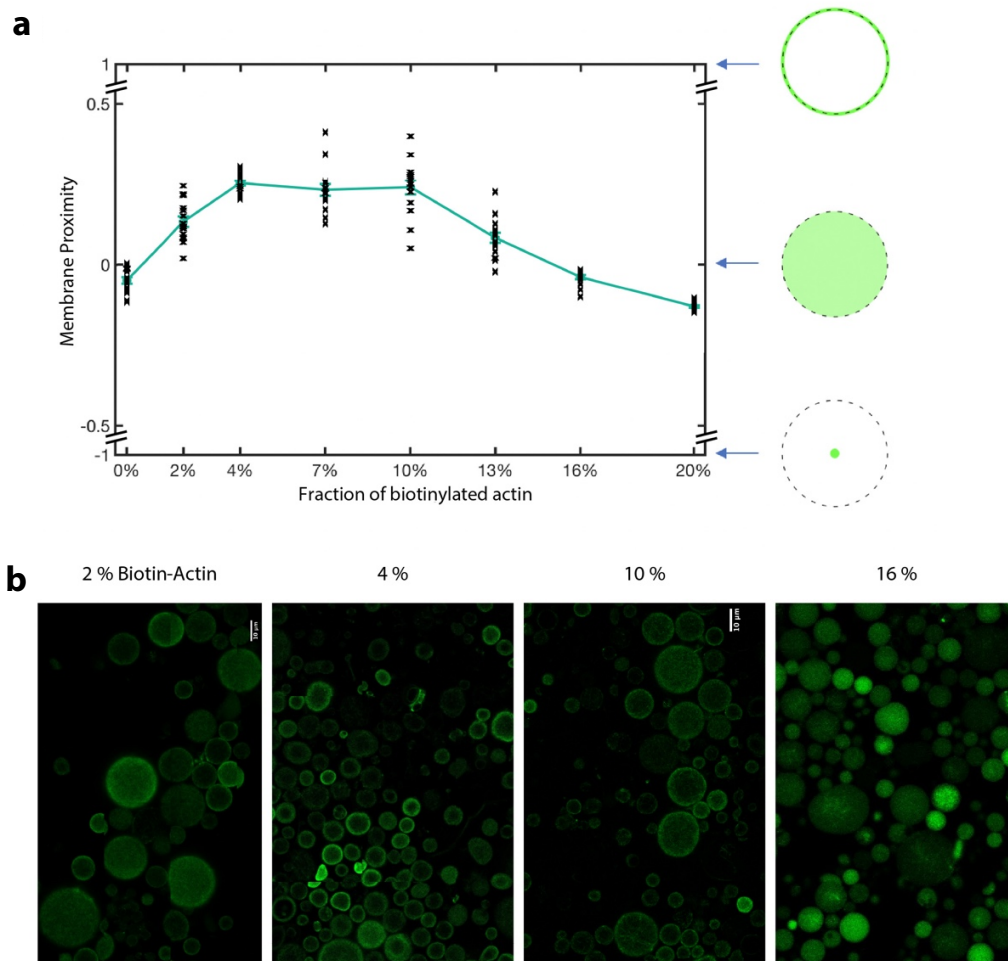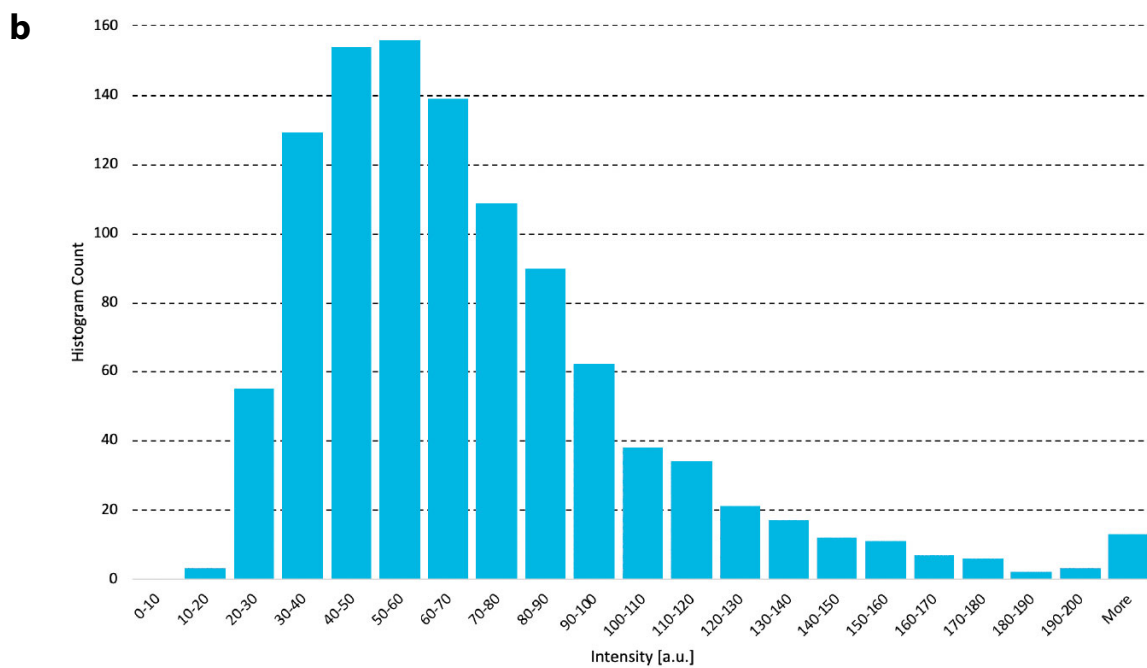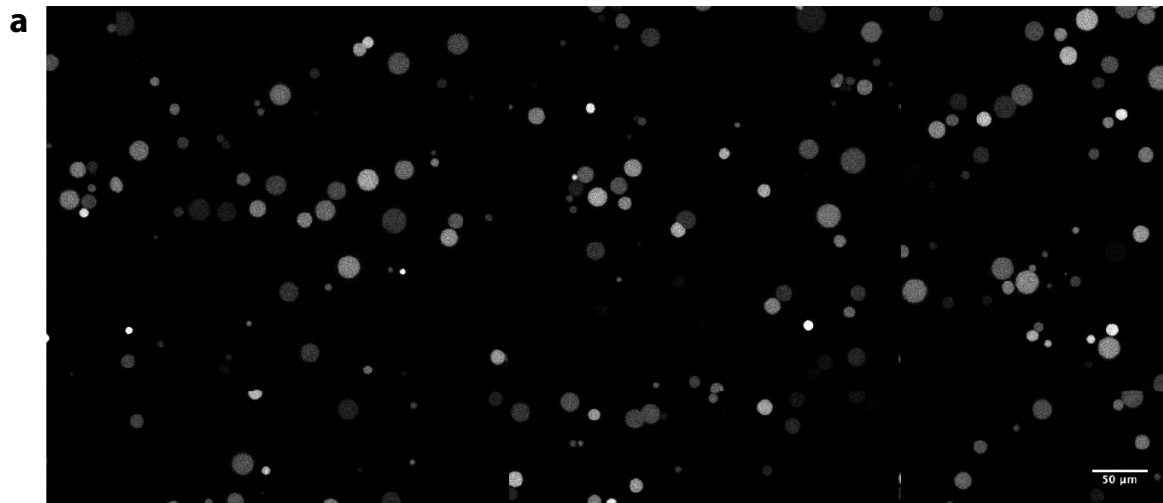
Supplementary Figures

center confocal slice

b z-projection of all confocal slices

c side view of 3D reconstruction
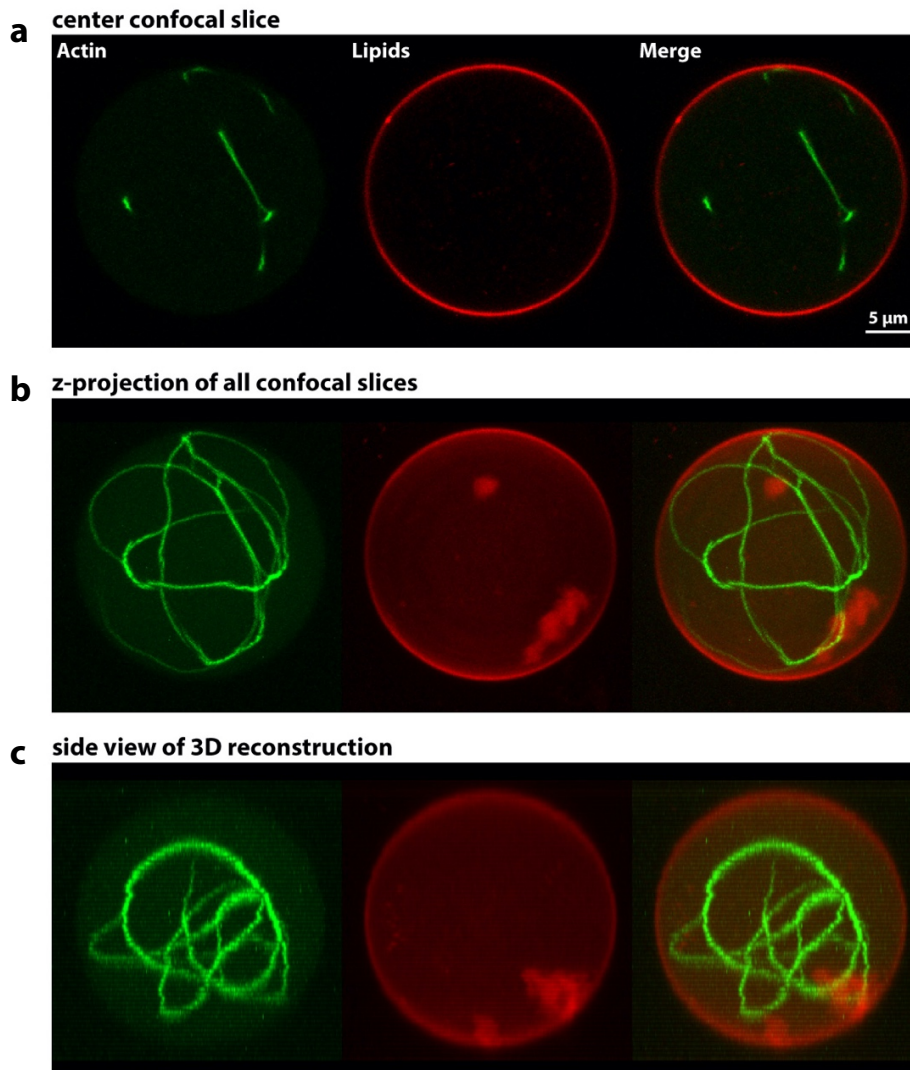
Supplementary Fig. 1: GUV with labelled membrane containing actin bundles bundled by α-actinin. Vesicle is made from POPC with 0.015% DOPE-ATTO655. Images in this paper are taken as z-stacks of confocal slices. **a** Center z-slice of a data set with 62 confocal slices. **b** Projection of all confocal slices. **c** Side-view of a 3D reconstruction of the vesicles.
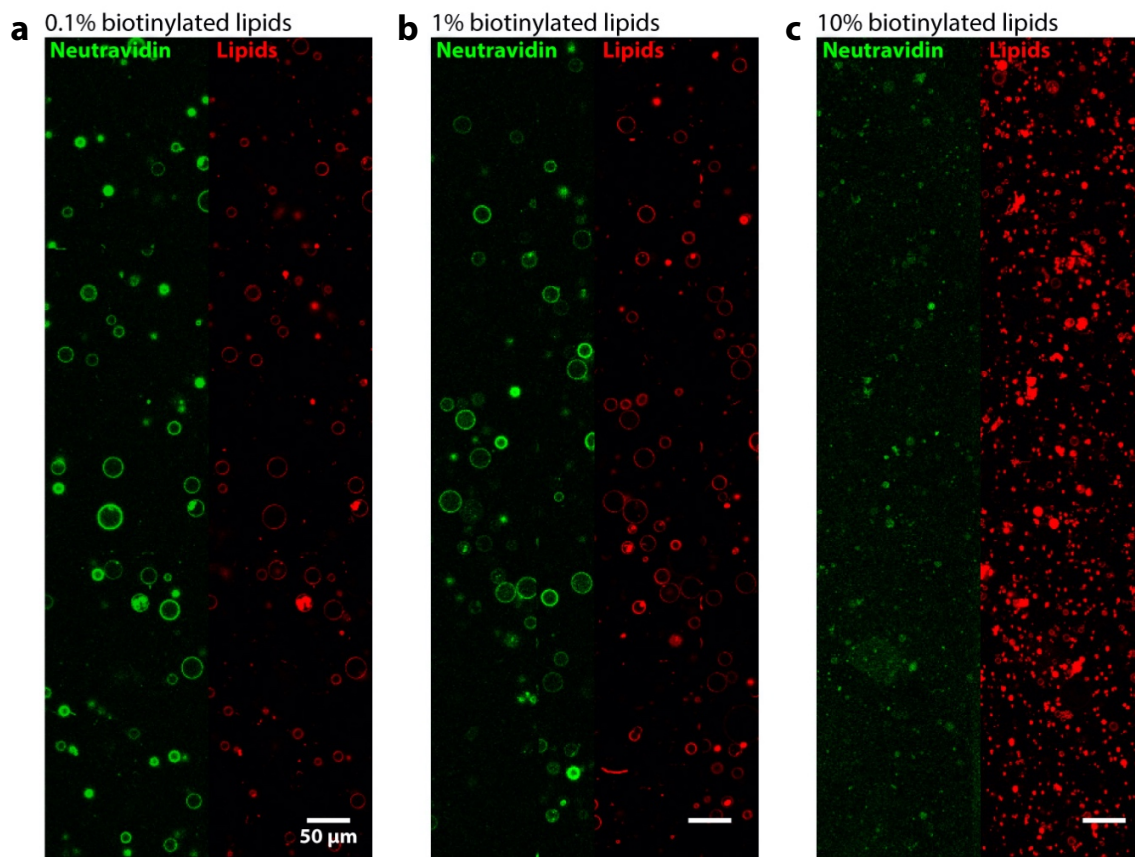
Supplementary Fig. 2: We tested three concentrations of biotinylated lipids (DSPE-PEG(2000) Biotin) in GUVs. **a**, **b** and **c** show fractions of 0.1%, 1% and 10% respectively. The GUVs contain NeutrAvidin™ labeled with OregonGreen™. OregonGreen is shown in green, lipids (POPC with DOPE-ATTO655) are shown in red. Binding of NeutrAvidin to the membrane seems equally efficient for 0.1% and 1% biotinylated lipids, while the vesicle yield is very low with 10% biotinylated lipids. Most of the lipid signal in (**c**) is not from vesicles, but from lipid aggregates or similar lipid structures.

Supplementary Fig. 3: Membrane binding of unbundled actin in dependency of concentration of biotinylated actin. Vesicle membranes contain 1% biotinylated lipid and 0.17 μM Neutravidin. We tested a range of different fractions of biotinylated actin for their effect on binding efficiency in experiments with unbundled actin. Equatorial focal planes of GUVs were analyzed to quantify the average proximity of actin signal to the membrane and plotted on a normalized range from -1 (all signal in the center of the vesicle) to +1 (all signal on the membrane). We found an optimum between 4 % and 10 % biotinylated actin. At fractions of more than 10 %, membrane binding seems to decrease, likely because binding between actin filaments competes with binding to the membrane. n = 15 per condition. Error bars show SEM.

a

b

Supplementary Fig. 4: Concentration distribution of encapsulated solubles: Control experiment in which we encapsulate a fluorescent dye (Alexa Fluor 546 NHS-Ester). **a** Field of view section of analyzed vesicles. **b** Fluorescence intensities of 1061 vesicles
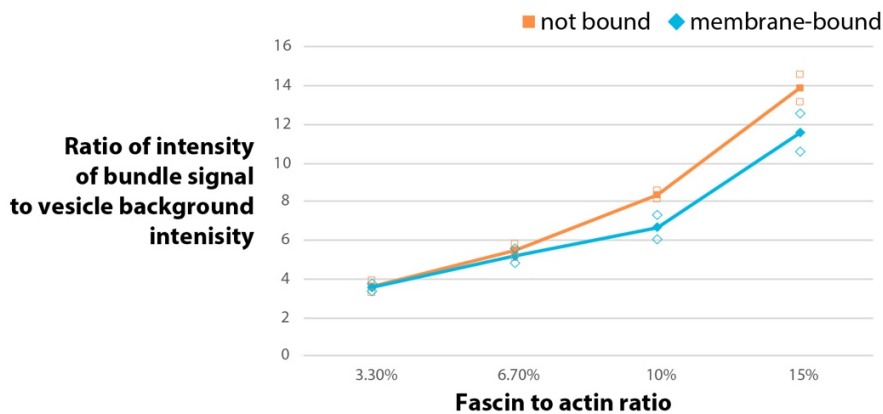
Supplementary Fig. 5: Ratio of bundle signal intensity to background intensity in dependency of fascin to actin ratio in vesicles seen in Fig. 3a. With increasing amounts of fascin, actin bundles get thicker, while the amount of unbundled actin filaments in the vesicle decreases. By plotting the ratio of the fluorescence intensity of the bundles to the intensity of the lumen, we visualize this shift of actin from the bulk phase into bundles. For each condition we analyzed two vesicles. We did 4 measurements per vesicles by plotting the spatial intensity along 4 straight lines (0°,45°, 90°, 135°) and calculated the ratio between highest and lowest intensity within the vesicles. Hollow squares: averages for vesicles. Solid squares: averages for conditions.

6 µM Actin
fascin:actin = 6.7%
not bound

6 µM Actin
fascin:actin = 6.7%
membrane-bound
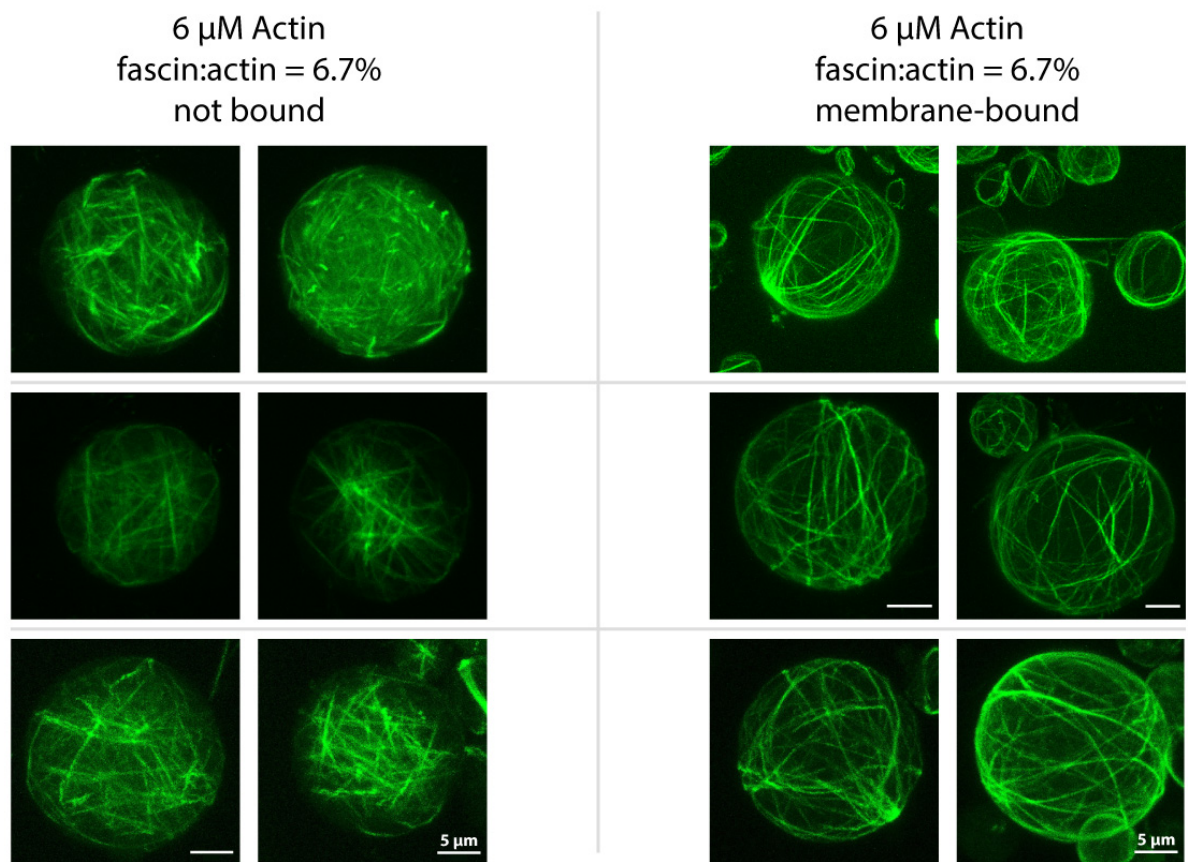
Supplementary Fig. 6: Cytoskeletal vesicles with 6 μM actin and a fascin to actin ratio of 6.7 to 100. For this actin and fascin concentration, in experiments without membrane binding (left), bundles are relatively short and below the threshold for which we see long bundles that wrap around the inner circumference of the vesicle membrane and often connect to other bundles (which is the case for conditions with higher fascin concentrations without membrane-binding, see Fig. 3a). With the addition of membrane binding (right), this threshold seems to be lowered so that bundles can extend to form longer structures. Three separate experimental runs are shown for each condition (each row corresponds to one experimental run).

a $c = 2\,\mu\text{M}$ $L = 6\,\mu\text{m}$ $R = 5\,\mu\text{m}$ $l_P = 17\,\mu\text{m}$	$k_{atr} = 0.3$ pN/µm		$k_{atr} = 1.0$ pN/µm		$k_{atr} = 2.0$ pN/µm		$k_{atr} = 3.0$ pN/µm	
	-	+	-	+	-	+	-	+
	1,870 s	2,170 s	2,343 s	3,612 s	1,818 s	1,983 s	1,648 s	2,308 s

b $c = 4\,\mu\text{M}$ $L = 3.8\,\mu\text{m}$ $R = 4\,\mu\text{m}$ $l_P = 17\,\mu\text{m}$	$k_{atr} = 0.3$ pN/µm		$k_{atr} = 1.0$ pN/µm		$k_{atr} = 2.0$ pN/µm		$k_{atr} = 3.0$ pN/µm	
	-	+	-	+	-	+	-	+
	634 s	608 s	1,399 s	3,334 s	1,565 s	2,269 s	492 s	1,797 s

c $c = 6\,\mu\text{M}$ $L = 3.8\,\mu\text{m}$ $R = 3\,\mu\text{m}$ $l_P = 40\,\mu\text{m}$	$k_{atr} = 0.3$ pN/µm		$k_{atr} = 1.0$ pN/µm		$k_{atr} = 2.0$ pN/µm		$k_{atr} = 3.0$ pN/µm	
	-	+	-	+	-	+	-	+

250 s

500 s

750 s

| Last frame | 961 s | 993 s | 1,798 s | 3,000 s | 781 s | 872 s | 780 s | 787 s |
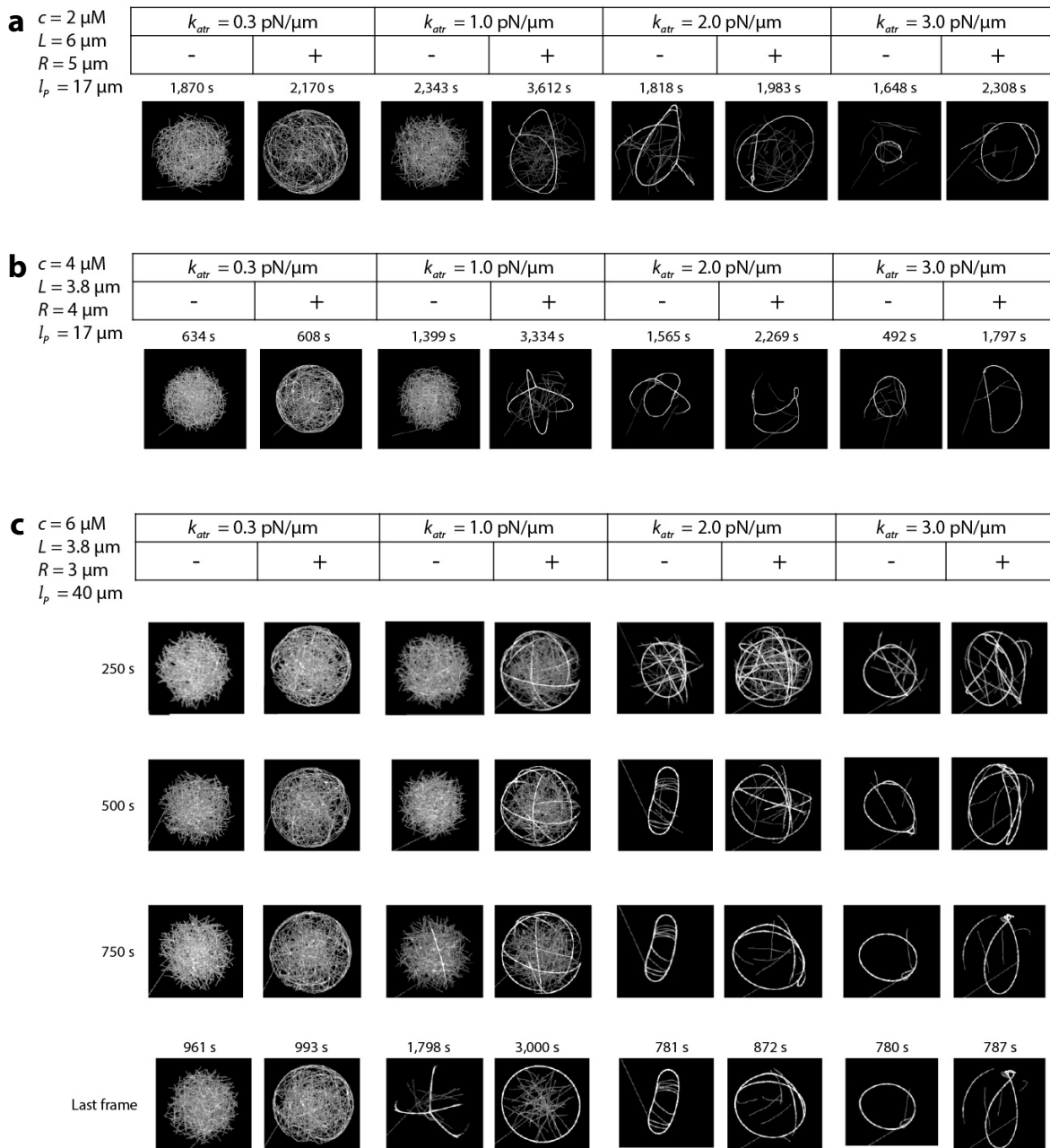
Supplementary Fig. 7: Snapshots (maximum intensity projections) of simulations of confined actin filaments with varying cross-linking interaction strength k_{atr}, with or without attraction to confining boundary, for comparison to experiments of Fig. 3a. All simulations are for final filament lengths L shorter than the confining diameter $2R$, corresponding to experimental measurements. Simulations were run for long enough times such that the bundle/loop configurations reach a stationary shape. Results show a transition from unbundled/weakly bundled to bundled configurations with increasing k_{atr}. Attraction to confining boundary promotes bundling (cases $k_{atr} = 0.3$, 1 pN/μm) and leads to larger circular structures (cases $k_{atr} =$
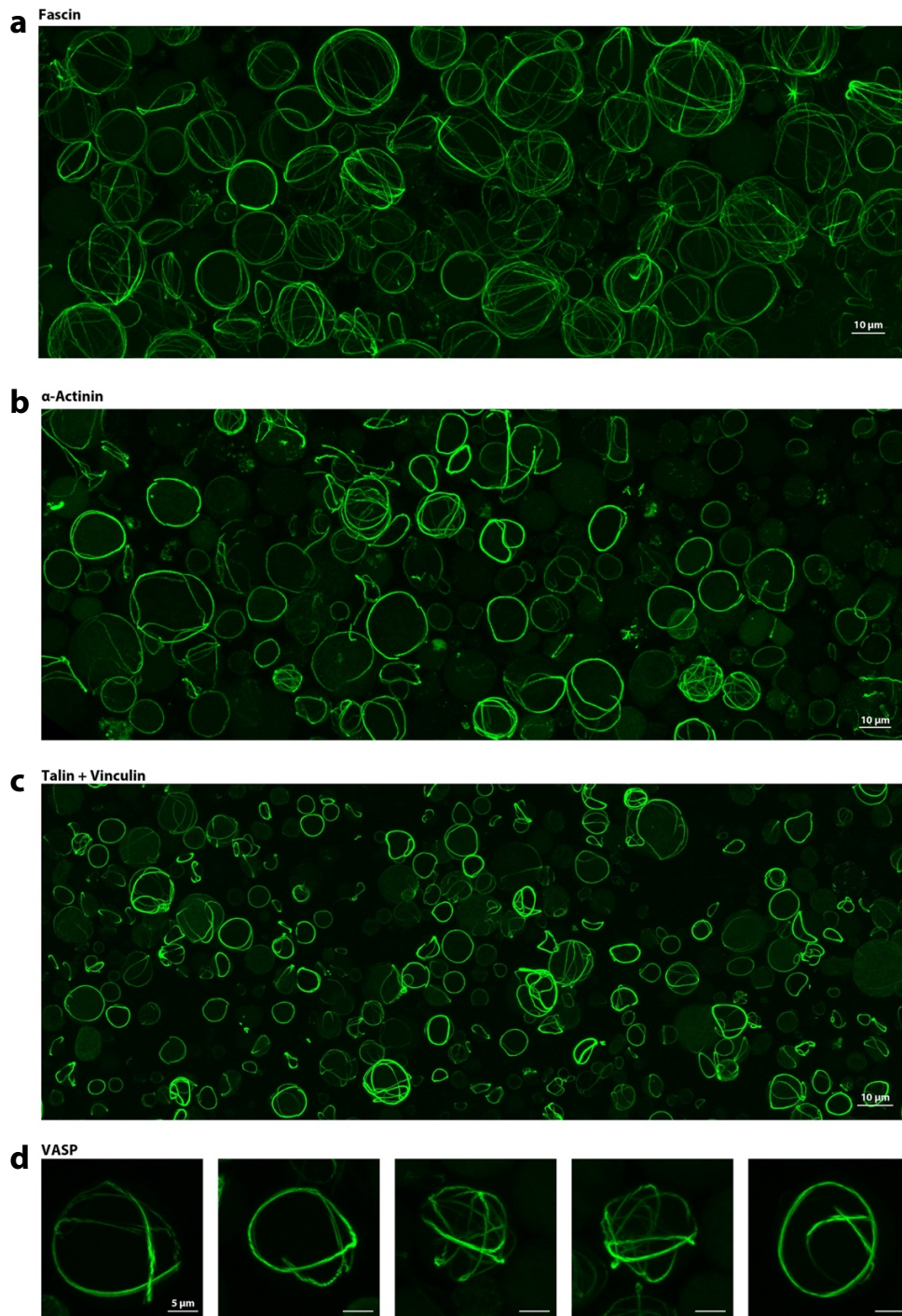
2, 3 pN/μm). The confining radius was decreased with increasing concentration for reasons of computational efficiency. **a** At the lowest actin concentration ($c = 2$ µM, $R = 5$ μm, initial number of nuclei 284) single actin rings and ring-like structures are observed at high k_{atr}, similar to bundles of the experiments of Fig. 3a at 2 µM (where fascin promoted bundling at all concentrations). **b** Behavior similar to panel A is seen at intermediate actin concentrations ($c = 4$ µM, $R = 4$ μm, initial number of nuclei 498). **c** At the highest actin concentration ($c = 6$ µM, $R = 3$ μm, initial number of nuclei 315) and at the higher k_{atr} values, bundle networks at early times resembling the corresponding experimental measurements of Fig. 3a. In panel (**c**) the individual filament persistence length was increased to 40 μm to simulate the effect of stiffening of fascin-actin bundles.
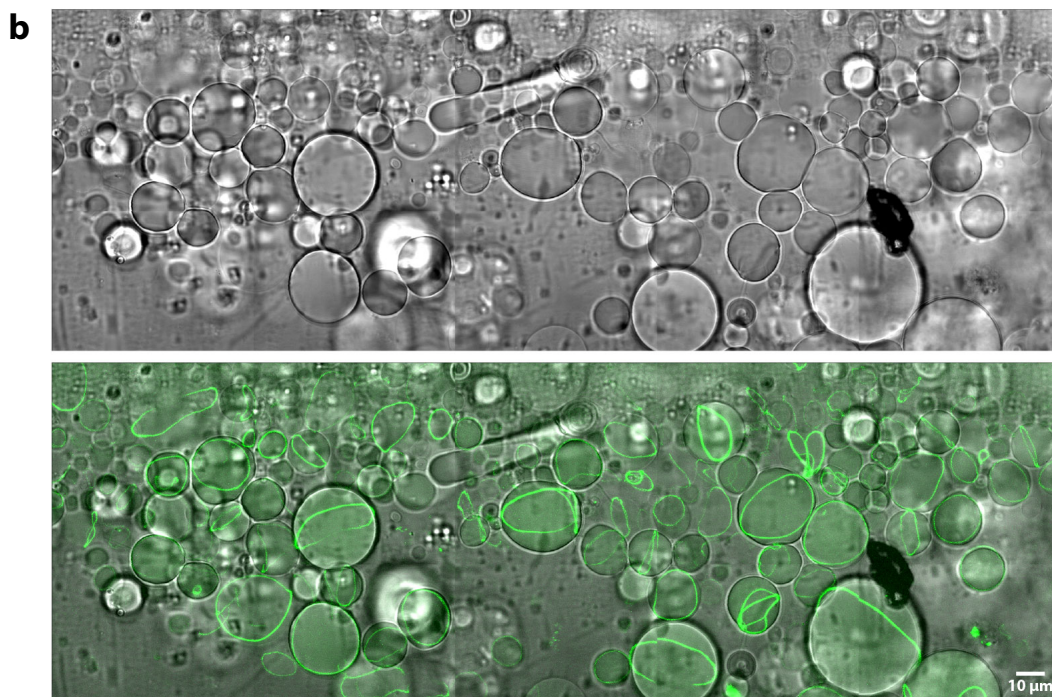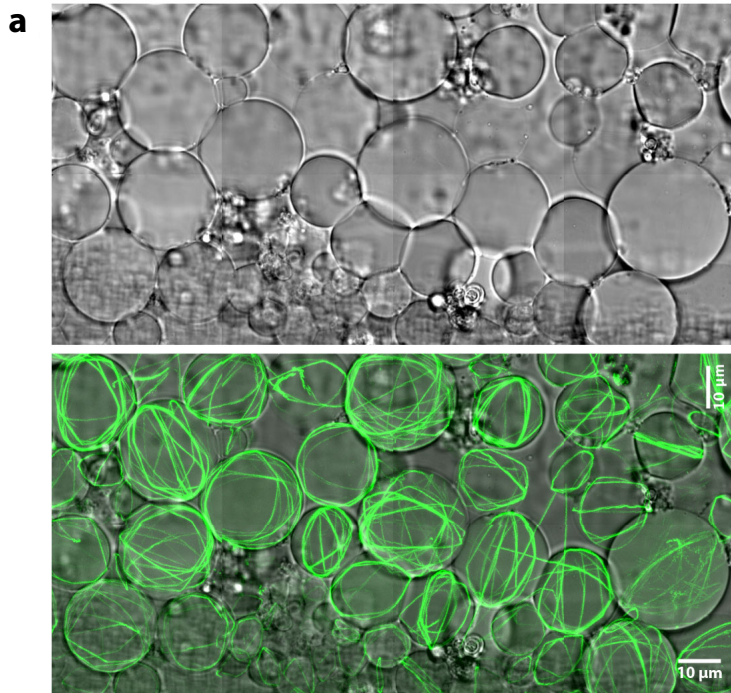
Supplementary Fig. 8: Differential Interference Contrast Images (DIC): **a** Section view from Fig. 1b as DIC image and overlay of fluorescence image (maximum projection of a z-stack of images) on DIC image. **b** Section view from Fig. 4c as DIC image and overlay of fluorescence image (maximum projection of a z-stack of images)
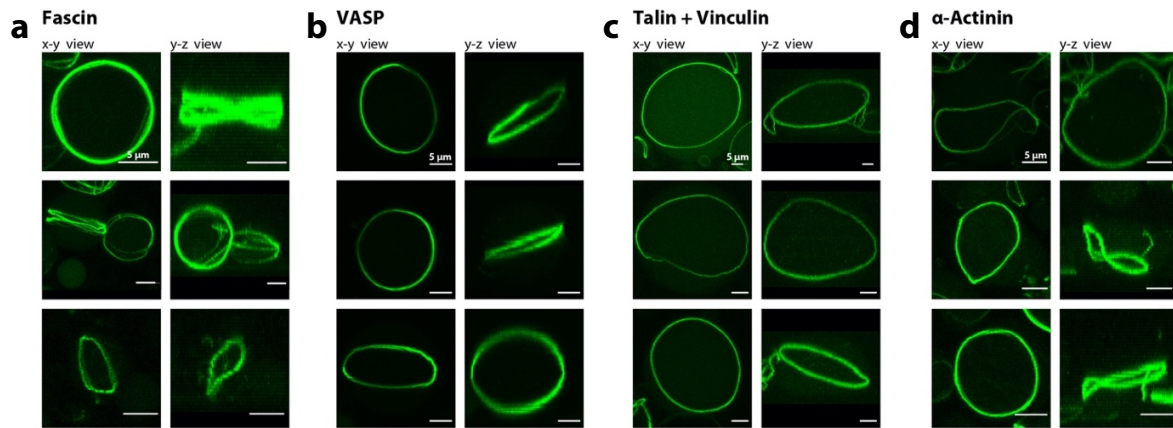
Supplementary Fig. 9: Membrane-bound rings form from actin bundled by fascin (**a**), VASP (**b**), talin with vinculin (**c**) and α-actinin (**d**)). All images are maximum projections of confocal z-stacks. We used 2 μM actin in all cases, but due to differences in bundling activity, different concentrations of bundling protein: 0.3 μM fascin, 0.9 μM VASP, 1 μM α-actinin, 2 μM talin and 2 μM vinculin.

Supplementary Fig. 10: Additional images of vesicles with actin bundled by the four bundlers. Actin is bound to the vesicle membrane by biotin-neutravidin-biotin links. Large area scans of vesicles containing actin bundled by fascin (**a**), α-actinin (**b**) and talin with vinculin (**c**). **d** Images of vesicles with actin bundled by VASP. All images ((**a**)-(**d**)) are maximum projections of confocal z-stacks. We used $2\,\mu$M actin in all cases, but due to differences in bundling activity,

different concentrations of bundling protein: 0.3 μM fascin, 0.9 μM VASP, 1 μM α-actinin, 2 μM talin and 2 μM vinculin.

a

c = 2 μM   L = 1.2 μm k_{atr} = 2 pN/μm
R = 2.5 μm l_P = 17 μm   t = 1,500 s

| No Surface Attraction | With Surface Attraction |

b

c = 2 μM   L = 6 μm k_{atr} = 2 pN/μm
R = 5 μm l_P = 17 μm

| No Surface Attraction | With Surface Attraction |

1,544 s   2,059 s   2,010 s   4,127 s   1,858 s   2,033 s   2,835 s   2,296 s   2,850 s   4,385 s
1,396 s   1,689 s   1,914 s   1,100 s   1,836 s   1,522 s   2,665 s   3,330 s   3,610 s   2,242 s
1,390 s   1,300 s   2,040 s   2,390 s   2,056 s   2,240 s   2,580 s   1,983 s   2,450 s   2,838 s
1,970 s   1,818 s   1,785 s   1,333 s   1,182 s   2,242 s   2,542 s   2,179 s   2,805 s   2,577 s

c

c = 2 μM   L = 6 μm k_{atr} = 2 pN/μm
R = 5 μm l_P = 40 μm

| No Surface Attraction | With Surface Attraction |

1,821 s   1,833 s   1,174 s   1,976 s   1,119 s   2,819 s   2,485 s   2,392 s   3,735 s   1,804 s
2,197 s   1,148 s   1,109 s   1,324 s   1,780 s   1,500 s   1,873 s   2,282 s   2,232 s   2,702 s
2,357 s   1,701 s   1,814 s   1,767 s   1,891 s   1,914 s   3,048 s   3,033 s   2,936 s   2,829 s
2,282 s   1,568 s   1,500 s   1,538 s   1,119 s   2,062 s   2,185 s   2,133 s   2,473 s   2,967 s
1,024 s   2,515 s

Supplementary Fig. 11: Snapshots of simulations to examine ring formation probability with and without attraction of filaments to confining surface. Snapshots show maximum intensity projections at long enough times such that the bundle/loop configurations reach a stationary shape. All cases show concentration $c = 2 \, \mu\text{M}$, cross-linking strength $k_{\text{atr}} = 2 \, \text{pN}/\mu\text{m}$ with varying confining radius R, final filament length L, and persistence length l_{P}. **a** Simulations in small confinement ($R = 2.5 \, \mu\text{m}$). We classified cases with circular arcs covering 75% of the circumference as ring-like. **b** Simulations in larger confinement ($R = 5 \, \mu\text{m}$). Ring and ring-like configurations indicated by "R" and "RL". **c** Simulations as in panel B but with a higher individual filament persistence length ($l_{\text{p}} = 40 \, \mu\text{m}$) to mimic the stiffer fascin bundles. Simulations with radii 2.5 and 5 μm began with 177 and 284 nuclei respectively.
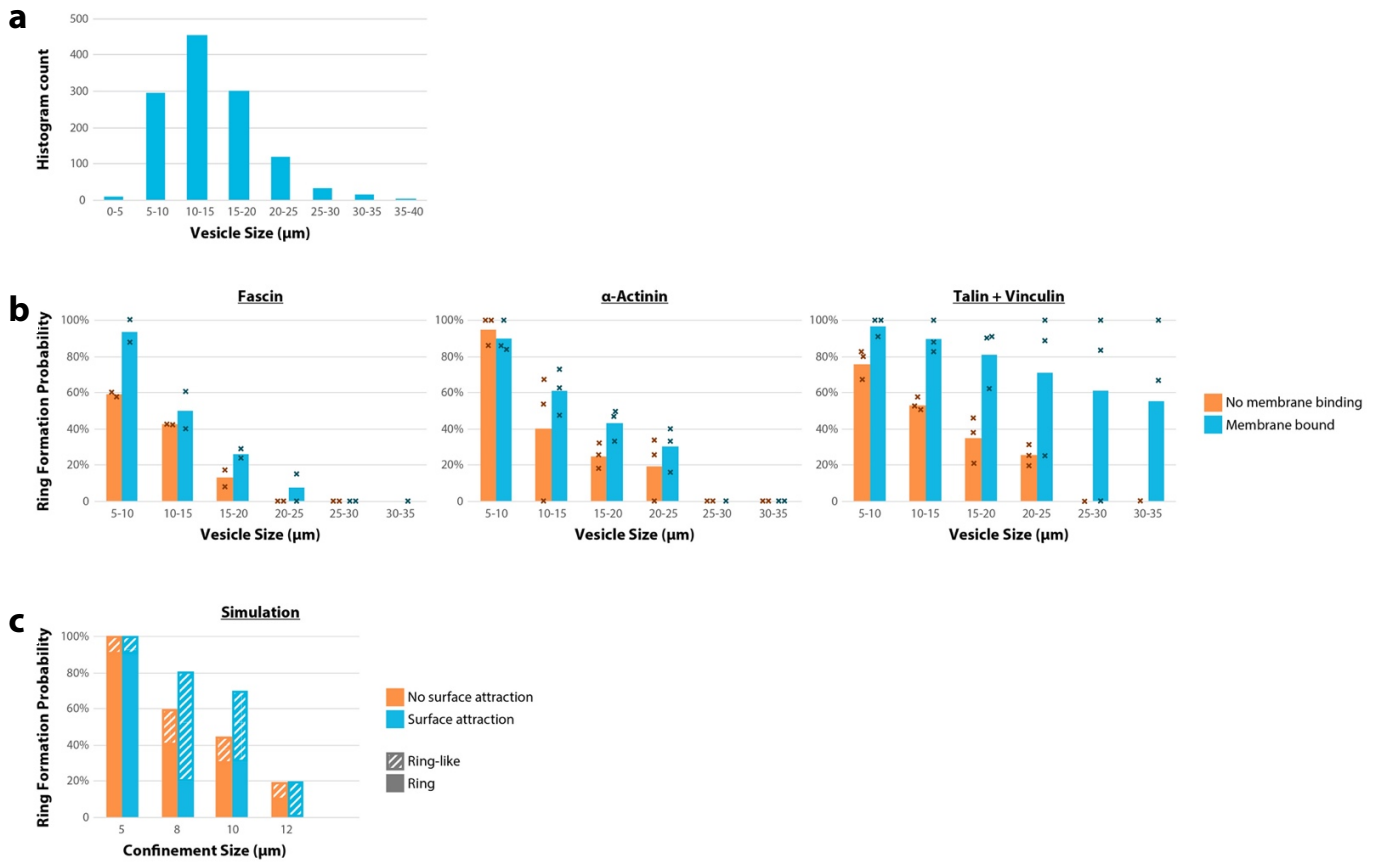
Supplementary Fig. 12: Dependency of ring formation probability on vesicle size. **a** Histogram showing the distribution of vesicle sizes (vesicle diameters). **b** Average probability of formation of single actin bundle rings in dependency of vesicle size. **c** Confinement size dependency of computer simulations. The x axis is diameter ($2R$). Simulations show concentration $c = 2\,\mu\mathrm{M}$, cross-linking strength $k_{\mathrm{atr}} = 2\ \mathrm{pN}/\mu\mathrm{m}$ with final filament length $L = 6\ \mu\mathrm{m}$, and persistence length $l_{\mathrm{P}} = 17\ \mu\mathrm{m}$. For confinement sizes with diameters of 5, 8, and 10 μm, n = 20 for each condition (surface attraction and no surface attraction) and with a diameter of 12 μm n = 10 for each condition. The number of starting filament nuclei were 36, 145, 284 and 491 respectively.
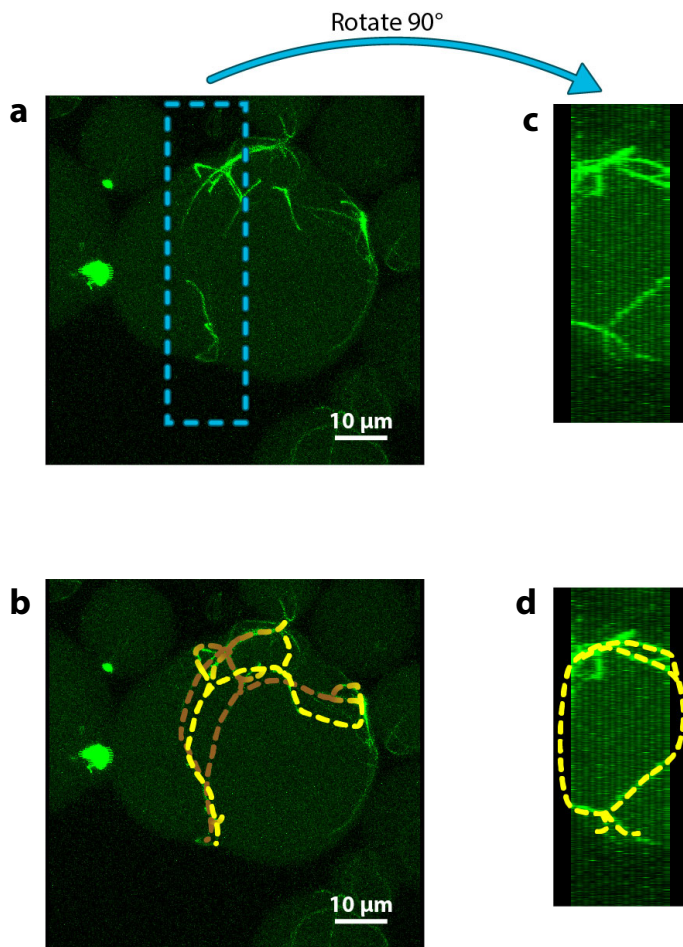
Supplementary Fig. 13: Microscopy representations illustrating the ring-like character of the actin bundles shown in Fig. 5a (at time point t = 60 min). **a** Projection of z-stack slices. Unfortunately we did not record the full volume (i.e. full z-range) of the vesicle, bottom and top are missing. **b** Overlay of suspected actin bundle network. Yellow: bundles in the upper half of the vesicle; brown: bundles towards bottom of vesicle (towards microcopy glass slide). **c** "side view" of center section (blue dotted rectangle in (**a**)). Z-stack was cropped to center area shown with blue dotted rectangle in (**a**). After 3D reconstruction was generated, viewing angle was determined to show a 90 degree angle compared to (**a**). **d** same image as (**c**), but again with yellow dotted lines indicating the suspected position of actin bundles, forming a ring within the vesicle.
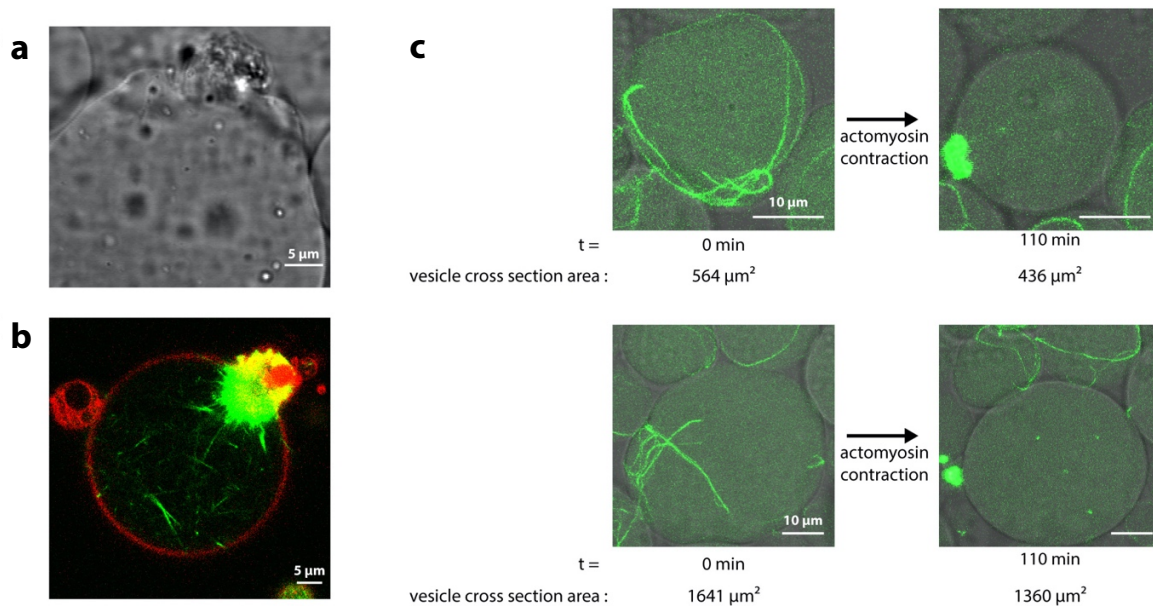
Supplementary Fig. 14: Membrane crumpling through actomyosin contraction. **a** Close-up of DIC image of the vesicle in Fig. 5a. Actomyosin deforms membrane and "crumples" it into one spot, thus presumably increasing membrane tension. **b** Experiment with actin bundled by fascin and contraction through myosin activity. Membrane (DOPE-ATTO655) in red. The vesicle's membrane concentrated into one spot in the upper right corner. **c** Two more examples of contracting actomyosin networks that cause a decrease in xy-cross section area through increasing membrane tension. We assume the vesicles become more spherical, thus becoming smaller in x and y, but taller in z-direction. While we did not record full z-stacks which allow to measure the full height of the vesicles, the phase contrast indicates that the vesicle is becoming taller: in the frames on the left (t = 0), the DIC image shows only a faint contour of the vesicle, indicating that the focal plane is approximately at the equator of the vesicle (the center of the vesicle is in focus), after contraction (t = 110 min) the vesicle contour resembles an outer shadow (negatively defocused), indicating that the equator of the vesicle shifted in +z direction.

Supplementary Fig. 15: Rare example of vesicles that endured drying and freezing that do not contain an actin cortex. These visibly flattened vesicles contain short actin bundles that are not bound to the membrane (see Supplementary Fig. 6, 6 μM actin, 6.7% fascin, no membrane-binding).

Supplementary References

1   Adeli Koudehi, M., Rutkowski, D. M. & Vavylonis, D. Organization of Associating or Crosslinked Actin Filaments in Confinement. *Cytoskeleton* **76**, 532-548, doi:10.1002/cm.21565 (2019).

2   Schneider, C. A., Rasband, W. S. & Eliceiri, K. W. NIH Image to ImageJ: 25 years of image analysis. *Nature Methods* **9**, 671-675, doi:10.1038/nmeth.2089 (2012).

3   Schindelin, J. *et al.* Fiji: an open-source platform for biological-image analysis. *Nature Methods* **9**, 676-682, doi:10.1038/nmeth.2019 (2012).

4   Li, K. The image stabilizer plugin for ImageJ. *http://www.cs.cmu.edu/~kangli/code/Image_Stabilizer.html* (2008).

5   Rizk, A. *et al.* Segmentation and quantification of subcellular structures in fluorescence microscopy images using Squassh. *Nature Protocols* **9**, 586-596, doi:10.1038/nprot.2014.037 (2014).

6   Xu, T., Vavylonis, D. & Huang, X. 3D actin network centerline extraction with multiple active contours. *Medical Image Analysis* **18**, 272-284, doi:https://doi.org/10.1016/j.media.2013.10.015 (2014).

7   Xu, T. *et al.* SOAX: A software for quantification of 3D biopolymer networks. *Scientific Reports* **5**, 9081, doi:10.1038/srep09081 (2015).

8   Pettersen, E. F. *et al.* UCSF Chimera—A visualization system for exploratory research and analysis. *Journal of Computational Chemistry* **25**, 1605-1612, doi:10.1002/jcc.20084 (2004).

3. Min protein reconstitution in GUVs

3.1. Introduction and context

Biological pattern formation is one of the most intriguing phenomena in nature and equally fascinates both biologists and physicists. Patterns, like the reaction-diffusion patterns described by Alan Turing[37] are ubiquitous in nature and key to many processes that guide biological function. In cells, these patterns lead to the formation of chemical gradients and thus to symmetry breaking and self-organization, which are a requirement for many processes central to life.

There are only a handful of reaction-diffusion systems that have been well studied and characterized in laboratory settings. A noteworthy chemical reaction-diffusion system is the Belousov-Zhabotinsky reaction, an oscillatory chemical reaction that can form 3-dimensionally propagating waves.[38] A prime example of a biological reaction system is the Min protein system, which was first reconstituted in vitro by Schwille and coworkers in 2008[1] on planar supported lipid bilayers. In the following years, both the molecular interactions within the Min system[39-45] as well as the spatiotemporal organization[41,46-50] of this reaction diffusion system were studied in great detail.

In the work presented in this chapter we took the aim of reconstituting the system in a cell-like environment one step further, by encapsulating the functional proteins for the first time in GUVs. On the one hand, this led to the expected result of pattern formation in these membrane compartments, including the pole-to-pole oscillations that can be observed in living bacterial cells, therefore paving the way to a full reconstitution of bacterial cell division. But on the other hand, and just as excitingly, this also led to some very unexpected results, namely periodic deformations of the encapsulating vesicles. While these membrane-deforming property of the Min proteins have not (yet) been shown relevant in vivo, this observation was of interest to the synthetic biology community, particularly in the context of creating artificial cells. A comparable behavior has not yet been engineered for any vesicle-based system. These vesicles convert biological energy in the form of ATP into highly dynamic morphological changes of the vesicle compartment. This aspect is also the subject of the second publication in this chapter, which shows a theoretical investigation into a specific type of these shape oscillations.

3.2. The Min protein system

The Min system is E. coli's answer to the problem of "how does a cell find its center?" and to the task of where to assemble the bacterial cell division ring. An answer to the question of what happens when a cell does not find its center can be found in E.coli mutants lacking a functioning Min system. This is also where these proteins found their name: Due to mislocalized cell division occurring near the bacterial poles, these mutant cells produce a large amount of non-living so-called minicells, which are not only smaller than their counterparts, but also lack essential cellular constituents.[51] To prevent this type of unproductive cell division in E. coli, the Min system positions the divisome mid-cell to ensure a cell division into two equally sized daughter cells by the cytokinetic machinery.

The Min system achieves that through a reaction-diffusion mechanism powered by ATP hydrolysis. The Min protein system consists of three proteins, the proteins MinC, MinD and MinE. MinC is essential for the interaction with the divisome, as it inhibits the polymerization of FtsZ.[52] The pole-to-pole oscillations of the Min system result in a time-averaged concentration gradient of MinC with its minimum in the cell center, restricting FtsZ assembly to this region. The pole-to-pole oscillations are the results of a reaction-diffusion mechanism for which the proteins MinD and MinE are the main actors. These proteins oscillate back and forth between a membrane-bound and a cytosolic state. Upon ATP-binding and dimerization, MinD binds the membrane via an amphipathic membrane-targeting sequence. It then recruits both further MinD-ATP and MinE to the membrane. In turn, MinE stimulates MinD's ATPase activity which results in MinD's detachment from the membrane.

Lateral coupling of this reaction across the membrane, which is granted by the cooperative initial binding of MinD, is crucial to the function of the Min system as a spatial regulator,. In vitro, e.g. on planar SLBs, this leads to excitation waves which propagate across the membrane. To achieve the standing waves as seen in E. coli, geometrical confinement is a requirement. In bacterial cells the reaction diffusion dynamics are manifested in one particular mode of dynamic behavior, referred to as pole-to-pole oscillations. Here the proteins bind and unbind in a periodic fashion on and off the membrane - synchronous within one pole of the cell, but antiphase between the two opposing poles. This results in the above-mentioned time-averaged MinC gradient and therefore for the positioning of the bacterial proto-ring.

3.3. Membrane deformations through membrane-protein interactions

Cell biologists have long been fascinated with the question of how cells regulate membrane shape. In vitro reconstitution with model membranes is an ideal tool to investigate this question. While science is still pretty far from providing a comprehensive answer, one thing is certain: the answer is long and complex. There are myriads of different mechanisms that are employed to regulate cell and membrane shape, and different factors play roles on different length scales.

The actual macroscopic shape of the cell, for example, can be affected by the cytoskeleton, as also demonstrated through in vitro experiments with GUVs in the previous chapter. Further, in multicellular life, the cellular environment plays maybe the most important role, as the cell's shape is largely determined by the surrounding tissue or the extracellular matrix. In a large variety of organisms, cell shape can also be determined by the cell wall, which involves an entirely different set of structural determinants.

On a smaller scale however, other factors like peripheral membrane proteins and the lipid composition of the membrane play an important role in actively regulating membrane shape. These processes and mechanisms are generally referred to as 'membrane remodeling'.[53] One major consideration for the growing field studying membrane remodeling is the question of how membrane curvature is induced on a local level. This plays an important role for many crucial cell processes like endocytosis, exocytosis, phagocytosis and intracellular trafficking.

One way the cell can determine local curvature is by the binding of proteins. As such, peripheral membrane proteins are prime targets for the study of membrane remodeling. Peripheral membrane proteins bind to the membrane transiently, either by binding to lipid head groups or even by insertion into one leaflet of the membrane. Peripheral membrane proteins can affect membrane shape in a number of ways, as summarized in the associated Publication 1.

One and the same type of protein can deform a membrane in several ways, and often it is not known which mechanism is the important one in vivo. One of the most prominent types of membrane remodeling proteins are proteins with BAR domains.[53] Given their distinct curved shapes – often referred to as banana-shape – the most intuitive way in which they determine membrane

curvature is by imposing their own protein shape into the membrane. However, most BAR proteins also bind to membranes via insertion of amphipathic protein domains, potentially causing an asymmetry in leaflet areas and therefore curvature induction. Many BAR domain proteins oligomerize, therefore could induce curvature via scaffolding and others even form links with the cytoskeleton, offering another way of determining membrane shape.

For studying these proteins and processes in vitro, naturally, model membranes are essential. More precisely, deformable free-standing bilayers are required. One of the only ways to achieve that in the laboratory, is with GUVs. Often it is sufficient to add the protein to the outside of the vesicle. However in some cases, encapsulation of the proteins is required, for example to achieve certain curvatures. Publication 1 names a few examples were encapsulation within GUVs was key.

In the case of the Min proteins, the encapsulation within GUVs causes a synchronized protein oscillation (in the paper referred to as 'pulsing' mode). This enabled the synchronous insertion of amphipathic helices along the entire inner leaflet of the vesicle, which in turn causes membrane deformations. Therefore we make use of two essential properties of GUVs and use them as a confining compartment and free standing bilayers. The kind of dynamic behavior of vesicles – self-powered from within the vesicle and in a oscillatory way - as we show it in this chapter, has never been achieved previously and was one of the most exciting discoveries from my doctoral work.

3.4. Publication 3: Beating vesicles: Encapsulated protein oscillations cause dynamic membrane deformations

Research paper published in Angewandte Chemie International Edition.[54]

Litschel T, Ramm B, Maas R, Heymann M, Schwille P. "Beating vesicles: Encapsulated protein oscillations cause dynamic membrane deformations". *Angew Chem Int Ed* **57** (2018) 16286–16290

https://doi.org/10.1002/anie.201808750

Beating Vesicles: Encapsulated Protein Oscillations Cause Dynamic Membrane Deformations

Thomas Litschel, Beatrice Ramm, Roel Maas, Michael Heymann, and Petra Schwille*
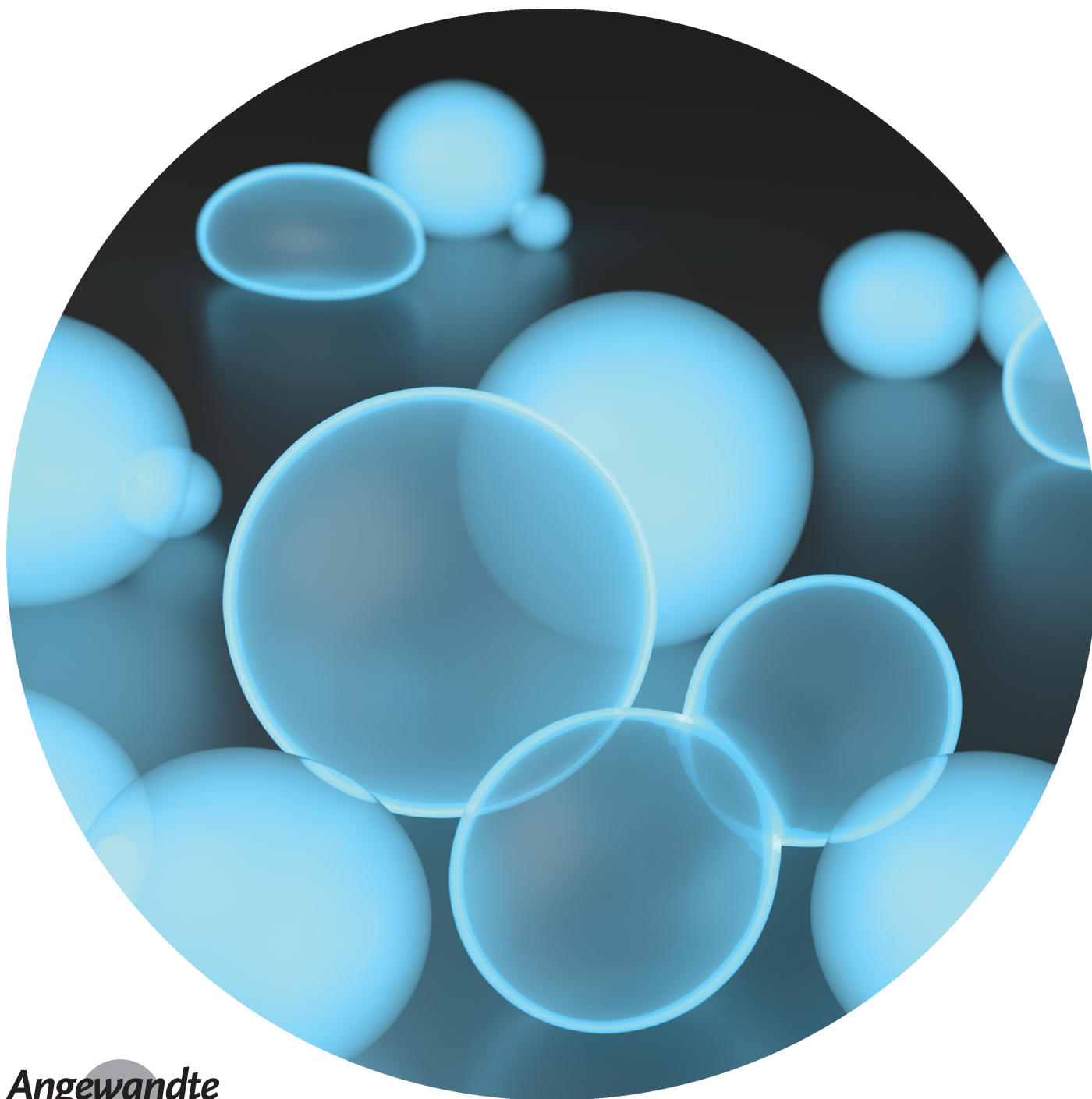
Angewandte
International Edition *Chemie*

Abstract: *The bacterial Min protein system was encapsulated in giant unilamellar vesicles (GUVs). Using confocal fluorescence microscopy, we identified several distinct modes of spatiotemporal patterns inside spherical GUVs. For osmotically deflated GUVs, the vesicle shape actively changed in concert with the Min oscillations. The periodic relocation of Min proteins from the vesicle lumen to the membrane and back is accompanied by drastic changes in the mechanical properties of the lipid bilayer. In particular, two types of oscillating membrane-shape changes are highlighted: 1) GUVs that repeatedly undergo fission into two connected compartments and fusion of these compartments back into a dumbbell shape and 2) GUVs that show periodic budding and subsequent merging of the buds with the mother vesicle, accompanied by an overall shape change of the vesicle reminiscent of a bouncing ball. These findings demonstrate how reaction–diffusion-based protein self-organization can directly yield visible mechanical effects on membrane compartments, even up to autonomous division, without the need for coupling to cytoskeletal elements.*

Creating synthetic materials that imitate properties of living organisms is a persistent challenge in science that often leads to technological advances and furthers our understanding of biological systems. One of the most prominent attributes of many living organisms is their motility. While great innovations have come from mimicking life on a macroscopic level,[1] there are few artificial systems that exhibit autonomous motion on a cellular scale.[2] Previously, cell-like vesicles were created from synthetic components that exhibit oscillatory dynamic behavior driven by chemical reactions and osmotic effects.[3] In recent years, first attempts were made to encapsulate biological building blocks in lipid vesicles to create structures capable of more distinct actuation.[4] Herein, we present cell-sized GUVs that autonomously and reversibly change their shape in response to the oscillatory, membrane-interacting Min protein system.
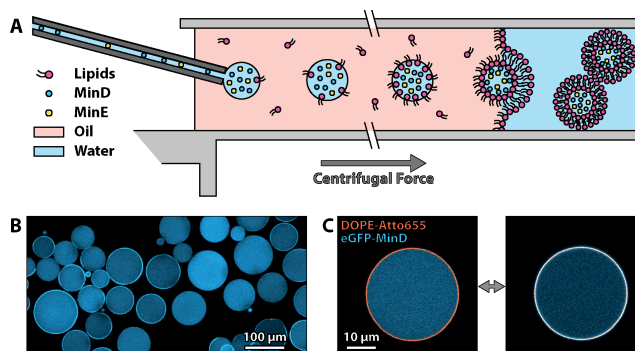
The Min system consists of the proteins MinC, MinD, and MinE, and positions the bacterial cell division machinery in *Escherichia coli*.[5] Based on a reaction–diffusion mechanism, the proteins MinD and MinE oscillate between the cell poles and thereby spatially regulate the assembly of the cell division complex, restricting the formation of the division ring to the cell center.[6] MinD dimerizes upon adenosine triphosphate (ATP) binding, which enhances its affinity to the membrane. Membrane-bound MinD recruits MinE, which in turn stim-

ulates the ATPase activity of MinD, causing both proteins to detach again (see the Supporting Information, Figure S1).[7]

In previous work, we reconstituted MinDE protein self-organization in vitro on supported lipid bilayers (SLBs), reproducing oscillatory patterns on a planar membrane and rendering the Min system an attractive biological model to study reaction–diffusion dynamics in 2D.[8] In further research, Min protein patterns were confined within SLB-lined microfluidic scaffolds to probe geometry sensing and recreate spatial properties of bacterial cells.[9] However, these non-deformable microstructures lack many features of living cells, in particular their plasticity and ability to ultimately divide. In a continuing attempt to confine the Min system to more cell-like compartments, we recently fully enclosed the proteins in microdroplets and were able to observe pole-to-pole oscillations on the lipid monolayer at the water–oil interface, similar to the oscillations seen in *E. coli*.[10] Unfortunately, owing to the surface tension at the water–oil interphase, microdroplets are still very rigid compartments, and the difference in the refractive indices between the two phases hampers confocal imaging of the full 3D volume of the droplets.

In spite of being conceptually straightforward, the Min oscillations had not been enclosed within a free-standing lipid bilayer up to now, owing to several technical challenges. Herein, we report the successful encapsulation of the Min system in giant liposomes, finally leading to fully confined Min oscillations in mechanically transformable compartments.

We adapted the cDICE method,[11] an emulsion transfer technique that allowed us to encapsulate purified MinD (50% eGFP-MinD) and MinE proteins in GUVs with negatively charged membranes (1,2-dioleoyl-*sn*-glycero-3-phosphocholine (DOPC) and 1,2-dielaidoyl-*sn*-glycero-3-phospho-(1′-*rac*-glycerol) (DOPG) in a ratio of 4:1;[12] Figure 1). We slightly modified the original procedure, used a customized

[*] T. Litschel, B. Ramm, R. Maas, Dr. M. Heymann, Prof. Dr. P. Schwille
Department of Cellular and Molecular Biophysics
Max Planck Institute of Biochemistry
Am Klopferspitz 18, 82152 Martinsried (Germany)
E-mail: schwille@biochem.mpg.de

Supporting information and the ORCID identification number(s) for the author(s) of this article can be found under:
https://doi.org/10.1002/anie.201808750.

Figure 1. Encapsulation of MinD and MinE into giant unilamellar vesicles. A) Schematic depiction of the vesicle generation process. The aqueous protein solution is injected into a rotating chamber through a glass capillary. Droplets form at the capillary tip in the oil phase, which contains lipid aggregates. The droplets then pass through a water–oil interphase lined with lipids, forming the GUVs. B) Representative confocal image of several GUVs containing oscillating Min proteins. C) Confocal images showing the two states of a protein oscillation. Composite of fluorescence signals and the differential interference contrast (DIC) channel. eGFP-MinD in cyan and DOPE-ATTO655 in orange.

3D-printed rotating chamber and larger capillaries, and dispersed the lipids in oil as aggregates,[13] rather than in solution. More details about vesicle generation and protein encapsulation can be found in the Supporting Information. The generated vesicles are between 5 μm and 100 μm in diameter (Figure S2). While we detected eGFP-labeled MinD in almost all vesicles, the fraction of GUVs exhibiting dynamic behavior varied from 50% to 100% between samples. After 4–5 hours, the Min oscillations began to fade owing to protein aggregation and a general decrease in protein activity.

Sequential confocal images of the equatorial plane of the GUVs reveal several distinct modes of Min oscillations. Consistent with previous observations for Min dynamics within microdroplets,[10] we observed two types of standing wave patterns and circling traveling waves (Figure 2 A–I). We further identified a second mode of traveling waves (Figure 2 J–L) and a qualitatively different type of pole-to-pole oscillations, which can be asymmetric and appeared to be linked to the aggregation of protein in a ring-like structure that sets the boundary between the two poles (Figure S3 and Movie S3).

GUVs are ideal for confocal fluorescence microscopy and therefore allowed us to compile time series of z-stacks of entire vesicles (Movies S2–S4), enabling the observation of reaction–diffusion dynamics on a closed 3D surface (here a sphere). Spatiotemporal reaction–diffusion patterns on closed surfaces are ubiquitous in nature and have been studied extensively in theory,[14] but the only experimental record of a 3D observation thereof under controlled conditions is on catalyst-coated millimeter-sized beads in a Belousov–Zhabotinsky reaction solution on which spiral waves (similar to Figure 2 G–I) and trigger waves (similar to Figure 2 J–L) were observed.[15]

Often we see one mode transitioning into another (Movies S4 and S5 and Figure S3 D). In fact, none of the oscillation modes seemed to be temporally stable, with the exception of the pulsing mode. We observed vesicles transitioning between as many as three different modes before settling into the pulsing mode. As a general trend, the traveling wave modes (Figure 2 G–L) seemed to be the shortest lived, switching into standing wave oscillations (Figure 2 A–F) within minutes. Even though a single vesicle can exhibit different types of oscillations, our experiments indicate that vesicle size, protein concentrations, and other factors heavily affect the type of oscillations that a vesicle exhibits. Further experiments will be required to map out this large parameter space.

In addition to the spatiotemporal patterns within the spherical vesicles, we observed an unexpected effect of the protein oscillations on the morphology of the GUVs. Under hypertonic stress, vesicles that were visibly osmotically deflated (i.e., not spherical) underwent extensive shape fluctuations in concert with the MinDE oscillations.

A number of different membrane shape oscillations were observed; the two most prevalent types are shown in Figure 3. In the first case, referred to as periodic dumbbell splitting (Figure 3 A–C), the deflated vesicles assume a dumbbell-like shape when the Min proteins are bound to the membrane. With the relocation of the Min proteins to the lumen, the "dumbbell" splits into two spherical compartments (connected by a narrow neck), before these fuse back together when the proteins bind to the membrane again. Figure 3 B shows the narrow membrane neck between the two compartments whilst split. In Figure 3, we chose a different example of a vesicle for each Figure panel, but movies for all cases are shown in Movie S6, demonstrating consistent behavior and the reproducibility of these observations. The Movie also
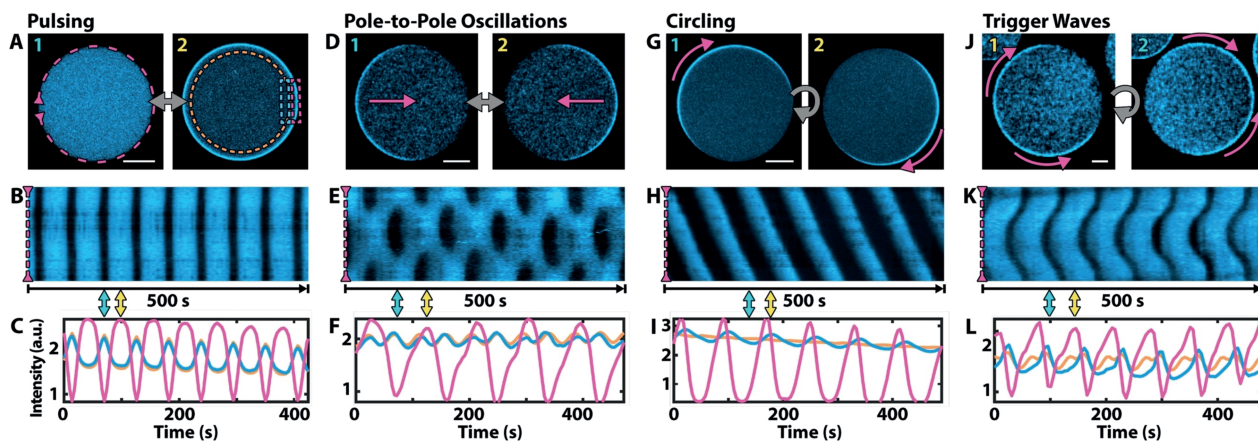
Figure 2. Different modes of Min oscillations in GUVs. A–C) Pulsing oscillations: MinD oscillates between the inside of the vesicles and the inner membrane surface. Dotted lines in (A) indicate ROIs for kymograph and intensity plots. D–F) Pole-to-pole oscillations: A protein binds alternately to the membrane of the two hemispheres of the vesicle. A second type of pole-to-pole oscillation is shown in Figure S3. G–I) Circling waves: Traveling waves that continuously revolve on the inside surface of the GUV. J–L) Trigger waves: Traveling waves that originate and terminate on opposing poles; here the wave origin is on the left side of the vesicle. The top panels [(A), (D), (G), and (J)] show two frames from a time series of confocal images of each oscillation mode. The fluorescence signal of eGFP-MinD is shown in cyan. Magenta arrows indicate the directions of the waves. Scale bars: 10 μm. The center panels [(B), (E), (H), and (K)] show kymographs along the circumference of each vesicle [indicated as a magenta dotted line in (A)(1)]. The bottom panels [(C), (F), (I), and (L)] show average intensities in certain ROIs for each vesicle. ROIs are indicated by the dotted circle and boxes in (A)(2) in the respective colors of the curves. Magenta: Intensity of a membrane section (normalized); blue: intensity of the lumen close to the membrane section; orange: average intensity of entire lumen. Movie S1 shows all oscillation modes sequentially.

includes a fourth example, which was recorded as *z*-stacks, confirming the separation (by a neck) from a side view.

In the second case, which we refer to as periodic budding (Figure 3D–F), the relocation of the proteins from the membrane to the lumen and back induces budding and subsequent fusion of the buds with the mother compartment (Figure 3D). Along with the budding, the mother compartment also contracts in its *x–y* cross-section (Figure 3D,E) and expands in the *z* dimension (Figure 3F), taking on an almost spherical shape, like a bouncing ball. Movie S7 includes examples of three different vesicles. Figure S4 shows sequential images of the second example, revealing further details about its shape change cycle. Most notably, the vesicle first switches from a flattened (oblate) to an elongated (prolate) shape before forming a bud and assuming a spherical shape. Similarly, when oscillations are not strong enough to trigger fission or budding, vesicles solely oscillate back and forth between a flattened and an elongated geometry, but do not become spherical (Movie S8).

We only saw extensive shape changes in vesicles that exhibited oscillations of the pulsing type; occasionally, slight deformations can be observed in other cases (e.g., in Movie S5 for the circling wave oscillation). Generally, only a small fraction of vesicles show more extensive membrane dynamics as most vesicles respond to the osmotic stress with the formation of thin membrane tubules and therefore maintain a static spherical shape (Figure S5).

For all cases in which we saw shape fluctuations, a comprehensive correlation between the changes in vesicle geometry and the location of the Min proteins can be identified. The behavior that we observed indicates that the binding of the Min proteins directly affects the membrane properties. A variety of methods have been used to study shape changes in GUVs, such as inducing these by temperature,[16] changes in osmolarity,[17] insertion of additional lipids into the membrane,[18] and through other substances interacting with the membrane.[19] In these studies, budding and fission events similar to those that we observed were reported, but they were induced externally and mostly unidirectional and were never repetitive by nature. Here, we present a system that allowed us to observe extensive shape transitions, which are not only reversible, but oscillate back and forth autonomously. Hence, we suggest that these vesicles provide a unique test bed for the study of dynamic membrane transformations in conjunction with peripheral protein association.

The specific shape oscillations that we observed seem to be a result of changes in membrane curvature caused by the periodic relocation of the proteins. The membrane-inserted amphipathic helix of MinD[7b] presumably increases the surface area of the inner membrane leaflet and potentially also decreases the intrinsic spontaneous curvature of the membrane. This would result in an
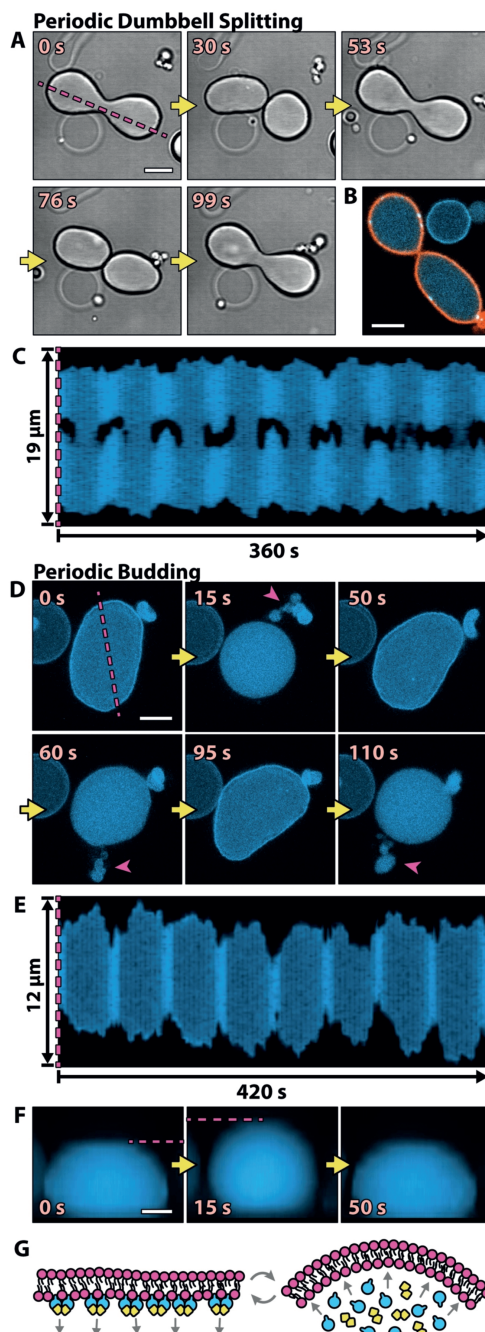
Figure 3. The vesicle shapes change in concert with Min oscillations. A) Time series of DIC images of a dumbbell-shaped GUV that repetitively splits into two compartments connected by a narrow membrane neck. B) The confocal image of a shape-oscillating GUV with fluorescently labeled lipids (orange) shows that the GUV does not undergo a full fission into two separate GUVs, but rather that the two compartments are still connected by a membrane neck. C) Kymograph along the line parallel to the axis of rotational symmetry of a dynamic GUV (see the magenta line in (A)). Whenever MinD is in the lumen, the GUV is split into two, almost separate compartments. Movie S6 features all three vesicle examples in (A) to (C). D) A GUV that undergoes periodic budding and subsequent fusion of the buds with the mother vesicle. Buds are highlighted with magenta arrows. Shown are *z* projections of five confocal planes. E) Kymograph (see the magenta line in (D)) of a repetitively budding vesicle, showing the reduction in size in the *x* and *y* dimensions of a GUV whenever budding occurs. F) Sequential images of a side view of a periodically budding vesicle, showing that the reduction in size in the *x–y* plane is accompanied by an increase in size in the *z* direction (see also Figure S6C). Movie S7 shows the vesicles from (D), (E), and (F) sequentially. Scale bars: 5 μm. G) Suspected mechanism: Membrane-bound MinD increases the surface area of the inner membrane leaflet. Upon protein detachment, the intrinsic curvature of the bilayer increases, and membrane deformations occur.

increase in the overall membrane curvature when the protein unbinds upon ATP hydrolysis, which would be in accord with the observed changes in vesicle morphology (Figure 3 G). The effects of inserted amphipathic helices on membrane curvature have been investigated for proteins involved in vesicular transport.[20] Previous investigations on the interactions of MinD alone with free-standing bilayers in a static system showed an increase in membrane viscosity[21] and even membrane tubulation,[22] but further investigations will be required to reveal the precise mechanism on a molecular level.

Dynamics and actuation of lipid vesicles as reported here have, to the best of our knowledge, not been described before. These extreme and rapid shape deformations could prove important for synthetic biology and the growing interest in creating actuation on a microscopic scale by engineering active vesicles or bioinspired "molecular robots". Lastly, the encapsulation of the Min oscillating system in GUVs represents a crucial and necessary step for the in vitro, bottom-up reconstitution of bacterial cell division. In this respect, it is particularly exciting that the presumed role of the Min oscillations (i.e., the positioning of the bacterial cytoskeleton to mechanically drive cell division) is, in simple vesicle compartments, accompanied by a distinctive mechanical cue itself. This may point to an even more archetypal function of this fascinating protein system, indicating how cyclic self-organization of encapsulated biomolecules may result in autonomous division of phospholipid compartments.

Conflict of interest

The authors declare no conflict of interest.

[1] G. Taubes, *Science* **2000**, *288*, 80.
[2] M. Hagiya, A. Konagaya, S. Kobayashi, H. Saito, S. Murata, *Acc. Chem. Res.* **2014**, *47*, 1681–1690.
[3] a) R. Tamate, T. Ueki, M. Shibayama, R. Yoshida, *Angew. Chem. Int. Ed.* **2014**, *53*, 11248–11252; *Angew. Chem.* **2014**, *126*, 11430–11434; b) K. Oglecka, P. Rangamani, B. Liedberg, R. S. Kraut, A. N. Parikh, *eLife* **2014**, *3*, e03695.
[4] a) F. C. Keber, E. Loiseau, T. Sanchez, S. J. DeCamp, L. Giomi, M. J. Bowick, M. C. Marchetti, Z. Dogic, A. R. Bausch, *Science* **2014**, *345*, 1135–1139; b) Y. Sato, Y. Hiratsuka, I. Kawamata, S. Murata, S.-i. M. Nomura, *Science Robotics* **2017**, *2*, eaal3735; c) S. Tanaka, K. Takiguchi, M. Hayashi, *Commun. Phys.* **2018**, *1*, 18.
[5] P. A. de Boer, R. E. Crossley, A. R. Hand, L. I. Rothfield, *EMBO J.* **1991**, *10*, 4371–4380.
[6] a) D. M. Raskin, P. A. de Boer, *Proc. Natl. Acad. Sci. USA* **1999**, *96*, 4971–4976; b) Z. Hu, J. Lutkenhaus, *Mol. Microbiol.* **1999**, *34*, 82–90.
[7] a) Z. Hu, J. Lutkenhaus, *Mol. Cell* **2001**, *7*, 1337–1343; b) Z. Hu, J. Lutkenhaus, *Mol. Microbiol.* **2003**, *47*, 345–355.
[8] a) M. Loose, E. Fischer-Friedrich, J. Ries, K. Kruse, P. Schwille, *Science* **2008**, *320*, 789–792; b) J. Schweizer, M. Loose, M. Bonny, K. Kruse, I. Monch, P. Schwille, *Proc. Natl. Acad. Sci. USA* **2012**, *109*, 15283–15288.
[9] a) K. Zieske, P. Schwille, *Angew. Chem. Int. Ed.* **2013**, *52*, 459–462; *Angew. Chem.* **2013**, *125*, 477–481; b) Y. Caspi, C. Dekker, *eLife* **2016**, *5*, e19271.
[10] K. Zieske, G. Chwastek, P. Schwille, *Angew. Chem. Int. Ed.* **2016**, *55*, 13455–13459; *Angew. Chem.* **2016**, *128*, 13653–13657.
[11] M. Abkarian, E. Loiseau, G. Massiera, *Soft Matter* **2011**, *7*, 4610–4614.
[12] A. G. Vecchiarelli, M. Li, M. Mizuuchi, K. Mizuuchi, *Mol. Microbiol.* **2014**, *93*, 453–463.
[13] a) C. Claudet, M. In, G. Massiera, *Eur. Phys. J. E* **2016**, *39*, 9; b) E. Loiseau, J. A. Schneider, F. C. Keber, C. Pelzl, G. Massiera, G. Salbreux, A. R. Bausch, *Sci. Adv.* **2016**, *2*, e1500465.
[14] a) P. Grindrod, J. Gomatam, *J. Math. Biol.* **1987**, *25*, 597–610; b) V. S. Zykov, S. C. Müller, *Phys. D* **1996**, *97*, 322–332; c) P. C. Matthews, *Phys. Rev. E* **2003**, *67*, 036206; d) E. J. Fuselier, G. B. Wright, *J. Sci. Comput.* **2013**, *56*, 535–565.
[15] J. Maselko, K. Showalter, *Nature* **1989**, *339*, 609–611.
[16] a) K. Berndl, J. Käs, R. Lipowsky, E. Sackmann, U. Seifert, *Europhys. Lett.* **1990**, *13*, 659–664; b) J. Käs, E. Sackmann, *Biophys. J.* **1991**, *60*, 825–844.
[17] H. G. Döbereiner, J. Käs, D. Noppl, I. Sprenger, E. Sackmann, *Biophys. J.* **1993**, *65*, 1396–1403.
[18] a) E. Farge, P. F. Devaux, *Biophys. J.* **1992**, *61*, 347–357; b) J. M. Alam, M. Yamazaki, *Chem. Phys. Lipids* **2011**, *164*, 166–174; c) M. Mally, B. Bozic, S. V. Hartman, U. Klancnik, M. Mur, S. Svetina, J. Derganc, *RSC Adv.* **2017**, *7*, 36506–36515.
[19] a) T. Tanaka, Y. Tamba, S. M. Masum, Y. Yamashita, M. Yamazaki, *Biochim. Biophys. Acta Biomembr.* **2002**, *1564*, 173–182; b) Y. Yamashita, S. M. Masum, T. Tanaka, M. Yamazaki, *Langmuir* **2002**, *18*, 9638–9641.
[20] a) M. G. Ford, I. G. Mills, B. J. Peter, Y. Vallis, G. J. Praefcke, P. R. Evans, H. T. McMahon, *Nature* **2002**, *419*, 361–366; b) M. C. Lee, L. Orci, S. Hamamoto, E. Futai, M. Ravazzola, R. Schekman, *Cell* **2005**, *122*, 605–617.
[21] S. Mazor, T. Regev, E. Mileykovskaya, W. Margolin, W. Dowhan, I. Fishov, *Biochim. Biophys. Acta Biomembr.* **2008**, *1778*, 2496–2504.
[22] H. Zhou, J. Lutkenhaus, *J. Bacteriol.* **2003**, *185*, 4326–4335.

Supporting Information

Beating Vesicles: Encapsulated Protein Oscillations Cause Dynamic Membrane Deformations

Thomas Litschel, Beatrice Ramm, Roel Maas, Michael Heymann, and Petra Schwille*

anie_201808750_sm_miscellaneous_information.pdf
anie_201808750_sm_Video_S1.mp4
anie_201808750_sm_Video_S2.mp4
anie_201808750_sm_Video_S3.mp4
anie_201808750_sm_Video_S4.mp4
anie_201808750_sm_Video_S5.mp4
anie_201808750_sm_Video_S6.mp4
anie_201808750_sm_Video_S7.mp4
anie_201808750_sm_Video_S8.mp4

Supporting Information

Methods:

Proteins

The plasmids for the purification of His-MinD[1], His-EGFP-MinD[2] and His-MinE[1] have been described previously.

Purification of His-MinD, His-EGFP-MinD and His-MinE was performed essentially as described earlier[1]. For a detailed protocol see Ramm and Glock *et al*.[3] In brief, the His-tagged proteins were expressed in *E. coli* BL21 (DE3) and purified via Ni-NTA affinity purification. If needed, protein was further purified using gel filtration chromatography on a HiLoad 16/600 Superdex 200 prep-grade column (GE Healthcare, Chicago, USA) in storage buffer (50 mM HEPES, pH 7.25, 150 mM KCl, 10 % Glycerol, 0.1 mM EDTA) or buffer was exchanged to storage buffer using a gravity desalting column. Protein purity was assessed via SDS-PAGE and mass spectrometry. Proteins were quick frozen and stored in aliquots at -80°C until further use.

Inner and Outer Solution

All inner and outer solutions contain 25 mM tris-HCl (pH 7.5), 150 mM KCl and 5 mM $MgCl_2$ (i.e. 'Min protein reaction buffer' in previous publications).[1] In addition, the solution encapsulated in the GUVs contained 1.5 µM MinD, 1.4 µM eGFP-MinD, 3 µM MinE and 5 mM ATP. The chosen ATP concentration should in theory supply the reaction for several days; in practice, other factors limit the lifetime of the oscillations, for example, usually after 4-5 hours the proteins inside the GUVs start to aggregate.

As solvent we use deionized water (Merck Milli-Q®) with 15% iodixanol (from OptiPrep™, Sigma Aldrich). Iodixanol is used to increase the density of the encapsulated solution, in order to create a difference in density between the encapsulated solution and the GUV-surrounding solution, which is a necessary requirement for inverse emulsion methods for generating GUVs. Iodixanol allows for a high difference in density (which we found to increase vesicle yield) while not affecting the osmolarity of the solution considerably. The prepared solution has an osmolarity of 560 mOsm/kg (measure with Fiske® Micro-Osmometer Model 210).

As the GUV-surrounding solution we use the Min protein reaction buffer and adjust the osmolarity through different concentrations of glucose. For the experiments shown in Figure 1, 2 and S3 and Videos S1 – S5 we use 200 mM glucose to match the osmolarity of the inner solution (560 mOsm/kg). To obtain osmotically deflated GUVs (Figure 3, S4 and S5 and Videos S6 - S8) we use outer solution with 300 mM glucose, resulting in a higher osmolarity of 635 mOsm/kg, so that GUVs osmotically deflate while they are generated.

Lipids

We use DOPC (1,2-Dioleoyl-sn-glycero-3-phosphocholine, Avanti Polar Lipids, Inc.) and DOPG (1,2-Dioleoyl-sn-glycero-3-phosphoglycerol, Avanti Polar Lipids, Inc.) (both 25 mg/ml in chloroform) in a ratio of 4:1. A low fraction of the anionic DOPG lipids was chosen to improve vesicle yield. Vecchiarelli et al. investigated the effects of different DOPC:DOPG ratios and found that stable and long lived Min patterning dynamics can be observed within a certain range below and above the physiological ratio of uncharged to negatively charged lipids of 2:1.[5]

The preparation of the lipid-in-oil mixture is based on published protocols.[4] 77 µl of the lipid mix is given in a 10 ml glass vial and 600 µl chloroform is added. In experiments with labeled membranes, 3 µl DOPE-ATTO655 (0.1 mg/ml in chloroform) is added. While being mixed on a vortex mixer, 10 ml of a silicon oil (5 cSt) and mineral oil (Sigma-Aldrich, M5904) mix (4:1 ratio) is slowly added to the lipid solution. Since the lipids are not soluble in this mix of silicon oil, mineral oil and chloroform, the resulting liquid is cloudy.

Vesicle generation

Vesicles were produced using the cDICE method as described by Abkarian et al.[6] Instead of utilizing petri dishes as in the original protocol, we 3D printed the rotating chamber in which the vesicles are generated with a 3D printer (Formlabs Form 2, Clear Resin). Inner diameter of chamber: 7 cm, diameter top opening: 3 cm, height of chamber: 2 mm. A magnetic stirring device (outdated IKA-COMBIMAG RCH) served as a motor, after the heating unit was removed to expose the motor shaft.

The inner solution is loaded into a syringe (BD Luer-Lock™ 1-mL syringe) which is then placed into a syringe pump system (neMESYS base 120 with neMESYS 290N) and connected through tubing to a glass capillary (100 µm inner diameter). We use capillaries with a larger diameter than in the original publication, providing much less surface per volume for the Min proteins to bind to (although also resulting in GUVs that are more polydisperse).

700 µl of the outer solution is pipetted into the rotating chamber, followed by approximately 5 ml of the lipid-in-oil mixture. The capillary tip is then immersed in the oil phase and the inner phase injected at a flow rate of 50 µl/hr for 15 minutes. The vesicles are withdrawn from the cDICE chamber with a micropipette.

Imaging

The vesicles are pipetted into a microtiter plate for imaging (Greiner Bio-One, 96-well glass bottom SensoPlate™), which has been passivated beforehand with 50 µl of 5 mg/mL casein (Sigma Aldrich) for 20 minutes.

Imaging is then performed with an LSM 780/CC3 confocal microscope (Carl Zeiss, Germany) equipped with a C-Apochromat, 40x/1.2 W objective. We use PMT detectors (integration mode)

to detect fluorescence emission (excitation at 488 nm for eGFP and 633 nm for Atto655) and record confocal images.

All experiments were conducted at room temperature.

Data analysis

To create the kymographs in Figure 2, the GUVs were stabilized within each time series with Fiji's "Image Stabilizer" plugin and compensated for slight focus drifts (and thus a change in the diameter of the cross section of the GUV) by gradually scaling up the size of the GUV by a maximum of 2% over the course of the time series. The plots in Figure 2 (bottom row) were also generated with these stabilized time series. Video S1 shows the unedited time series of the experiments.

The z-stack time series in Videos S2 – S5 are created with Fiji's "3D Project" function without interpolating z-stack planes. The z-stack time series in Video S6, S7 and Figure 3F (perspective from a 90° "side view" angle) were created with the same tool, but with an activated interpolate function.
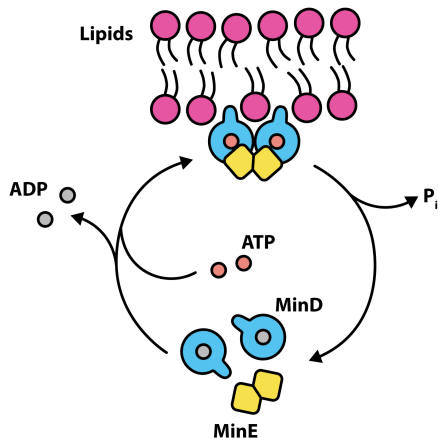
Figure S1. Min mechanism. Monomeric MinD binds ATP, which causes its dimerization and membrane binding. It then recruits further MinD-ATP (not shown here, but essential for pattern formation) and MinE, forming the membrane bound MinDE complex (top). MinE stimulates MinD's ATPase activity. ATP hydrolysis leads to the disintegration of the complex and detachment from the membrane. After detachment, monomeric MinD exchanges ADP for ATP before the cycle starts over again.
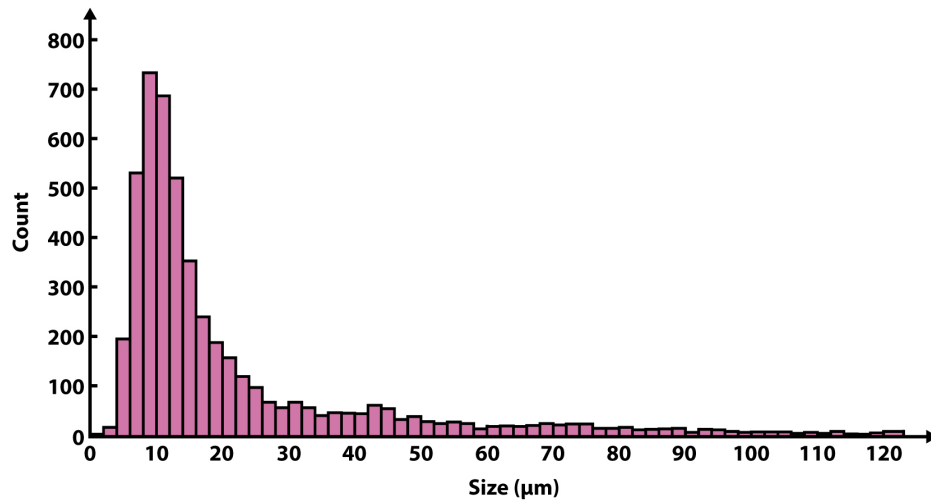
Figure S2. Size distribution of vesicles. The diameters of 4804 GUVs from 5 experiments were plotted in a histogram. Sizes were measured using DIC images with an overlaid fluorescent channel to confirm that the vesicles contain eGFP-MinD. The last bin on the right includes all vesicles with diameters of more than 120 µm.
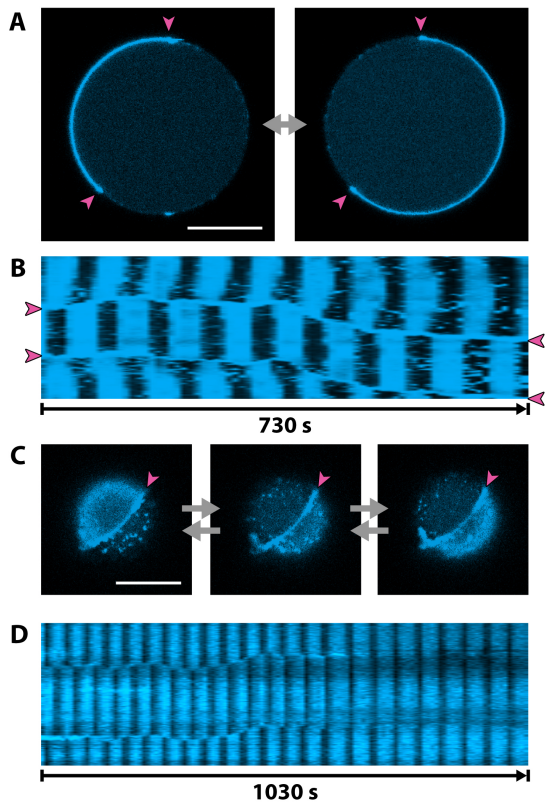
Figure S3. Second type of pole-to-pole oscillation. A) Confocal images of the equatorial plane. eGFP-MinD in cyan. B) Kymograph along the circumference of the GUV (equatorial plane). C) Confocal images of the GUV close to the glass surface. Magenta arrows in A) - C) highlight a ring-like structure made from MinD that spans once around the GUV and sets a boundary between the two oscillating poles of the GUV. Especially in C) the character of this ring is visible. Video S3 shows a time series of a 3D reconstruction of this vesicle. D) Kymograph along the circumference of a different GUV, showing a pole-to-pole oscillation of the second type, which then transition into a pulsing oscillation (see Figure 2 A-C). Scale bars are 10 µm.
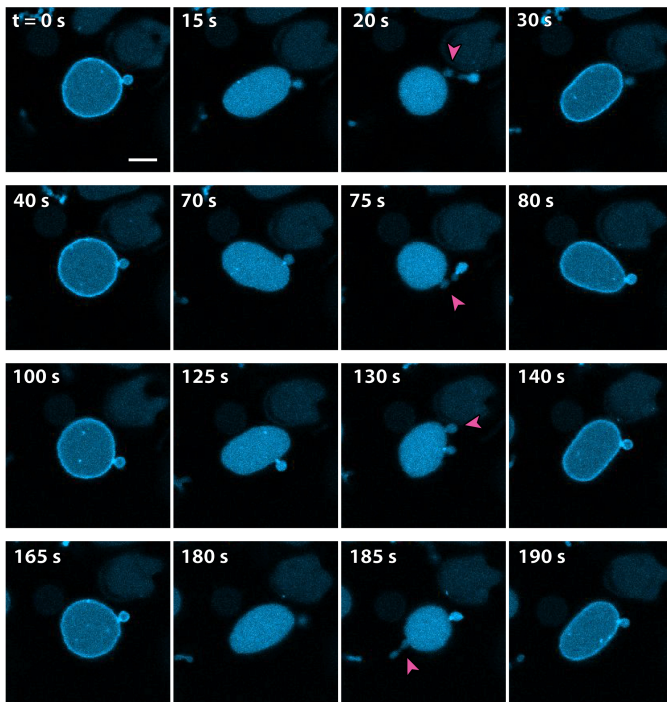
Figure S4. Sequential confocal images of a time series of a periodically budding vesicle. The vesicle undergoes a cycle of different shapes. Each row of images represents one cycle. In the first image in each row, the vesicle has an oblate-like shape (flattened), then changes to a prolate-like shape (elongated). After budding occurs, the shape of the vesicle becomes close to spherical. When the mother compartment merges with the vesicle bud, the vesicle takes on a prolate-like shape once more before the cycle starts over with an oblate-like shape. The vesicle buds are marked with magenta arrows. In the first two cycles the budding occurs at a position with a pre-existing bud, creating a chain of two buds (pearls). The scale bar in the first frame is 5 μm.
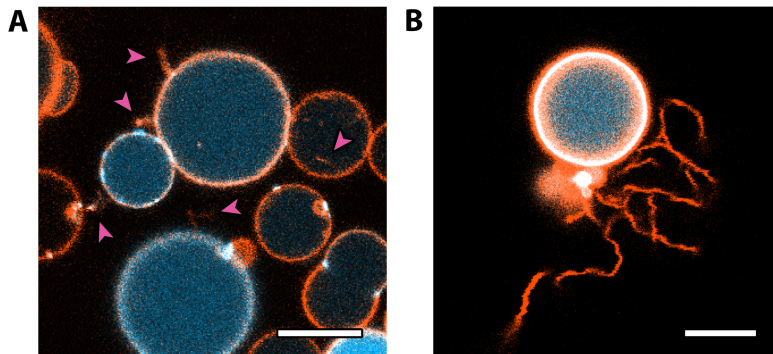
Figure S5. Membrane tubulation due to osmotic stress. A) Oscillating Min-containing GUVs (pulsing oscillation) with visible membrane tubules (purple arrows). When vesicles are generated with a difference in osmolarity between the inside and the outside phase, the resulting vesicles differ in morphology from simple spherical GUVs. Most vesicles respond with membrane tubulation, while only few assume vesicle shapes like in Figure 3. Through the formation of tubules, vesicles compensate for excess membrane (an increase in surface area to volume ratio) und hence can maintain a spherical shape. B) A single oscillating GUV generated under conditions with a high difference in osmolarity between inside and outside phase. Long membrane tubules can be seen. Scale bars are 10 µm.
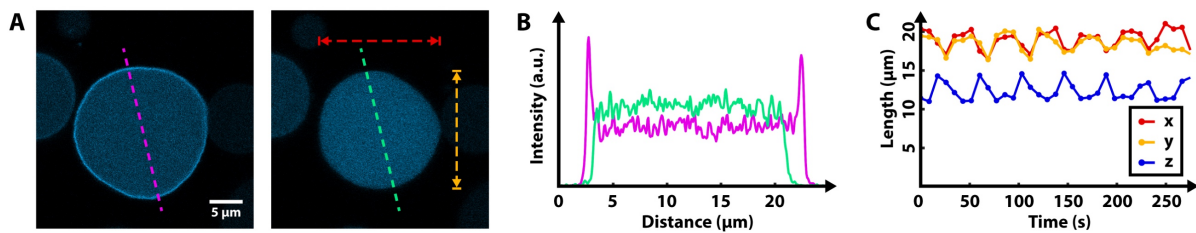
Figure S6. Analysis of the main compartment of periodically budding vesicle. Same vesicle as in Figure 3F. (A) Confocal sections of equatorial plane of GUV. In contrast to Figure 3D, which shows z-projections of confocal stacks, here only a single slice is shown, making the distribution of the protein clearer. Vesicle bud is not visible, because budding often occurs below the equatorial plane, closer to the glass surface. (B) Fluorescence intensity profile along purple and green dotted lines in (A). (C) Diameters of vesicle in y, x and z direction over time.
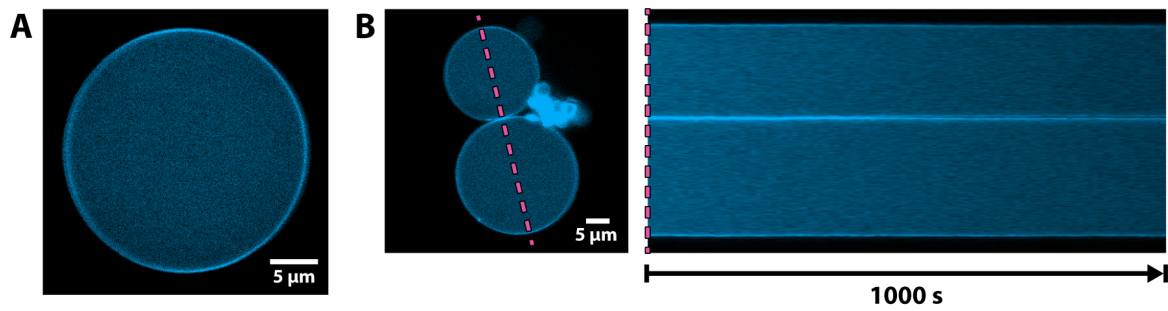
Figure S7. Control experiment without MinE. MinD-ATP binds to membrane, but cannot hydrolyze ATP due to the lack of MinE. MinD permanently binds to the membrane and no oscillations occur. (A) Single vesicle with membrane bound eGFP-MinD (cyan). (B) Image of two vesicles and kymograph along the dotted purple line. The kymograph shows no oscillations (only some photobleaching) over the course of 1000 s.

Supplementary References:

[1]   M. Loose, E. Fischer-Friedrich, J. Ries, K. Kruse, P. Schwille, *Science* **2008**, *320*, 789-792.
[2]   K. Zieske, J. Schweizer, P. Schwille, *FEBS Lett* **2014**, *588*, 2545-2549.
[3]   B. Ramm, P. Glock, P. Schwille, *J Vis Exp* **2018**, e58139.
[4]   a) C. Claudet, M. In, G. Massiera, *Eur Phys J E Soft Matter* **2016**, *39*, 9; b) E. Loiseau, J. A. Schneider, F. C. Keber, C. Pelzl, G. Massiera, G. Salbreux, A. R. Bausch, *Sci Adv* **2016**, *2*, e1500465.
[5]   A. G. Vecchiarelli, M. Li, M. Mizuuchi, K. Mizuuchi, *Mol Microbiol* **2014**, *93*, 453-463.
[6]   M. Abkarian, E. Loiseau, G. Massiera, *Soft Matter* **2011**, *7*, 4610-4614.

3.5. Publication 4: Active shape oscillations of giant vesicles with cyclic closure and opening of membrane necks

Research paper published in Soft Matter.[55]

Christ S, **Litschel T**, Schwille P, Lipowsky R. "Active shape oscillations of giant vesicles with cyclic closure and opening of membrane necks". *Soft Matter* **17** (2021) 319-330

https://doi.org/10.1039/D0SM00790K

PAPER

Check for updates

Active shape oscillations of giant vesicles with cyclic closure and opening of membrane necks†

Simon Christ, [ID] [a] Thomas Litschel, [ID] [b] Petra Schwille [ID] [b] and Reinhard Lipowsky [ID] *[a]

Reaction-diffusion systems encapsulated within giant unilamellar vesicles (GUVs) can lead to shape oscillations of these vesicles as recently observed for the bacterial Min protein system. This system contains two Min proteins, MinD and MinE, which periodically attach to and detach from the GUV membranes, with the detachment being driven by ATP hydrolysis. Here, we address these shape oscillations within the theoretical framework of curvature elasticity and show that they can be understood in terms of a spontaneous curvature that changes periodically with time. We focus on the simplest case provided by a attachment−detachment kinetics that is laterally uniform along the membrane. During each oscillation cycle, the vesicle shape is transformed from a symmetric dumbbell with two subcompartments of equal size to an asymmetric dumbbell with two subcompartments of different size, followed by the reverse, symmetry-restoring transformation. This sequence of shapes is first analyzed within the spontaneous curvature model which is then extended to the area-difference-elasticity model by decomposing the spontaneous curvature into a local and nonlocal component. For both symmetric and asymmetric dumbbells, the two subcompartments are connected by a narrow membrane neck with a circular waistline. The radius of this waistline undergoes periodic oscillations, the time dependence of which can be reasonably well fitted by a single Fourier mode with an average time period of 56 s.

1 Introduction

Both biological and biomimetic membranes such as lipid bilayers in their fluid state are highly flexible and can attain a striking variety of different morphologies. Particularly useful model systems for this polymorphism are giant unilamellar vesicles (GUVs) which are formed by single lipid bilayers.[1–3] So far, most studies of GUVs have focussed on their equilibrium shapes or on their morphological response to external perturbations such as hydrodynamic flows and external electric fields. The shape transformations of cellular membranes, on the other hand, are often driven by molecular processes coupled to nucleotide hydrolysis. One example is provided by the endocytosis of nanoparticles by the outer plasma membrane which requires

membrane fission, often achieved by GTP-hydrolyzing proteins such as dynamin.[4] Another example is the Min protein system which hydrolyzes ATP to position the bacterial cell division machinery in *Escherichia coli*.[5]

In a recent experimental study, the Min protein system was encapsulated within GUVs which were then observed to undergo cyclic shape oscillations.[6] The protein system contained two Min proteins, MinD and MinE, which periodically attach to and detach from the inner leaflet of the GUV membranes. MinD attaches to lipid membranes when bound to ATP.[7,8] MinE binds to membrane-bound MinD-ATP and the resulting MinD-ATP-MinE complex stimulates ATP hydrolysis by MinD, causing both proteins to unbind again from the membrane.

Here, we address these shape oscillations within the theoretical framework of curvature elasticity as recently reviewed in ref. 9. We first focus on the spontaneous curvature model[10–12] and show that the vesicle shape oscillations can be understood in terms of a preferred or spontaneous membrane curvature that changes periodically in time. The spontaneous curvature provides a quantitative measure for the molecular asymmetry between the two leaflets of the lipid bilayers. For the GUV membranes considered here, only the inner leaflets are exposed to the Min proteins and the resulting bilayer asymmetry will depend on the coverage of the inner leaflet by these proteins. Because this coverage changes with time, so does the resulting

[a] Theory and Bio-Systems, Max Planck Institute of Colloids and Interfaces, 14424 Potsdam, Germany. E-mail: lipowsky@mpikg.mpg.de; Fax: +49 331 5679602; Tel: +49 331 5679600

[b] Cellular and Molecular Biophysics Max Planck Institute of Biochemistry, 82152 Martinsried, Germany

† Electronic supplementary information (ESI) available: Supplementary text on shape equations for and numerical computation of axisymmetric vesicle shapes; Fig. S1 with parametrization of shape contours; Fig. S2 with time dependence of local spontaneous curvature; Fig. S3 for ADE model with $\kappa_\Delta/\kappa = 2$; captions of Movie 1 and Movie 2; Movie 1 with observed vesicle shapes; Movie 2 with computed vesicle shapes. See DOI: 10.1039/d0sm00790k

Paper

bilayer asymmetry and the associated spontaneous curvature. In addition, we generalize the spontaneous curvature model and consider the area-difference-elasticity (ADE) model[13–15] to take into account that the lipid bilayers studied in ref. 6 were composed of two phospholipids that are not expected to undergo frequent flip-flops between the two bilayer leaflets.

In the absence of flip-flops, the number of lipids is conserved separately in each leaflet of the bilayer membrane, which implies that the area difference between the two leaflets has a preferred value. In the ADE model, this constraint is taken into account by a nonlocal term that is added to the membrane's local bending energy, which has the same form as in the spontaneous curvature model. Therefore, in the present paper, we will view the area-difference-elasticity model as a generalization of the spontaneous curvature model.[9,15] Alternatively, one may start from the bilayer coupling model,[16] which considers the area difference between the two bilayers as another geometric control parameter in addition to membrane area and vesicle volume, and regard the ADE model as a generalized bilayer coupling model.[17]

As far as the recent experiments[6] are concerned, we focus on the simplest case in which the cyclic changes of the membrane fluorescence were observed to be laterally uniform, corresponding to a laterally uniform attachment–detachment kinetics of the Min proteins. Furthermore, our detailed analysis of the observed shape oscillations as described here reveals that the GUVs conserve both vesicle volume and membrane area during these oscillations. As a consequence, the vesicle shapes are calculated for constant volume-to-area ratio and a laterally uniform spontaneous curvature that changes periodically in time. Furthermore, for each time point, we determine the (meta)stable GUV shape(s) corresponding to the instantaneous value of the spontaneous curvature.

These GUV shapes exhibit two subcompartments which are connected by narrow membrane necks as displayed in Fig. 1 and 2. These membrane necks are a direct consequence of curvature elasticity[9,12,18,19] and have been experimentally observed for a variety of lipid compositions.[20,21] More recently, it was shown that these necks are essential for the formation of multispherical vesicle shapes[22] and for the controlled division of GUVs into two daughter vesicles.[23] *In vivo*, membrane necks are also formed by cellular membranes, *e.g.*, during endo- and exocytosis.[24]

A priori, our theoretical approach can be justified by the observed separation of time scales between the time period of the Min oscillations, which is about one minute,[25,26] and the time it takes a giant vesicle to relax to a new stable state, which takes only a few seconds.[27,28] Because of this time scale separation, one should be able to describe the observed non-equilibrium shape transformations by a sequence of stable shapes corresponding to the instantaneous value of the spontaneous curvature. Such a description is indeed possible as shown here.

During each complete oscillation cycle, the vesicle shape is transformed from an up-down symmetric dumbbell with two subcompartments of equal size to an asymmetric dumbbell
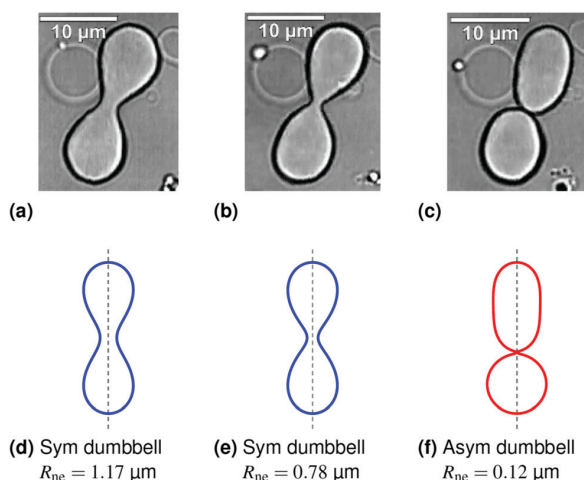

Fig. 1 Symmetry-breaking transformation during one shape oscillation: comparison of experimentally observed vesicle shapes in (a–c) with theoretically calculated shapes in (d–f). The neck radius R_{ne} attains its largest value of 1.17 µm in (a and d) and its smallest value of 0.12 µm in (c and f). The up-down symmetry of the symmetric dumbbells (blue shape contours) in (a and d) and (b and e) is broken for the asymmetric dumbbell (red shape contour) in (c and f). The three images in panels a–c were obtained by differential interference contrast microscopy[6] and represent three subsequent frames of the time-lapse Movie 1 (ESI†). The dashed vertical lines in panels d–f represent axes of rotational symmetry.
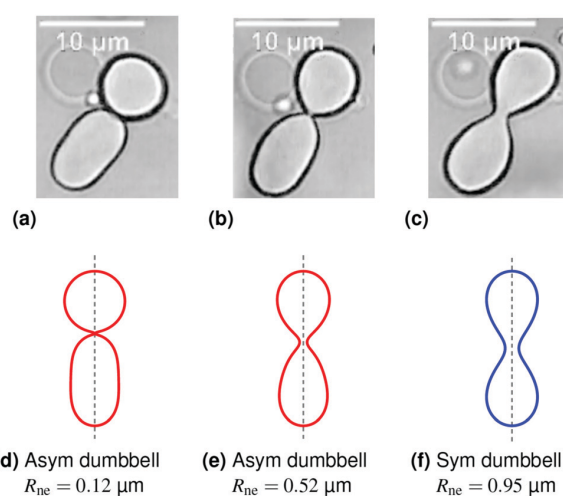

Fig. 2 Symmetry-restoring transformation during one shape oscillation: comparison of experimentally observed vesicle shapes in (a–c) with theoretically calculated shapes in (d–f). The neck radius R_{ne} attains its smallest value of 0.12 µm in (a and d) and its largest value of 0.95 µm in (c and f). The up-down symmetry is broken for the red shapes in (a and d) and (b and e) but restored for the blue shape in (c and f). The asymmetric shape in (a and d) is the same shape as in Fig. 1c and f but flipped upside-down. The three images in panels a–c represent three subsequent frames of the time-lapse Movie 1 (ESI†).

with two subcompartments of different size, see Fig. 1, followed by the reverse, symmetry-restoring transformation, see Fig. 2.
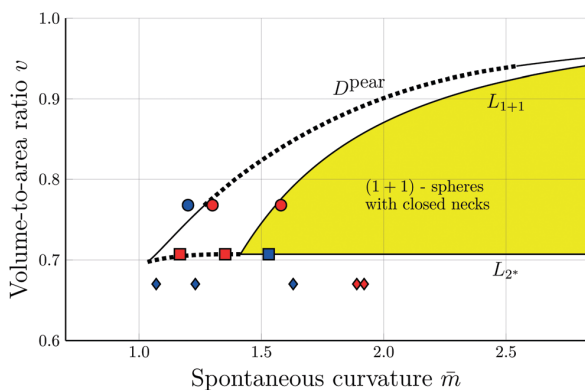
Fig. 3 Morphology diagram of prolates and dumbbells for positive spontaneous curvature $\bar{m}$ with $0.7 \leq \bar{m} \leq 2.8$ and volume-to-area ratio $v \geq 0.6$. The horizontal line with $v = 1$ corresponds to a single sphere. Along the solid line L_{1+1}, the vesicles form limit shapes consisting of two different spheres connected by a closed membrane neck. The location of this line is given by the algebraic expression in eqn (8). Along the solid line L_{2*} with $v = 1/\sqrt{2} = 0.707$ and $\bar{m} \geq \sqrt{2}$, the vesicles consist of two equally sized spheres connected by a closed neck. The parameter region between the two lines L_{1+1} and L_{2*} defines the yellow stability regime for $(1 + 1)$-spheres, in which the vesicle shape depends only on v but is independent of $\bar{m}$. The black dotted line D^{pear} separates up-down symmetric from asymmetric dumbbells with open necks. The latter line is obtained using cubic splines to connect numerical and analytical solutions. The solid blue and red circles correspond to shapes with $v = 0.768$ as displayed in Fig. 4a, the solid red and blue squares to shapes with $v = 1/\sqrt{2}$ as in Fig. 4b. The solid blue and red diamonds with $v = 0.670$ represent the selected shapes in Fig. 1 and 2 with the parameter values as in Table 2. The symmetric (blue) and asymmetric (red) diamonds belong to two different energy branches, see Fig. 6 and 7 further below.

In these two figures, the symmetric and asymmetric dumbbells are displayed in blue and red color, respectively. This color code will be used throughout the paper. These two types of dumbbells belong to two different branches of the GUV's bending energy. In the spontaneous curvature model, the symmetric branch is stable whereas the asymmetric one is metastable. In the area-difference-elasticity model, both branches represent stable shapes.

The narrow membrane necks in Fig. 1 and 2 have a waistline that defines the neck radius R_{ne}. This neck radius changes during each shape oscillation as shown in the two figures. In the spontaneous curvature model, the neck radius exhibits a different dependence on the spontaneous curvature $\bar{m}$ for the symmetric and asymmetric branches of dumbbells: along the symmetric branch, the neck radius decreases with increasing $\bar{m}$ whereas it increases along the asymmetric dumbbell. In the area-difference-elasticity model, the neck radius decreases with increasing local spontaneous curvature, both along the symmetric and along the asymmetric branch.

Our article is organized as follows. In the next section, we briefly describe our experimental system, consisting of Min proteins encapsulated in GUVs, as experimentally studied in ref. 6. The following section contains a reminder about the theory of curvature elasticity. We will first use the spontaneous curvature model, for which the GUV shapes are solely determined

by two dimensionless shape parameters, the volume-to-area ratio v and the rescaled spontaneous curvature $\bar{m}$. We then analyze the experimentally observed shapes as shown in Fig. 1a–c and 2a–c and conclude that these shapes have constant volume-to-area ratio which we will take to be $v = 0.670$. For this v-value, we study the possible vesicle shapes as we vary the spontaneous curvature $\bar{m}$ and find both symmetric and asymmetric dumbbells for a certain range of $\bar{m}$-values. In Section 4.6, we extend the spontaneous curvature model to the area-difference-elasticity model by decomposing the spontaneous curvature $\bar{m}$ into a local and a nonlocal component.

2 Min proteins enclosed by GUVs

The aqueous buffer enclosed by the GUVs contained two Min proteins, MinD and MinE, as well as ATP. The corresponding solution concentrations were 1.5 μM MinD, 1.4 μM eGFP-MinD, 3 μM MinE, and 5 mM ATP.[6] Thus, about half of the MinD proteins were fluorescently labeled and the overall MinD concentration was roughly equal to the MinE concentration. The lipid bilayer of the GUVs was composed of zwitterionic DOPC (1,2-dioleoyl-*sn-glycero*-3-phosphocholine) and anionic DOPG (1,2-dioleoyl-*sn-glycero*-3-phosphoglycerol) in a ratio of 4 : 1.

MinD can bind ATP and then attaches onto lipid membranes.[7] MinE binds to membrane-bound MinD-ATP and the resulting MinD-ATP-MinE complex stimulates ATP hydrolysis by MinD, causing both proteins to desorb again from the membrane. In the presence of a sufficient amount of ATP, this MinDE system undergoes many cycles of membrane attachment and detachment. For osmotically deflated vesicles, this periodic molecular process leads to shape oscillations of the vesicles which can be directly observed in the optical microscope.[6] Different types of shape oscillations have been detected; the two most frequent types of oscillations were denoted by 'periodic dumbbell splitting' and 'periodic budding' in ref. 6.

Here, we will focus on the dumbbell case as displayed in Fig. 1 and 2. In this case, the fluorescence of the GFP-labeled MinD adjacent to the inner leaflet of the GUV membrane was observed to be laterally uniform. Therefore, membrane segments with a lateral extension of about 300 nm can be considered to have a laterally uniform molecular composition which implies that they have uniform elastic properties as well. Furthermore, it is well understood that the shape of uniform GUV membranes strongly depends on the preferred or spontaneous curvature of these membranes.[9]

3 Spontaneous curvature model

The GUV membranes have a lateral dimension of many μm and a molecular thickness of only 4 to 5 nm. Based on this separation of length scales, we ignore the molecular structure of these membranes and describe them as smoothly curved surfaces. Any such surface can be characterized locally by its two principal curvatures, C_1 and C_2, which define the

mean curvature $M \equiv \frac{1}{2}(C_1 + C_2)$ and the Gaussian curvature $G \equiv C_1 C_2$.

The spontaneous curvature model[9,10–12] is then defined by the membrane's bending energy as given by‡

$$E_{be} = 2\kappa \int dA (M - m)^2, \tag{1}$$

which depends on the bending rigidity κ and on the area integral over the squared deviation of the (local) mean curvature M of the membrane from its preferred or spontaneous curvature m. In general, the spontaneous curvature model also involves another curvature term as provided by the area integral over the Gaussian curvature $G = C_1 C_2$. However, for the shape transformations considered here, the vesicles do not change their topology which implies that the area integral over the Gaussian curvature has a shape-independent value and can be ignored.

In order to actually compute the shape of a GUV, we need to take two additional constraints into account as provided by the membrane area A and the vesicle volume V.[9,11,12] These constraints are included *via* two Lagrange multipliers, the mechanical membrane tension Σ and the difference $\Delta P \equiv P_{in} - P_{ex}$ between the pressures P_{in} and P_{ex} within the interior and exterior aqueous solutions. The stable membrane shapes, corresponding to minimal bending energy, are then obtained by minimizing the shape energy

$$F = -\Delta P V + \Sigma A + E_{be} \tag{2}$$

with the bending energy E_{be} as given by eqn (1).

3.1 Two independent shape parameters

The shape energy in eqn (2) depends on two curvature-elastic parameters, the bending rigidity κ and the spontaneous curvature m, as well as on two geometric parameters, the membrane area A and the vesicle volume V. It is convenient to take the bending rigidity κ as the basic energy scale and to consider the area-derived vesicle size

$$R_{ve} \equiv \sqrt{A/(4\pi)} \tag{3}$$

as the basic length scale. Using this length scale, we are left with two dimensionless shape parameters, the volume-to-area ratio (or 'reduced' volume)

$$v = \frac{V}{\frac{4\pi}{3}R_{ve}^3} = 6\sqrt{\pi}\frac{V}{A^{3/2}} \tag{4}$$

and the rescaled spontaneous curvature

$$\bar{m} = m R_{ve}. \tag{5}$$

In the following, we will discuss the stable vesicle shapes in the context of two-dimensional morphology diagrams that

‡ Strictly speaking, the expression in eqn (1) is the bending energy functional that is defined for an arbitrary vesicle shape and should be distinguished from the bending energy as obtained for a certain stable shape. For notational simplicity, we will ignore this distinction here.

depend on the two independent shape parameters v and $\bar{m}$. By definition, the volume parameter v satisfies

$$0 \leq v \leq 1 \quad \text{with } v = 1 \text{ for a single sphere.} \tag{6}$$

Furthermore, we will focus on vesicle shapes as in Fig. 1 and 2 which imply that the spontaneous curvature $\bar{m} \geq 0$.

It is important to note that the stable GUV shapes depend on the two shape parameters v and $\bar{m}$ but are not uniquely determined by these two parameters alone. Indeed, for given values of v and $\bar{m}$, the vesicle can usually attain several (meta)stable shapes that form distinct branches of the bending energy.[12] The number of distinct branches becomes particularly large when one considers multispherical shapes consisting of a variable number of small and large spheres.[9,22]

3.2 Computational methods for stable vesicle shapes

The stable shapes of the GUVs are provided by the local minima of the bending energy for given membrane area and vesicle volume. In order to actually calculate these stable shapes, *i.e.*, to actually minimize the shape energy in eqn (2), two computational methods have been particularly useful. First, axisymmetric membrane shapes, which are completely determined by their 1-dimensional shape contours, can be obtained by solving a set of ordinary differential equations.[12,19] Second, one may consider multispherical shapes consisting of a variable number of large and small spheres connected by closed membrane necks.[9,22] Within the morphology diagrams, the axisymmetric shapes with smooth shape contours and the multispherical shapes are separated by boundary lines of limit shapes. As we approach such a line from one side, we obtain smoothly curved shapes with narrow membrane necks that become eventually closed at the boundary line. As we approach the latter line from the multispherical side, we observe multispherical shapes that depend only on v but not on $\bar{m}$. Thus, for constant v, the latter approach is characterized by a certain fixed multispherical shape.

The closure of a narrow membrane neck as obtained from a smoothly curved shape is somewhat counterintuitive. When viewed on molecular scales, the membrane neck has the shape of an hourglass. The corresponding waistline consists of saddle points, characterized by two principal curvatures, the negative contour curvature $C_{1,wl} < 0$ perpendicular to the waistline and the positive principal curvature $C_{2,wl} = 1/R_{ne} > 0$ parallel to the waistline. When the neck closes, the neck radius goes to zero and the principal curvature $C_{2,wl}$ diverges. However, the mean curvature

$$M_{wl} \equiv \frac{1}{2}(C_{1,wl} + C_{2,wl})$$

remains finite along the waistline and satisfies the asymptotic equality[9]

$$M_{wl} \approx M_{ne} \equiv \frac{1}{2}(M_a + M_b) = m \tag{7}$$

in the limit of small R_{ne}, with the curvature M_{ne} of the closed neck determined by the mean curvatures M_a and M_b of the two

membrane segments, a and b, adjacent to the neck. Thus, in the limit of small neck radii, the singular contribution from the second principal curvature $C_{2,\text{wl}} = 1/R_{\text{ne}} > 0$ is cancelled by another singular contribution arising from the contour curvature $C_{1,\text{wl}}$. This cancellation leads to a finite value of the mean curvature M_{wl} that can be used to estimate the spontaneous curvature m as demonstrated in ref. 22. For $(1 + 1)$-spheres consisting of one large sphere with radius R_l and one small sphere with radius R_s, the neck radius M_{ne} is equal to $(1/R_l + 1/R_s)/2$. The dimensionless neck closure condition $\bar{m}_{\text{ne}} \equiv M_{\text{ne}}R_{\text{ve}} = \bar{m}$ then implies a unique relationship between $\bar{m}$ and the volume-to-area ratio v, see eqn (8) further below.

The simplest multispherical shape is provided by $(1 + 1)$-spheres consisting of two spheres connected by a closed membrane neck. The corresponding stability regime for this morphology is displayed in Fig. 3 as the yellow subregion. This regime is bounded by two lines of limit shapes denoted by L_{1+1} and $L_{2^\star}$. Approaching the line L_{1+1} from outside the stability regime, the closure of the membrane neck leads to asymmetric dumbbells consisting of a large and a small sphere with two different radii. Approaching the line $L_{2^\star}$ from outside the stability regime, the closure of the membrane neck leads to symmetric dumbbells consisting of two equally sized spheres. The process of neck closure is illustrated in Fig. 4 for asymmetric dumbbells with $v = 0.768$ and for symmetric dumbbells with $v = 1/\sqrt{2} = 0.707$.

The line L_{1+1} is described by the functional relationship[12]

$$v = v_{1+1}(\bar{m}) \equiv -\frac{1}{4\bar{m}^3} + \left(1 - \frac{1}{2\bar{m}^2}\right)\sqrt{1 + \frac{1}{4\bar{m}^2}} \quad \text{for} \quad \bar{m} \geq \sqrt{2}. \tag{8}$$

The line $L_{2^\star}$ is located at[9]

$$v = v_\star \equiv \frac{1}{\sqrt{2}} = 0.707 \quad \text{and} \quad \bar{m} \geq \bar{m}_\star \equiv \sqrt{2} = 1.414. \tag{9}$$

The two boundary lines meet in a corner point with $\bar{m} = \bar{m}_\star = \sqrt{2}$ and $v = v_\star = 1/\sqrt{2}$. At this corner point of the morphology diagram, the dumbbell shape consists of two equally sized spheres with radius $R_{\text{ve}}/\sqrt{2}$ and vanishing bending energy. In the following, the limit shapes along the two boundary lines will provide useful reference shapes.

In Fig. 3, we also included the dotted line D^{pear} at which the vesicle undergoes a discontinuous transition from up-down symmetric to up-down asymmetric dumbbells with open necks.[12] Along the transition line D^{pear}, the two types of dumbbells have the same bending energy.

The partial morphology diagram displayed in Fig. 3 contains additional stability regimes for multispheres consisting of N_l large spheres and N_s small spheres with $N_l + N_s \geq 3$. Such $(N_l + N_s)$-spheres have been observed for cholesterol-containing membranes which were exposed to asymmetric sugar solutions.[22] The general theoretical method to determine these multispheres has been developed in ref. 9 and has been used to determine their stability regimes within the spontaneous curvature model.[22]

Lines of multispherical limit shapes with up to $N_l + N_s = 3$ shapes were also obtained in the bilayer coupling model[12,16,17] and within the area-difference-elasticity model.[29] A graphical method to determine the shapes in the area-difference-elasticity model from those in the bilayer coupling model has also been described.[17]

However, in what follows, we will not consider $(N_l + N_s)$-spheres with $N_l + N_s \geq 3$ because the experimentally observed vesicle shapes with $v = 0.670$ as displayed in Fig. 1 and 2 involve only two subcompartments connected by a narrow membrane neck, in close analogy to the $(1 + 1)$-spheres, which are formed for somewhat larger v-values with $v \geq 1/\sqrt{2} = 0.707$, *i.e.*, at and above the line $L_{2^\star}$ displayed in Fig. 3 and described by eqn (9).

4 Analysis of experimental observations

4.1 Theoretical analysis of GUV shapes

Our theoretical analysis is based on the time-lapse Movie 1 (ESI†) which consists of 200 snapshots or frames, each of which displays a different image of the same GUV as obtained by differential interference contrast microscopy. This GUV represents one out of four individual GUVs for which the same mode of shape oscillations has been reported.[6] The time-lapse Movie 1 (ESI†) was taken with the predefined time interval $\Delta t = 7.61$ s between successive frames and displays the whole series of 200 frames within 20 s, corresponding to about 1500 s or 25 min real time. Apart from a few frames at the beginning and at the end, the movie consists of 26 complete shape oscillations with an average time period of 55.9 s as described in more detail further below.

All individual snapshots of Movie 1 (ESI†) are consistent with the view that the observed shapes represent essentially axisymmetric shapes that are tilted with respect to the focal plane and are deformed by relative displacements of the two
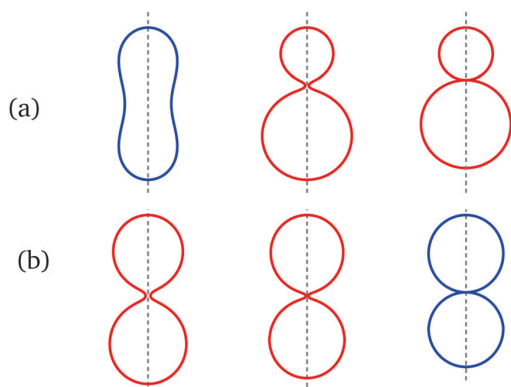

Fig. 4 Examples for dumbbell shapes with open and closed necks: (a) Dumbbells with $v = 0.768$, corresponding to the three solid circles in Fig. 3. From left to right, these shapes have the rescaled spontaneous curvatures $\bar{m} = 1.2$, 1.3 and ≥ 1.56, where the rightmost shape corresponds to the limit shape L_{1+1} with $v = 0.768$; (b) Dumbbells with $v = v_\star = 1/\sqrt{2} = 0.707$ corresponding to the three solid squares in Fig. 3. From left to right, these shapes have the spontaneous curvature $\bar{m} = 1.167$, 1.352, and $\bar{m} \geq \bar{m}_\star = \sqrt{2} = 1.414$.

subcompartments with respect to the closed membrane neck, which acts as a flexible hinge. The two shape sequences in Fig. 1a–c and 2a–c have been selected because they can be well approximated by axisymmetric shapes without additional deformations arising from relative displacements around the hinge-like membrane neck.

During the observed shape changes, both the membrane area and the volume of the GUVs were essentially conserved. These properties were explicitly demonstrated for the six snapshots in Fig. 1a–c and 2a–c by fitting splines to the shape contours of these images, assuming rotational symmetry of the shapes, and then measuring the membrane area A and the vesicle volume V as well as the neck radius R_{ne}.[30,31] The numerical estimates for these geometric quantities are given in Table 1 which also displays the resulting volume-to-area ratio v = 0.670 ± 0.01. The latter value implies that the vesicle has been significantly deflated, compared to a spherical shape with $v = 1$, by the osmotic pressure arising from the hypertonic conditions in the exterior aqueous solution.[6]

The theoretical shapes in Fig. 1d–f and 2d–f were then calculated using the volume-to-area ratio v = 0.670 and several values of the rescaled spontaneous curvature $\bar{m}$ as given in Table 2 and displayed in the morphology diagram of Fig. 3. Furthermore, to obtain the dimensionful quantities from the dimensionless ones, we used the vesicle size $R_{ve} = \sqrt{A/(4\pi)} = 5.57$ μm as obtained from the area A = 390 μm^2 of the image in Fig. 1a, see first row in Table 1.

4.2 Two branches of stable dumbbells

All dumbbells computed for the symmetry-breaking transformation in Fig. 1d–f and for the symmetry-restoring transformation in Fig. 2d–f have the same volume-to-area ratio v = 0.670 but differ in their $\bar{m}$-values, see Table 2. Both types of shape transformations involve up-down symmetric as well as asymmetric dumbbells. The symmetric dumbbells are formed for a wide range of $\bar{m}$-values as illustrated in Fig. 5. For these dumbbells, the neck radius monotonically decreases as we increase the spontaneous curvature $\bar{m}$.

In contrast, the asymmetric dumbbells with an open neck as in Fig. 1f and 2d, e are only found for a relatively small range of $\bar{m}$-values. Indeed, when we start from a certain asymmetric dumbbell and increase the spontaneous curvature, the

Table 1 Membrane area A, vesicle volume V, dimensionless volume-to-area ratio v defined in eqn (4), and neck radius R_{ne}, as estimated from the optical images in Fig. 1a–c and 2a–c via fitting with splines. In the third and fourth row, the upper bound for R_{ne} corresponds to the optical resolution of differential interference contrast microscopy. The error of the spline fitting was estimated with ±2 pixel which corresponds to ±132 nm

	A [μm^2]	V [μm^3]	v	R_{ne} [μm]
Fig. 1a	390 ± 30	490 ± 60	0.68 ± 0.01	1.1 ± 0.2
Fig. 1b	380 ± 30	470 ± 60	0.68 ± 0.01	0.8 ± 0.2
Fig. 1c	380 ± 30	460 ± 50	0.66 ± 0.02	<0.3
Fig. 2a	380 ± 30	470 ± 53	0.67 ± 0.01	<0.3
Fig. 2b	380 ± 30	463 ± 52	0.68 ± 0.01	0.6 ± 0.2
Fig. 2c	380 ± 30	483 ± 55	0.68 ± 0.01	0.9 ± 0.2

Table 2 Dimensionless shape parameters v and $\bar{m}$ that were used to compute the dumbbell shapes in Fig. 1d–f and 2d–f, see also Fig. 6. The third column contains the rescaled neck radius $\bar{R}_{ne} = R_{ne}/R_{ve}$ of the computed shapes. The spontaneous curvature $m = \bar{m}/R_{ve}$ and the neck radius $R_{ne} = \bar{R}_{ne}R_{ve}$ in the fourth and fifth column were computed using the vesicle size $R_{ve} = \sqrt{A/(4\pi)} = 5.57$ μm as obtained from the membrane area A = 390 μm^2 for the image in Fig. 1a

	v	$\bar{m}$	$\bar{R}_{ne}$	m [μm^{-1}]	R_{ne} [μm]
Fig. 1d	0.670	1.18	0.21	0.21	1.17
Fig. 1e	0.670	1.63	0.14	0.29	0.78
Fig. 1f	0.670	1.89	0.021	0.34	0.12
Fig. 2d	0.670	1.89	0.021	0.34	0.12
Fig. 2e	0.670	1.93	0.094	0.35	0.52
Fig. 2f	0.670	1.40	0.17	0.25	0.95
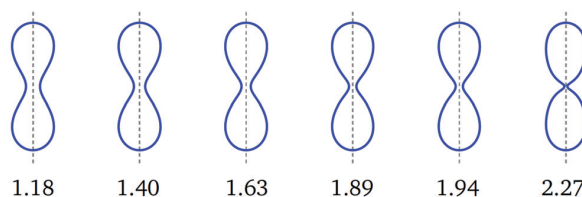
Fig. 5 Symmetric dumbbell shapes (blue) for constant volume-to-area ratio v = 0.670 and rescaled spontaneous curvature $\bar{m}$ as given by the numerals below the shapes. The first three shapes correspond to the blue diamonds in Fig. 3. This sequence of shapes illustrates the closure of the membrane neck along the symmetric branch as we increase the value of the spontaneous curvature $\bar{m}$ from 1.18 to 2.27.

resulting dumbbells become more and more symmetric until we reach the bifurcation point B_{op}, which is provided by a symmetric dumbbell with an open neck and has spontaneous curvature $\bar{m}(B_{op})$. At the latter $\bar{m}$-value, the asymmetric branch merges with the symmetric one and the asymmetric branch ceases to exist for $\bar{m} > \bar{m}(B_{op})$.

On the other hand, when we decrease the spontaneous curvature, the neck radius of the asymmetric dumbbell becomes smaller and smaller until we reach the limit shape L_{ps} with a closed neck for spontaneous curvature $\bar{m}(L_{ps})$. The closed neck of this limit shape connects a spherical with a prolate subcompartment. Therefore, the branch of stable asymmetric dumbbells with an open neck is limited to those values of the spontaneous curvature that satisfy
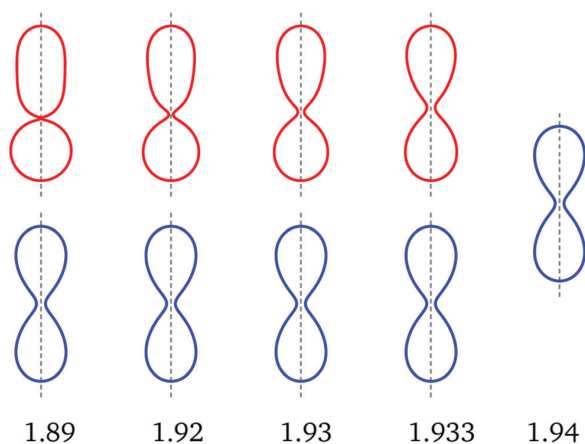
$$\bar{m}(L_{ps}) < \bar{m} < \bar{m}(B_{op}). \tag{10}$$

For v = 0.670, the value of $\bar{m}(L_{ps})$ is estimated to be 1.84 ± 0.04 and the value of $\bar{m}(B_{op})$ is somewhat larger than 1.933. For all $\bar{m}$-values within the interval as given by eqn (10), the vesicle can also form a symmetric dumbbell. Therefore, asymmetric dumbbells always coexist with symmetric ones. Examples for this coexistence of symmetric and asymmetric dumbbells are provided in Fig. 6. Inspection of this figure reveals that, in contrast to the symmetric dumbbells, the neck radius of the asymmetric dumbbells increases with increasing spontaneous curvature. At the bifurcation point B_{op} with $\bar{m}(B_{op}) \simeq 1.933$, the neck radius has the value $\bar{R}_{ne} = 0.11$.

Fig. 6 Up-down symmetric (blue) and asymmetric (red) dumbbells for $v = 0.670$ and five values of the rescaled spontaneous curvature $\bar{m}$ as indicated by the numerals below the shapes. The asymmetric dumbbells with $\bar{m} = 1.89$ and 1.93 correspond to the red diamonds in Fig. 3. The two types of shapes coexist between $\bar{m} = 1.89$ and $\bar{m} = 1.933$. For $\bar{m} = 1.94$, only the symmetric shape is found which implies that the asymmetric branch merges with the symmetric one at a critical value of the spontaneous curvature slightly above $\bar{m} = 1.933$. Comparison of the asymmetric and symmetric shapes reveals that the asymmetric shapes approach the symmetric ones in a continuous manner as we increase the spontaneous curvature towards its critical value. This conclusion is further corroborated by the corresponding energy branches in Fig. 7. Note that the neck radius of the asymmetric (red) dumbbells increases with increasing $\bar{m}$, in contrast to the behavior of the symmetric (blue) dumbbells. For more details on the dependence of the dumbbell shapes on the spontaneous curvature, see Movie 2 (ESI†).

It follows from the dumbbell shapes in Fig. 6 that the spontaneous curvature $\bar{m}(B_{op})$, at which the asymmetric branch merges with the symmetric one, is somewhat larger than $\bar{m} = 1.933$. Furthermore, the asymmetric dumbbell with $\bar{m} = 1.89$ must be quite close to the limit shape L_{ps} because the membrane neck of the latter dumbbell is almost closed and the smaller subcompartment has already an essentially spherical shape. To estimate the spontaneous curvature $\bar{m}(L_{ps})$ for the prolate-sphere limit shape, we compute the mean curvature M_{npol} at the north pole of the asymmetric dumbbells and the mean curvature M_{spol} at the south pole of these dumbbells. As we approach the limit shape L_{ps}, the rescaled mean curvatures $\bar{M}_{npol} \equiv M_{npol}R_{ve}$ and $\bar{M}_{spol} \equiv M_{spol}R_{ve}$ should satisfy the asymptotic equality

$$\bar{M}_{npol} + \bar{M}_{spol} \approx 2\bar{m}(L_{ps}), \tag{11}$$

as follows from the closure condition for membrane necks in eqn (7) and from the observation that both the spherical and the prolate subcompartments of L_{ps} are up-down symmetric. The neck closure condition as given by eqn (11) provides one estimate for the spontaneous curvature $\bar{m}(L_{ps})$ of the prolate-sphere limit shape. A second estimate is provided by extrapolating the asymmetric branch in Fig. 8 to $\bar{R}_{ne} = 0$, see red star in Fig. 8a.
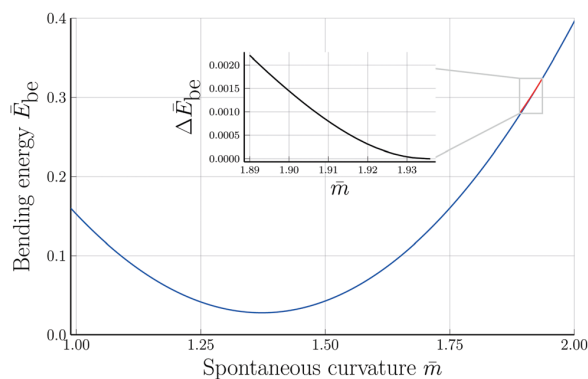
Fig. 7 Rescaled bending energy $\bar{E}_{be} = E_{be}/(8\pi\kappa)$ as a function of rescaled spontaneous curvature $\bar{m}$ for volume-to-area ratio $v = 0.670$. The $\bar{E}_{be}$-values are displayed in blue for the symmetric dumbbells and in red for the asymmetric ones. The inset shows the energy difference $\Delta\bar{E}_{be}$ between the metastable asymmetric and the stable symmetric branch, as defined in eqn (12). The asymmetric branch (red) has a slightly larger bending energy than the symmetric branch (blue). Therefore, the asymmetric branch represents a branch of metastable shapes. The two branches merge with a common tangent at a critical $\bar{m}$-value slightly above $\bar{m} = 1.933$, see Fig. 6. The symmetric branch exhibits a pronounced minimum at $\bar{m} = 1.373$ which reflects the vicinity of the corner point with $v = 1/\sqrt{2}$ and $\bar{m} = \sqrt{2}$, at which the bending energy vanishes, see the morphology diagram in Fig. 3.

### 4.3 Two branches of the bending energy

The symmetric and asymmetric dumbbells as displayed in Fig. 6 belong to two different branches of the bending energy E_{be} as shown in Fig. 7. As described in the previous subsection, these two branches coexist for the $\bar{m}$-interval with $\bar{m}(L_{ps}) < \bar{m} < \bar{m}(B_{op})$ with $\bar{m}(L_{ps}) \simeq 1.84$ and merge continuously into a single symmetric branch when the spontaneous curvature reaches the bifurcation value $\bar{m} = \bar{m}(B_{op})$ with $1.933 < \bar{m}(B_{op}) < 1.94$, where the numerical values apply to $v = 0.670$. The continuous bifurcation at spontaneous curvature $\bar{m}(B_{op})$ is confirmed by the functional form of the bending energy, see inset in Fig. 7. The latter inset displays the rescaled bending energy difference

$$\Delta\bar{E}_{be} \equiv (\bar{E}_{be}^{asy} - \bar{E}_{be}^{sy})/(8\pi\kappa) \tag{12}$$

between the bending energy $\bar{E}_{be}^{asy}$ of the asymmetric branch and the bending energy $\bar{E}_{be}^{sy}$ of the symmetric branch. Because this energy difference is always positive, the asymmetric branch represents a branch of metastable shapes. Furthermore, inspection of this inset reveals that the two energy branches merge with a common tangent for a critical $\bar{m}$-value close to 1.94. The latter behavior agrees with the shape evolution in Fig. 6, which directly demonstrates that the up-down asymmetric shapes become more and more symmetric as we approach the bifurcation value $\bar{m}(B_{op})$ of the spontaneous curvature.

In the spontaneous curvature model, the bending energy difference $\Delta\bar{E}_{be}$ displayed in the inset of Fig. 7 is always positive, *i.e.*, the asymmetric branch has an increased bending energy compared to the symmetric one. Further below, we will
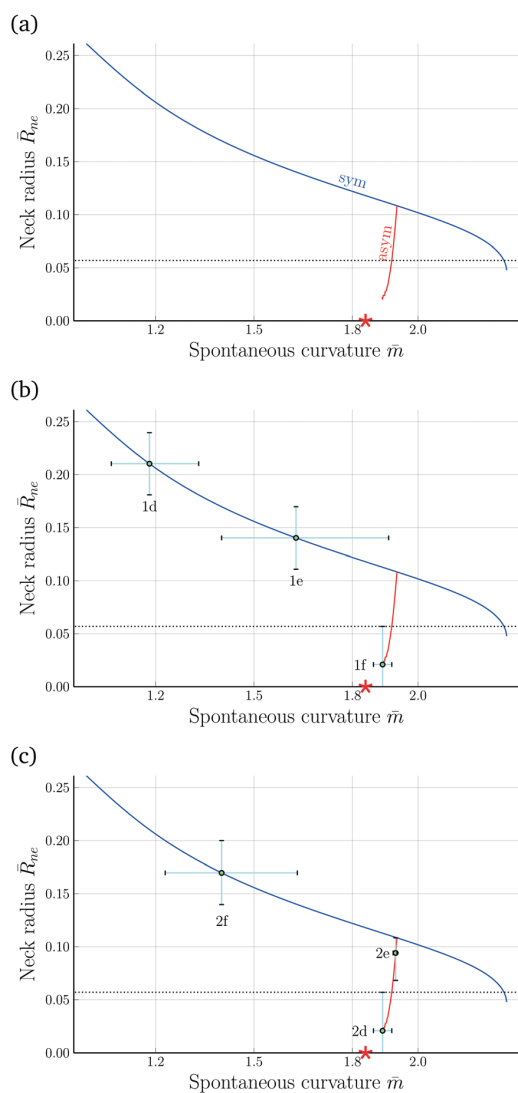
Fig. 8 Rescaled radius $\bar{R}_{ne} = R_{ne}/R_{ve}$ of membrane neck as a function of spontaneous curvature $\bar{m}$ for $v = 0.670$: (a) computed variation of the neck radius along the symmetric (blue) and asymmetric (red) dumbbell branches. The corresponding shapes are displayed in Fig. 6 and Movie 2 (ESI†). As we increase the spontaneous curvature $\bar{m}$, the neck radius decreases along the symmetric but increases along the asymmetric branch. The red star indicates the estimate $\bar{m} \simeq 1.84$ for the spontaneous curvature of the prolate-sphere limit shape L_{ps} with $\bar{R}_{ne} = 0$; (b) evolution of neck radius and spontaneous curvature for the three shapes in Fig. 1 that describe the symmetry-breaking transformation; and (c) evolution of neck radius and spontaneous curvature for the three shapes in Fig. 2 that describe the symmetry-restoring transformation. The error bars of the neck radius correspond to the uncertainty of the neck radius as obtained by approximating the experimental shape contours in Fig. 1a–c and 2a–c with splines, truncated at the bifurcation point and the threshold of the optical resolution. The error bars of the spontaneous curvature correspond to the resulting uncertainty of the spontaneous curvature given the non-linear shape of the curve. The horizontal dotted lines represent the optical resolution limit of 300 nm.

consider the area-difference-elasticity model and study the bending energies as a function of the local spontaneous

curvature m_{loc}. In the latter case, the branch of asymmetric shapes has a lower bending energy and, thus, becomes the stable state of minimal bending energy.

4.4 Closing and opening of membrane necks

For each dumbbell shape, the two subcompartments are connected by a membrane neck with a circular waistline. The radius of this waistline defines the neck radius R_{ne}, see Fig. 1 and 2, which changes during the shape oscillations. Thus, in addition to the global up-down symmetry of the dumbbells, these shapes can also be distinguished by their neck radius R_{ne} which represents a local property.

In Fig. 8a, we display the rescaled neck radius

$$\bar{R}_{ne} \equiv \frac{R_{ne}}{R_{ve}} = \frac{R_{ne}}{\sqrt{A/(4\pi)}} \qquad (13)$$

as a function of the spontaneous curvature $\bar{m} = mR_{ve}$, along the symmetric (blue) and asymmetric (red) branch of dumbbells. In addition to the two branches of the neck radius as a function of spontaneous curvature, the two panels b and c of Fig. 8 contain the numerical values of $\bar{R}_{ne}$ and $\bar{m}$ for the three dumbbell shapes in Fig. 1 and 2. The latter plots show once more that, in the spontaneous curvature model, the neck radius decreases and increases monotonically along the symmetric and asymmetric branches, respectively, as we increase the spontaneous curvature of the GUV membrane. These plots also show how the uncertainties in the neck radius lead to different uncertainties in the spontaneous curvature, depending on the value of the radius as well as the branch to which the shape belongs. The steeper the curve of the neck radius is, the more accurate can the spontaneous curvature be estimated. Additionally the branch bifurcation point and the optical limit are natural boundaries at which the error bars can be truncated.

4.5 Time dependence of active shape oscillations

The time-lapse Movie 1 (ESI†) consists of 200 individual snapshots or frames which were taken with the predefined time interval $\Delta t = 7.61$ s between successive frames. We number the frames by the index i from $i = 1$ to $i = 200$ and label each frame as 'open' if it displays an open neck and as 'closed' if the neck appears to be closed on the optical image. In this way, we map the sequence of 200 vesicle images onto a sequence of open and closed states. Both types of states are persistent and form short subseries of successive open states that alternate with short subseries of successive closed states.

We identify neck closure events to be provided by those frames that display a closed neck and are directly preceded by a frame with an open neck. Furthermore, a complete shape oscillation is defined by the sequence of Δi frames between two successive closure events. Such a sequence consists of a subseries of three to four successive images with closed necks, followed by a subseries of three to four successive images with open necks. Movie 1 (ESI†) displays 191 frames between the first and the last closure event, which form 26 complete shape oscillations. Thus, the average number of frames, $\langle \Delta i \rangle$, per complete

Soft Matter

Paper

shape oscillation is equal to 191/26 = 7.35 frames and the average time period for one complete oscillation is given by $\langle \Delta i \rangle \Delta t = 7.35 \times 7.61$ s = 55.9 s, which is similar to the cycle time observed for Min oscillations in other compartments.[25,26]

Most of the 26 complete shape oscillations consist of 7 or 8 successive images or frames. The 7-frame oscillations are observed 15 times, the 8-frame oscillations 10 times. In addition, we observe one complete oscillation with only 6 successive frames. Thus, including these statistical fluctuations, we obtain the estimate

$$\Delta i = \langle \Delta i \rangle \pm 1 = 7.35 \pm 1$$

for the number of frames of each individual shape oscillation which shows that these oscillations are quite regular and almost clock-like. The deviations from a perfect clock correspond to a variation by about 14 percent which reflect the stochastic attachment–detachment kinetics of the Min proteins.[7,8] Furthermore, when these molecular oscillations drive the shape transformations of the GUVs, small differences in the initial shapes tend to become amplified during the shape evolution and to generate relative displacements of the two subcompartments around the membrane neck. To obtain a quantitative description of the experimentally observed shapes in terms of axisymmetric shapes, we selected the images $i = 1, 2,$ and 3 for the symmetry-breaking transformation in Fig. 1 and the images $i = 68, 69,$ and 70 for the symmetry-restoring transformation in Fig. 2.

The theoretical shapes in Fig. 1 and 2 were obtained for the parameter values in Table 2. The resulting time-dependence of the spontaneous curvature $\bar{m}$ is shown in Fig. 9 where we plot $\bar{m}$ *versus* the frame index i which corresponds to the time

$$t = (i - 1)\Delta t = (i - 1) \times 7.61 \text{ s} \tag{14}$$

after the initial image $i = 1$. For each spontaneous curvature $\bar{m} = \bar{m}(i)$ in Fig. 9, the GUV shape has a certain neck radius $R_{ne} = R_{ne}(\bar{m})$ as plotted in Fig. 8b and c. When we combine these two relationships, we obtain the time dependence of the neck radius $R_{ne} = R_{ne}(i)$ as shown in Fig. 10.

Because of the relatively large error bars for the data in Fig. 10, depicting the time-dependence of the neck radius $\bar{R}_{ne}$, it is difficult to fit these data in a quantitative manner. The presumably simplest fit is provided by a single Fourier mode of the form

$$\bar{R}_{ne} = a + b \cos[2\pi(i - 1)/7], \tag{15}$$

where we identify the frame indices $i = 68, \ldots, 71$ in Fig. 10 with the indices $i = 5, \ldots, 8$ as well as the frame indices $i = 8$ and $i = 1$, thereby taking the oscillation period to be $\Delta i = 7$. Using the method of least squares provided by the Julia package LsqFit.jl,[32] we then obtain the parameter values $a = 0.10 \pm 0.02$ and $b = 0.09 \pm 0.03$ as used in Fig. 10.

4.6 Modifications arising from area-difference-elasticity

In the previous sections, we described the curvature elasticity of the vesicle membrane by the spontaneous curvature model as given by eqn (1). From the theoretical point of view, this model
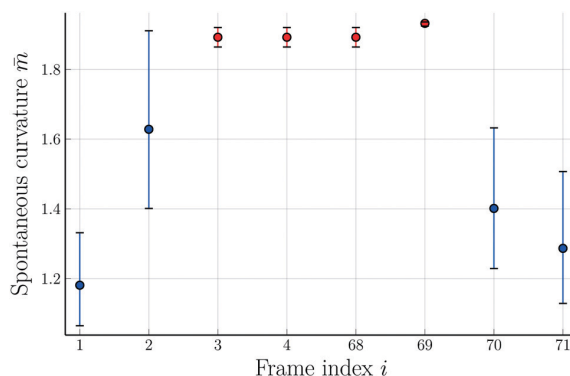

Fig. 9 Rescaled spontaneous curvature $\bar{m}$ *versus* frame index i. The frame i was taken at time $t = (i - 1) \times 7.61$ s after the initial frame with index $i = 1$. The blue data points correspond to up-down symmetric dumbbell shapes, the red data points to asymmetric ones. The symmetry-breaking transformation in Fig. 1 corresponds to $i = 1, 2,$ and 3, the symmetry-restoring transformation in Fig. 2 to $i = 68, 69,$ and 70. The image $i = 4$ displays a slightly distorted version of $i = 3$ and is thus taken to have the same $\bar{m}$-value as $i = 3$. The image $i = 71$ displays a symmetric dumbbell with an increased neck radius compared to $i = 70$. This increased radius implies the spontaneous curvature $\bar{m} = 1.32$. The combined sequence of all eight images represents one complete shape oscillation with an average time period of 55.9 s. The error bars are obtained as in Fig. 8.
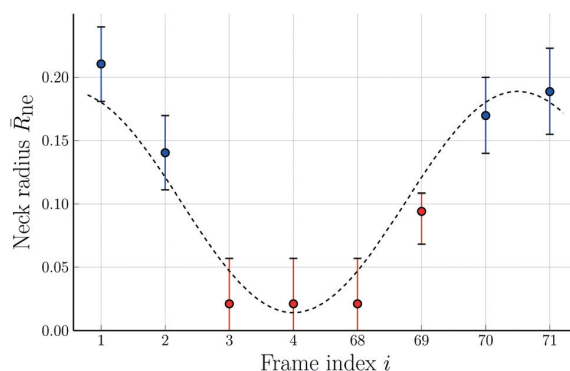

Fig. 10 Rescaled neck radius $\bar{R}_{ne}$ *versus* frame index i corresponding to time $t = (i - 1) \times 7.61$ s. Direct inspection of the frame with index $i = 71$ leads to the neck radius $\bar{R}_{ne} = 0.189$ for this image. The combined sequence of all eight images represents one complete shape oscillation which takes, on average, 55.9 s. The color code of the data points is the same as in Fig. 9. The trigonometric curve (dashed black line) through the data provides the best fit to a single Fourier mode as parametrized by eqn (15). The error bars are obtained as in Fig. 8.

directly applies to lipid bilayers with at least one lipid component that undergoes frequent flip-flops between the two bilayer leaflets, as recently confirmed experimentally for lipid bilayers with cholesterol.[22,23] The vesicle membranes studied in ref. 6, on the other hand, contained the two phospholipids DOPC and DOPG as well as a very small mole fraction of labeled DOPE, all of which are not expected to undergo frequent flip-flops on the experimentally relevant time scales. In the latter situation, we need to generalize the spontaneous curvature model to the area-difference-elasticity model,[13–15] which can, however,

Paper

be mapped back onto the spontaneous curvature model by decomposing the spontaneous curvature into a local and a nonlocal contribution.[9,15]

In the absence of flip-flops, each leaflet has a fixed number of lipids which generates an additional constraint on the area difference between the two leaflets. This area difference is proportional to the integrated (or total) mean curvature

$$I_M \equiv \int dA \, M \quad \text{or} \quad \bar{I}_M \equiv \frac{I_M}{R_{ve}} \tag{16}$$

where the vesicle size $R_{ve} = \sqrt{A/(4\pi)}$ in eqn (3) has been used to define the dimensionless curvature $\bar{I}_M$.§

When we include the constraint on the area difference and, thus, the integrated mean curvature, we arrive at the area-difference-elasticity (ADE) model with the energy[13–15]

$$E_{ADE} = E_{be}' + D_{ADE} \tag{17}$$

consisting of the local bending energy

$$E_{be}' = 2\kappa \int dA (M - m_{loc})^2 \tag{18}$$

and the nonlocal ADE term

$$D_{ADE} = \frac{2\pi\kappa_\Delta}{A}(I_M - I_{M,0})^2. \tag{19}$$

The local bending energy E_{be}' has the same form as the spontaneous curvature model in eqn (1) with the spontaneous curvature m replaced by the local spontaneous curvature m_{loc}. The nonlocal ADE term D_{ADE} is proportional to (i) the second bending rigidity κ_Δ¶ and to (ii) the squared deviation of the integrated mean curvature I_M from its reference value $I_{M,0}$. Thus, the nonlocal ADE term D_{ADE} involves two additional parameters, the second bending rigidity κ_Δ and the reference value $I_{M,0}$ of the integrated mean curvature.

The second bending rigidity κ_Δ is, in general, difficult to determine but is typically comparable to κ.[14] In order to eliminate one parameter, we will focus on the case with κ_Δ equal to κ. The reference value $I_{M,0}$, on the other hand, can be estimated from the integrated mean curvatures of the six shapes displayed in Fig. 1 and 2. The resulting numerical values of the dimensionless quantity $\bar{I}_M = I_M/R_{ve}$ are displayed in Table 3. The best estimate for the reference value $I_{M,0} \equiv x$ is now obtained by minimizing the root-mean-square deviation

$$\text{RMSD} = \sum_{i=1}^{6}(I_{M,i} - x)^2 \tag{20}$$

with respect to x where the index i runs over the six shapes in Fig. 1 and 2. As a result, we obtain the best estimate

$$\bar{I}_{M,0} = \frac{I_{M,0}}{R_{ve}} = \frac{1}{6}\sum_{i=1}^{6} \bar{I}_{M,i} = 17.63 \tag{21}$$

§ The dimensionless integrated mean curvature $\bar{I}_M$ is related to the dimensionless area difference Δa as discussed in ref. 12, 16 and 17 by $\bar{I}_M = 4\pi\Delta a$.

¶ In ref. 17, the prefactor π in eqn (19) is combined with the second bending rigidity κ_Δ to define the nonlocal bending energy $\kappa_r \equiv \pi\kappa_\Delta$.

Table 3 Integrated mean curvature $\bar{I}_M = I_M/R_{ve}$ for the six shapes in Fig. 1 and 2 as well as the deviation $\Delta\bar{I}_M \equiv \bar{I}_{M,0} - \bar{I}_M$ from the reference value $\bar{I}_{M,0} = 17.63$, the nonlocal spontaneous curvature $\bar{m}_{nlo}$ as obtained from eqn (23) with $\kappa_\Delta/\kappa = 1$, the spontaneous curvature $\bar{m}$ as in Table 2, and the local spontaneous curvature $\bar{m}_{loc} = \bar{m} - \bar{m}_{nlo}$. The nonlocal spontaneous curvature $\bar{m}_{nlo}$ is positive and negative for symmetric and asymmetric shapes, respectively. Apart from Fig. 1d, the local spontaneous curvature $\bar{m}_{loc}$ differs from $\bar{m}$ only by a few percent

	$\bar{I}_M$	$\Delta\bar{I}_M$	$\bar{m}_{nlo}$	$\bar{m}$	$\bar{m}_{loc}$
Fig. 1d, sym	17.01	+0.62	+0.16	1.18	1.02
Fig. 1e, sym	17.47	+0.16	+0.04	1.63	1.59
Fig. 1f, asy	18.14	−0.51	−0.13	1.89	2.02
Fig. 2d, asy	18.14	−0.51	−0.13	1.89	2.02
Fig. 2e, asy	17.72	−0.09	−0.02	1.93	1.95
Fig. 2f, sym	17.28	+0.35	+0.09	1.40	1.31

for the dimensionless integrated mean curvature. This curvature value is close to the one of a symmetric dumbbell or $(1 + 1)$-sphere, corresponding to the limit shape L_{2*} in Fig. 3, for which $\bar{I}_M = 8\pi/\sqrt{2} = 17.77$.

The stationary shapes of the area-difference-elasticity model are also stationary shapes of the spontaneous curvature model[13–15] provided we use the identification[9,15]

$$m = m_{loc} + m_{nlo} \quad \text{or} \quad \bar{m} = \bar{m}_{loc} + \bar{m}_{nlo} \tag{22}$$

with the nonlocal spontaneous curvature

$$m_{nlo} \equiv \pi\frac{\kappa_\Delta}{\kappa}\frac{I_{M,0} - I_M}{A} \quad \text{or} \quad \bar{m}_{nlo} \equiv \frac{\kappa_\Delta}{4\kappa}(\bar{I}_{M,0} - \bar{I}_M). \tag{23}$$

The local spontaneous curvature $\bar{m}_{loc}$ can then be computed via $\bar{m}_{loc} = \bar{m} - \bar{m}_{nlo}$.‖ The numerical values for the local and nonlocal spontaneous curvature obtained in this manner for the shapes in Fig. 1 and 2 are provided in Table 3.

The rescaled ADE energy is now given by

$$\bar{E}_{ADE} \equiv \frac{E_{ADE}}{8\pi\kappa} = \bar{E}_{be}' + \bar{D}_{ADE} \tag{24}$$

with the rescaled local bending energy

$$\bar{E}_{be}' = \frac{\bar{E}_{be}'}{8\pi\kappa} = \frac{1}{4R_{ve}^2}\int dA (\bar{M} - \bar{m}_{loc})^2 \tag{25}$$

and the rescaled nonlocal ADE term

$$\bar{D}_{ADE} = \frac{D_{ADE}}{8\pi\kappa} = \frac{1}{16\pi}\frac{\kappa_\Delta}{\kappa}(\bar{I}_{M,0} - \bar{I}_M)^2. \tag{26}$$

The ADE model depends on four dimensionless parameters: the volume-to-area ratio v, the local spontaneous curvature $\bar{m}_{loc}$, the reference value $\bar{I}_{M,0}$ of the integrated mean curvature, and the rigidity ratio κ_Δ/κ. For the fixed parameter values $v = 0.670$, $\bar{I}_{M,0} = 17.63$, and $\kappa_\Delta/\kappa = 1$, we are left with only one dimensionless parameter, the local spontaneous curvature $\bar{m}_{loc}$. Within the ADE model, this latter parameter depends on the amount of Min proteins bound to the inner leaflet of GUV membrane. The time-dependent oscillation of the local spontaneous curvature $\bar{m}_{loc}$ is displayed in Fig. S2 (ESI†). Comparison with the time

‖ All barred curvatures are dimensionless and obtained from the unbarred ones by multiplication with the basic length scale R_{ve}.

dependence of $\bar{m}$ in Fig. 9 shows that, in contrast to $\bar{m}$, the local curvature $\bar{m}_{\mathrm{loc}}$ decreases monotonically during the symmetry restoring transformation between frame 68 and 70.

The dependence of the ADE energies on $\bar{m}_{\mathrm{loc}}$ is displayed in Fig. 11. Note that the ADE energy of the asymmetric branch is now below the energy of the symmetric one and that the energy difference

$$\Delta \bar{E}_{\mathrm{ADE}} = \bar{E}_{\mathrm{ADE}}^{\mathrm{asy}} - \bar{E}_{\mathrm{ADE}}^{\mathrm{sy}} \qquad (27)$$

between the asymmetric and the symmetric branch is now negative, see Fig. 11d. The energy values displayed in this figure have been computed for $\kappa_\Delta/\kappa = 1$ but the same ordering of the energy levels applies to $\kappa_\Delta/\kappa = 2$ as well, see Fig. S3 (ESI†). For phospholipid membranes without flip-flops, the bending rigidity ratio is expected to lie within the range $1 \lesssim \kappa_\Delta/\kappa \lesssim 2$.[14] Therefore, the asymmetric energy branch is likely to be located below the symmetric one for realistic values of κ_Δ/κ.

5 Discussion

In this study, we analyzed the recently observed shape oscillations of giant vesicles in a quantitative manner, using the framework of curvature elasticity. In the latter framework, the simplest model is provided by the spontaneous curvature model in which the shape of a uniform vesicle membrane depends on two dimensionless parameters, the volume-to-area ratio v, see eqn (4), and the rescaled spontaneous curvature $\bar{m} = m R_{\mathrm{ve}}$. A detailed theoretical analysis of Movie 1 (ESI†) showed that the shape oscillations conserve both the vesicle volume and the membrane area which implies a constant value of v (Table 2). Our analysis also revealed that the observed

Fig. 11 Integrated mean curvature and different energy contributions in the ADE model as functions of the local spontaneous curvature $\bar{m}_{\mathrm{loc}}$ for rigidity ratio $\kappa_\Delta/\kappa = 1$. The symmetric and asymmetric branches are displayed as blue and red lines, respectively: (a) Integrated mean curvature $\bar{I}_M$ as in eqn (16); (b) Nonlocal area-difference-elasticity term $\bar{D}_{\mathrm{ADE}}$ as in eqn (26); (c) local bending energy $\bar{E}_{\mathrm{be}}'$ as in eqn (25); and (d) ADE energy $\bar{E}_{\mathrm{ADE}}$ which is equal to the sum of the local and nonlocal terms in panels b and c. In contrast to the spontaneous curvature model, see Fig. 7, the energy of the asymmetric branch is now below the energy of the symmetric one. All quantities were computed for volume-to-area ratio $v = 0.670$ and reference value $\bar{I}_{M,0} = 17.63$ of the integrated mean curvature.

shape oscillations can be understood in terms of a time-dependent spontaneous curvature, which varies in a cyclic, almost periodic manner.
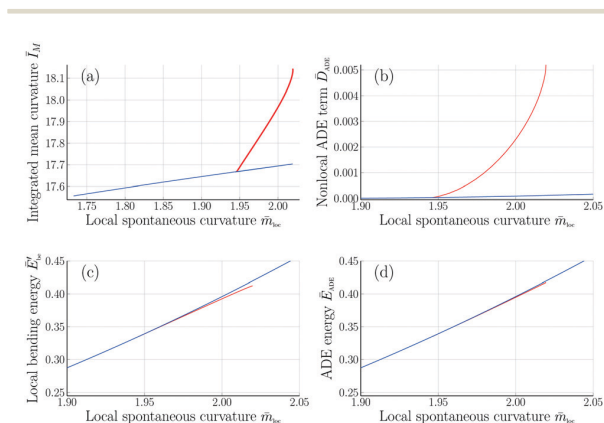
Surprisingly, these shape oscillations were found to involve two energy branches of the vesicle membrane, corresponding to up-down symmetric and up-down asymmetric dumbbells, see Fig. 6 and 7. The latter two figures imply that the two branches merge in a continuous manner. During each complete shape oscillation, the vesicle morphology undergoes a symmetry-breaking transformation (Fig. 1) at which an up-down symmetric dumbbell with two subcompartments of equal size transforms into an up-down asymmetric dumbbell with two subcompartments of different sizes, followed by the reverse, symmetry-restoring transformation (Fig. 2). In the spontaneous curvature model, the bending energy of the asymmetric branch exceeds the bending energy of the symmetric one (Fig. 7).

The phospholipids studied in ref. 6 are unlikely to undergo frequent flip-flops between the two leaflets of the bilayer membranes. To take this absence of flip-flops into account, we extended the spontaneous curvature model to the area-difference-elasticity (ADE) model by decomposing the spontaneous curvature $\bar{m}$ into a local and a nonlocal component, see eqn (22) and (23). In the ADE model, the attachment–detachment kinetics of the Min proteins leads to variations of the local spontaneous curvature $\bar{m}_{\mathrm{loc}}$ as given in Table 3 for the observed shapes in Fig. 1 and 2. Furthermore, the branch of asymmetric dumbbells is now located below the branch of symmetric ones, both for $\kappa_\Delta/\kappa = 1$ (Fig. 11) and for $\kappa_\Delta/\kappa = 2$ (Fig. S3, ESI†). Therefore, both the symmetric and the asymmetric dumbbells that have been observed experimentally (Fig. 1 and 2) are likely to represent stable shapes of minimal bending energy.

The branch of asymmetric dumbbell shapes observed here involves a prolate-sphere limit shape L_{ps}, consisting of a prolate and a spherical subcompartment which are connected by a closed membrane neck. In the present study, we studied the volume-to-area ratio $v = 0.670$ for which we obtained the estimate $\bar{m}(L_{\mathrm{ps}}) \simeq 1.84$ for the spontaneous curvature at which this limit shape L_{ps} is formed. Such prolate-sphere limit shapes are expected to be stable within a whole region of the morphology diagram as defined by the two shape parameters v and $\bar{m}$, in close analogy to the stability regime for the two-sphere vesicles in Fig. 3. For the prolate-sphere limit shapes, the corresponding stability regime remains to be determined and will add another layer to the morphological complexity of vesicle shapes.

One unexpected outcome of our analysis is that the coupling of membrane curvature to active processes can reveal new branches of vesicle shapes that have not been observed before. In the present study, such shapes are provided by asymmetric dumbbells with volume-to-area ratio $v < 1/\sqrt{2} = 0.707$. Thus, it should be rather interesting to extend our study, both experimentally and theoretically, to different values of v and to see whether or not the Min-induced shape oscillations typically involve distinct branches of (meta)stable shapes.

Finally, in the present study, the two subcompartments of the GUVs were always connected by a narrow membrane neck.

From the theoretical point of view, a sufficiently large sponta-neous curvature can cleave such a neck by curvature-induced constriction forces,[9] as recently demonstrated for GUVs that were exposed to His-tagged proteins.[23] Therefore, an interesting and challenging objective for future studies is to cleave these necks by combining the Min proteins studied here with other curvature-generating molecules.

Conflicts of interest

There are no conflicts to declare.

Acknowledgements

Notes and references

1 *Structure and Dynamics of Membranes*, ed. R. Lipowsky and E. Sackmann, Elsevier, Amsterdam, 1995.
2 *Physics of Biological Membranes*, ed. P. Bassereau and P. Sens, Springer Nature, 2018.
3 *The Giant Vesicle Book*, ed. R. Dimova and C. Marques, Taylor & Francis, 2020.
4 B. Antonny, C. Burd, P. de Camilli, E. Chen, O. Daumke, K. Faelber, M. Ford, V. A. Frolov, A. Frost, J. E. Hinshaw, T. Kirchhausen, M. M. Kozlov, M. Lenz, H. H. Low, H. McMahon, C. Merrifield, T. D. Pollard, P. J. Robinson, A. Roux and S. Schmid, *EMBO J.*, 2016, **35**, 2270–2284.
5 P. A. de Boer, R. E. Crossley, A. R. Hand and L. I. Rothfield, *EMBO J.*, 1991, **10**, 4371–4380.
6 T. Litschel, B. Ramm, R. Maas, M. Heymann and P. Schwille, *Angew. Chem., Int. Ed.*, 2018, **57**, 16286–16290.
7 Z. Hu, E. P. Gogol and J. Lutkenhaus, *Proc. Natl. Acad. Sci. U. S. A.*, 2002, **99**, 6761–6766.
8 M. Loose, E. Fischer-Friedrich, C. Herold, K. Kruse and P. Schwille, *Nat. Struct. Mol. Biol.*, 2011, **18**, 577–583.
9 R. Lipowsky, *The Giant Vesicle Book*, Taylor & Francis, 2020, pp. 73–168.
10 W. Helfrich, *Z. Naturforsch.*, 1973, **28c**, 693–703.
11 H. Deuling and W. Helfrich, *J. Phys.*, 1976, **37**, 1335–1345.
12 U. Seifert, K. Berndl and R. Lipowsky, *Phys. Rev. A: At., Mol., Opt. Phys.*, 1991, **44**, 1182–1202.
13 U. Seifert, L. Miao, H.-G. Döbereiner and M. Wortis, *The Structure and Conformation of Amphiphilic Membranes*, Springer-Verlag, 1992, pp. 93–96.
14 L. Miao, U. Seifert, M. Wortis and H.-G. Döbereiner, *Phys. Rev. E: Stat. Phys., Plasmas, Fluids, Relat. Interdiscip. Top.*, 1994, **49**, 5389–5407.
15 H.-G. Döbereiner, E. Evans, M. Kraus, U. Seifert and M. Wortis, *Phys. Rev. E: Stat. Phys., Plasmas, Fluids, Relat. Interdiscip. Top.*, 1997, **55**, 4458–4474.
16 S. Svetina and B. Žekš, *Eur. Biophys. J.*, 1989, **17**, 101–111.
17 S. Svetina and B. Žekš, *The Anatomical Record*, 2002, **268**, 215–225.
18 B. Fourcade, L. Miao, M. Rao, M. Wortis and R. Zia, *Phys. Rev. E: Stat. Phys., Plasmas, Fluids, Relat. Interdiscip. Top.*, 1994, **49**, 5276–5286.
19 J. Agudo-Canalejo and R. Lipowsky, *Soft Matter*, 2016, **12**, 8155–8166.
20 H.-G. Döbereiner, J. Käs, D. Noppl, I. Sprenger and E. Sackmann, *Biophys. J.*, 1993, **65**, 1396–1403.
21 T. Tanaka, R. Sano, Y. Yamashita and M. Yamazaki, *Langmuir*, 2004, **20**, 9526–9534.
22 T. Bhatia, S. Christ, J. Steinkühler, R. Dimova and R. Lipowsky, *Soft Matter*, 2020, 1246–1258.
23 J. Steinkühler, R. L. Knorr, T. Bhatia, S. Bartelt, S. Wegner, R. Dimova and R. Lipowsky, *Nat. Commun.*, 2020, **11**, 905.
24 P. Bassereau, R. Jin, T. Baumgart, M. Deserno, R. Dimova, V. A. Frolov, P. V. Baskirov, H. Grubmüller, R. Jahn, H. J. Risselada, L. Johannes, M. M. Kozlov, R. Lipowsky, T. J. Pucadyil, W. F. Zeno, J. C. Stachowiak, D. Stamou, A. Breuer, L. Lauritsen, C. Simon, C. Sykes, G. A. Voth and T. R. Weikl, *J. Phys. D: Appl. Phys.*, 2018, **51**, 343001.
25 A. Dajkovic and J. Lutkenhaus, *J. Mol. Microbiol. Biotechnol.*, 2006, **11**, 140–151.
26 K. Zieske and P. Schwille, *eLife*, 2014, **3**, e03949.
27 F. Brochard and J. Lennon, *J. Phys.*, 1975, **36**, 1035–1047.
28 H. Duwe, J. Käs and E. Sackmann, *J. Phys.*, 1990, **51**, 945–962.
29 B. Božič, G. Gomišček, V. Kralj-Iglič, S. Svetina and B. Žekš, *Eur. Biophys. J.*, 2002, **31**, 487–496.
30 J. Schindelin, I. Arganda-Carreras, E. Frise, V. Kaynig, M. Longair, T. Pietzsch, S. Preibisch, C. Rueden, S. Saalfeld, B. Schmid, J.-Y. Tinevez, D. J. White, V. Hartenstein, K. Eliceiri, P. Tomancak and A. Cardona, *Nat. Methods*, 2012, **9**, 676–682.
31 H. H. Ku, *J. Res. N.B.S. C Eng. Inst.*, 1966, **70**, 263–273.
32 P. K. Mogensen and A. N. Riseth, *J. Open Source Software*, 2018, **3**, 615.

Electronic Supplementary Information (ESI)

Active shape oscillations of giant vesicles with cyclic closure and opening of membrane necks

Simon Christ[a], Thomas Litschel[b], Petra Schwille[b], and Reinhard Lipowsky[*a]

[a] *Theory and Bio-Systems, Max Planck Institute of Colloids and Interfaces, Science Park Golm, 14424 Potsdam, Germany*
[b] *Cellular and Molecular Biophysics, Max Planck Institute of Biochemistry, 82152 Martinsried, Germany*

This Electronic Supplementary Information contains the supplementary sections S1, S2, and S3, the supplementary Figs. S1, S2, and S3 as well as the captions of Movie1 and Movie2.

In Section S1, we review the shape equations as originally derived in Ref. [1] and previously applied to the engulfment of nanoparticles in Ref. [2]. In addition, we describe the scheme that we used to regularize these shape equations close to the south and north pole of the vesicle, where the radial coordinate r vanishes. The shape is parametrized by the arc length s of the shape contour. The south pole is located at $s = 0$, the north pole at $s = s_1$ which defines the total arc length s_1. The regularization scheme is based on Taylor expansions for small arc length s around the south pole and for small deviations $\epsilon = s_1 - s$ around the north pole.

In Section S2, we introduce rescaled and dimensionless variables which involve two different length scales. The arc length s is rescaled by the total arc length s_1 which leads to the dimensionless arc length $\bar{s} \equiv s/s_1$ while all other quantities that have the dimension of a length or a curvature are rescaled using the the vesicle size R_{ve} as introduced in eqn (3) of the main text. We then express both the shape equations and the regularization scheme in terms of these rescaled variables, which now involve the dimensionless ratio $\mho \equiv s_1/R_{\mathrm{ve}}$ as an additional parameter. Finally, in Section S3, we describe the protocol for the numerical solution of the rescaled shape equations. This protocol combines the Taylor expansions at the two poles with the solution for intermediate values of the arc length. The details of our computational procedure, as described in Sections S2 and S3, have not been published before but should be useful for future studies.

S1   Shape equations for axisymmetric shapes

Contour parametrization and principal curvatures.   We consider an axisymmetric vesicle shape and denote the Cartesian coordinate along the rotational symmetry axis by z. The shape of such a vesicle is completely determined by its 1-dimensional shape contour as displayed in Fig. S1. We parametrize the contour line by its arc length s and choose the contour point with $s = 0$ to be the south pole of the vesicle. The shape
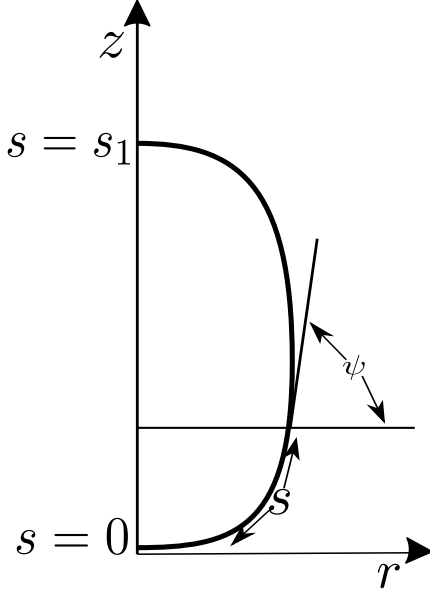
Figure S1: Contour line of an axisymmetric shape that is rotationally symmetric with respect to the z-axis. The shape of this line is parametrized in terms of the arc length s, the tilt angle $\psi = \psi(s)$, and the radial coordinate $r = r(s)$. The arc length s measures the distance along the contour line from the south pole with $s = 0$ and attains its maximum value $s = s_1$ at the north pole. The tilt angle ψ describes the angle between the radial coordinate r and the tangent to the contour. The two shape parameters $r(s)$ and $\psi(s)$ are related via $dr/ds = \cos(\psi)$, a constraint that is imposed by the Lagrange multiplier function $\gamma(s)$.

of the contour is then described by the tilt angle $= \psi(s)$ and the radial coordinate $r = r(s)$, both of which vary with s. [1] The two principal curvatures, C_1 and C_2, are given by

$$C_1 = \frac{d\psi}{ds} \equiv \dot{\psi} \quad \text{and} \quad C_2 = \frac{\sin\psi}{r} \tag{S1}$$

which implies the mean curvature

$$M = \frac{1}{2}(C_1 + C_2) = \frac{1}{2}\left(\dot{\psi} + \frac{\sin\psi}{r}\right). \tag{S2}$$

Here and below, a dot indicates the derivative with respect to the dimensionful arc length s.

Bending energy and shape energy. Using this contour parametrization, we now rewrite the bending energy E_{be} as given by eqn (1) in the main text which leads to

$$E_{\text{be}} = 2\pi\kappa \int_0^{s_1} ds\, \frac{r}{2}\left(\dot{\psi} + \frac{\sin\psi}{r} - 2m\right)^2. \tag{S3}$$

where s_1 denotes the total arc length of the contour line. The shape energy F in eqn (2) of the main text now becomes [1]

$$F = 2\pi\kappa \int_0^{s_1} ds\, L(\psi, \dot{\psi}, r, \dot{r}, \gamma) \tag{S4}$$

where we defined the 'Lagrange function'

$$L(\psi, \dot{\psi}, r, \dot{r}, \gamma) = L_{\text{be}}(\psi, \dot{\psi}, r) - \frac{\Delta P}{2\kappa}r^2 \sin\psi + \frac{\Sigma}{\kappa}r + \gamma(\dot{r} - \cos\psi) \tag{S5}$$

2

with the bending energy density

$$L_{\mathrm{be}}(\psi, \dot{\psi}, r) \equiv \frac{r}{2}\left(\dot{\psi} + \frac{\sin\psi}{r} - 2m\right)^2.$$ (S6)

To take into account that the radial coordinate r and the tilt angle ψ are not independent but related via $\dot{r} = \cos\psi$, the Lagrange multiplier function γ has been added to the shape energy F via the contribution

$$\Delta\mathcal{F} = 2\pi\kappa \int_0^{s_1} \mathrm{d}s\, \gamma(\dot{r} - \cos\psi)$$ (S7)

which implies that γ has the dimension of an inverse length or curvature.

Euler-Lagrange equations of shape energy. The shape equations are now obtained as the Euler-Lagrange equations of the shape energy in eqn (S4). Using the definition $C_1 = \dot{\psi}(s) \equiv u(s)$ for the contour curvature, one obtains the shape equations in the form [1]

$$\dot{r} = \cos\psi,$$ (S8)

$$\dot{\psi} = u,$$ (S9)

$$\dot{u} = \frac{\sin\psi\cos\psi}{r^2} - \frac{\cos\psi}{r}u - \frac{\Delta P}{2\kappa}r\cos\psi + \frac{\sin\psi}{r}\gamma,$$ (S10)

and

$$\dot{\gamma} = \frac{1}{2}(u - 2m)^2 - \frac{\sin^2\psi}{2r^2} - \frac{\Delta P}{\kappa}r\sin\psi + \frac{\Sigma}{\kappa},$$ (S11)

which represent four ordinary differential equations of first order. Note that these shape equations depend on the spontaneous curvature m as well as on the parameter combinations $\Delta P/\kappa$ and Σ/κ. Physically meaningful vesicle shapes correspond to smooth solutions of these differential equations which fulfill certain boundary conditions at the south pole with $s = 0$ and at the north pole with $s = s_1$.

Boundary conditions at south and north pole. The parametrization of the contour line as displayed in Fig. S1 implies the obvious boundary conditions

$$r(s = 0) = 0 \quad \text{and} \quad r(s = s_1) = 0$$ (S12)

for the radial coordinate $r(s)$ as well as

$$\psi(s = 0) = 0 \quad \text{and} \quad \psi(s = s_1) = \pi$$ (S13)

for the tilt angle $\psi(s)$. The boundary values of the contour curvature $C_1 = \dot{\psi} = u$ at the two poles are denoted by

$$u(s = 0) = U_0 \quad \text{and} \quad u(s = s_1) = U_1.$$ (S14)

3

Finally, using the fact that the 'Hamilton function'

$$H \equiv \dot{\psi}\frac{\partial L}{\partial \dot{\psi}} + \dot{r}\frac{\partial L}{\partial \dot{r}} - L \tag{S15}$$

is conserved along the contour, we obtain the additional boundary conditions [1]

$$\gamma(s=0) = 0 \quad \text{and} \quad \gamma(s=s_1) = 0 \tag{S16}$$

for the Lagrange multiplier function $\gamma(s)$.

Partial membrane area and vesicle volume. We now introduce the partial membrane area $\Delta A(s)$ via

$$\Delta A(s) \equiv 2\pi \int_0^s \mathrm{d}s'\, r(s') \tag{S17}$$

and the partial vesicle volume

$$\Delta V(s) \equiv \pi \int_0^s \mathrm{d}s'\, r^2(s')\,\sin\psi(s')\,. \tag{S18}$$

The partial area satisfies the evolution equation and boundary conditions as given by

$$\frac{\mathrm{d}\Delta A(s)}{\mathrm{d}s} = 2\pi r \quad \text{with} \quad \Delta A(0) = 0 \quad \text{and} \quad \Delta A(s_1) = A \tag{S19}$$

with the total membrane area A as introduced in the main text. Likewise, the partial volume satisfies

$$\frac{\mathrm{d}\Delta V(s)}{\mathrm{d}s} = \pi r^2 \sin\psi \quad \text{with} \quad \Delta V(0) = 0 \quad \text{and} \quad \Delta V(s_1) = V \tag{S20}$$

with the total vesicle volume V as in the main text.

Regularization of shape equations close to the poles. The shape eqns S10 and S11 for $\dot{u}$ and $\dot{\gamma}$ contain several terms proportional to $1/r$ and $1/r^2$. In particular, each of the first two terms on the right hand side of eqn S10 diverges individually close to the poles with $r = 0$. Even though these two singularities cancel, they do impede the numerical integration of the shape equations in the vicinity of the poles. To facilitate this integration, it is convenient to regularize the equations by using Taylor expansions for the parameter functions $r(s)$, $\psi(s)$, and $\gamma(s)$ around the two poles. [1, 2]

Regularization close to south pole. The expansion around the south pole with $s = 0$ corresponds to an expansion in powers of s and has the general form

$$r(s) = \sum_{k=1} \frac{r_k}{k!}s^k \quad \text{and} \quad \psi(s) = \sum_{k=1} \frac{\psi_k}{k!}s^k \tag{S21}$$

as well as

$$u(s) = \dot{\psi}(s) = \sum_{k=1} \frac{\psi_k}{(k-1)!}s^{k-1} \quad \text{and} \quad \gamma(s) = \sum_{k=1} \frac{\gamma_k}{k!}s^k\,. \tag{S22}$$

4

The boundary condition in eqn (S14) then implies that

$$u(s=0) = U_0 = \psi_1 \,. \tag{S23}$$

When we insert these expansions into the shape eqns S8 - S11 and equate the polynomial coefficients, the boundary conditions at the south pole imply that all coefficients of the Taylor series can depend on the contour curvature U_0 at this pole as well as on the three parameters m, $\Delta P/\kappa$, and Σ/κ. By matching the coefficients of the expansions on both sides of the shape equations, we find the Taylor coefficients

$$r_1 = 1 \,, \quad r_2 = r_4 = 0, \quad \text{and } r_3 = -U_0^2 \tag{S24}$$

for the radial coordinate $r(s)$ as well as the coefficients

$$\psi_1 = U_0 \,, \quad \psi_2 = \psi_4 = 0 \,, \tag{S25}$$

and

$$\psi_3 = \frac{3}{8}\left[-\frac{\Delta P}{\kappa} + 2U_0\gamma_1\right] = \frac{3}{8}\left[4mU_0(m-U_0) - \frac{\Delta P}{\kappa} + 2U_0\frac{\Sigma}{\kappa}\right] \tag{S26}$$

for the tilt angle $\psi(s)$. The Taylor coefficients for the Lagrange multiplier function γ have the form

$$\gamma_1 = -2U_0m + 2m^2 + \frac{\Sigma}{\kappa} = 2m(m-U_0) + \frac{\Sigma}{\kappa} \,, \quad \gamma_2 = 0 \tag{S27}$$

and

$$\gamma_3 = \frac{2}{3}(U_0 - 3m)\psi_3 - 2\frac{\Delta P}{\kappa}U_0 \tag{S28}$$

or

$$\gamma_3 = mU_0(m-U_0)(U_0 - 3m) - \frac{1}{4}(9U_0 - 3m)\frac{\Delta P}{\kappa} + \frac{1}{2}U_0(U_0 - 3m)\frac{\Sigma}{\kappa} \,. \tag{S29}$$

Likewise, the expansion of the partial area $\Delta A(s)$ and the partial volume $\Delta V(s)$ for small s leads to

$$\Delta A(s) \approx \pi s^2 - \frac{\pi}{12}U_0^2 s^4 \quad \text{and} \quad \Delta V(s) \approx \frac{\pi}{4}U_0 s^4 \tag{S30}$$

up to order s^4.

Regularization close to north pole. The expansion around the north pole with $s = s_1$ can be performed in an analogous manner using the expansion parameter

$$\epsilon \equiv s_1 - s \quad \text{with} \quad 0 \leq \epsilon \ll s_1 \,, \tag{S31}$$

which represents the arc length measured from the north pole. It will be convenient to define the functions

$$r^{\mathrm{no}}(\epsilon) \equiv r(s) \,, \quad \psi^{\mathrm{no}}(\epsilon) \equiv \pi - \psi(s) \quad \text{and} \quad \gamma^{\mathrm{no}}(\epsilon) \equiv \gamma(s) \quad \text{with} \quad s = s_1 - \epsilon \tag{S32}$$

5

as well as the contour curvature

$$u^{\mathrm{no}}(\epsilon) \equiv \frac{\mathrm{d}\psi^{\mathrm{no}}(\epsilon)}{\mathrm{d}\epsilon} = \frac{\mathrm{d}\psi(s)}{\mathrm{d}s} = u(s) \quad \text{with} \quad s = s_1 - \epsilon. \tag{S33}$$

The expansion around the north pole then has the form

$$r^{\mathrm{no}}(\epsilon) = \sum_{k=1} \frac{r_k^{\mathrm{no}}}{k!}\epsilon^k \quad \text{and} \quad \psi^{\mathrm{no}}(\epsilon) = \sum_{k=1} \frac{\psi_k^{\mathrm{no}}}{k!}\epsilon^k \tag{S34}$$

as well as

$$u^{\mathrm{no}}(\epsilon) = \frac{\mathrm{d}^{\mathrm{no}}}{\mathrm{d}\epsilon} = \sum_{k=1} \frac{\psi_k^{\mathrm{no}}}{(k-1)!}\epsilon^{k-1} \quad \text{and} \quad \gamma^{\mathrm{no}}(s) = \sum_{k=1} \frac{\gamma_k^{\mathrm{no}}}{k!}\epsilon^k. \tag{S35}$$

The boundary condition in eqn (S14) now implies that

$$u(s = s_1) = U_1 = u^{\mathrm{no}}(\epsilon = 0) = \psi_1^{\mathrm{no}}. \tag{S36}$$

By again equating coefficients on the two sides of the shape equations, we now find

$$r_1^{\mathrm{no}} = 1, \quad r_2^{\mathrm{no}} = r_4^{\mathrm{no}} = 0, \quad \text{and} \quad r_3^{\mathrm{no}} = -U_1^2, \tag{S37}$$

for the radial coordinate $r^{\mathrm{no}}(\epsilon)$ and the coefficients

$$\psi_1^{\mathrm{no}} = U_1, \qquad {}_2^{\mathrm{no}} = \psi_4^{\mathrm{no}} = 0, \tag{S38}$$

and

$$_3^{\mathrm{no}} = -\frac{3}{8}\left[\frac{\Delta P}{\kappa} + 2U_1\gamma_1^{\mathrm{no}}\right] = \frac{3}{8}\left[4mU_1(m - U_1) - \frac{\Delta P}{\kappa} + 2U_1\frac{\Sigma}{\kappa}\right] \tag{S39}$$

for the tilt angle $\psi^{\mathrm{no}}(\epsilon)$. The coefficients for the Lagrange multiplier function $\gamma^{\mathrm{no}}(\epsilon)$ are now given by

$$\gamma_1^{\mathrm{no}} = 2m(U_1 - m) - \frac{\Sigma}{\kappa}, \quad \gamma_2^{\mathrm{no}} = \gamma_4^{\mathrm{no}} = 0, \tag{S40}$$

and

$$\gamma_3^{\mathrm{no}} = \frac{2}{3}(3m - U_1)\psi_3^{\mathrm{no}} + 2\frac{\Delta P}{\kappa}U_1 \tag{S41}$$

or

$$\gamma_3^{\mathrm{no}} = mU_1(m - U_1)(3m - U_1) + \frac{1}{4}(9U_1 - 3m)\frac{\Delta P}{\kappa} + \frac{1}{2}U_1(3m - U_1)\frac{\Sigma}{\kappa}. \tag{S42}$$

Likewise, we define the partial area and volume functions close to the north pole according to

$$\Delta A^{\mathrm{no}}(\epsilon) \equiv \Delta A(s_1 - \epsilon) \quad \text{and} \quad \Delta V^{\mathrm{no}}(\epsilon) \equiv \Delta V(s_1 - \epsilon). \tag{S43}$$

These partial functions behave as

$$\Delta A^{\mathrm{no}}(\epsilon) \approx A - \pi\epsilon^2 + \frac{\pi}{12}U_1^2\epsilon^4 \quad \text{and} \quad \Delta V^{\mathrm{no}}(\epsilon) \approx V - \frac{\pi}{4}U_1\epsilon^4 \tag{S44}$$

for small $\epsilon = s_1 - s$ up to up to $\mathcal{O}(\epsilon^4)$ with the total membrane area A and the total vesicle volume V as in the main text.

6

S2 Rescaled parameters and shape equations

Rescaled parameters. Because the total arc length $s = s_1$ is an unknown, shape-dependent parameter, it is convenient to introduce the rescaled arc length

$$\bar{s} \equiv \frac{s}{s_1} \quad \text{which implies} \quad \bar{s}_1 = 1 \,. \tag{S45}$$

The other quantities that have the dimension of a length or curvature are rescaled by the vesicle size $R_{\mathrm{ve}} = \sqrt{A/(4\pi)}$ as defined in eqn (3) of the main text, which leads to the rescaled variables

$$\bar{r}(\bar{s}) \equiv \frac{r(s)}{R_{\mathrm{ve}}} \,, \quad \bar{u}(\bar{s}) \equiv R_{\mathrm{ve}} u(s) \,, \quad \text{and} \quad \bar{\gamma}(\bar{s}) \equiv R_{\mathrm{ve}} \gamma(s) \quad \text{with} \quad s = s_1 \bar{s} \,. \tag{S46}$$

For the tilt angle which is dimensionless, we use the analogous notation

$$\bar{\psi}(\bar{s}) \equiv \psi(s) \quad \text{with} \quad s = s_1 \bar{s} \,. \tag{S47}$$

The resulting shape equations for these rescaled variables then depend on another dimensionless parameter, the length scale ratio

$$\mho \equiv \frac{s_1}{R_{\mathrm{ve}}} \quad \text{with} \quad \mho \geq \pi \tag{S48}$$

where the lowest possible value $\mho = \pi$ corresponds to a spherical vesicle shape.

Rescaled shape equations. Indeed, in terms of the rescaled variables, the first three shape eqns (S8) - (S10) become

$$\frac{\mathrm{d}\bar{r}}{\mathrm{d}\bar{s}} = \mho \cos \bar{\psi} \,, \tag{S49}$$

$$\frac{\mathrm{d}\bar{\psi}}{\mathrm{d}\bar{s}} = \mho \bar{u} \,, \tag{S50}$$

and

$$\frac{\mathrm{d}\bar{u}}{\mathrm{d}\bar{s}} = \mho \left(\frac{\sin \bar{\psi} \cos \bar{\psi}}{\bar{r}^2} - \frac{\cos \bar{\psi}}{\bar{r}} \bar{u} - \frac{1}{2} \Delta \bar{P} \, \bar{r} \cos \bar{\psi} + \frac{\sin \bar{\psi}}{\bar{r}} \bar{\gamma} \right) \tag{S51}$$

with the rescaled pressure difference

$$\Delta \bar{P} \equiv \Delta P \frac{R_{\mathrm{ve}}^3}{\kappa} \,. \tag{S52}$$

Likewise, the fourth shape eqn (S11) becomes

$$\frac{\mathrm{d}\bar{\gamma}}{\mathrm{d}\bar{s}} = \mho \left[\frac{1}{2} (\bar{u} - 2\bar{m})^2 - \frac{\sin^2 \bar{\psi}}{2\bar{r}^2} - \Delta \bar{P} \, \bar{r} \sin \bar{\psi} + \bar{\Sigma} \right] \tag{S53}$$

with the rescaled membrane tension

$$\bar{\Sigma} \equiv \Sigma \frac{R_{\mathrm{ve}}^2}{\kappa} \,. \tag{S54}$$

7

Rescaled partial area and volume. The rescaled partial area $\Delta\bar{A}$ of the membrane is defined by

$$\Delta\bar{A}(\bar{s}) \equiv \frac{\Delta A(s)}{4\pi R_{\mathrm{ve}}^2} = \frac{\mho}{2}\int_0^{\bar{s}} \mathrm{d}\bar{s}'\, \bar{r}(\bar{s}') \tag{S55}$$

which implies the evolution equation

$$\frac{\mathrm{d}\Delta\bar{A}(\bar{s})}{\mathrm{d}\bar{s}} = \frac{\mho}{2}\,\bar{r}\,. \tag{S56}$$

On the other hand, the rescaled partial volume $\Delta\bar{V}$ is taken to be

$$\Delta\bar{V}(\bar{s}) \equiv \frac{\Delta V(s)}{\frac{4\pi}{3}R_{\mathrm{ve}}^3} = \frac{3\mho}{4}\int_0^{\bar{s}} \mathrm{d}\bar{s}'\, \bar{r}^2(\bar{s}')\,\sin\bar{\psi}(\bar{s}') \tag{S57}$$

and satisfies the evolution equation

$$\frac{\mathrm{d}\Delta\bar{V}(\bar{s})}{\mathrm{d}\bar{s}} = \frac{3\mho}{4}\,\bar{r}^2\sin\bar{\psi}\,. \tag{S58}$$

Boundary conditions for rescaled variables. The boundary conditions for the rescaled shape functions are

$$\bar{r}(\bar{s}=0) = 0 \quad \text{and} \quad \bar{r}(\bar{s}=1) = 0\,, \tag{S59}$$

$$\bar{\psi}(\bar{s}=0) = 0 \quad \text{and} \quad \bar{\psi}(\bar{s}=1) = \pi\,, \tag{S60}$$

$$\bar{u}(\bar{s}=0) = \bar{U}_0 \quad \text{and} \quad \bar{u}(s=s_1) = \bar{U}_1 \tag{S61}$$

with the rescaled contour curvatures

$$\bar{U}_0 \equiv U_0 R_{\mathrm{ve}} \quad \text{and} \quad \bar{U}_1 \equiv U_1 R_{\mathrm{ve}} \tag{S62}$$

at the two poles as well as

$$\bar{\gamma}(\bar{s}=0) = 0 \quad \text{and} \quad \bar{\gamma}(\bar{s}=1) = 0\,. \tag{S63}$$

In addition, the boundary values for the rescaled membane area are

$$\Delta\bar{A}(\bar{s}=0) = 0 \quad \text{and} \quad \Delta\bar{A}(\bar{s}=1) = 1\,, \tag{S64}$$

those for the rescaled vesicle volume are

$$\Delta\bar{V}(\bar{s}=0) = 0 \quad \text{and} \quad \Delta\bar{V}(\bar{s}=1) = v \tag{S65}$$

with the dimensionless volume-to-area ratio v as defined in eqn (4) of the main text.

Dimensionless parameters. The shape equations and boundary conditions for the rescaled variables as described in the previous paragraphs depend on seven dimensionless parameters: the shape parameters v and $\bar{m}$, the contour curvatures $\bar{U}_0$ and $\bar{U}_1$ at the two poles, the pressure $\Delta\bar{P} = \Delta P R_{\mathrm{ve}}^3/\kappa$, the tension $\bar{\Sigma} = \Sigma R_{\mathrm{ve}}^2/\kappa$, and the length scale ratio $\mho = s_1/R_{\mathrm{ve}}$. When we consider certain fixed values of the shape parameters v and $\bar{m}$, see main text, the different branches of solutions then correspond to different values of the five parameters $\bar{U}_0$, $\bar{U}_1$, $\Delta\bar{P}$, $\bar{\Sigma}$, and $\mho$. In order to construct such solutions in practise, we need to deal with the numerical difficulties close to to two poles and to regularize the rescaled equations as well.

8

Regularization of rescaled equations close to south pole. Close to the south pole, the expansion of the rescaled radial coordinate $\bar{r}$ in powers of $\bar{s}$ leads to

$$\bar{r} = \bar{r}_1 \bar{s} + \frac{1}{6}\bar{r}_3\,\bar{s}^3 + \mathcal{O}(\bar{s}^5) \tag{S66}$$

with the Taylor coefficients

$$\bar{r}_1 = \mho r_1 = \mho \quad \text{and} \quad \bar{r}_3 = \mho^3 r_3 = -\mho^3 U_0^2\,. \tag{S67}$$

Likewise, the tilt angle ψ becomes

$$\bar{\psi}(\bar{s}) = \bar{\psi}_1 \bar{s} + \frac{1}{6}\bar{\psi}_3\,\bar{s}^3 + \mathcal{O}(\bar{s}^5) \tag{S68}$$

with the coefficients

$$\bar{\psi}_1 = \psi_1 s_1 = U_0 s_1 = \mho \bar{U}_0 \quad \text{and} \quad \bar{\psi}_3 = \psi_3 s_1^3 \tag{S69}$$

or

$$\bar{\psi}_3 = \frac{3\mho^3}{8}\left[4\bar{m}\bar{U}_0(\bar{m} - \bar{U}_0) - \Delta\bar{P} + 2\bar{U}_0\bar{\Sigma}\right] \tag{S70}$$

where we used the expressions for ψ_1 and ψ_3 in eqns (S25) and (S26) as well as the rescaled pressure and tension in eqns (S52) and (S54). It then follows that the Taylor expansion of the rescaled contour curvature

$$\bar{u}(\bar{s}) = R_{\mathrm{ve}}u(s) = R_{\mathrm{ve}}\frac{\mathrm{d}\psi(s)}{\mathrm{d}s} = \frac{1}{\mho}\frac{\mathrm{d}\bar{\psi}(\bar{s})}{\mathrm{d}\bar{s}} \tag{S71}$$

has the form

$$\bar{u}(\bar{s}) = \bar{U}_0 + \frac{1}{2}\frac{\bar{\psi}_3}{\mho}\,\bar{s}^2 + \mathcal{O}(\bar{s}^4)\,. \tag{S72}$$

In addition, the expansion of the rescaled Lagrange multiplier function $\bar{\gamma}$ is given by

$$\bar{\gamma}(\bar{s}) = R_{\mathrm{ve}}\gamma(s) = \bar{\gamma}_1 \bar{s} + \frac{1}{6}\bar{\gamma}_3\,\bar{s}^3 + \mathcal{O}(\bar{s}^5) \tag{S73}$$

with the coefficients

$$\bar{\gamma}_1 = R_{\mathrm{ve}}s_1\gamma_1 = \mho\left[2\bar{m}(\bar{m} - \bar{U}_0) + \bar{\Sigma}\right] \tag{S74}$$

and

$$\bar{\gamma}_3 = R_{\mathrm{ve}}s_1^3\gamma_3 \tag{S75}$$

or

$$\bar{\gamma}_3 = \mho^3\left[\bar{m}\bar{U}_0(\bar{m} - \bar{U}_0)(\bar{U}_0 - 3\bar{m}) - \frac{1}{4}(9\bar{U}_0 - 3\bar{m})\Delta\bar{P} + \frac{1}{2}\bar{U}_0(\bar{U}_0 - 3\bar{m})\bar{\Sigma}\right] \tag{S76}$$

where eqn (S29) for γ_3 has been used.

Close to the south pole, the rescaled partial area $\Delta\bar{A}$ and the rescaled partial volume $\Delta\bar{V}$ as defined in eqns (S55) and (S57) behave as

$$\Delta\bar{A}(\bar{s}) \approx \frac{\mho^2}{4}\,\bar{s}^2 - \frac{\mho^4}{48}\bar{s}^4 \quad \text{and} \quad \Delta\bar{V}(\bar{s}) \approx \frac{3\mho^4}{16}\bar{s}^4 \tag{S77}$$

for small $\bar{s}$ up to $\mathcal{O}(\bar{s}^4)$.

9

Regularization of rescaled equations close to north pole. Close to the north pole, we use the dimensionless expansion parameter

$$\bar{\epsilon} \equiv \frac{\epsilon}{s_1} = \frac{s_1 - s}{s_1} = 1 - \bar{s} \quad \text{with} \quad 0 \leq \bar{\epsilon} \ll 1, \tag{S78}$$

which measures the arc length from the north pole in units of s_1. We now introduce the functions

$$\bar{r}^{\mathrm{no}}(\bar{\epsilon}) \equiv \bar{r}(\bar{s}) = \frac{r(s)}{R_{\mathrm{ve}}} = \frac{r^{\mathrm{no}}(\epsilon)}{R_{\mathrm{ve}}}, \tag{S79}$$

$$\bar{\psi}^{\mathrm{no}}(\bar{\epsilon}) = \pi - \bar{\psi}(\bar{s}) = \pi - \psi(s) = \psi^{\mathrm{no}}(\epsilon), \tag{S80}$$

$$\bar{u}^{\mathrm{no}}(\bar{\epsilon}) \equiv \bar{u}(\bar{s}) = R_{\mathrm{ve}} u(s) = R_{\mathrm{ve}} u^{\mathrm{no}}(\epsilon) \tag{S81}$$

and

$$\bar{\gamma}^{\mathrm{no}}(\bar{\epsilon}) = \bar{\gamma}(\bar{s}) = R_{\mathrm{ve}} \gamma(s) = R_{\mathrm{ve}} \gamma^{\mathrm{no}}(\epsilon) \tag{S82}$$

where the different arc length are related, according to their definitions, via

$$\bar{s} = 1 - \bar{\epsilon}, \quad s = s_1 \bar{s} = s_1(1 - \bar{\epsilon}), \quad \text{and} \quad \epsilon = s_1 \bar{\epsilon}.$$

The expansion of the rescaled radial coordinate $\bar{r}^{\mathrm{no}}$ in powers of $\bar{\epsilon}$ is then given by

$$\bar{r}^{\mathrm{no}}(\bar{\epsilon}) = \bar{r}_1^{\mathrm{no}} \bar{\epsilon} + \frac{1}{6} \bar{r}_3^{\mathrm{no}} \bar{\epsilon}^3 + \mathcal{O}(\bar{\epsilon}^5) \tag{S83}$$

with the coefficients

$$\bar{r}_1^{\mathrm{no}} = \mho r_1^{\mathrm{no}} = \mho \quad \text{and} \quad \bar{r}_3^{\mathrm{no}} = \frac{s_1^3}{R_{\mathrm{ve}}} r_3^{\mathrm{no}} = -\mho^3 \bar{U}_1^2. \tag{S84}$$

The expansion of the tilt angle $\bar{\psi}^{\mathrm{no}} = \pi - \bar{\psi}$ has the form

$$\bar{\psi}^{\mathrm{no}}(\bar{\epsilon}) = \bar{\psi}_1^{\mathrm{no}} \bar{\epsilon} + \frac{1}{6} \bar{\psi}_3^{\mathrm{no}} \bar{\epsilon}^3 + \mathcal{O}(\bar{\epsilon}^5) \tag{S85}$$

with the coefficients

$$\bar{\psi}_1^{\mathrm{no}} = \psi_1^{\mathrm{no}} s_1 = U_1 s_1 = \mho \bar{U}_1 \quad \text{and} \quad \bar{\psi}_3^{\mathrm{no}} = \psi_3^{\mathrm{no}} s_1^3 \tag{S86}$$

or

$$\bar{\psi}_3^{\mathrm{no}} = \frac{3\mho^3}{8} \left[4\bar{m} \bar{U}_1(\bar{m} - \bar{U}_1) - \Delta\bar{P} + 2\bar{U}_1 \bar{\Sigma} \right] \tag{S87}$$

where eqns (S38) and (S39) for ψ_1^{no} and ψ_3^{no} have been used. It then follows that the rescaled contour curvature

$$\bar{u}^{\mathrm{no}}(\bar{\epsilon}) = R_{\mathrm{ve}} u^{\mathrm{no}}(\epsilon) = R_{\mathrm{ve}} \frac{\mathrm{d}\psi^{\mathrm{no}}(\epsilon)}{\mathrm{d}\epsilon} = \frac{1}{\mho} \frac{\mathrm{d}\psi^{\mathrm{no}}(\bar{\epsilon})}{\mathrm{d}\bar{\epsilon}} \tag{S88}$$

has the expansion

$$\bar{u}^{\mathrm{no}}(\bar{\epsilon}) = \bar{U}_1 + \frac{1}{2} \frac{\bar{\psi}_3^{\mathrm{no}}}{\mho} \bar{s}^2 + \mathcal{O}(\bar{\epsilon}^4). \tag{S89}$$

10

Furthermore, the expansion of the Lagrange multiplier function $\bar{\gamma}^{\mathrm{no}}$ is found to be

$$\bar{\gamma}^{\mathrm{no}}(\bar{\epsilon}) = R_{\mathrm{ve}}\gamma^{\mathrm{no}}(\epsilon) = \bar{\gamma}_1^{\mathrm{no}}\bar{\epsilon} + \frac{1}{6}\bar{\gamma}_3^{\mathrm{no}}\bar{\epsilon}^3 + \mathcal{O}(\bar{\epsilon}^5) \tag{S90}$$

with the coefficients

$$\bar{\gamma}_1^{\mathrm{no}} = R_{\mathrm{ve}}s_1\gamma_1^{\mathrm{no}} = \mho\left[2\bar{m}(\bar{U}_1 - \bar{m}) - \bar{\Sigma}\right] \tag{S91}$$

and

$$\bar{\gamma}_3^{\mathrm{no}} = R_{\mathrm{ve}}s_1^3\gamma_3^{\mathrm{no}} \tag{S92}$$

or

$$\bar{\gamma}_3^{\mathrm{no}} = \mho^3\left[\bar{m}\bar{U}_1(\bar{m} - \bar{U}_1)(3\bar{m} - \bar{U}_1) + \frac{1}{4}(9\bar{U}_1 - 3\bar{m})\Delta\bar{P} + \frac{1}{2}\bar{U}_1(3\bar{m} - \bar{U}_1)\bar{\Sigma}.\right] \tag{S93}$$

Close to the north pole, the rescaled partial area behaves as

$$\Delta\bar{A}^{\mathrm{no}}(\bar{\epsilon}) \equiv \frac{\Delta A^{\mathrm{no}}(\epsilon)}{4\pi R_{\mathrm{ve}}^2} = 1 - \frac{1}{4}\mho^2\bar{\epsilon}^2 + \frac{1}{48}\mho^4\bar{U}_1^2\bar{\epsilon}^4 + \mathcal{O}(\bar{\epsilon}^6) \tag{S94}$$

and the rescaled partial volume as

$$\Delta\bar{V}^{\mathrm{no}}(\bar{\epsilon}) \equiv \frac{\Delta V^{\mathrm{no}}(\epsilon)}{\frac{4\pi}{3}R_{\mathrm{ve}}^3} = v - \frac{1}{16}\mho^4\bar{U}_1\bar{\epsilon}^4 + \mathcal{O}(\bar{\epsilon}^6) \tag{S95}$$

where the relationships in eqn (S44) have been used.

S3   Protocol for computation of axisymmetric shapes

To obtain a specific axisymmetric vesicle shape, we solve the rescaled shape equations using the following protocol that consists of four steps.

First, to avoid the numerical instabilities at the south pole with $\bar{s} = 0$, we start from the Taylor expansions close to this pole and choose a certain trial set of the five parameters $\bar{m}$, $\bar{U}_0$, $\Delta\bar{P}$, $\bar{\Sigma}$, and $\mho$ that enter these expansions. We use the Taylor series for $\bar{r}(\bar{s})$ as given by eqn (S66) and calculate the $\bar{r}$-values for $\bar{s} = \bar{s}_n = n\Delta\bar{s}$ with positive integer n and increment $\Delta\bar{s} = 10^{-3}$ until we reach the smallest value $n = n*$ for which $\bar{r}(\bar{s}_{n*}) > 10^{-2}$. The corresponding arc length $\bar{s}_{n*}$ is taken to be the new initial value

$$\bar{s}_{\mathrm{ini}} \equiv \bar{s}_{n*} > 0 \quad \text{of the arc length.} \tag{S96}$$

We then apply the Taylor expansions of all six shape functions $\bar{r}(\bar{s})$, $\bar{\psi}(\bar{s})$, $\bar{u}(\bar{s})$, $\bar{\gamma}(\bar{s})$, $\Delta\bar{A}(\bar{s})$, and $\Delta\bar{V}(\bar{s})$ for small $\bar{s}$ to calculate the values of these functions at the initial arc length $\bar{s} = \bar{s}_{\mathrm{ini}}$. These expansions are provided by eqn (S66) for the radial coordinate $\bar{r}(\bar{s})$, by eqn (S68) for the tilt angle $\bar{\psi}(\bar{s})$, by eqn (S72) for the contour curvature $\bar{u}(\bar{s})$, by eqn (S73) for the Lagrange multiplier function $\bar{\gamma}(\bar{s})$, and by eqn (S77) for the partial membrane area $\Delta\bar{A}(\bar{s})$ and the partial vesicle volume $\Delta\bar{V}(\bar{s})$. In this way, we determine

11

the six initial values $\bar{r}(\bar{s}_{\text{ini}})$, $\bar{\psi}(\bar{s}_{\text{ini}})$, $\bar{u}(\bar{s}_{\text{ini}})$, $\bar{\gamma}(\bar{s}_{\text{ini}})$, $\Delta\bar{A}(\bar{s}_{\text{ini}})$, and $\Delta\bar{V}(\bar{s}_{\text{ini}})$ which are located close to the south pole.

Second, for the given choice of the five parameters $\bar{m}$, $\bar{U}_0$, $\Delta\bar{P}$, $\bar{\Sigma}$, and $\eth$, we start from the six initial values and integrate the six shape eqns (S49), (S50), (S51), (S53), (S56), and (S58) numerically up to the final value

$$\bar{s}_{\text{fin}} = 1 - \bar{s}_{\text{ini}} \quad \text{of the arc length.} \tag{S97}$$

For this numerical integration, we use the same fixed integration-step $\Delta\bar{s} = 10^{-3}$ and the Julia package DifferentialEquations.jl [3] with the Rodas4 algorithm, corresponding to an implicit Runge-Kutta procedure. As a result of this computation, we obtain the values of the six shape functions at $\bar{s} = \bar{s}_{\text{fin}}$ close to the north pole, i.e., the numerical values of $\bar{r}(\bar{s}_{\text{fin}})$, $\bar{\psi}(\bar{s}_{\text{fin}})$, $\bar{u}(\bar{s}_{\text{fin}})$, $\bar{\gamma}(\bar{s}_{\text{fin}})$, $\Delta\bar{A}(\bar{s}_{\text{fin}})$, and $\Delta\bar{V}(\bar{s}_{\text{fin}})$.

Third, we calculate the values of the shape functions at $\bar{s} = \bar{s}_{\text{fin}}$ by using the Taylor expansions of these functions in powers of $\bar{\epsilon} = 1 - \bar{s}$, with $\bar{\epsilon} = 0$ at the north pole. The latter expansions are provided by eqn (S83) for the radial coordinate $\bar{r}^{\text{no}}(\bar{\epsilon})$, by eqn (S85) for the tilt angle $\bar{\psi}^{\text{no}}(\bar{\epsilon})$, by eqn (S89) for the contour curvature $\bar{u}^{\text{no}}(\bar{\epsilon})$, by eqn (S90) for the Lagrange multiplier function $\bar{\gamma}^{\text{no}}(\bar{\epsilon})$, by eqn (S94) for the partial membrane area $\Delta\bar{A}^{\text{no}}(\bar{\epsilon})$, and by eqn (S95) for the partial vesicle volume $\Delta\bar{V}^{\text{no}}(\bar{\epsilon})$. These expansions close to the north pole depend on the six parameters $\bar{m}$, $\bar{U}_1$, $\Delta\bar{P}$, $\bar{\Sigma}$, $\eth$, and v.

Finally, we compare the numerical values of the shape functions obtained via the numerical integration for $\bar{s} = \bar{s}_{\text{fin}}$ with those obtained from the expansion in powers of $\bar{\epsilon} = 1 - \bar{s}$ for $\bar{\epsilon}_{\text{fin}} = 1 - \bar{s}_{\text{fin}}$. The six differences as given by $\bar{r}(\bar{s}_{\text{fin}}) - \bar{r}^{\text{no}}(\bar{\epsilon}_{\text{fin}})$ ... $\Delta\bar{V}(\bar{\epsilon}_{\text{fin}}) - \Delta\bar{V}^{\text{no}}(\bar{\epsilon}_{\text{fin}})$ provide the residuals for finding the five parameters $\bar{U}_0$, $\bar{U}_1$, $\Delta\bar{P}$, $\bar{\Sigma}$, and $\eth$ for fixed values of the volume-to-area v and spontaneous curvature $\bar{m}$. The adjustment of the parameters was done with the non-linear trust-region root-finding algorithm provided by the Julia package NLsolve.jl [4].

References

[1] Udo Seifert, Karin Berndl, and Reinhard Lipowsky. Shape transformations of vesicles: Phase diagram for spontaneous- curvature and bilayer-coupling models. *Phys. Rev. A*, 44(2):1182–1202, 1991.

[2] Jaime Agudo-Canalejo and Reinhard Lipowsky. Stabilization of membrane necks by adhesive particles, substrate surfaces, and constriction forces. *Soft Matter*, 12(39):8155–8166, 2016.

[3] Christopher Rackauckas and Qing Nie. DifferentialEquations.jl – A Performant and Feature-Rich Ecosystem for Solving Differential Equations in Julia. *J. Open Res. Softw.*, 2017.

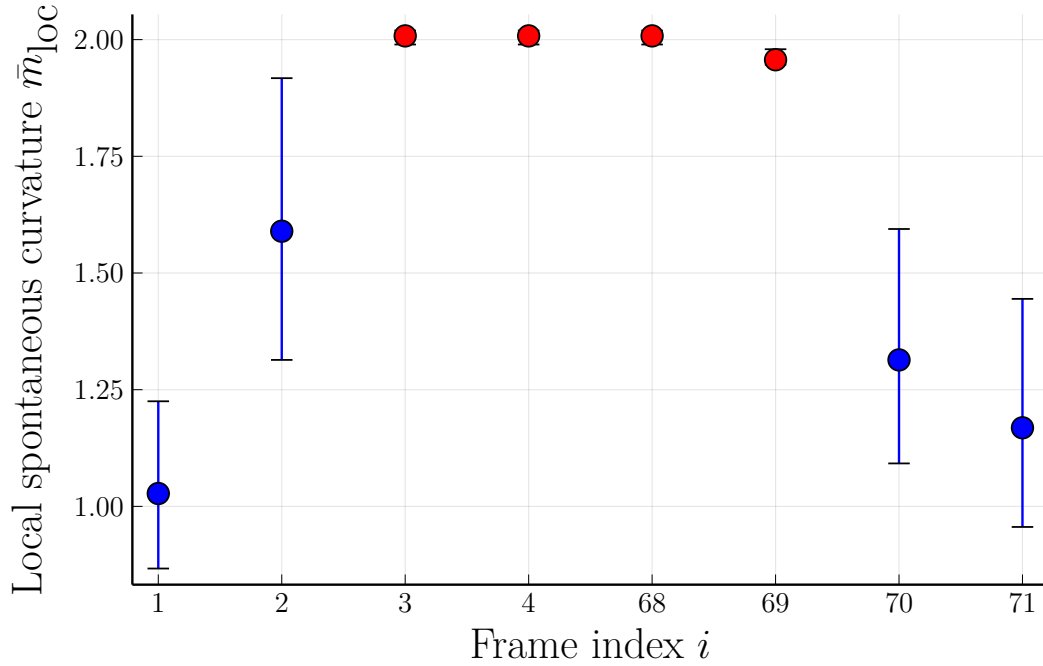[4] Patrick Kofod Mogensen and Spencer Lyon. JuliaNLSolvers/NLsolve.jl: Zenodo release. may 2019.

Figure S2: Rescaled local spontaneous curvature $\bar{m}_{\mathrm{loc}}$ versus frame index i. The frame i was taken at time $t = (i-1) \times 7.61\,\mathrm{s}$ after the initial frame with index $i = 1$. The blue data points correspond to up-down symmetric dumbbell shapes, the red data points to asymmetric ones. The symmetry-breaking transformation in Fig. 1 corresponds to $i = 1, 2$, and 3, the symmetry-restoring transformation in Fig. 2 to $i = 68, 69$, and 70. The image $i = 4$ displays a slightly distorted version of $i = 3$ and is thus taken to have the same $\bar{m}_{\mathrm{loc}}$-value as $i = 3$. The image $i = 71$ displays a symmetric dumbbell with an increased neck radius compared to $i = 70$. This increased radius implies the local spontaneous curvature $\bar{m}_{\mathrm{loc}} = 1.17$. The combined sequence of all eight images represents one complete shape oscillation with an average time period of $55.9\,\mathrm{s}$. The error bars are obtained as in Fig. 9.
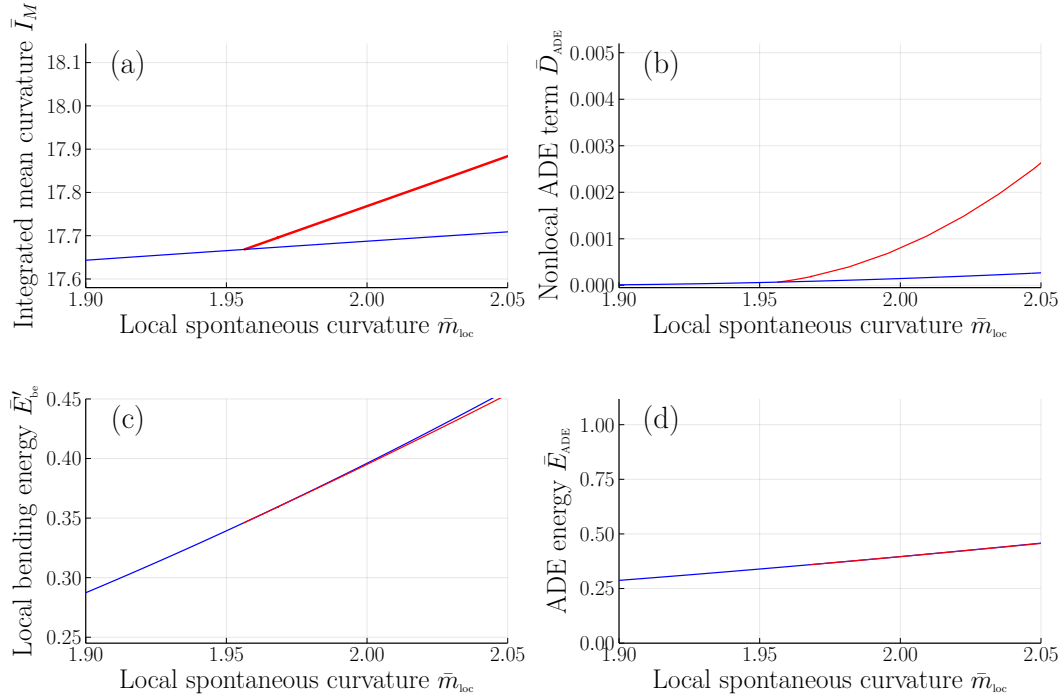
13

Figure S3: Integrated mean curvature and different energy contributions as functions of the local spontaneous curvature $\bar{m}_{\mathrm{loc}}$ for rigidity ratio $\kappa_\Delta/\kappa = 2$. The symmetric and asymmetric branches are displayed as blue and red lines, respectively: (a) Integrated mean curvature $\bar{I}_M$ as in eqn (16); (b) Nonlocal area-difference-elasticity term $\bar{D}_{\mathrm{ADE}}$ as in eqn (26); (c) Local bending energy $\bar{E}'_{\mathrm{be}}$ as in eqn (25); and (d) ADE energy $\bar{E}_{\mathrm{ADE}}$ which is equal to the sum of the local and nonlocal terms in panels b and c. As in Fig. 11, the energy of the asymmetric branch is located below the energy of the symmetric one. All quantities were computed for volume-to-area ratio $v = 0.670$ and reference value $\bar{I}_{M,0} = 17.63$ of the integrated mean curvature.

14

Movie captions

Movie1. Active shape oscillations of a single GUV: The movie consists of 200 snapshots or frames, each of which displays a different image of the same GUV as obtained by differential interference contrast (DIC) microscopy. The movie was taken with the pre-defined time interval $\Delta t = 7.61\,$s between successive frames and displays the whole series of 200 frames within 20 s, corresponding to about 1500 s or 25 min real time. Apart from a few frames at the beginning and at the end, the movie consists of 26 complete oscillation cycles with an average period of 55.9 s. This movie corresponds to the DIC part of Video_S6 in `https://onlinelibrary.wiley.com/action/downloadSupplement?doi=10.1002%2Fanie.201808750&file=anie201808750-sup-0001-Video_S6.mp4` which is a Supplement to Ref. [4] of the main text.

Movie2. Up-down symmetric and asymmetric dumbbells for fixed volume-to-area ratio $v = 0.670$ and variable spontaneous curvature $\bar{m}$: The left panel displays the up-down symmetric dumbbells (blue) for $0.99 \leq \bar{m} \leq 2.27$, the right panel the up-down asymmetric ones (red), which are present in the restricted $\bar{m}$-range with $1.89 \leq \bar{m} < 1.94$. For $\bar{m} = 1.94$, the branch of asymmetric dumbbells has merged with the branch of symmetric ones. Both types of dumbbells are obtained as smooth solutions of the shape equations for axisymmetric shapes. The rotational symmetry axis is parallel to the z-axis as indicated by the broken vertical lines. The second Cartesian coordinate is taken to be the x-axis.

15

4. Manipulation of GUVs through microfabricated structures for reconstitution studies

4.1. Introduction and context

As the previous two chapters demonstrate, giant unilamellar vesicles are a promising tool for in vitro reconstitution studies requiring model membranes. Encapsulation within GUVs offers a number of cell-like features over other popular membrane reconstitution approaches like adding protein to the outside of GUVs, encapsulation within lipid-lined water-in-oil droplets or reconstitution on SLBs. However, there are still many fundamental physical properties of cells that GUVs lack. Of course, it is central to the concept of in vitro reconstitution and bottom-up biology to use simple, minimal systems that are relative easy to understand and study compared to actual biological cells; however, there are some desirable properties that GUVs by themselves cannot offer. One such feature is control over the confinement geometry. Vesicles have an intrinsic spherical shape. This geometrical shape with an extreme degree of symmetry can only be found as an outer barrier in few biological cells. In principle, vesicle shape can be affected by manipulating their volume to membrane-ratio, which can, for example, result in flatter, oblate shapes, or dumbbell shapes (see chapter 2). However, shape control via this parameter can be difficult to achieve in experiments and also affects other properties, including membrane tension. Depending on the content, these shapes can be unstable, and, for example, will clearly be affected when encapsulating cytoskeletal filaments.

'Custom shaped' geometries were previously achieved by confining biological reactions in membrane-less microfabricated compartments,[56-60] or microfabricated compartments lined with (but not fully enclosed within) membranes.[50,61] Studies using these methods have offered valuable insights into how geometrical parameters affect biological self-organization and pattern formation. In addition to using bottom-up approaches with purified proteins, these effects have also been studies with live cells within microfabricated structures.[62-64]

One of the common aims of chapter 2 and 3 was the study of processes related to cytokinesis and the long term aim of reconstituting cell division with model membranes. We assume that this requires GUVs as model membrane systems, as none of the other above mentioned systems provide a deformable

membrane or any kind of compartments that could be divided by a protein-based cell division machinery. However, the results from the work in chapter 2 indicate that the division of a spherical compartment is a difficult task. We show (at least in one instance), that a contractile ring-like structure is prone to just 'slip' and contract into a cluster, rather than actually divide the vesicle. This effect has also be shown with live cells lacking a cell wall,[65] as discussed in Publication 2. We speculate that the outcome could be different for an elongated vesicle, which would provide a smaller chance for a ring to slip, and providing more 'excess' membrane due to the higher membrane-to-volume area. Likewise, the Min protein system (chapter 3) demonstrate the importance of the confinement geometry, as the Min system is a prime example of a geometry sensing biological system. While we do occasionally observe pole-to-pole oscillations (which are required for the positioning of the divisome) in spherical vesicles (Publication 3), previous studies have shown that these are far more likely to occur in elongated, rod-like confinement, more similar to the actually shape of E.coli.[47,50]

In this chapter I present two studies I was able to contribute to, which were tasked with achieving a common goal: the deformation of GUVs into geometries different from a spherical shape. The two studies use quite different approaches, however. The first publication (Publication 5) uses 3D-printed hydrogel structures which are 'top-loaded' with GUVs. By changing the pH, these structures start swelling and therefore deform the vesicles. The second publication (Publication 6) uses relatively popular soft-lithography methods to fabricated devices with flow-channels. GUVs are flushed through these channels and trapped in funnel-like structures within the channels. Subsequently the vesicles are osmotically deflated, therefore the vesicles are pushed further into the 'funnel' through the surrounding flow. push them further into the 'funnel' of the surrounding aqueous media then pushes the vesicles further into the 'funnel' thereby deforming them.

In the first study of this chapter, we test our vesicle-deforming device on MinDE containing vesicles (see chapter 3). While changes in oscillation modes (e.g. into pole-to-pole oscillations, as expected from the papers discussed above[47,50]) were less noticeable and frequent than expected, the most obvious change upon vesicle 'squeezing' was a change in oscillation frequency, most likely caused by an increase in membrane tension. Likewise, we used Min-encapsulating vesicles within the device presented in the second study in this chapter (Publication 6).[66] This however resulted in even less noticeable changes in the oscillatory behavior. Here we neither observed

changes in oscillation mode nor in oscillation frequency. The discrepancy regarding the (non-existent) frequency change can most likely be explained by the fact that here, vesicle membrane tension is not significantly altered through the vesicle deformation process. The forces exerted by this device on the vesicles are much weaker; therefore, in order to cause deformations, the vesicles had to first be deflated. Due to these rather unspectacular observations, in the case of this second study, the Min protein experiments did not end up in the final peer-reviewed publication. It can, however, still be found in the published preprint.[66] The main focus of the final publication is on the bacterial cytoskeletal protein FtsZ which plays a major role in E.coli cell division alongside the Min protein system (see Publication 1).

4.2. Microfluidic technologies

Microfabrication has long found a home in biosciences, particularly in cell biology and biophysics, but also biochemistry and molecular biology.[67] Microfabrication devices are also particularly popular in medical sciences and for medical applications where scaling down sample sizes to a few nano- or picoliters allows for high throughput screening. Typically these devices contain micrometer sized-channels or chambers that enclose small amounts of liquid, making them subject to the field of 'microfluidics'.

In many ways, the development of soft lithography methods with the silicone polydimethylsiloxane (PDMS) is central to the history and current state of the fabrication of microfluidic devices.[68] While there were early efforts with other materials to use small volumes and flow channels for medical and scientific research, PDMS soft lithography methods allowed the breakthrough of such approaches in an academic setting.[68]

Interestingly, despite being so central to the field, PDMS is typically not used for the commercial production of microfluidic devices, where materials like glass and thermoplastics are common.[69] Among problems in scalability, this is due to a number of properties of PDMS that result in a general lack of durability of the material. It is, however, some of these same properties that allow for its use in lithography methods, which typically consist of: master creation (often with photolithography), molding in PDMS (soft lithography) and sealing. Soft lithography with PDMS requires little and relatively inexpensive equipment, little technical expertise, and allows for the rapid creation of new designs. This makes PDMS an ideal material for prototyping and attractive for research related work. The overwhelming majority of

microfluidic devices fabricated for academic research is fabricated from PDMS through soft lithography methods.[67]

As we discuss in the literature review in chapter 1, PDMS microfluidic devices are even used for generating vesicle production, where they offer some advantages over more traditional methods, such as enabling the formation of monodisperse vesicles, i.e. producing vesicles with consistent sizes. A number of microfluidic devices for the manipulation of GUVs were introduced by Robinson and Dittrich et al. over the past ten years. In P6 (the second publication in the chapter), we used a microfluidic device based on these earlier designs, but that further allowed us to deform the GUV into a shape desired for the investigation of cytoskeletal proteins and potentially for further investigation into the division of GUVs. This device is a microfluidic flow chip in it's typical sense, which contains channels through which an aqueous medium (which contains the GUVs) is flushed.

In recent years, 3D printing technologies have become more and more advanced and have great potential for applications on the microscale, including for cell-biology or bottom-up biology.[70,71] 3D printing offers several advantages over typical soft lithography techniques, which have some restriction regarding the fabrication of "3-dimensional" designs.[72] Currently, disadvantages still include the choice of materials and the high cost of the required equipment for high-resolution printing (two-photon-printing). Generally, open microfluidic devices are easier to print, but sealed, continuous flow microfluidic devices can also be printed while still exploiting the advantages of 3D printing technology.[71] In Publication 5 we apply 3D-printing technology to fabricate a top-loaded (i.e. open) device for the manipulation of GUVs.

4.3. Publication 5: Shaping giant membrane vesicles in 3D-printed protein hydrogel cages

Research paper published in Small.[73]

Jia H, **Litschel T**, Heymann M, Eto H, Franquelim HG, Schwille P. "Shaping Giant Membrane Vesicles in 3D-Printed Protein Hydrogel Cages". *Small* **16** (2020) 1906259

https://doi.org/10.1002/smll.201906259

NANO · MICRO
small
www.small-journal.com

Shaping Giant Membrane Vesicles in 3D-Printed Protein Hydrogel Cages

*Haiyang Jia, Thomas Litschel, Michael Heymann, Hiromune Eto, Henri G. Franquelim, and Petra Schwille**

Giant unilamellar phospholipid vesicles are attractive starting points for constructing minimal living cells from the bottom-up. Their membranes are compatible with many physiologically functional modules and act as selective barriers, while retaining a high morphological flexibility. However, their spherical shape renders them rather inappropriate to study phenomena that are based on distinct cell shape and polarity, such as cell division. Here, a microscale device based on 3D printed protein hydrogel is introduced to induce pH-stimulated reversible shape changes in trapped vesicles without compromising their free-standing membranes. Deformations of spheres to at least twice their aspect ratio, but also toward unusual quadratic or triangular shapes can be accomplished. Mechanical force induced by the cages to phase-separated membrane vesicles can lead to spontaneous shape deformations, from the recurrent formation of dumbbells with curved necks between domains to full budding of membrane domains as separate vesicles. Moreover, shape-tunable vesicles are particularly desirable when reconstituting geometry-sensitive protein networks, such as reaction-diffusion systems. In particular, vesicle shape changes allow to switch between different modes of self-organized protein oscillations within, and thus, to influence reaction networks directly by external mechanical cues.

1. Introduction

Bottom-up reconstitution of well-characterized functional biomaterials, such as molecular entities, parts, and modules, with the final goal of constructing a synthetic cell, is a fascinating variant of Synthetic Biology.[1] Although this goal may not easily be within reach in the next years and potentially decades, cell-free reconstitution of fundamental biological functions has interesting implications for research on the origin of life[2] on one hand, and may open up new potential applications from medicine to technology

on the other hand.[3] In order to accomplish large-scale biomimetic behavior and realize the vision of a fully functional synthetic cell, a large number of cutting-edge tools or technologies inspired by nanotechnology and material science have been developed and favorably employed.[4] With regard to providing a maximally biocompatible and biomimetic compartment as a first step toward a cell-like reaction space, giant unilamellar vesicles (GUVs) composed of phospholipids have in the past years gained great attention.[5] GUV membranes mimic cellular membranes in many relevant aspects, their lipid composition can be tuned over a wide range,[6] they can be supported by a minimal cortex,[7] and even large transmembrane proteins can be reconstituted into them.[8] However, many advanced protein functionalities like cell division, differentiation, migration, and signaling require the establishment of spatial anisotropy, or in other words, polarization,[9] which is hard to realize in spherical vesicles. In particular, reconstituted bacterial cell division machineries that are supposed to ultimately induce controlled vesicle splitting have been shown to require elongated geometries with distinct symmetry axes.[10]
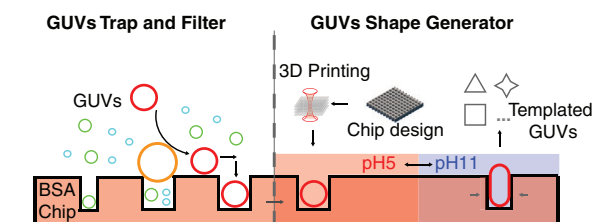
Thus, developing ways for a controlled deformation of GUVs into desired shapes, resulting in an anisotropic membrane or a polar physical microenvironment, will greatly improve our toolbox for the bottom-up reconstitution of biological functionality toward a synthetic cell. So far, several methods to template membrane vesicles and induce anisotropic structure in vitro have been developed, like microfluidics,[11] micropipette aspiration, optical tweezers, and dielectrophoretic field cages.[12] However, most of them require sophisticated technology or are unable to dynamically control the membrane geometry in a well-defined, i.e., precise and programmable, manner. On the other hand, cell biology-derived tools like 2D micropatterning,[13] hydrogels in 3D-printed microchannels,[14] and 3D soft lithography of hydrogel[15] have been successfully applied to control interfacial geometry in order to define the extracellular environment. Since the development of 3D printing technology, rationally designed 3D objects can be produced from various materials on different scales. In this context, stimuli-responsive hydrogels, which can cycle between expanded and condensed states in response to environmental triggers (e.g., pH, ionic strength), could constitute an attractive material for 3D or 4D Printing.[16] In fact, pH-responsive Bovine serum albumin (BSA) hydrogels are already widely used to fabricate 3D

Dr. H. Jia, T. Litschel, Dr. M. Heymann, H. Eto, Dr. H. G. Franquelim, Prof. P. Schwille
Max Planck Institute of Biochemistry
Am Klopferspitz 18, D-82152 Martinsried, Germany
E-mail: schwille@biochem.mpg.de

**ADVANCED
SCIENCE NEWS**

www.advancedsciencenews.com

NANO · MICRO
small
www.small-journal.com

GUVs Trap and Filter

GUVs Shape Generator

Figure 1. Concept of 3D-printed protein hydrogel trapping and templating giant vesicles (GUVs).

tissue scaffolds[17] and generating smart 4D stimuli-responsive microactuators.[16,18]

Here, we varied and expanded this technology toward the goal of selectively trapping GUVs within a customized 3D printed BSA hydrogel chip, and dynamically inducing structural anisotropy by applying external pH stimuli to the gel. The basic working principle is illustrated in **Figure 1**. 3D printed protein hydrogel can be designed as microchambers in appropriate sizes for capturing GUVs. The variable protein hydrogel structure acts as a geometrical cue to establish synthetic cell polarity in vitro by compressing vesicles into different shapes upon pH stimuli. This spatially well-defined microenvironment can mimic the dynamic native cell matrix, allowing us to investigate how synthetic cells react to and interact with external mechanical cues.

2. Results and Discussion

GUVs themselves can be generated either by electroformation, gentle hydration of dehydrated lipids, inverted emulsion transfer, or by microfluidic jetting. Procedures to handle these delicate objects are still not consummate.[19] They encompass sedimentation with high-density fluids, immobilization on functionalized surfaces,[20] manipulation by micropipette aspiration,[21] or microfluidic systems.[12,19] As an alternative, but still being compatible with these established protocols, our 3D BSA protein hydrogel GUVs traps were fabricated in a layer-by-layer procedure via two-photon polymerization process, using Rose bengal as the photoinitiator for BSA monomers (Scheme S1, Supporting Information). In contrast to other trapping approaches, surface functionalization for avoiding GUV-surface adhesion is not required for the 3D printed hydrogel chips. The electroformed GUVs filled with high-density solution, like sucrose, can spontaneously sink down into the hydrogel microchambers. Trapping in the chambers prevents GUVs from being flushed away and from being mechanically deformed by applied flow. To rationally design a trap that can be easily adapted to different sizes of GUVs, we chose a simple module consisting of a solid cube ($14 \times 14 \times 14$ μm) extrude-cut by half-cylinders (Diameter: 10 μm) on both sides (Figure S3a, Supporting Information). These GUV traps were then arranged into a 10×10-module array. By controlling the distance of rows and columns in the array, we can generate two different types of trap chips: individual traps, or group traps. With 1 μm distance for both rows and columns, the individual trap chip can be used to capture GUVs one by one within 81 separated cylinder wells (**Figure 2**a; and Figure S1a, Supporting

Information). The GUVs here utilized were obtained through electroformation,[22] composed of DOPC(1,2-dioleoyl-sn-glycero-3-phosphocholine) and doped with 0.5 mol% Atto655-DOPE(1,2-dioleoyl-sn-glycero-3-phosphoethanolamine) for fluorescence detection. By extending the row distance to 15 μm, groups of GUVs can be trapped between two full rows (Figure 2b; and Figure S1b, Supporting Information), in order to manipulate many vesicles at once, or to enforce their communications and interactions. The sizes of GUVs to be trapped depend on the diameters or distances, respectively (Figure 2c). GUVs with diameters larger than the gap distance are filtered out. The selective trapping of GUVs by the hydrogel chip, either as individuals or in groups, allows their size to be roughly controlled, as a first criterion toward establishing geometric anisotropy of vesicles.

In addition to allowing for a flexible size-filtering design, BSA hydrogel also shows great potential in generating smart pH stimuli-responsive microdevices that can be used to dynamically mimic the native cellular microenvironment in vitro. The isoelectric point of BSA is close to pH 5, where a protein has no net charge and fewer ion–dipole interactions. Therefore, the structures absorb less water than at higher pH and thus cover the smallest area at pH 5.[18a,23] Due to the larger number of ionized amino acids in BSA, swelling of the structures can be induced at higher pH. However, precisely controlling pH can be difficult. To improve controllability, the swelling capability can be effectively tuned by fabrication parameters, such as slicing distance (layer distance), laser power, and laser scan speed, as shown in **Figure 3**; and Figure S2 (Supporting Information). The area swelling ratios of $14 \times 14 \times 15$ μm cubes can be tuned from 1.1 to 1.7 (Figure 3b–d). A larger slicing distance results in lower crosslinking density and allows more water to enter inside the hydrogel, which in turn increases the swelling ability. Similarly, lower laser power also increases the swelling ratio to 1.7 (Figure 3c), but loses the spatial resolution of printing. Because of the lower crosslinking degree under low laser power, the structures printed at 30 mW laser power are ≈30% larger than when printed at 50 mW (Figure S2d, Supporting Information). When varying the scan speed, structures at pH between 5 and 8 have weak swelling capability and the maximal swelling ratio at pH 11 can only reach a factor of 1.5 (Figure 3d).

The controllable swelling ratios of 3D printed hydrogel structures enable a programmable templating of GUV geometries with pH-stimuli responsive GUVs traps. Due to the swelling effect of the traps, the total structure occupies a larger volume, which should in turn shrink the free inner volume of the chambers. The swelling behavior of a square-frame trap was first investigated. It was designed by extruding cut $15 \times 15 \times 15$ μm square wells in the center of $45 \times 45 \times 15$ μm cuboid (Figure 3e). The hydrogel frame can swell 1.57 ± 0.15 fold (mean $\pm$ s.d.) at pH 11 compared to pH 5; however, no shrinking of the inner area was observed. The potential reason is the increased surface tension at the inner side of the hydrogel frame, scaling inversely with radius. To improve the design toward a truly contractible and at the same time anisotropic trap, the structure was divided into eight separate small rectangular modules (Figure 3f). Allowing 2 μm distance between the modules in the relaxed state should support swelling in all directions. Because there exists no

ADVANCED
SCIENCE NEWS
www.advancedsciencenews.com

NANO · MICRO
small
www.small-journal.com
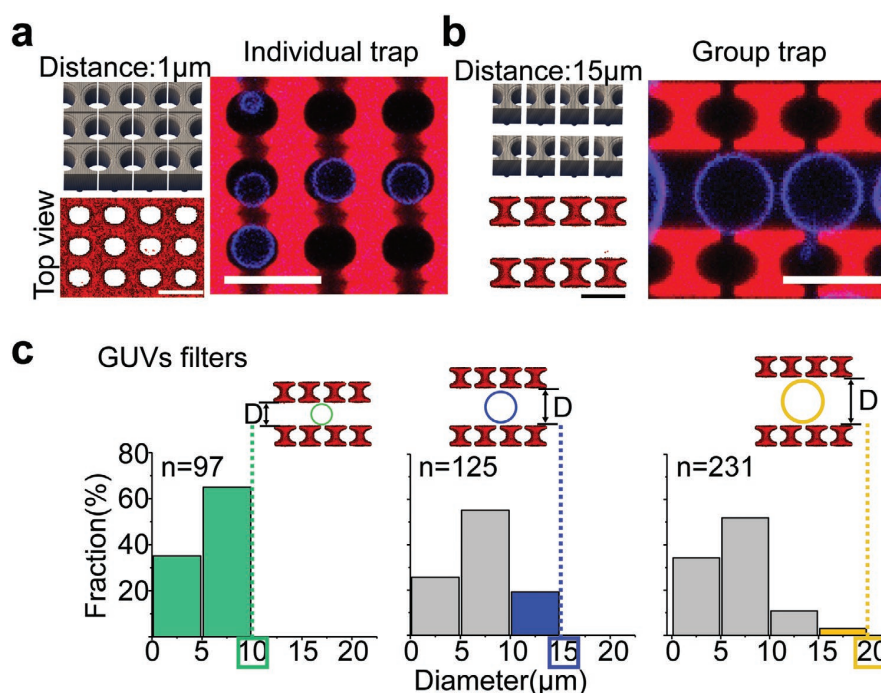
Figure 2. 3D-printed protein hydrogel chips filtering and trapping different-sized vesicles. a) Chip design for trapping individual GUVs, scale bar 20 µm. Left (top): All microchambers were integrated in one chip. Left (bottom): top view. Right: trapping individual GUVs in separated hydrogel chambers. b) Chip design for group trapping, scale bar 20 µm. Left (top): The chip was combined with separated units as barriers with certain distance. Left (bottom): top view. Right: trapping GUVs in between the hydrogel barriers. c) 3D printed hydrogel traps as GUV filters with different row distances. n: number of trapped GUV numbers. D: distance.

physical connection between the module surfaces as in the previous design, the section area of the inner free space could be decreased to 75% (±2.2%) in the swollen state when the pH was changed from 5 to 11 (Figure 3f, bottom right). Another advantage of the modular design is that the distance between the modules can be varied, in order to accommodate a larger growth regime and anisotropic compression. Small distances may lead to surface contact between the modules during swelling, which induces shape changes and restricts the overall compression effect (Figure S4, Supporting Information).

In order to evaluate the mechanical effects that can be obtained by vesicle compression, the pH stimuli-responsive hydrogel chambers were now applied to deform trapped membrane vesicles. The basic module of the group trap can swell in both x- and y- directions and thus occupies free space between modules after shifting pH from 5 to 11 (**Figure 4**a). In the rows, the distance between the modules was significantly reduced. Perpendicularly to this, two neighboring modules fused to yield a lens-shaped well, but with larger diameter than the half-cylinder at pH5. The channels between the individual barriers were also narrowed to about 50% (Figure 4a). In response to the pH stimuli, the hydrogel can process fast swelling within 1 min, supporting a dynamic mimicry of the cell microenvironment in vitro (Figure 4b; and Movie S1, Supporting Information). The trapped GUVs were now investigated by optical microscopy (Figure 4c). After shifting the pH to 11, the spherical vesicles were compressed by the closing

walls, flattening them and forcing them into nonspherical symmetry (Figure 4d,e). The distance between the two rows was 11.97 ± 0.34 µm at pH 11, so that vesicles larger than ≈12 µm in diameter were compressed. With increasing confinement under swelling conditions over a time course of 6 min, the curvature became anisotropic, with flat areas facing the hydrogel and increased curvatures in the free zone (Figure 4d). At the same time, the membrane tension was increased, due to the loss of spherical symmetry and volume conservation, which imposes some constraints on the aspect ratio σ (length vs width) of the vesicles that can be reached by this procedure without compromising membrane integrity. An aspect ratio of up to about twofold (length vs width) could, however, be easily reached by this setup (Figure S5, Supporting Information). Importantly, the hydrogel swelling is reversible, and the vesicle shapes can thus be switched between spherical and elongated by alternating between the two pH values (Figure 4e).

Furthermore, different designs of the hydrogel structures allow us to induce unusual shapes of the GUVs, and thus, membrane geometries, by varying the contact zones between the hydrogel and the vesicles. The cylindrical chip was designed by extruding a cylinder (diameter, 15 µm) in the center of a cube (20 × 20 × 20 µm) (**Figure 5**a; and Figure S3d, Supporting Information). Then the cube with the cylindrical well was quartered. This chip was used to trap vesicles of ≈15 µm diameter. When the pH was increased from 5 to 11, the four separated modules swelled centripetally and compressed the captured membrane

**ADVANCED
SCIENCE NEWS**

www.advancedsciencenews.com

NANO · MICRO

small

www.small-journal.com
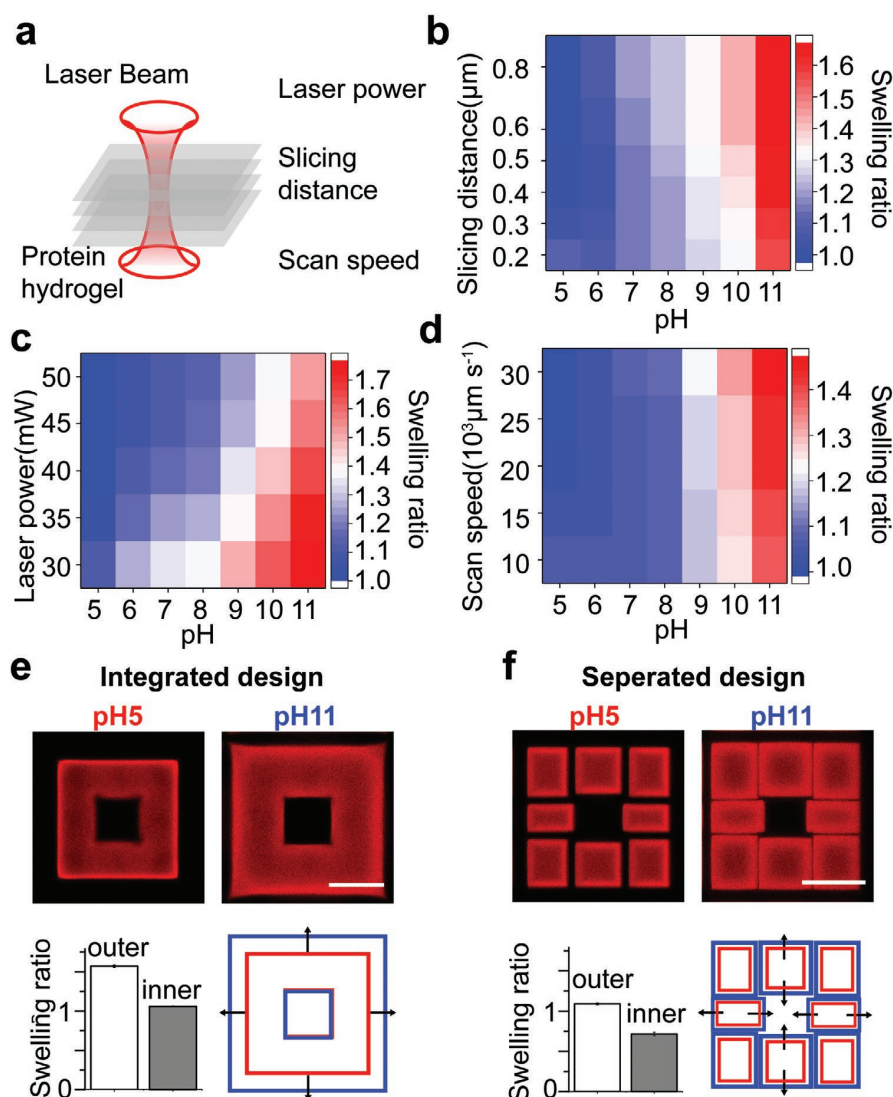
Figure 3. pH-stimuli responsive protein hydrogel. a) Laser fabrication of hydrogel layer by layer with two-photon excitation. b–d) Tuning pH-stimuli swelling ratio by varying slicing distance (b), laser power (c), and laser scan speed (d). Printing parameters: b) laser power: 50 mW, Scan speed: 30 000 µm s^{-1}; c) Slicing distance: 0.5 µm, Scan speed: 30 000 µm s^{-1}; d) Slicing distance: 0.5 µm; laser power: 50 mW. e,f) pH-dependent swelling of integrated chip and the combined chip (Slicing distance: 0.5 µm; laser power: 50 mW; Scan speed: 30 000 µm s^{-1}), scale bar 20 µm. Top: confocal imaging of the swelling effect under different pH. Bottom (left): swelling ratios of outer and inner area. Bottom (right): directional swelling. Area swelling ratio is defined as A/A_0, where A_0 is the area of the structure at pH 5, printed under slicing distance: 0.5 µm, laser power: 50 mW, scan speed: 30 000 µm s^{-1}.

vesicle. The area of the cross-section was reduced, in turn the height was increased. Similarly, with alternative designs, GUVs can be deformed to other shapes like cross prisms, cubes, and triangular prisms (Figure 5b,c). Due to the surface tension of membrane vesicles, the templated cross-prismatic, cubic, and triangular prismatic vesicles all formed curved corners and spherical domes.

Having shown that GUVs can not only be reversibly compressed, but also molded into arbitrary nonspherical shapes by our laser-printed BSA pH-responsive hydrogel structures, we next aim to demonstrate how these mechanical constraints may

influence membrane structure and dynamics in the shaped vesicles. In particular, GUVs have long been used to elucidate the molecular details of lipid phase separation; however, their usually spherical symmetry and isotropic structure have significantly limited the comparability of these model membranes with biological ones. In physiological environments, cells acquire and maintain spatial and functional asymmetry of their plasma membrane[24] in response to external mechanical cues. Similarly, in model membrane systems exhibiting visible lipid domains enriched in cholesterol and saturated lipids, strong correlations between membrane composition and 3D
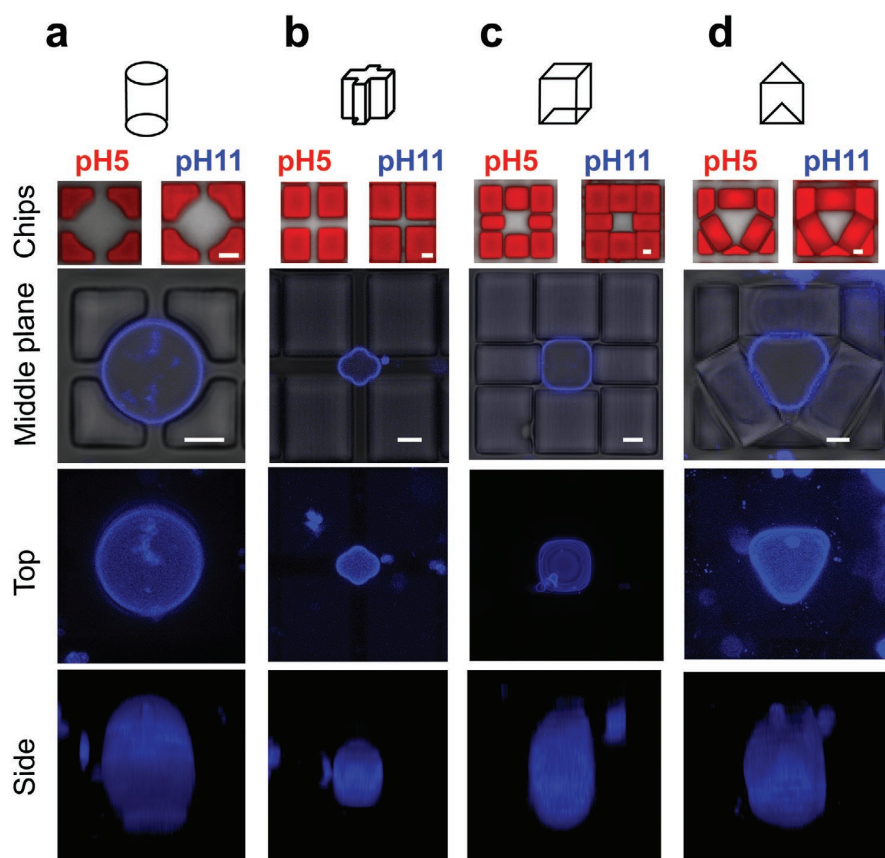
1906259 (4 of 10)
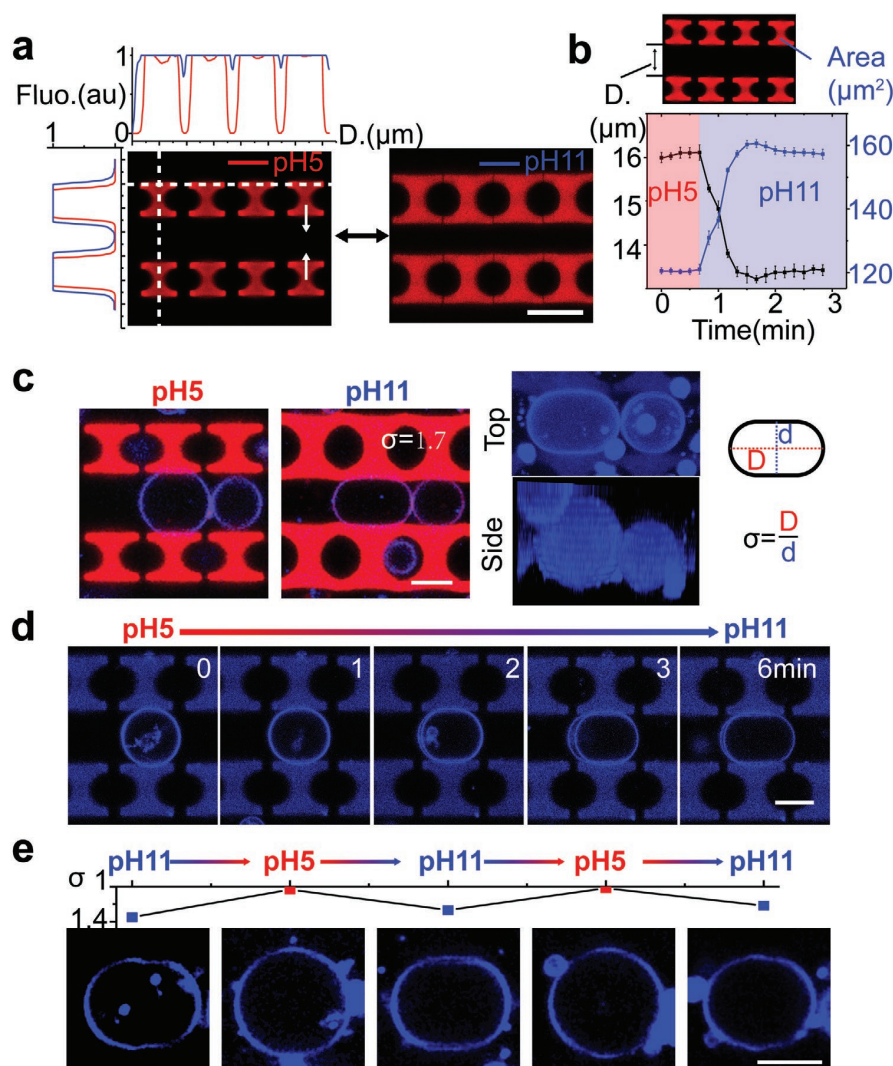
Figure 4. Reversibly deforming membrane vesicles by pH. a) Swelling effect of group trap at increased pH, scale bar 20 µm. The line plots demonstrate the swelling in both x- and y-axis, respectively. b) Response of geometry factors area and distance when transitioning to pH 11 solution. c) Swelling chip deforming DOPC GUV, scale bar 10 µm. Right: top and side view of deformed GUVs. d) Dynamic deformation of GUV by exchanging pH from 5 to 11, scale bar 10 µm. e) Reversibility of GUV aspect ratio (σ) by alternating pH, scale bar 10 µm.

vesicle shape could be observed, which suggest that, in turn, mechanical constraints will lead to significant membrane transformations.[24,25]

The phase-separated GUVs we investigated in our stimuli-responsive hydrogel cages consisted of ternary lipid mixtures composed of cholesterol (Ch), sphingomyelin (SM), and the unsaturated phospholipid DOPC, with a molar ratio of 2:2:1 at room temperature.[26] The mixture can separate into two coexisting membrane phases: a liquid-ordered phase (L_o) enriched in SM and Ch; and a liquid-disordered (L_d) phase consisting primarily of DOPC. To discriminate between the L_o and L_d phases by fluorescence microscopy, we used 0.3%NBD-DSPE and 0.2% Atto655-DOPE, respectively. The spherical phase-separated GUVs were trapped in the triangular prismatic hydrogel

chips (Figure S3c, Supporting Information). When the GUVs were compressed by the swelling hydrogel chamber under pH stimuli, the vesicles deformed to fit the diminished inner area, often accompanied by a large-scale reorganization and fusion of the domains on their membrane surface (Figure S6, Supporting Information). In several cases, particularly for vesicles with large domains, the spherical vesicle was transiently deformed upon compression into a dumbbell geometry, due to line tension between L_o–L_d domains,[27] acquiring a clear curved neck at the domain boundary. Typically, the dumbbell-shaped phase-separated vesicle then rotated within the contracted hydrogel cavity, in order to adapt the space change and relax back into a spherical (yet compacted) energetically favorable shape (**Figure 6**b; and Figure S7, Movie S2 for top view of 3D

**ADVANCED
SCIENCE NEWS**

www.advancedsciencenews.com

NANO · MICRO
small

www.small-journal.com

Figure 5. Various 3D hydrogel designs for templating DOPC vesicles into different shapes: a) cylinder, b) cross prism, c) cube, d) triangular prism. The schemes in the first row show the 3D geometries of trap wells. Below the schemes are the top views of the chips in response to different pH, scale bar 5 µm. Third row from top: confocal imaging of the middle cross-section of vesicles, scale bar 5 µm. The bottom two rows represent the 3D z-stack reconstitution of different geometrical vesicles.

imaging, and Movie S3 for orthogonal view, Supporting Information). Occasionally, however, the compression led to the fission of a Lo domain away from the trapped GUV membrane (i.e., budding as a way to overcome line tension,[28] ultimately changing the overall membrane composition of the remaining "mother" vesicle (Figure 6c; and Movie S4, Supporting Information). In the control experiment without the swelling traps, no triggered deformation events were detected upon pH change from 5 to 11 (Figure S8, Supporting Information). Thus, the ability to exert gentle but significant mechanical pressure on GUVs in our custom-designed protein hydrogel cages opens up a new way of manipulating vesicle model systems, inducing features that could be of great relevance in the design of cellular mimicries, such as shape and differential membrane curvature, respectively, tension.

The surface geometry that determines membrane dynamics also affects the spatiotemporal patterns and oscillations formed by reaction-diffusion systems.[29] A striking example of a reaction-diffusion system is the Min protein system, consisting of the proteins MinC, MinD, and MinE, which oscillate between the cell poles and spatially position the bacterial cell division machinery in *Escherichia coli*.[30] In vitro reconstitution of the

Min system on micropatterned surfaces or in microcompartments has shown that the geometry of the boundaries plays a pivotal role in its pattern formation and pace-making.[10,31] Recently, the Min system has been encapsulated into 3D spherical compartments, motivated by the long-term goal of creating a self-reproducible synthetic cell.[32] Unlike in vivo, this reconstituted reaction-diffusion system reveals several distinct oscillation modes, namely pulsing oscillations, pole-to-pole oscillations, and circling and trigger waves.[32b] Causes for such diverse behaviors are differences in protein concentration, vesicle size, proteins ratio, or the isotropic geometry. Here, we used the 3D hydrogel shaped vesicles to demonstrate how the anisotropy of microenvironment influences the reaction-diffusion system.
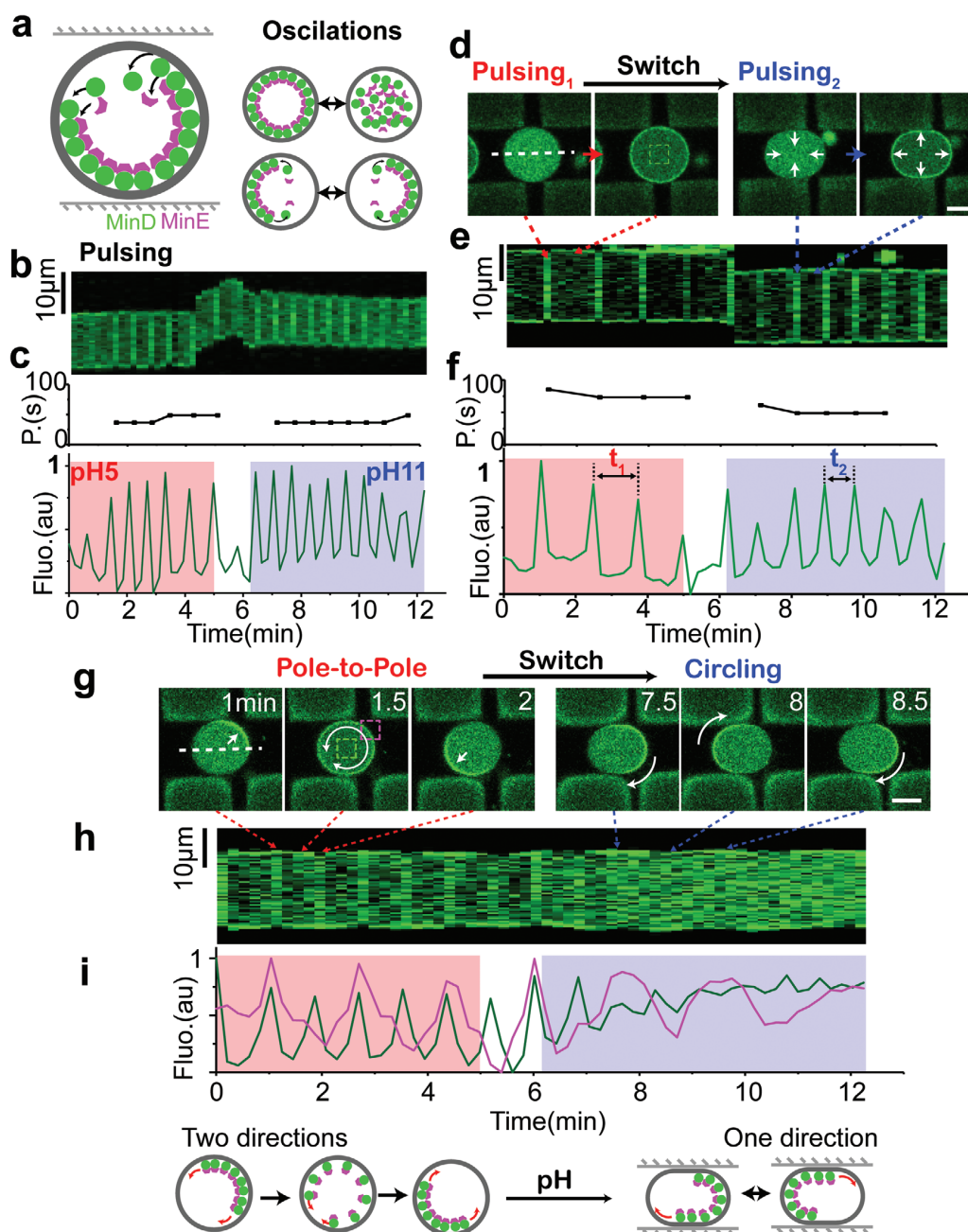
We encapsulated the oscillating Min system (MinD (50% EGFP-MinD) & MinE) in negatively charged GUVs (DOPC:DOPG(1,2-dielaidoyl-sn-glycero-3-phospho-(1'-rac-glycerol); molar ratio, 4:1) with an inverted emulsion method (cDICE method[33]). Subsequently, the vesicles were trapped within the hydrogel chips. Similar to what has been reported before,[32b] the majority of the uncompressed vesicles was showing pulsing oscillations, for which all proteins simultaneously oscillate

**ADVANCED
SCIENCE NEWS**

www.advancedsciencenews.com

NANO · MICRO

small

www.small-journal.com
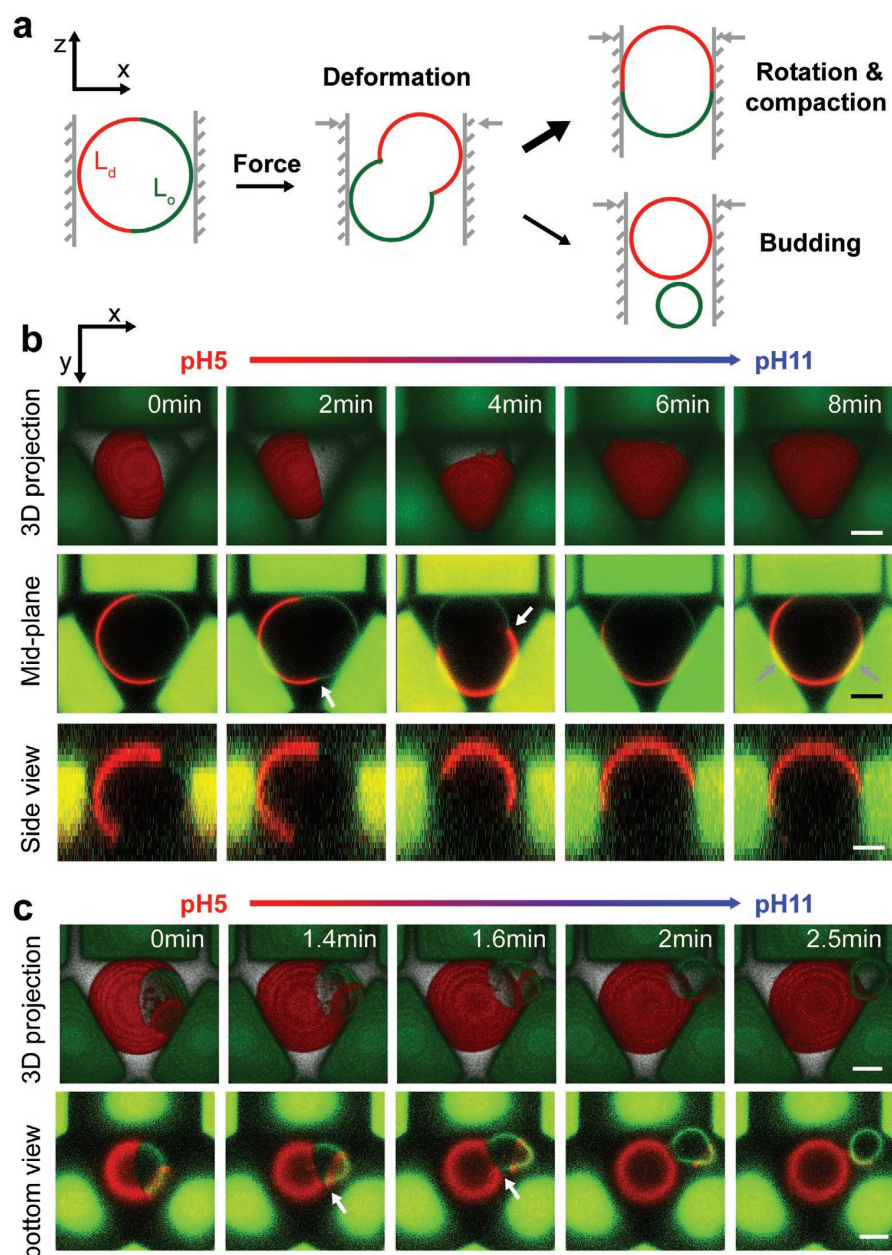
Figure 6. a) Scheme of dynamic lipid phase reorganization adapting to the space-induced membrane deformation. b) Dynamic membrane domain reorganization under pH-induced compression in the hydrogel chambers, scale bar 5 μm. c) Membrane budding driven by the compression of the hydrogel chambers, scale bar 5 μm. GUVs were produced from DOPC:SM:cholesterol (2:2:1) and labeled with NBD-DSPE (green) and Atto655-DOPE (red). The 3D projections of 3D images were compiled from Z-stack confocal images with ZEN software.

between the vesicle lumen and the inner membrane leaflet (**Figure 7**a). After the pH change from 5 to 11, vesicles that did not get deformed by the hydrogel structures, approximately maintained the oscillation frequency (Figure [7b,c]). Since the electrical gradient across the vesicle membrane restricts proton transfer to the inside, intact vesicles showed minor and slow changes of the pH in the vesicle lumen.[34] This minor change

can be buffered away by the chosen buffer system. However, for vesicles that were compressed due to the hydrogel swelling, we observed an increase in oscillation frequency compared to their uncompressed state (Figure 7d–f; and Movie S5, Supporting Information). We suspect a correlation to the resulting change in aspect ratio of the vesicles (Figure S9, Supporting Information). Larger aspect ratios result in shorter diffusion paths from

1906259 (7 of 10)

**ADVANCED
SCIENCE NEWS**
www.advancedsciencenews.com

NANO · MICRO
small
www.small-journal.com

Figure 7. Protein oscillation modes transition in response to change in vesicle geometry. a) Schematic of Min protein oscillations in vesicles. b,c) Pulsing oscillation in a spherical vesicle under different pH conditions. d–f) Pulsing oscillation acceleration during vesicles compression. g–i) Min oscillation modes transition from pole-to-pole to circling. (d), (g), and (j) show imaging frames from the confocal time series of oscillation (1.5×10^{-6} M MinD, 1.5×10^{-6} M eGFP-MinD, 3×10^{-6} M MinE, 5×10^{-3} M ATP). Scale bar: 10 µm. (b), (e), and (h) demonstrate the kymograph of the oscillation. The white dash lines on the vesicles indicate the position for the kymograph analysis. (c) and (f) (top) show the periods change inside vesicles. (c), (f) (bottom), and (i) either describe the fluorescence oscillation inside vesicles (green) or on the membrane (purple). The green and purple dash box shows the position for measuring the oscillation curves.

vesicle lumen to vesicle membrane and could explain a shorter period of oscillation. On the other hand, membrane vesicle compression leads to changes in membrane tension, which could also affect the affinity of Min proteins to lipid bilayer and, consequently, alter the reaction diffusion rates. Indeed, in vitro reconstitution revealed that a reduced membrane affinity

of Min proteins results in faster traveling waves.[35] As tense membranes resist the deformation, compressed vesicles would display an increasing membrane tension when compared to uncompressed spherical vesicles. Many studies have shown that protein–membrane interactions are strongly inhibited at high membrane tension.[36] Thus, to evaluate this hypothesis, only MinD was encapsulated inside GUVs. Indeed, the compression of vesicles with the swelling hydrogel reduced the overall binding of MinD to the membranes (Figure S10a, Supporting Information). This result could be corroborated, as similar findings were observed in trapped vesicles under increased membrane tension undergoing a hypotonic shock (Figure S10b, Supporting Information).

Intriguingly, besides the changes in oscillation frequency, in some cases we observed that the oscillation mode transitioned into a different mode in response to the change in geometry. Figure 7g–i; and Movie S6 (Supporting Information) show a vesicle that initially exhibited pole-to-pole oscillations, in which the maximum protein concentration alternates between the two opposing membrane poles of the vesicle. Upon hydrogel swelling and thus vesicle compression, the protein oscillation switched to a different mode, which was previously described as circling waves:[32,36b] the protein still is only bound to a small region on the membrane at a time, but now continuously revolves, i.e., "circles," on the inside surface of the vesicle. Thus, we showed that dynamically regulating the anisotropy of spherical vesicles with pH-stimuli 3D hydrogel chip provides us with new mechanical cues for the investigation of reaction-diffusion systems in 3D artificial microenvironments.

3. Conclusion

We have developed a new toolbox for mechanical manipulation of GUVs—model membrane vesicles that constitute the basis for the engineering of advanced protocells and that should ideally be subject to defined shape transformations. This is particularly desirable when reconstituting membrane polarity- or shape-dependent protein systems, such as bacterial cell division machineries that request explicitly nonspherical geometries.[10] Our hydrogel devices are based on custom-printed BSA protein that can be switched by pH, and are thus fully biocompatible. Their dimensions are limited only by the optical resolution of the two-photon laser used for printing. We demonstrated that the swelling ratio depends on the laser power used for printing, such that even more complex designs with differential volume expansion could in principle be realized. This opens up a fully new way of using GUVs as custom-made platforms to probe the functionality of reconstituted cellular modules in bottom-up synthetic biology. Our technique thus opens up exciting potential applications for synthetic cell and tissue engineering.

Supporting Information

Supporting Information is available from the Wiley Online Library or from the author.

Conflict of Interest

The authors declare no conflict of interest.

[1] H. Jia, P. Schwille, *Curr. Opin. Biotechnol.* **2019**, *60*, 179.
[2] H. Jia, M. Heymann, F. Bernhard, P. Schwille, L. Kai, *New Biotechnol.* **2017**, *39*, 199.
[3] C. Xu, S. Hu, X. Chen, *Mater. Today* **2016**, *19*, 516.
[4] K. Göpfrich, I. Platzman, J. P. Spatz, *Trends Biotechnol.* **2018**, *36*, 938.
[5] R. Dimova, M. Carlos *The Giant Vesicle Book*, CRC Press, Boca Raton, FL **2019**.
[6] E. Sezgin, I. Levental, S. Mayor, C. Eggeling, *Nat. Rev. Mol. Cell Biol.* **2017**, *18*, 361.
[7] S. K. Vogel, F. Greiss, A. Khmelinskaia, P. Schwille, *eLife* **2017**, *6*, e24350.
[8] M. Dezi, A. Di Cicco, P. Bassereau, D. Lévy, *Proc. Natl. Acad. Sci. USA* **2013**, *110*, 7276.
[9] C. Yeaman, K. K. Grindstaff, W. J. Nelson, *Physiol. Rev.* **1999**, *79*, 73.
[10] K. Zieske, P. Schwille, *eLife* **2014**, *3*, e03949.
[11] a) A. Yamada, S. Lee, P. Bassereau, C. N. Baroud, *Soft Matter* **2014**, *10*, 5878; b) F. Fanalista, A. Birnie, R. Maan, F. Burla, K. Charles, G. Pawlik, S. Deshpande, G. H. Koenderink, M. Dogterom, C. Dekker, *ACS Nano* **2019**, *13*, 5439; c) T. Robinson, P. S. Dittrich, *ChemBioChem* **2019**, *20*, 1701.
[12] J. Korlach, C. Reichle, T. Müller, T. Schnelle, W. Webb, *Biophys. J.* **2005**, *89*, 554.
[13] M. Théry, V. Racine, M. Piel, A. Pépin, A. Dimitrov, Y. Chen, J.-B. Sibarita, M. Bornens, *Proc. Natl. Acad. Sci. USA* **2006**, *103*, 19771.
[14] Y. T. Kim, S. Bohjanen, N. Bhattacharjee, A. Folch, *Lab Chip* **2019**, *19*, 3086.
[15] M. Bao, J. Xie, A. Piruska, W. T. Huck, *Nat. Commun.* **2017**, *8*, 1962.
[16] B. Kaehr, J. B. Shear, *Proc. Natl. Acad. Sci. USA* **2008**, *105*, 8850.
[17] P.-S. Li, I.-L. Lee, W.-L. Yu, J.-S. Sun, W.-N. Jane, H.-H. Shen, *Sci. Rep.* **2014**, *4*, 5600.
[18] a) M. R. Lee, I. Y. Phang, Y. Cui, Y. H. Lee, X. Y. Ling, *Small* **2015**, *11*, 740; b) C. L. Lay, M. R. Lee, H. K. Lee, I. Y. Phang, X. Y. Ling, *ACS Nano* **2015**, *9*, 9708.
[19] T. Robinson, P. Kuhn, K. Eyer, P. S. Dittrich, *Biomicrofluidics* **2013**, *7*, 044105.
[20] D. Stamou, C. Duschl, E. Delamarche, H. Vogel, *Angew. Chem.* **2003**, *115*, 5738.

[21] B. Sorre, A. Callan-Jones, J.-B. Manneville, P. Nassoy, J.-F. Joanny, J. Prost, B. Goud, P. Bassereau, *Proc. Natl. Acad. Sci. USA* **2009**, *106*, 5622.

[22] A. Khmelinskaia, H. G. Franquelim, E. P. Petrov, P. Schwille, *J. Phys. D: Appl. Phys.* **2016**, *49*, 194001.

[23] T. Peters Jr., *All About Albumin: Biochemistry, Genetics, and Medical Applications*, Academic Press, San Diego, CA **1995**.

[24] D. Hoekstra, O. Maier, J. M. van der Wouden, T. A. Slimane, S. C. van IJzendoorn, *J. Lipid Res.* **2003**, *44*, 869.

[25] K. Bacia, P. Schwille, T. Kurzchalia, *Proc. Natl. Acad. Sci. USA* **2005**, *102*, 3272.

[26] S. L. Veatch, S. L. Keller, *Biophys. J.* **2003**, *85*, 3074.

[27] A. J. García-Sáez, S. Chiantia, P. Schwille, *J. Biol. Chem.* **2007**, *282*, 33537.

[28] F. Jülicher, R. Lipowsky, *Phys. Rev. Lett.* **1993**, *70*, 2964.

[29] a) E. Frey, J. Halatek, S. Kretschmer, P. Schwille, *Physics of Biological Membranes*, Springer, Cham, Switzerland **2018**, p. 229;

[30] M. Loose, E. Fischer-Friedrich, J. Ries, K. Kruse, P. Schwille, *Science* **2008**, *320*, 789.

[31] a) J. Schweizer, M. Loose, M. Bonny, K. Kruse, I. Mönch, P. Schwille, *Proc. Natl. Acad. Sci. USA* **2012**, *109*, 15283; b) K. Zieske, P. Schwille, *Angew. Chem., Int. Ed.* **2013**, *52*, 459.

[32] a) K. Zieske, G. Chwastek, P. Schwille, *Angew. Chem., Int. Ed.* **2016**, *55*, 13455; b) T. Litschel, B. Ramm, R. Maas, M. Heymann, P. Schwille, *Angew. Chem., Int. Ed.* **2018**, *57*, 16286.

[33] M. Abkarian, E. Loiseau, G. Massiera, *Soft Matter* **2011**, *7*, 4610.

[34] M. Megens, C. E. Korman, C. M. Ajo-Franklin, D. A. Horsley, *Biochim. Biophys. Acta* **2014**, *1838*, 2420.

[35] B. Ramm, T. Heermann, P. Schwille, *Cell. Mol. Life Sci.* **2019**, *76*, 4245.

[36] a) M. Saleem, S. Morlot, A. Hohendahl, J. Manzi, M. Lenz, A. Roux, *Nat. Commun.* **2015**, *6*, 6249; b) M. Simunovic, G. A. Voth, *Nat. Commun.* **2015**, *6*, 7219.

b) D. Thalmeier, J. Halatek, E. Frey, *Proc. Natl. Acad. Sci. USA* **2016**, *113*, 548.

NANO MICRO

small

Supporting Information

Shaping Giant Membrane Vesicles in 3D-Printed Protein Hydrogel Cages

Haiyang Jia, Thomas Litschel, Michael Heymann, Hiromune Eto, Henri G. Franquelim, and Petra Schwille*

Supporting Information

Shaping giant membrane vesicles in 3D-printed protein hydrogel cages

Haiyang Jia, Thomas Litschel, Michael Heymann, Hiromune Eto, Henri G. Franquelim, Petra Schwille

Table of Contents

Experimental Procedures

Preparation of BSA Solution

4.2g bovine serum albumin (BSA) (Lyophilized powder, A7030, Sigma Aldrich) and 1.62 mL of DMSO (18v/v%) were added to 20 mM HEPES buffer to make up a total volume of 9 mL solution. The mixture was centrifuged (20000g) for 15min to remove impurities and foam before use. 85mM rose bengal (Sigma Aldrich, 330000) was prepared separated. The BSA photoresist (420g L^{-1}) was prepared by mixing BSA resin and rose bengal at the ratio of 9:1v/v.

3D BSA Hydrogel printing

3D BSA hydrogel printing was processed with the Nanoscribe Photonic Professional (Nanoscribe GmbH). 3D structures were design with Solidwork. The parameters were defined with Describe. If without specifying, the following parameters were used, laser power: 50mW (100%), scan speed: 30000μm s^{-1}, slicing distance: 0.5μm, hatching distance: 0.2μm. All structures were printed with 63x NA1.4 objective in silicone isolator chamber (Thermo Fisher Scientific, 0717104) pasted on round glass coverslip (Diameter= 30mm, thickness #1.5).

During printing, the chambers were covered a small coverslip to avoid strong evaporation. After fabrication, structures were rinsed with Phosphate Buffered Saline (PBS) buffer (pH7) to remove the excess BSA resin and photoresist.

Swelling Studies

Five repeat free-form solid cuboids (14x14x15μm) with slicing distance 0.2–0.8μm were fabricated with different laser power (30mW-50mW) and scan speed (10000-30000μm s^{-1}). The swelling of structures were observed at different pHs (5-11) using confocal microscope. Structures swelling were studied from low pH to high pH. Structures were equilibrated in different pH solution for 10 minutes before they were transferred for imaging. Areas of the cubes were measure with Fiji (Analyze particles). Then the swelling ratios were calculation as A_{pH}/A_{pH5}, where A means area. Confocal imaging was performed on a commercial Zeiss LSM 780 laser scanning microscope, using a water immersion objective (C-Apochromat, 40 × /1.2W, Zeiss). Samples were excited with the 561 nm laser.

GUVs preparation

Giant unilamellar vesicles (GUVs) were produced by electroformation in PTFE chambers with Pt electrodes according to the published protocol[20] with minor changes. Six microliter of lipid mixture (1mg/mL in chloroform) was spread onto two Pt wires and dried in a desiccator for 30 min. The chamber was filled with 350μL of an aqueous solution of sucrose (~ 300mOsm kg^{-1}). An AC electric field of 1.5 V (RMS) was applied at a frequency of 10Hz for 1.5h, followed by 2Hz for 0.25 h. Unless otherwise stated, vesicles composed of DOPC, containing additional 0.5mol% Atto655-DOPE, were electroformed in an aqueous solution of sucrose iso-osmolar compared to imaging buffer (~ 300mOsm kg^{-1}). For the phase separation, GUVs were prepared from mixtures of DOPC, SM (18:0), and cholesterol (2:2:1) plus 0.2mol% Atto655-DOPE and 0.3mol%NBD-DSPE.

GUVs trapping and shaping

3D structures were exchanged into pH5 PBS buffer (~294mOsm kg^{-1}) for 10min. Then, 20 μL or more of the GUV suspension (without-diluted) were added on top of the printed structures in the imaging chambers. Samples were incubated for at least 0.5 h at room temperature. After GUVs sinking down and diffusing inside the traps, samples were transferred for imaging. Then, samples were gently equilibrated into pH11 PBS buffer for 10min to reach the maximal swelling. The deformation of the trapped GUVs were imaged with confocal microscopy. To

avoid bursting the GUVs during deformation, the osmolality of pH11 PBS buffer (~307mOsm kg^{-1}) was slightly higher than sucrose solution inside GUVs.

Min oscillation in vesicles

1. Proteins

The plasmids for the expression of His-MinD[28], His-EGFP-MinD[32] and His-MinE[28] have been described previously. His-MinD, His-EGFP-MinD and His-MinE were purified according to the published protocols. In brief, proteins were expressed in *E. coli BL21* (DE3) pLysS and further were purified via Ni-NTA affinity purification. Then proteins were further purified using gel filtration chromatography in storage buffer (50mM HEPES, pH 7.25, 150mM KCl, 10% Glycerol, 0.1mM EDTA). Proteins were quick-frozen and stored in aliquots at -80°C until further use.

2. Proteins Encapsulation in vesicles

Min system was encapsulated in vesicles by emulsion transfer (the cDICE method[31]) according to the published protocol[30b]. Briefly, both inner and outer solution contain Min protein buffer (25mM tris-HCl (pH 7.5), 150mMKCl and 5mM MgCl2). In addition, the solution encapsulated in the GUVs contained 1.5μM MinD, 1.5μM eGFP-MinD, 3μM MinE, 5mM ATP, v/v 15% iodixanol (from OptiPrep™, Sigma Aldrich) and an oxygen scavenger system (3.7U ml^{-1} pyranose oxidase, 90U/ml catalase, 0.8% glucose. Osmolarity of encapsulated solution was about 560mOsm kg^{-1}, measured with Fiske® Micro-Osmometer Model 210). As the GUV-surrounding solution, Min protein reaction buffer and 200 mM glucose were used to match the osmolarity of the inner solution.

The lipid we used is DOPC (1,2-Dioleoyl-sn-glycero-3-phosphocholine, Avanti Polar Lipids, Inc.) and DOPG (1,2-Dioleoyl-sn-glycero-3-phosphoglycerol, Avanti Polar Lipids, Inc.) (Both 25mg ml^{-1} in chloroform) in a ratio of 4:1. The lipids were mixed in a silicon oil (5 cST) and mineral oil (sigma-aldrich. M5904) mixture (ratio, 4:1).

Then the inner solution was loaded into a 1 mL syringe, which was then placed into a syringe pump system (neMESYS base 120 with neMESYS 290N) and connected through tubing to a glass capillary (100μm inner diameter). 700μl of outer solution was pipetted into a spinning cDICE chamber, followed by approximately 5ml of the lipid-in-oil mixture. The capillary tip

was then immersed in the oil phase and the inner phase injected at a flow rate of 50µl h^{-1} for 15 minutes. The vesicles were withdrawn from the cDICE chamber with a micropipette.
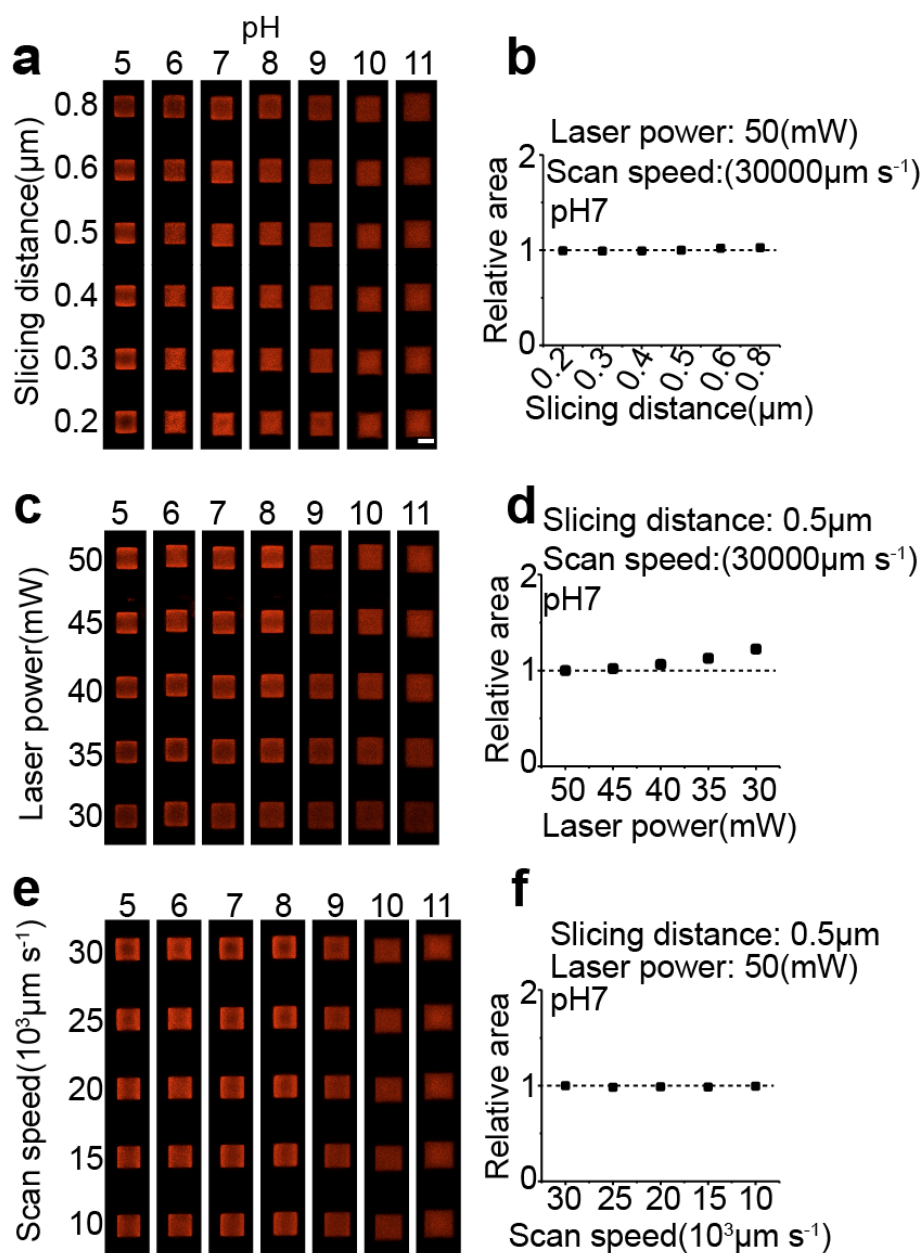
Supplement figures
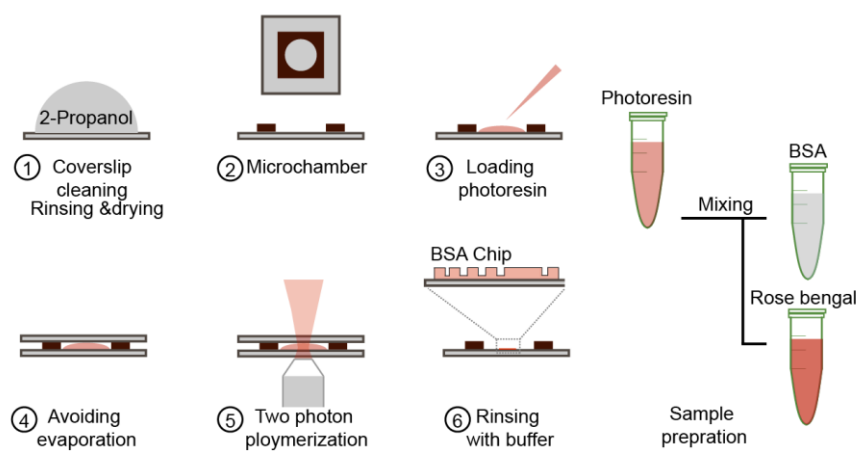

Scheme S1. Schematics of 3D printing BSA hydrogel
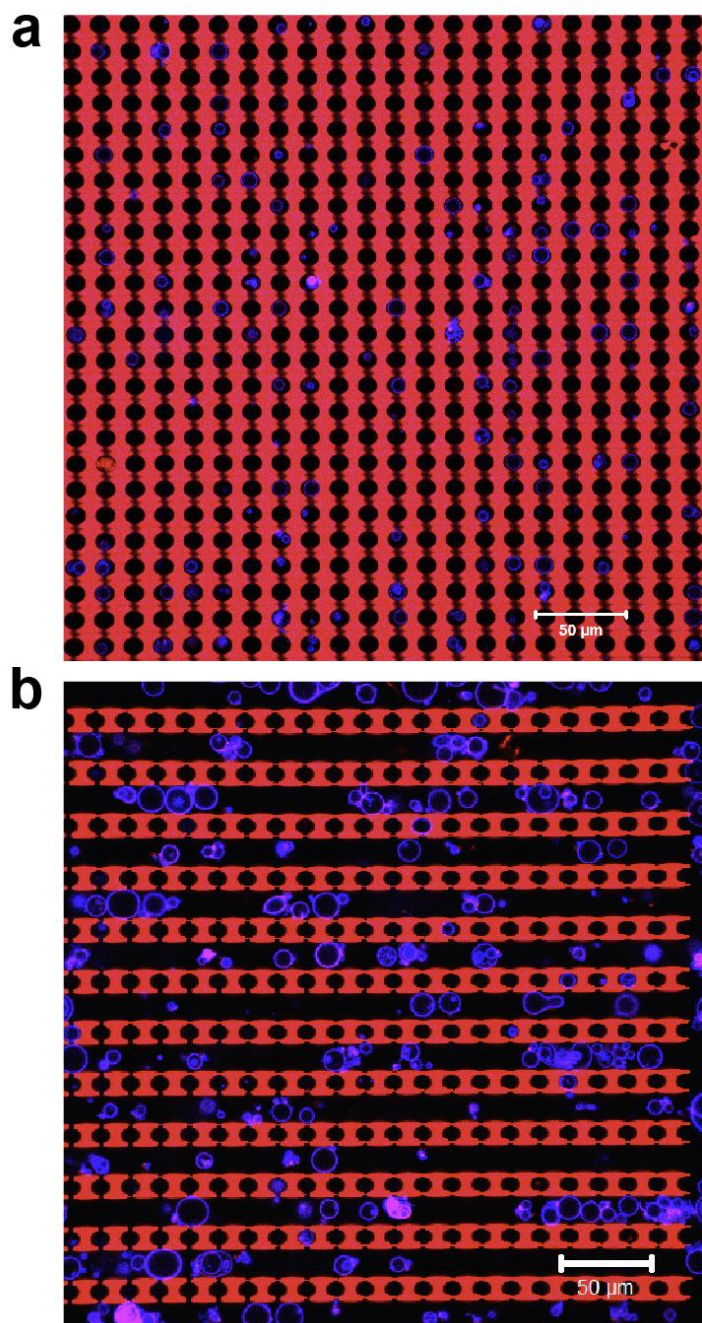
Figure S1. Overviews of the GUVs trapped in a.) The individual trap chip (22x 25 array) and b.) The group trap chip (11 channels), scale bar 50µm. GUVs were produced with DOPC and labelled with 0.5mol% Atto655-DOPE.

Figure S2. pH-dependent swelling of 3D printed cubic hydrogels fabricated with different fabrication parameters a.) pH responsive swelling of hydrogel cube with different slicing distances from 0.2 to 0.8μm (Laser power: 50mW, Scan speed: 30000μm s^{-1}), scale bar 10μm. b.) relative area of structures printed with different slicing distance at pH7. The slicing distance will not influence printing size of the structures. c.) pH responsive swelling of hydrogel cube with different laser power from 30 to 50mW (Slicing distance: 0.5μm, Scan speed: 30000μm s^{-1}). d.) Relative area of structures printed with different laser power at pH7. Printing with laser power lower than 40mW increased structure size. e.) pH responsive

swelling of hydrogel cube with different laser scan speed from 10000 to 30000μm s^{-1} (Slicing distance: 0.5μm; laser power: 50mW). f.) Relative area of structures printed with different scan speed at pH7. The relative area calculated with A/A_0, where A_0 means the area of structure printed with fabrication parameters (Slicing distance: 0.5μm, Laser power: 50mW, Scan speed: 30000μm s^{-1}).
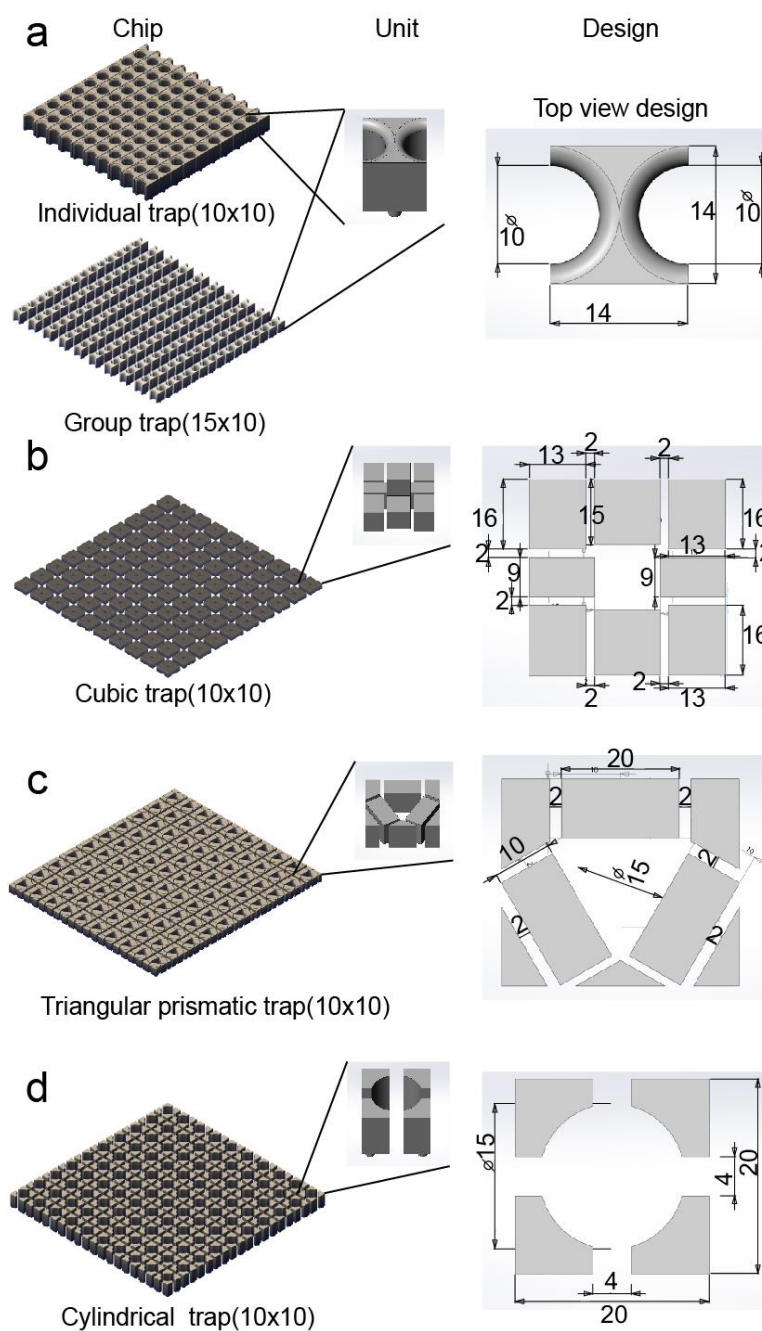
Figure S3. Schematic designs and dimensions of 3D protein hydrogel traps a.) Individual traps with 10x10 array in Fig. 1a. and group traps in Fig. 1b ,c, Fig.3 . b. and Fig.6.) Cubic traps with a 10x10 array in Fig.2f and Fig. 4. c.) Triangular prismatic traps with a 10x10 array in Fig. 4 and Fig. 5. d.) 10x10 cylindrical traps array in Fig. 4. If without specifying, all the structures used in this research are freestanding designs with pillars as supports (Diameters 2μm, Height 2μm)
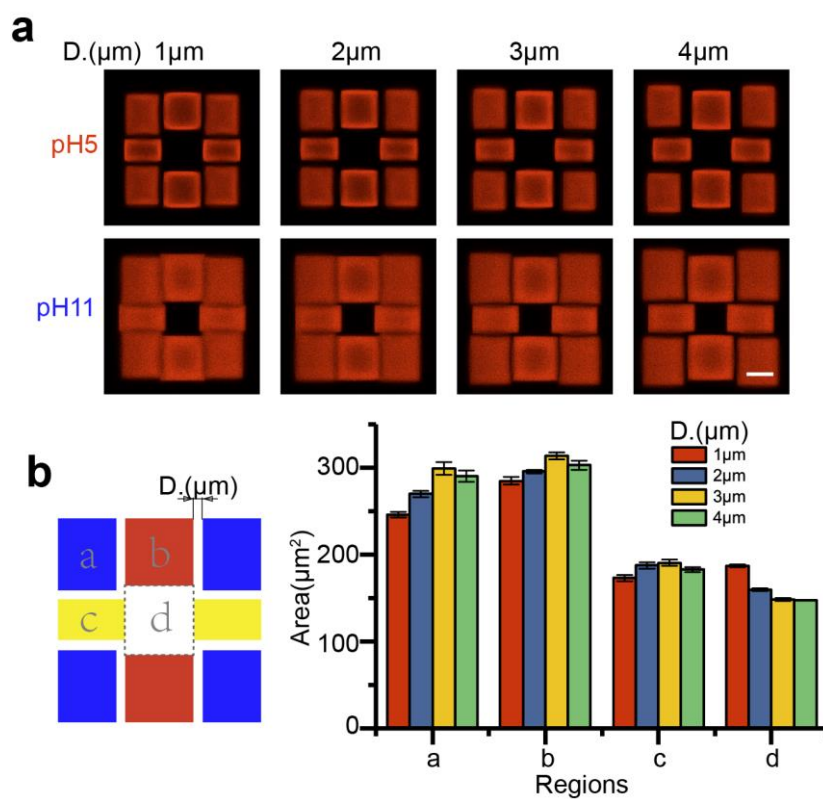
Figure S4. Distances between modules influence structure swelling capability. a.) pH responsive swelling of cubic traps with different distances between modules, scale bar, 10μm. b.) Area swelling of different regions in the cubic trap with different distances, when pH was changed from 5 to 11. Module b and c are freestanding structures with pillar supports. Module a were cuboid without pillar supports.
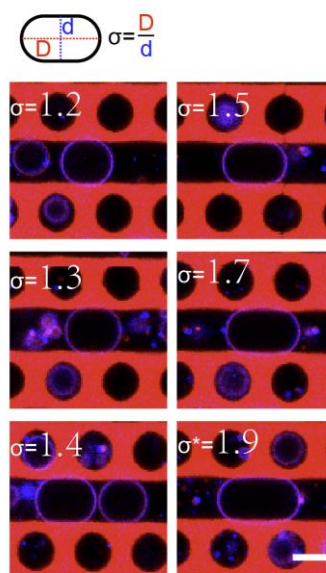
Figure S5. Swelling hydrogel compressing GUVs with different aspect ratios σ (width compared to length), scale bar 10μm. The deformation of GUVs were processed in the group trap chip. Due to the size difference, GUVs with different aspect ratio can be obtained from the swelling compression. * GUV (Diameter>15μm) trapped in the chip had been compressed at pH5.
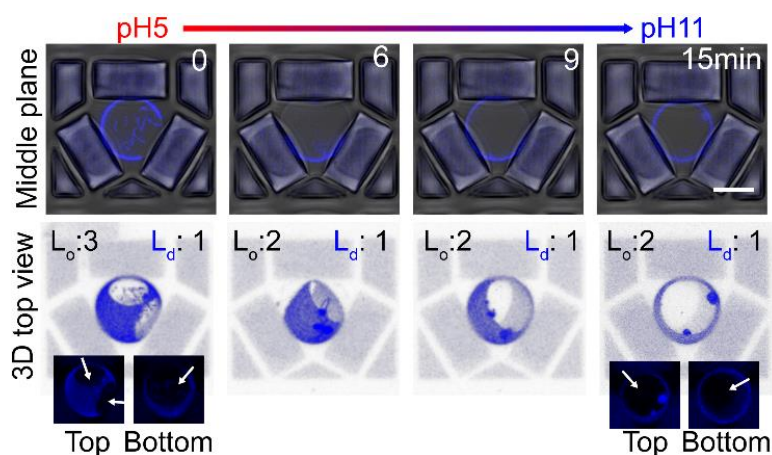
Figure S6. Dynamic lipid domain fusion and reorganization adapting to the space-induced membrane deformation, Scale bar, 10µm. Top: confocal imagines of middle plane of the vesicle. Bottom: top view of the 3D z-stack reconstitution. The numbers show the domain numbers of L_o and L_d phase. GUVs were produced from DOPC:SM:cholesterol (2:2:1). GUV
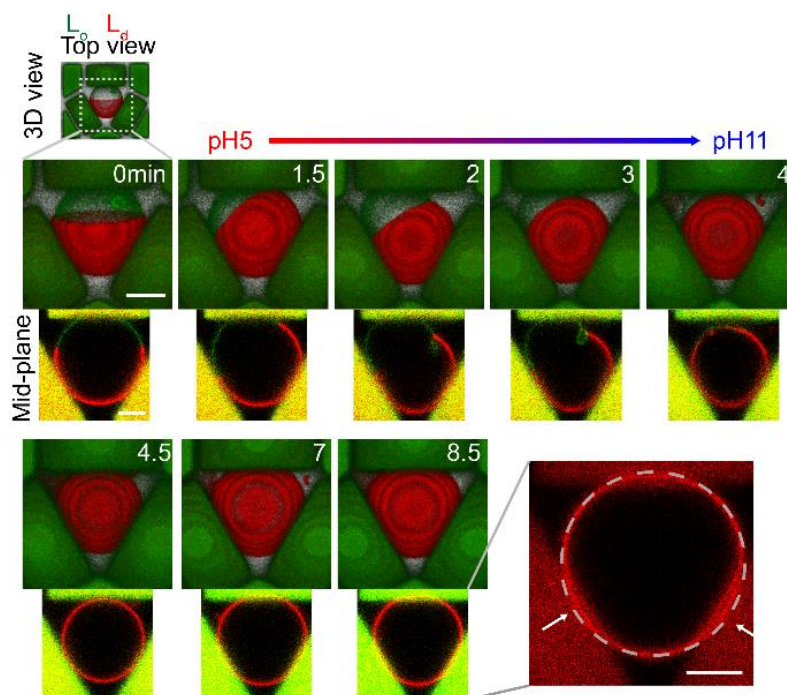
in the images was labelled with Atto655-DOPE (blue).

Figure S7. Dynamic membrane domain reorganization under pH-induced compression in the hydrogel chambers, scale bar 5µm. GUVs were produced from DOPC:SM:cholesterol (2:2:1) and labelled with NBD-DSPE(green) and Atto655-DOPE (red). The top views of 3D images were compiled from Z-stack confocal images with ZEN software.
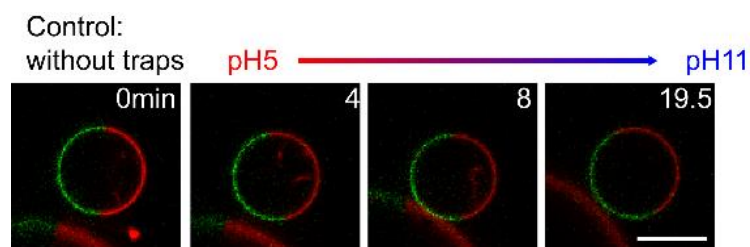
Figure S8. Free standing phase-separated GUVs upon pH stimuli, scale bar, 10µm. GUV in the images was labelled NBD-DSPE (green) and Atto655-DOPE (red).
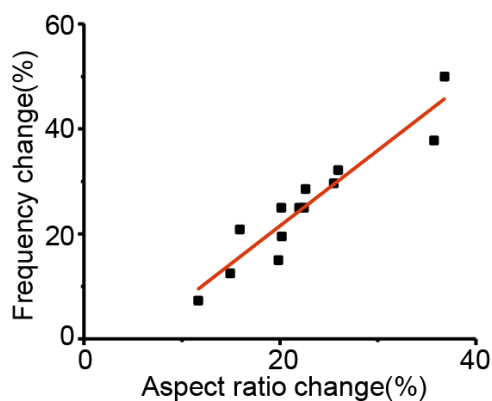
Figure S9. Pulsing oscillation acceleration during vesicles compression (1.5μM MinD, 1.5μM eGFP-MinD, 3μM MinE, 5mM ATP). Pulsing frequency change versus aspect ratio (W/H) change of vesicles that were before- and after- compressed.
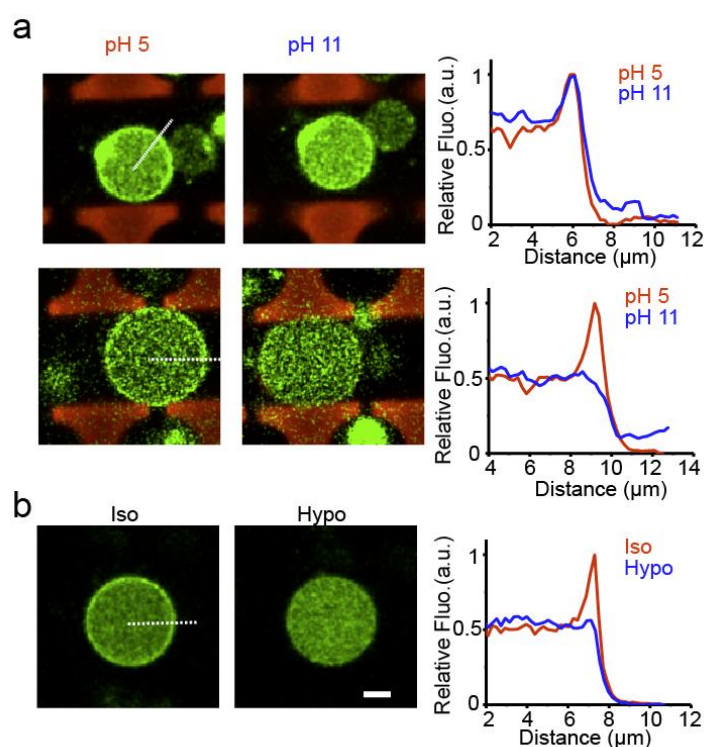
Figure S10. a.) Vesicle compression could oppose Min protein binding (1.5μM MinD). b.) MinD-membrane interaction under hypotonic and isotonic condition. To generate the hypotonic shock, the outer solution osmolality was increased about 20mOsm by adding water in the surrounding buffer. Scale bar, 5μm. The white dash lines show the position for radial plot profiles.

Supplement Movies

Supplement Movie S1. pH responsive swelling of group trap, when pH was shift from 5 to 11.

Supplement Movie S2. Dynamic membrane phase separation and reorganization in pH-stimuli 3D hydrogel chamber (top view)

Supplement Movie S3. Dynamic membrane phase separation and reorganization in pH-stimuli 3D hydrogel chamber (orthogonal view)

Supplement Movie S4. Membrane budding driven by the space compression of the pH-stimuli 3D hydrogel chambers (top view)

Supplement Movie S5. Pulsing oscillation acceleration during vesicles compression

Supplement Movie S6. Min oscillation modes transition from pole-to-pole to circling.

References

[1] A. Khmelinskaia, H. G. Franquelim, E. P. Petrov, P. Schwille, *J. Phys. D* **2016**, 49, 194001.
[2] M. Loose, E. Fischer-Friedrich, J. Ries, K. Kruse, P. Schwille, *Science* **2008**, 320, 789.
[3] K. Zieske, J. Schweizer, P. Schwille, *FEBS letters* **2014**, 588, 2545.
[4] M. Abkarian, E. Loiseau, G. Massiera, *Soft Matter* **2011**, 7, 4610.
[5] T. Litschel, B. Ramm, R. Maas, M. Heymann, P. Schwille, *Angew Chem. Int. Ed. Engl.* **2018**, 57, 16286.

4.4. Publication 6: FtsZ reorganisation facilitates deformation of giant vesicles in microfluidic traps

Research paper published in Angewandte Chemie International Edition.[74]

Ganzinger KA, Merino-Salomón A, García-Soriano DA, Butterfield AN, **Litschel T**, Siedler F, Schwille P. "FtsZ reorganisation facilitates deformation of giant vesicles in microfluidic traps". *Angew Chem Int Ed* **59** (2020) 21372–21376

https://doi.org/10.1002/anie.202001928

Synthetic Biology

FtsZ Reorganization Facilitates Deformation of Giant Vesicles in Microfluidic Traps**

Kristina A. Ganzinger+,* Adrián Merino-Salomón+, Daniela A. García-Soriano,
A. Nelson Butterfield, Thomas Litschel, Frank Siedler, and Petra Schwille*

Abstract: The geometry of reaction compartments can affect the local outcome of interface-restricted reactions. Giant unilamellar vesicles (GUVs) are commonly used to generate cell-sized, membrane-bound reaction compartments, which are, however, always spherical. Herein, we report the development of a microfluidic chip to trap and reversibly deform GUVs into cigar-like shapes. When trapping and elongating GUVs that contain the primary protein of the bacterial Z ring, FtsZ, we find that membrane-bound FtsZ filaments align preferentially with the short GUV axis. When GUVs are released from this confinement and membrane tension is relaxed, FtsZ reorganizes reversibly from filaments into dynamic rings that stabilize membrane protrusions; a process that allows reversible GUV deformation. We conclude that microfluidic traps are useful for manipulating both geometry and tension of GUVs, and for investigating how both affect the outcome of spatially-sensitive reactions inside them, such as that of protein self-organization.

One hallmark of living entities is their ability to self-organize into complex architectures, both on the level of cells and tissues, with molecular gradients controlling cell polarity, division, and the spatial dynamics of signaling.[1,2] Interestingly, cell geometry itself can induce the required spatial symmetry breaks in signaling activity.[3] In eukaryotes, cell shape is controlled by both plasma membrane properties and components of the membrane-proximal cytoskeleton, most importantly the actin network.[4] Recently, bottom-up syn-thetic biology has been increasingly able to reconstitute these cellular phenomena in vitro, including spatially organized processes such as cell division.[5,6]

Reconstituting cell division in vitro represents a desirable, albeit ambitious, goal towards the bottom-up construction of an artificial cell.[7–9] Cell division involves the segregation of chromosomes and other intracellular components, concluding with cytokinesis, the physical splitting of the cell envelope. In bacteria, cytokinesis requires constriction and fission of the cell membrane as well as the peptidoglycan layer.[10] Cell division in many bacteria involves the GTPase protein and tubulin homologue FtsZ.[10] FtsZ polymerizes into a dynamic ring-like structure at the division site ("Z-ring"), where it is anchored to the membrane by adaptor proteins FtsA and ZipA.[11–13] The Z-ring serves then as a platform to recruit further divisome proteins.[7] The process of FtsZ assembly has been reconstituted in vitro at supported lipid bilayers.[14] On these, FtsZ spontaneously assembles into dynamic ring structures, in which individual FtsZ filaments undergo treadmilling to drive chiral ring rotations.[15] Reconstituting FtsZ in spherical aqueous droplets in oil showed dynamic FtsZ bundles, while studying FtsZ behavior inside rod-shaped droplets was also attempted.[16] FtsZ behavior in membrane-bound compartments (polymersomes or giant unilamellar vesicles (GUVs)) has also been studied.[8,17] However, bacteria are not spherical, and it is clear that cell shape has a great impact on the boundary conditions of these processes.

In the present study, we therefore introduce a single-layer microfluidic chip based on previous work[18,19] in which GUVs can be reversibly deformed into cigar-like shapes by capturing them between narrowing PDMS posts. After several iterations (Figures S1–4), we found that the design shown in Figure 1 was optimal for GUV capture and deformation (Figure S1, design FS814): adjacent columns of traps (in 2 channels with 280 traps each) are vertically offset to maximize GUV capture, and post spacing is step-wise reduced towards the chip outlet, such that differently-sized GUVs are efficiently captured. Since we were interested in reconstituting elements of a synthetic cell division machinery in these elongated GUVs, we also designed the traps to mimic the "neck" of the division site (Figure 1 a). Each trap has multiple indentations for stable GUV trapping, and a "stopper" to prevent GUVs from escaping if they slip through the posts. Since the constriction features are small with a high aspect ratio $(2 \times 2 \times 13 \ \mu m)$, we imaged both wafer using laser scanning based profilometry (Figure S5) and PMDS mold using scanning electron microscopy (SEM) for quality control (Figure 1 b). To test how encapsulated FtsZ filaments respond to compartment geometry, we made GUVs containing

[*] Dr. K. A. Ganzinger,[+] A. Merino-Salomón,[+]
Dr. D. A. García-Soriano, A. N. Butterfield, T. Litschel, Dr. F. Siedler,
Prof. Dr. P. Schwille
Department of Cellular and Molecular Biophysics,
Max Planck Institute of Biochemistry
Am Klopferspitz 18, 82152 Martinsried (Germany)
E-mail: schwille@biochem.mpg.de

Dr. K. A. Ganzinger[+]
Living Matter, AMOLF
P.O. Box 41883-1009 DB Amsterdam (The Netherlands)
E-mail: k.ganzinger@amolf.nl

[+] These authors contributed equally to this work.
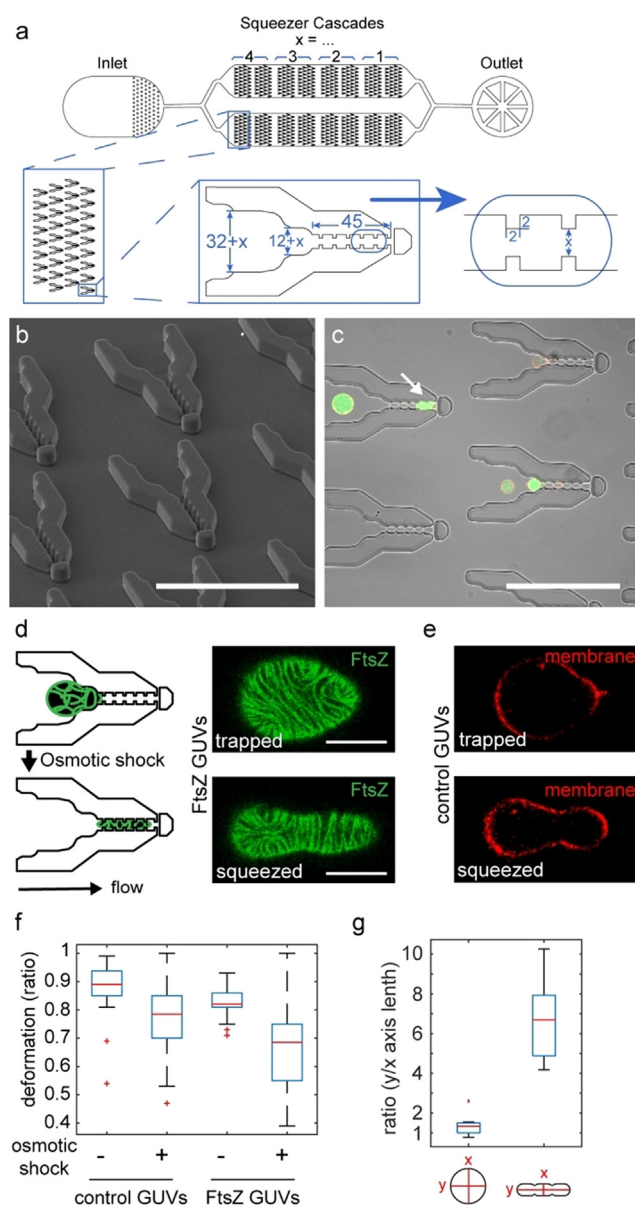
Figure 1. Design of microfluidic GUV traps. a) Schematic depiction of chip design, zooming in on the trap features. All dimensions in μm. b) SEM image of PDMS mold as a quality control step showing clean trap features. c) Brightfield and fluorescent microscopy composite image showing traps and trapped GUVs (containing FtsZ-YFP-mts, green and DOPE-ATTO655 in the membrane, red). Scale bars for (b,c) are 100 μm. d) Schematic depiction and confocal images of trapped (top) and deformed (bottom) FtsZ-GUVs (GUVs containing FtsZ-YFP-mts, green) and e) GUVs containing FtsZ buffer (control, DOPE-ATTO655 in membrane, red). Scale bars are 10 μm. f) Maximum deformation of FtsZ- or control GUVs before and after osmotic deflation. g) GUV aspect ratios before and after squeezing. Box plots in (f,g) denote median in red, interquartile range as blue box, the 2.7σ (99.3%) confidence interval as whiskers and outliers with a red cross. n(GUVs) > 10 from > 4 independent experiments.

purified FtsZ-YFP-mts (henceforth referred to as FtsZ) in polymerizing conditions. The membrane targeting sequence (mts) included in the protein's C-terminal domain circumvents the need for ZipA or FtsA by directly attaching FtsZ to

the membrane, and YFP allows direct visualization of FtsZ polymerization.[15,20–22] Importantly, this construct has also been shown to form functional Z-rings in vivo.[22] Using a syringe pump to apply negative pressure from the outlet to suck FtsZ-containing GUVs (FtsZ-GUVs) into the chip, we were able to capture and trap GUVs for minutes (flow rates 5–10 μL h^{-1}, Figure 1 c). Some GUVs deformed from a spherical to an elongated shape (Figure 1 c, white arrow), but most trapped GUVs remained spherical. Using up to 50 times higher flow rates, we succeeded in "squeezing" GUVs fully into the trap funnels (Figure 1 d,e, bottom images). Interestingly, compared to GUVs only containing FtsZ buffer (control GUVs), FtsZ-GUVs deformed strongly and at lower flow rates, but only if FtsZ was membrane-bound and GTP was present (Figure 1 f, Figure S6a). This suggests that FtsZ filament attachment and treadmilling at membranes may affect spontaneous membrane curvature and hence extent of vesicle deformation obtained under forces. When we applied a mild osmotic deflation (14–23% increase in buffer osmolarity), GUV deformation was greatly facilitated, even more so in the presence of FtsZ (Figure 1 f). GUVs assumed non-spherical shapes likely more readily as osmotic deflation likely increased the membrane area-to-volume ratio, although we could not reliably quantify GUV volumes by confocal microscopy (see SI methods for further discussion). After the initial deformation flow rates of 5 μL h^{-1} were sufficient to keep GUVs stable in rod-like shapes and the mean aspect ratio from ≈1 for spherical GUVs changed to 6.7 ± 1.9 (Figure 1 g). We were thus able to create GUVs with a height of 13 μm and width of 7 μm (or 5 μm at the constriction sites), corresponding to the trap dimensions, and lengths up to ≈50 μm depending on initial GUV size (Figure S6b).

In elongated FtsZ-GUVs, FtsZ filaments aligned preferentially perpendicular to the GUVs' long axis (Figure S7), particularly at GUVs' necks (Figure 2 a,b). Releasing GUVs from the traps by reversing flow direction, they reassumed spherical shapes within a minute (Figure 2 c,d, S8a). Strikingly, this shape change was accompanied by FtsZ filament reorganization: elongated FtsZ filaments re-polymerized into ring-like structures (Figure 2 d, i-ii). Although our image resolution is insufficient to discern filament organization, the dimensions make it likely that these structures correspond to the dynamic rings previously described (see Figure S9 for experiments under identical conditions to[23]). These ring-like filaments formed in short cone-like membrane protrusions at GUV surfaces, as soon as the mechanical membrane tension was decreased upon isosmotic GUV release from the traps (σ_{mec} (shape change) = −70 ± 10 mN m^{-1}; n(GUV) = 10, Figure 2 e–f, Figure S8b; see SI for details on calculation of σ_{mec} from Figure S6 data). The change from filaments to rings was also apparent from a shorter mean filament length (Figure 2 g). Interestingly, we observed that osmotic deflation instead of FtsZ-GUV trapping and elongation also induced FtsZ-stabilized membrane protrusions (Figure S10a–c). Taken together, these results suggest that lowering elastic membrane tension, either by releasing external forces (GUV release from traps) or by osmotic deflation, both lead to FtsZ reorganization and FtsZ-driven membrane shape changes.
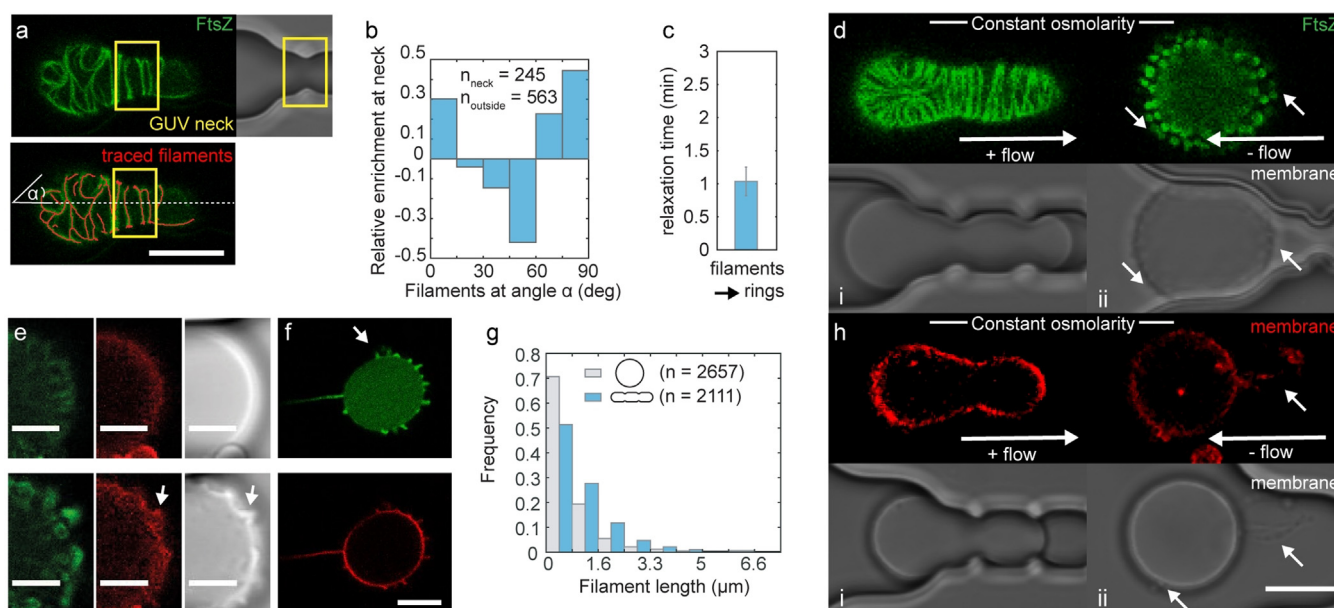
Figure 2. GUV deformation affects FtsZ filament alignment and filaments reorganize as constraints on GUV shape are released. a) Confocal images of trapped FtsZ-GUVs (FtsZ in green, top), the same image overlaid with automatically traced filaments (red, bottom) and DIC image (right). Neck region marked with yellow box (manually defined from brightfield image). Scale bar is 10 µm. b) Relative enrichment of filaments at angles α with the GUV axis at GUV necks; n(filaments) > 245. c) Mean relaxation times for FtsZ reorganization. Error bars are s.d. d,h) Confocal images of the equatorial plane of a trapped and reversibly elongated FtsZ-GUV (d, i-ii, top) or a control GUV (h, i-ii, top, membrane labelled with DOPE-ATTO655) and corresponding DIC images (d,h, bottom). The scale bar is 10 µm. e) Close-up images of FtsZ reorganization, from left to right: confocal images of FtsZ-GUVs (FtsZ, green; DOPE-ATTO655, red) and corresponding DIC images. Elongated GUV (top) and the same GUV after isosmotic release from the trap, having reassumed a spherical shape (bottom). Scale bars are 5 µm. f) Membrane protrusions are filled with FtsZ. (FtsZ, green; DOPE-ATTO655, red) Scale bar is 10 µm. g) Distribution of filament lengths in FtsZ-GUVs. n is the number of filaments analyzed. For all experiments, n(GUVs) > 12 from > 4 independent experiments.

Importantly, higher solute concentrations alone, as expected for osmotically deflated GUVs, did not result in increased FtsZ-stabilized membrane protrusions, but even at higher solute concentrations, FtsZ-protrusions could still be reliably induced by osmotic deflation (Figure S10d).[23] We also note that elastic membrane tension only affects membrane-bound FtsZ, as for GUVs containing FtsZ without a membrane targeting sequence (FtsZ wt) FtsZ organization was unaffected by osmotic deflation (Figure S11a). In contrast to the short cone-like protrusions observed for FtsZ-GUVs, we observed that in control GUVs, the excess membrane area upon reobtaining spherical shapes was stored by the formation of longer and percolated membrane tubules, as previously described (Figure 2h, white arrows). Similar tubules were also observed when relaxing mechanically-tensioned GUVs containing FtsZ wt, confirming that FtsZ needs to be membrane-bound to affect GUV membrane shapes (Figure S11b). In summary, our data suggest that FtsZ filaments reorganize on low-tension membranes into ring-like structures at membrane regions of higher curvature ("cones"), possibly driven by an intrinsic preference of membrane-bound FtsZ for higher membrane curvature.

With membrane area being "stored" in membrane protrusions (cones), we tested whether these structures could act as membrane area reservoirs to facilitate deformation of GUVs into aspherical shapes, analogously to applying an osmotic shock before deforming GUVs. When we pushed FtsZ-GUVs with membrane protrusions back into the traps

after a first (osmotically facilitated) deformation cycle, we observed that deformation was now indeed fully reversible under isosmotic conditions, merely by changing flow direction (Figure 3a, S12). Again, GUV shape changes were accompanied by FtsZ filament reorganization: in a few minutes, rings gave way to elongated filaments as protrusions were reincorporated into the membranes of elongated GUVs (Figure 3a, i-iii, S8, Movie 1). While almost all FtsZ-GUVs repeatedly deformed, the majority of control GUVs did not (success rate of individual attempt ≈ 90% for FtsZ-GUVs versus < 50% for all controls, Figure 3b). In addition, more deformation cycles could be achieved, on average, for FtsZ-GUVs (up to 5, mean of 2.5 versus < 2 for all controls, Figure S13a). Even when control GUVs could be successfully deformed, higher flow rates were required for shorter vesicle deformation compared to FtsZ-GUVs (Figure 3c, S13b). Taken together, our data suggest that membrane-bound FtsZ filament reorganization facilitates GUV membrane shape changes. This facilitation required FtsZ to cycle between different polymerization states (rings and filaments) in an energy-dependent (i.e. GTP-dependent) process depending on overall membrane tension, allowing to reversibly store excess membrane area (Figure 3d).

In summary, we have designed microfluidic traps for deforming GUVs with constriction sites mimicking the indentation of a division furrow and at mean aspect ratios close to that of rod-like bacterial shapes. Fanalista et al. have also developed microfluidic traps to deform water-in-oil
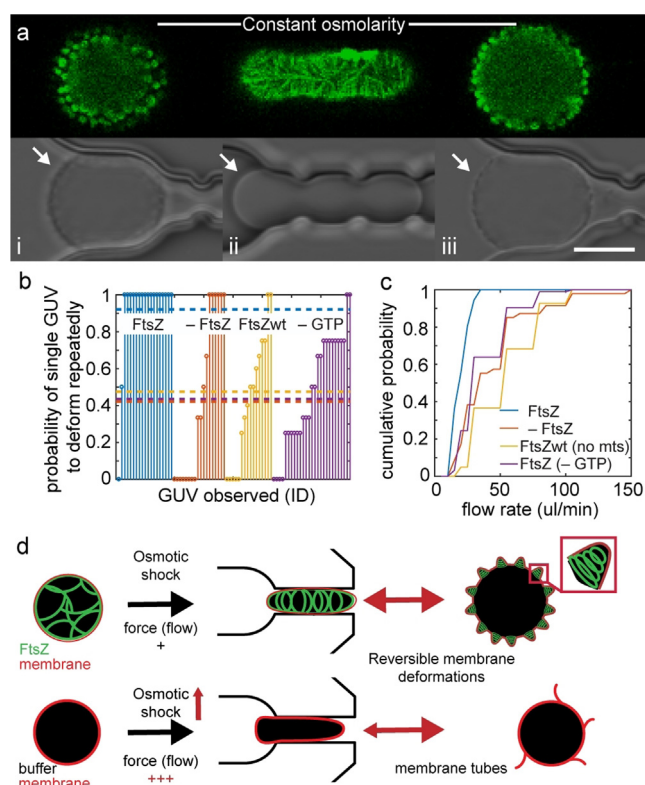
Figure 3. Reversible transitions between FtsZ filaments and rings allow reversible deformation of FtsZ-GUVs. a) Confocal images of a trapped and elongated GUV containing FtsZ filaments (i-iii, FtsZ shown in green, top) and corresponding DIC images (bottom). White arrows point to membrane topography changes. Scale bar is 10 μm. b) Probability that an individual GUV could be deformed five times for FtsZ-GUVs or control GUVs without FtsZ (red), with FtsZ-wt without membrane targeting sequence (-mts, purple) and with FtsZ without GTP in the buffer (no dynamic FtsZ polymerization, yellow). The value for the mean deformation probability for each experimental condition is plotted as a horizontal line (color-coded). c) Cumulative probability of flow rate required to deform FtsZ- or control GUVs (controls as in (b)). d) Schematic depiction of model: FtsZ structural reorganization from filaments to rings stores membrane reversibly in protrusions, facilitating transitions between GUV shapes. n(GUVs) = 17–35 (controls) and 19 (FtsZ) from >10 independent experiments.

droplets to spheroid-like shapes.[24] In contrast to our observations, they reported FtsZ alignment along the long axis of deformed droplets.[24] In their experiments, however, FtsZ is not membrane-anchored which likely explains the discrepancy. In principle, our microfluidic chip can deform many GUVs in parallel. In practice, we studied single GUVs at a time to resolve the GUVs' responses at maximal temporal resolution. However, the large number of traps was still advantageous to select specific GUVs (e.g. those encapsulating FtsZ) from a heterogeneous population.

Using these traps to deform FtsZ-GUVs, we show that imposing a rod-like geometry with a central membrane neck is sufficient to align FtsZ filaments along the short axis, preferentially at the neck location, mimicking FtsZ assembly into the Z-ring at the division site in live bacteria. This is in agreement with previous results for elongated lipid-bilayer coated containers or liposomes.[14,25,26] When rod-shaped

GUVs were released from the traps, GUVs relaxed back into a spherical shape with a lower surface/volume ratio. As expected, the concomitant excess of membrane area led to the formation of membrane tubules in absence of FtsZ. However, FtsZ-GUVs showed highly-curved membranes in form of cone-like, FtsZ-filled membrane protrusions as filaments reorganized into ring-like structures, independently of GUV size. Low membrane tension has been shown to play an important role for FtsZ filaments to induce membrane shape changes:[27] FtsZ reorganization similar to that observed by us has also been shown on deflated vesicles decorated with FtsZ on the outside.[23]

Interestingly, changes in membrane and filament organization were fully reversible: repeated GUV trapping and release cycled FtsZ-GUVs between (1) a state of tense GUV membranes, with elongated FtsZ filaments and macroscopically smooth membrane surfaces, and (2) a state of relaxed GUV membranes, with GUV membranes showing protrusions stabilized by ring-like FtsZ filaments (see Movie 2 and 3).[23] In contrast, shape changes in control GUVs required increasingly higher forces and/or repeated osmotic deflation. Therefore, we conclude that FtsZ on its own is able to not only actively influence membrane shapes, but also facilitates externally-induced changes by conserving and releasing excess membrane area (in an energy-dependent process). Our results suggest that FtsZ organization into ring-like filaments and FtsZ-driven membrane deformation may only occur as membrane tension is decreased during the division process (e.g. by de novo membrane synthesis), and that this could contribute to controlling the timing of cell division machinery assembly and thus cytokinesis. Reorganized FtsZ filaments may then also constrict lipid membranes, generating forces by GTP-fueled treadmilling.[28,29]

Overall, we present this microfluidic device as a platform for studying the effect of compartment geometry and membrane tension on processes reconstituted in and on the membrane of GUV-based minimal cells. In future experiments, these membrane tension changes could be measured quantitatively using tension-sensitive dyes or by quantifying the hydrodynamic forces in our microfluidic devices.[30] Beyond GUVs, our traps could also be used to deform vesicle-like membranes derived from cells, such as spheroblasts[31] and giant plasma membrane-derived vesicles.[32,33] Likewise, it will be interesting to study compartment geometry effects on other processes, such as MreB, the Min reaction-diffusion system, or the cell-polarity inducing Cdc42 system.[34,35] With the increasing capacity to create artificial, minimal cells, for example, by encapsulation of cell-free expression systems,[36] a device such as the one presented herein will be useful for studying how compartment geometry affects the behavior of increasingly complex molecular networks.

Acknowledgements

Conflict of interest

The authors declare no conflict of interest.

Keywords: cell division · membranes · microfluidics · protocells · vesicles

[1] P. Niethammer, *Science* **2004**, *303*, 1862–1866.
[2] M. Schmick, P. I. H. Bastiaens, *Cell* **2014**, *156*, 1132–1138.
[3] D. Thalmeier, J. Halatek, E. Frey, *Proc. Natl. Acad. Sci. USA* **2016**, *113*, 548–553.
[4] A. Haupt, N. Minc, *J. Cell Sci.* **2018**, *131*, jcs214015.
[5] K. A. Ganzinger, P. Schwille, *J. Cell Sci.* **2019**, *132*, jcs227488.
[6] M. D. Vahey, D. A. Fletcher, *Curr. Opin. Cell Biol.* **2014**, *26*, 60–68.
[7] A. Martos, M. Jiménez, G. Rivas, P. Schwille, *Trends Cell Biol.* **2012**, *22*, 634–643.
[8] P. Schwille, J. Spatz, K. Landfester, E. Bodenschatz, S. Herminghaus, V. Sourjik, T. J. Erb, P. Bastiaens, R. Lipowsky, A. Hyman, P. Dabrock, J.-C. Baret, T. Vidakovic-Koch, P. Bieling, R. Dimova, H. Mutschler, T. Robinson, T.-Y. D. Tang, S. Wegner, K. Sundmacher, *Angew. Chem. Int. Ed.* **2018**, *57*, 13382–13392; *Angew. Chem.* **2018**, *130*, 13566–13577.
[9] S. Kretschmer, K. A. Ganzinger, H. G. Franquelim, P. Schwille, *BMC Biol.* **2019**, *17*, 43.
[10] J. Xiao, E. D. Goley, *Curr. Opin. Microbiol.* **2016**, *34*, 90–96.
[11] E. Bi, J. Lutkenhaus, *Nature* **1991**, *354*, 161–164.
[12] C. A. Hale, P. A.. de Boer, *Cell* **1997**, *88*, 175–185.
[13] S. Pichoff, J. Lutkenhaus, *Mol. Microbiol.* **2005**, *55*, 1722–1734.
[14] S. Arumugam, Z. Petrášek, P. Schwille, *Proc. Natl. Acad. Sci. USA* **2014**, *111*, E1192–E1200.
[15] D. A. Ramirez-Diaz, D. A. García-Soriano, A. Raso, J. Mücksch, M. Feingold, G. Rivas, P. Schwille, *PLOS Biol.* **2018**, *16*, e2004845.
[16] S. Mellouli, B. Monterroso, H. R. Vutukuri, E. te Brinke, V. Chokkalingam, G. Rivas, W. T. S. Huck, *Soft Matter* **2013**, *9*, 10493.
[17] T. J. Lagny, P. Bassereau, *Interface Focus* **2015**, *5*, 20150038.
[18] T. Robinson, P. Kuhn, K. Eyer, P. S. Dittrich, *Biomicrofluidics* **2013**, *7*, 044105.
[19] Q. Wang, M. Taschner, K. A. Ganzinger, C. Kelley, A. Villasenor, M. Heymann, P. Schwille, E. Lorentzen, N. Mizuno, *Nat. Commun.* **2018**, *9*, 4684.
[20] S. Pautot, B. J. Frisken, D. Weitz, *Langmuir* **2003**, *19*, 2870–2879.
[21] E. J. Cabré, A. Sánchez-Gorostiaga, P. Carrara, N. Ropero, M. Casanova, P. Palacios, P. Stano, M. Jiménez, G. Rivas, M. Vicente, *J. Biol. Chem.* **2013**, *288*, 26625–26634.
[22] M. Osawa, D. E. Anderson, H. P. Erickson, *Science* **2008**, *320*, 792–794.
[23] D. A. Ramirez-Diaz, A. Merino-Salomon, F. Meyer, M. Heymann, G. Rivas, M. Bramkamp, P. Schwille, *bioRxiv* **2020**, https://doi.org/10.1101/587790.
[24] F. Fanalista, A. Birnie, R. Maan, F. Burla, K. Charles, G. Pawlik, S. Deshpande, G. H. Koenderink, M. Dogterom, C. Dekker, *ACS Nano* **2019**, *13*, 5439–5450.
[25] K. Zieske, P. Schwille, *eLife* **2014**, *3*, e03949.
[26] M. Osawa, H. P. Erickson, *Mol. Microbiol.* **2011**, *81*, 571–579.
[27] S. Arumugam, E. P. Petrov, P. Schwille, *Biophys. J.* **2015**, *108*, 1104–1113.
[28] E. Godino, J. N. López, I. Zarguit, A. Doerr, M. Jimenez, G. Rivas, C. Danelon, *bioRxiv* **2020**, https://doi.org/10.1101/2020.03.29.009639.
[29] L. T. Nguyen, C. M. Oikonomou, G. J. Jensen, *bioRxiv* **2019**, https://doi.org/10.1101/737189.
[30] A. Goujon, A. Colom, K. Straková, V. Mercier, D. Mahecic, S. Manley, N. Sakai, A. Roux, S. Matile, *J. Am. Chem. Soc.* **2019**, *141*, 3380–3384.
[31] T. G. Chew, J. Huang, S. Palani, R. Sommese, A. Kamnev, T. Hatano, Y. Gu, S. Oliferenko, S. Sivaramakrishnan, M. K. Balasubramanian, *J. Cell Biol.* **2017**, *216*, 2657–2667.
[32] H. Pick, A. C. Alves, H. Vogel, *Chem. Rev.* **2018**, *118*, 8598–8654.
[33] E. Sezgin, H.-J. Kaiser, T. Baumgart, P. Schwille, K. Simons, I. Levental, *Nat. Protoc.* **2012**, *7*, 1042–1051.
[34] K. J. A. Vendel, S. Tschirpke, F. Shamsi, M. Dogterom, L. Laan, *J. Cell Sci.* **2019**, *132*, jcs217554.
[35] H. Shi, B. P. Bratton, Z. Gitai, K. C. Huang, *Cell* **2018**, *172*, 1294–1305.
[36] D. Garenne, V. Noireaux, *Curr. Opin. Biotechnol.* **2019**, *58*, 19–27.

Supporting Information

FtsZ Reorganization Facilitates Deformation of Giant Vesicles in Microfluidic Traps**

Kristina A. Ganzinger+, Adrián Merino-Salomón+, Daniela A. García-Soriano,
A. Nelson Butterfield, Thomas Litschel, Frank Siedler, and Petra Schwille*

anie_202001928_sm_miscellaneous_information.pdf
anie_202001928_sm_Movie1.mp4
anie_202001928_sm_Movie2.mp4
anie_202001928_sm_Movie3.mp4

Material and Methods

Chemicals

All reagents used in this work were from Sigma-Aldrich. Lipid compositions were prepared with DOPG (1,2-Dioleoyl-sn-glycero-3 phosphoglycerol, Avanti Polar Lipids, Inc.), EggPC (L-α-phosphatidylcholine (Egg, Chicken), Avanti Polar Lipids. Inc.), DOPC (1,2-Dioleoyl-sn-glycero-3-phosphocholine, Avanti Polar Lipids, Inc.) and DOPE-ATTO655 (ATTO-tec).

Microfluidic device fabrication

The microfluidic vesicle trap squeezer devices were fabricated from PDMS using rapid prototyping and standard soft lithography techniques. The geometry was inspired by the traps we used in a previous study[1], but here extended the trapping structure along the flow axis with a narrow squeezing channel containing evenly spaced indentations, and added a larger entrance funnel to increase GUV capture efficiency (Figure S1). We found it advantageous to design device channels with a high density of traps, which have progressively narrower funnels and squeezing channels towards the outlet.

Wafer fabrication and coating. Master moulds of 13µm height were produced on a 4-inch silicon wafer (University Wafer) using SU-8 3010 (Microchem corp.) according to the manufacturer's data sheet and developed in PGMEA (process parameters were optimized by direct laser writing (uPG101, Heidelberg Instruments, Germany) as described in Figure S2 to S4). Due to the small size of the PDMS features to be released from the mould, fluorophilic coating with Cytop was used routinely prior to the hard-baking step. In brief, 250 µL of a 1:10 dilution of Cytop CTL-809M in CTSOLV180 (Asahi Glass Co. Ltd., Japan) was dispensed on the SU-8 features and excess removed by spinning at 4000rpm for 1min. The coated wafer was then hard-baked for 30min at 180°C on a hot-plate and then allowed to cool down to room temperature slowly by turning off the heating. Quality control of the final SU-8 molds was done by laser profilometry (VKX1100, Keyence, Japan; Figure S5).

PDMS moulding. A 10:1 mixture of PDMS base and curing agent (Sylgart 184, Dow Corning) was homogenized and degased simultaneously for 2min using a Thinky Planetary Vacuum Mixer (ARV-310, Thinky Corp., Japan) and subsequently poured to about 4mm height onto the master in a petri-dish. After curing over-night in an oven at 75°C the PDMS was peeled off the wafer and cut to size. Fluid ports were then punched with a 3 mm and 0.75 mm diameter biopsy puncher (World-Precision-Instuments) for the reservoir and outlet, respectively. For quality control, images of PDMS chips were taken by Scanning Electron Microscopy (Mira3, Tescan) using sputter coated samples (1.5nm Pd/Pt, Cressington 208HR). In brief, samples were sputter coated with platinum/palladium on a high-resolution automatic sputter coater (Cressington 208HR) at 20 mA and 0.1mbar Ar for 3x 20s. Thickness of the applied coatings was measured with a build-in thickness controller to be 2.0 nm. Coated surfaces were viewed using a TESCAN MIRA3 FESEM operating at an accelerating voltage of 10 kV in SE mode. The microchannels of chips with well-resolved structures were then sealed by plasma bonding them onto glass cover slips (24 × 32 mm, thickness 1.5, VWR) using oxygen plasma (15 s at 0.3mbar, 50% power, model ZEPTO, Diener electronic, Germany) and baking them for 15–30 min at 75 °C on a hot-plate.

1

Preparation of FtsZ-containing GUVs

Giant unilamellar vesicles (GUVs) were prepared using a water-in-oil (w/o) emulsion transfer method.[2] The lipid-oil-suspension was made by first drying lipid films from lipids dissolved in chloroform (Uvasol): L-α-phosphatidylcholine (Egg, Chicken; EggPC) and 1,2-dioleoyl-sn-glycero-3-phospho-(1'-rac-glycerol (DOPG) in a ratio of 80:20 mol % (both Avanti Lipids), adding 0.02 or 0.07 mol % of 1,2-dioleoyl-sn-glycero-3-phosphoethanolamine (DOPE)-ATTO655 (ATTO-TEC) to label the lipid membrane. For this, the chloroform was evaporated from the lipid mixture by placed in a desiccator connected to a vacuum pump for >1h. The phospholipid-oil suspension was prepared by dissolving the lipid film in mineral oil (M5904, Sigma Aldrich) and sonicating the suspension for 30 min, reaching a homogeneous suspension with 0.5 mg/mL as final lipid concentration. GUVs were prepared by adding 15 μl of inner buffer into 500 μl phospholipid oil suspension pipetting carefully up and down to create a homogeneous emulsion. This emulsion was deposited over a lipid monolayer previously formed for >1h between 500 μl of phospholipid-oil suspension and 500 μl of the outer buffer in 2 ml Eppendorf tubes. The mixture was centrifuged for 10 min at 100 rcf to deposit the GUVs at the bottom of the tube. GUVs were collected and added into the inlet reservoir of the microfluidic chip or into microtitre plates for visualization.

Inner solution of FtsZ samples was prepared by diluting purified FtsZ-YFP-mts[3] to a final concentration of 2 μM in its buffer (25 mM Tris-HCl, 125 mM KCl, 6.25mM $MgCl_2$ pH 7.5) and adding 20% iodixanol (OptiPrep™, Sigma Aldrich) to increase the density of the encapsulated solution, in order to improve the vesicle yield obtained.[4] FtsZ samples were encapsulated in the polymeric form by adding 2 mM GTP and previously described GTP regeneration system (RS) to prolong the polymerised FtsZ lifetime[5]. Control FtsZ without GTP was prepared without the presence of the regeneration system. In all experiments, the outer and inner buffer solutions were the same but an additional 180 mM glucose was added to the outer solution to match the osmolarity of the inner solution (~480 mOsm/kg) (measured with Fiske Micro-Osmometer Model 210).

Samples containing FtsZ wt were prepared by diluting FtsZ wt to a final concentration of 2 μM including 0.8 μM FtsZ-wt-Alexa 488 as a fluorescent tracer. Both proteins were cordially provided by German Rivas' laboratory, purified and labelled as described.[5] (We note similar results were obtained using 1.65 μM, 1.4mM GTP and 2mM $MgCl_2$ as in reference [6](Figure S9). Experiments using GUVs with higher concentrated content were made by proportionally increasing all inner buffer components (including FtsZ, GTP regeneration system and iodixanol) by 20% or 50%. Glucose content of both outer solutions were also increased to match the osmolarities of the inner and outer buffers (620 mOsm/kg and 740 mOsm/kg for 20% and 50% respectively). Control GUVs without FtsZ were prepared using FtsZ buffer adding 160 mM glucose and 20% iodixanol to match the osmolarity of FtsZ-GUVs so the outer buffer was identical in all conditions.

We note that the yield of FtsZ-containing GUVs of desired sizes (10-20μm diameter) was variable even under identical experimental conditions, and that not all GUVs showed FtsZ filaments at the GUV membranes, likely due to variations in the final FtsZ concentration inside the vesicles. A high degree of variation in both vesicle content and yield is commonly observed for GUVs made by emulsion transfer. As we trapped many GUVs in our microfluidic device, we could focus our studies on those GUVs that initially showed visible FtsZ filaments when trapped and imaged by confocal microscopy.

2

Handling of microfluidic device and experimental setup

Microfluidic devices were passivated to prevent vesicle rupture upon contact with the walls by adding 20 µL of pluronic F-127 (Sigma Aldrich) at 10-50 mg/mL in phosphate buffered saline (PBS) in the inlet reservoir and centrifuging at 800 rcf for 10 min. The remaining pluronic was removed and cleaned with outer buffer. After passivation, the microfluidic devices were loaded with approximately 40 µl volume of vesicles in the inlet reservoir. A syringe joined to a pump system (neMESYS base 120 with neMESYS 290N, cetoni, Germany) and filled with 250 µl of ~60% ethanol was connected to the outlet of the device, avoiding any air in between the device and the syringe. Negative flow was applied at a rate of approximately 5-10 µl/h to draw the vesicle solution and reagents through the fluid channels during the experiments. After 10-20 min, a high number of vesicles were collected in the microfluidic traps. To deform the GUVs, we osmotically deflated them by replacing the buffer solution in the inlet reservoir with fresh buffer with a higher osmolarity. Some buffer exchanges with progressively higher osmolarity were sometimes necessary to induce vesicle deformation. Osmolarity was not increased more than 10-15% at a time to avoid vesicle rupture. Once the vesicles were partially deformed, the flow rate was progressively increased to introduce the GUVs completely into the trap, deforming them slowly. To move the vesicles out of the traps (and back in again, this time keeping osmolarity constant), the flow rate was usually changed within a range of ±15-20 µL/h for FtsZ experiments, although this flow rate range was increased depending on the conditions we tested. Our pump set up does not allow to calculate the forces exerted by the fluid flow on the vesicles inside the chip.

Experiments with FtsZ GUVs in the absence of trapping

FtsZ vesicles were deposited in a microtite plate for imaging (Greiner Bio-One, 364-well glass bottom SensoPlate™) previously passivated by 1 min of plasma cleaning (air plasma; model MiniFlecto®, Plasma Technology, Germany) and followed by a 30 min incubation with 10 mg/mL pluronic F-127 to avoid vesicle rupture. The plate was incubated tilted at ~45˚C for 10 min to favour vesicle accumulation in one of the borders improving thus their visualization. Vesicle deflation was then induced by replacing most of the buffer solution with fresh buffer with a higher osmolarity. For experiments with FtsZ GUVs, the osmotic difference varies from ~480 mOsm/kg in its initial buffer to ~560 mOsm/kg in the higher osmotic buffer, while for higher concentrated FtsZ vesicles, the osmolarity varies from ~620 to ~740 mOsm/kg in vesicles with 20% increased content and from ~740 to ~840 mOsm/kg for vesicles with 50% higher concentrated content. "Undetermined" category shown in Figure S9 includes vesicles with no protein in the membrane (depolymerized) and GUVs with no obvious filament or ring structures but showing protein binding to the membranes (likely meaning that the protein is polymerized in filaments smaller than the resolution of our confocal imaging (<1µm)).

Microscopy setup

All the experimental data were recorded with an LSM 780 confocal microscope (Carl Zeiss, Germany) equipped with a C-Apochromat, 40x/1.2 W objective. Fluorescence emission was detected by using laser excitation at 488 nm for YFP (FtsZ experiments) and Alexa 488 (FtsZ-wt

3

experiments), while 633 nm was used for Atto655. All the experiments were conducted at room temperature.

Image analysis

All image data was manually prepared for visualisation using ImageJ[7]. Image data was further analysed using ImageJ[7], either manually or using ImageJ plugins, or by MATLAB scripts as described in the following section.

Vesicle deformation (Figures 1f,g; 3b,c; S6; S12) was quantified using ImageJ by fitting an ellipse to the vesicle through the ATTO 655 laser channel. Aspect ratios in deformed or partially deformed vesicles were analysed by using the major and minor axis of the ellipses fitted in vesicles under different osmotic conditions and flow rates. Excel and MATLAB (2014/18b, The MathWorks; Statistics Toolbox) were used for plotting and descriptive statistics. For Figures 3b,c and S12a, the threshold for counting a GUV as successfully deformed was a deformation ratio of 0.7, which corresponds the mean value achieved for FtsZ-GUVs after an initial osmotic deflation.

Quantification of the volume change before and after osmotic shock was attempted but measurement scatter was very large, due to GUVs movement during z-stack acquisition, and as volume change was small this error was to large to allow us to discriminate volumes size before and after osmotic shock with confocal microscopy.

For Figure 2, filament angles were calculated using first the RidgeDetection plug-in from ImageJ (https://zenodo.org/badge/latestdoi/18649/thorstenwagner/ij-ridgedetection) that is based on the ridge / line detection algorithm by Steger.[8] The settings used were: line width '1.5', high Contrast '300', low contrast '100' and method for overlap resolution: 'slope'. The coordinates for the traced filaments were then exported to MATLAB via the ImageJ ROI tool for further automated analysis. We (1) calculated filament angles with respect to the GUV axis (Figure S7) and assigned whether they were positioned in the 'neck' region of the elongated GUV or not (Figure 2b; this region was manually defined around trap feature using the bright field image) and (2) analysed filament lengths and plotted the distribution of filament lengths for trapped (elongated) and released (spherical) vesicles (Figure 2g). Calculation of relaxation times (Figure 2c; S8a) was done manually by counting frames between trapping/releasing GUVs and complete resolution of FtsZ filaments or rings/protrusions.

Filament and ring detection in experiments with non-trapped vesicles (Figure S9) was done by collecting Z-stacks images from different positions selected in a tile image of the whole sample well. Z-stack spacing 2 μm was selected to optimize the vesicle visualization. The same procedure is repeated after the addition of the higher osmolarity fresh buffer to deflate the vesicles. Addition of new buffer involves a vesicle movement that makes difficult to track single vesicle state before and after the osmotic change. Filament and Ring detection was done manually using ImageJ. Further data analysis was done using MATLAB and Excel.

Estimate of mechanical membrane tension upon iso-osmotic GUV release from geometric confinement (microfluidic traps) from microscopy data

To infer the change in membrane tension that a GUV experiences as it is iso-osmotically released from the traps, we determine the GUV shape transformation upon trapping from our microscopy data and hence extrapolate the new GUV's surface area for elongated GUVs. In the absence of external forces or constraints (*i.e.* after release from the traps), a GUV membrane aims to attain

4

a new optimal area A_{opt} for its now spherical shape, which corresponds to the optimal packing of its molecules. The membrane thus experiences a mechanical tension, σ_{mec}, when its original area A deviates from this new optimal area A_{opt}. This mechanical tension can be expressed as[9]

$$\sigma_{mec}(A) = K_A \frac{A - A_{opt}}{A_{opt}} \text{ with } K_A \text{ being on the order of } 200 \frac{mN}{m} \text{ for lipid bilayers.}^{[10]}$$

Measuring the length and height of the deformed vesicles (Figure S6) and assuming a cylindrical shape, we obtain A_C and V_C of the cylinder. Then we can calculate the surface area A_S upon reassuming a spherical shape (at constant volume $V_C = V_S$). With $\frac{A - A_{opt}}{A_{opt}} = \frac{A_S - A_C}{A_C}$:

$$\sigma_{mec}(A_S) = -70 \pm 10 \frac{mN}{m}; \; n(GUV) = 10$$

References

[1]   Q. Wang, M. Taschner, K. A. Ganzinger, C. Kelley, A. Villasenor, M. Heymann, P. Schwille, E. Lorentzen, N. Mizuno, *Nat. Commun.* **2018**, *9*, 4684.

[2]   L. L. Pontani, J. van der Gucht, G. Salbreux, J. Heuvingh, J. F. Joanny, C. Sykes, *Biophys J* **2009**, *96*, 192–198.

[3]   M. Osawa, D. E. Anderson, H. P. Erickson, *Science (80-.).* **2008**, *320*, 792–794.

[4]   T. Litschel, B. Ramm, R. Maas, M. Heymann, P. Schwille, *Angew. Chemie Int. Ed.* **2018**, *57*, 16286–16290.

[5]   J. M. González, M. Jiménez, M. Vélez, J. Mingorance, J. M. Andreu, M. Vicente, G. Rivas, *J. Biol. Chem.* **2003**, DOI 10.1074/jbc.M305230200.

[6]   D. A. Ramirez-Diaz, A. Merino-Salomon, F. Meyer, M. Heymann, G. Rivas, M. Bramkamp, P. Schwille, *bioRxiv* **2020**, 587790.

[7]   C. T. Rueden, J. Schindelin, M. C. Hiner, B. E. DeZonia, A. E. Walter, E. T. Arena, K. W. Eliceiri, *BMC Bioinformatics* **2017**, *18*, 529.

[8]   C. Steger, *IEEE Trans. Pattern Anal. Mach. Intell.* **1998**, *20*, 113–125.

[9]   R. Lipowsky, *Adv. Colloid Interface Sci.* **2014**, *208*, 14–24.

[10]   E. Evans, D. Needham, *J. Phys. Chem.* **1987**, *91*, 4219–4228.

5
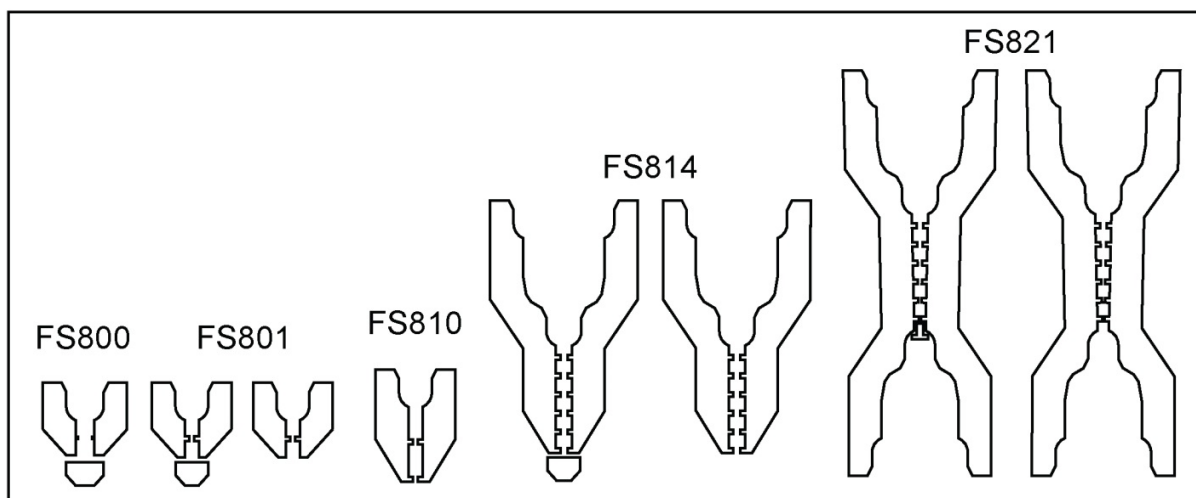
Figure S1. Evolution of microfluidic designs. To trap and squeeze GUVs in a microfluidic environment funnel like structures with various features were designed and tested. Structures are named by Experiment-ID. The central idea in the beginning was to capture GUVs in a funnel and then, by carefully rising the flow, to squeeze them past the subsequent neck. Indentations were intended to mimic the naturally occurring constriction site that is a part of cell division. Finally, the addition of stoppers was tested to prevent GUVs from escaping the traps too early.

In FS800 indentations were too small to be reproduced sufficiently precise and they did not induce a clear indentation of membranes of trapped GUVs. With FS801, a stopper was found to be necessary but the overall design showed already a reliable performance, and therefore all necessary exposure optimizations were done with this design. For some bigger GUVs, however, the relatively short neck section was a problem. Our preferred design was finally found with FS814, which was used in combination with a stopper for all experiments reported in this work. The prototype FS821 with a double funnel to facilitate back and forth shifting of GUVs and a slight narrowing of the central channel was not found to show any advantages.

6
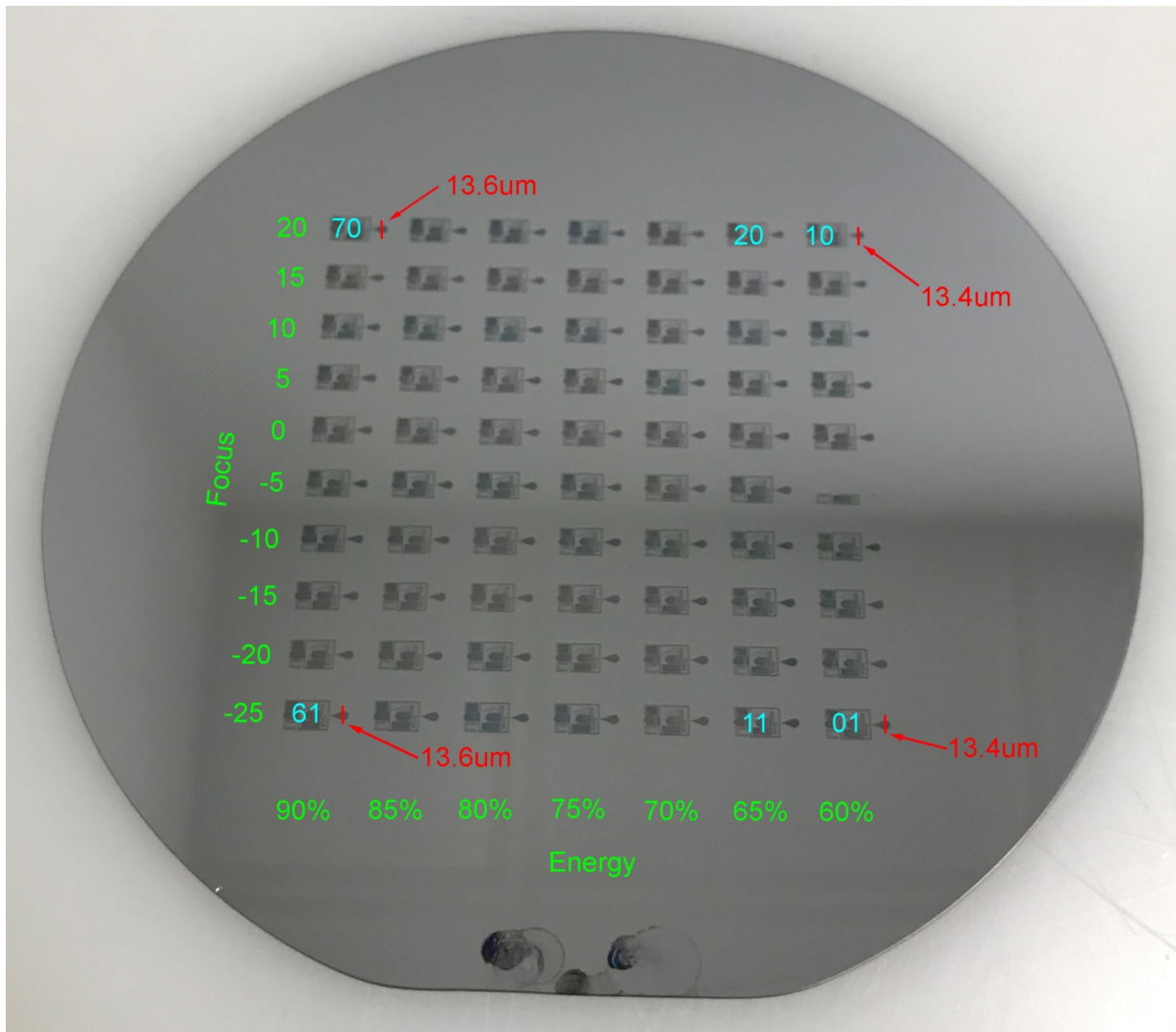
Figure S2. Optimization of Exposure Parameters. To find the best set of parameters for rapid prototyping via direct laser writing, a 7x10 array of test structures comprising the most delicate structural features was exposed on a 4 inch silicon wafer. Parameters varied were focus setting (y-direction; arbitrary units) and energy attenuation (x-direction; % of 10mW). For unique identification positions in the array are numbered from bottom to top and right to left as indicated by cyan numbers. Results of height measurements by laser profilometry are indicated in red.

7

Figure S3. Light-microscopic inspection of the test array from Fig.S2. For all positions, images were taken from the same part of the test structure at constant microscopic settings. This overview is best suited to narrow down the parameter space to useful values. Close-ups indicating the subsequent decision making process are shown in Fig.S4

8
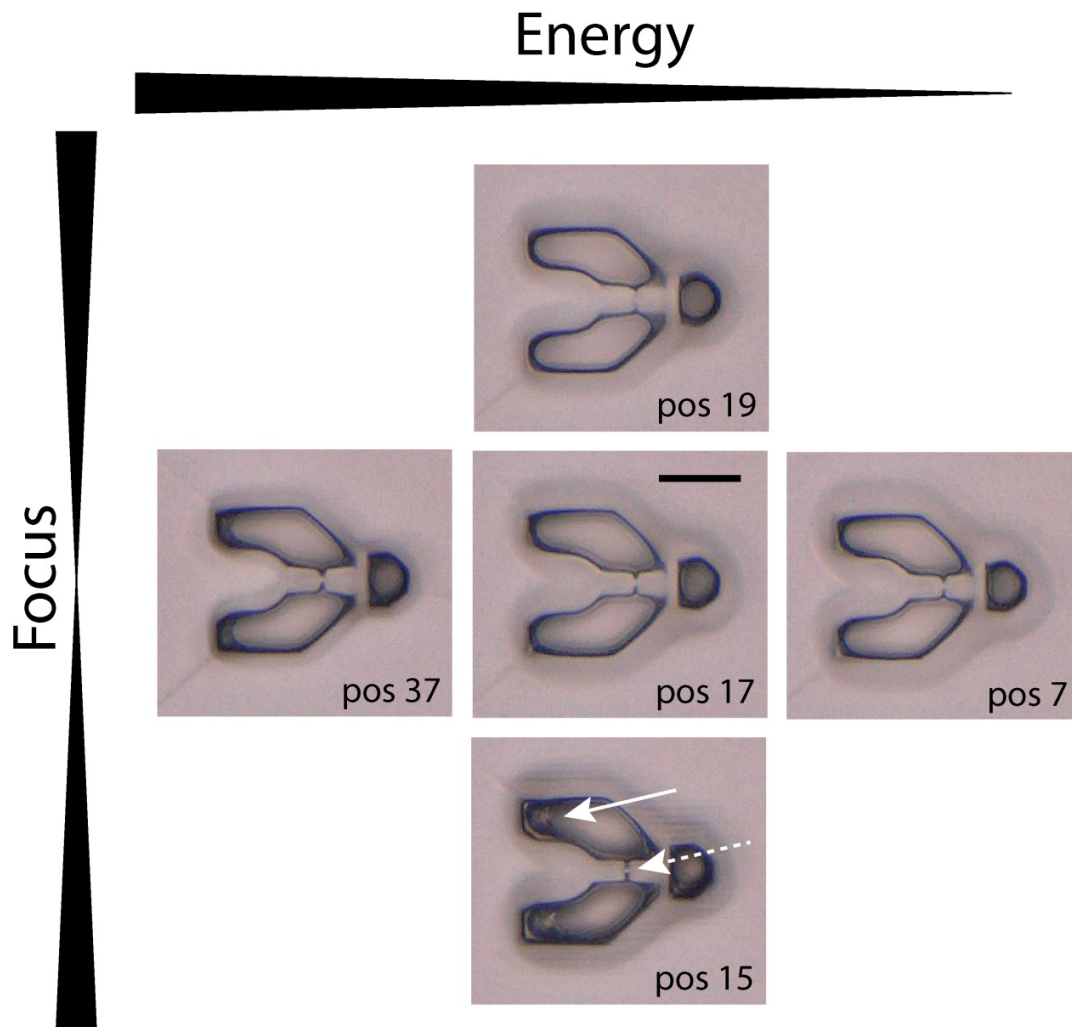
Figure S4. Optical inspection of the test structures from the array (Fig. S3) by light microscopy. In the course of the experiment, exposure energy and focus correction were varied as indicated on the top and left. Position numbers correspond to the ones given in the overview (Fig.S3). Areas important for quality judgement are marked by white arrows. Changing focus correction from negative values to zero (pos15 -> pos17) reduces unwanted reflections on the wafer surface (solid arrow) at the expense of sharpness (dashed arrow). Shifting focus correction even further to the positive (pos19) shows clearly a blurring of the structure.

A similar effect can be observed for the energy setting: Too high energy settings lead to reflections at the bottom and therefore cure resist in unwanted regions (pos37), whereas too low energy settings produce too soft and therefore undefined structures (pos7). In both directions, the best compromise appeared to be in pos17. Starting from these settings, the best parameter set for production could be estimated and tested (resist: SU8-3010, 13um height; laser writer: Heidelberg Instruments uPG101, 2mm writing head, energy 67% of 10mW, defoc +2). Scale bar 20µm.

9
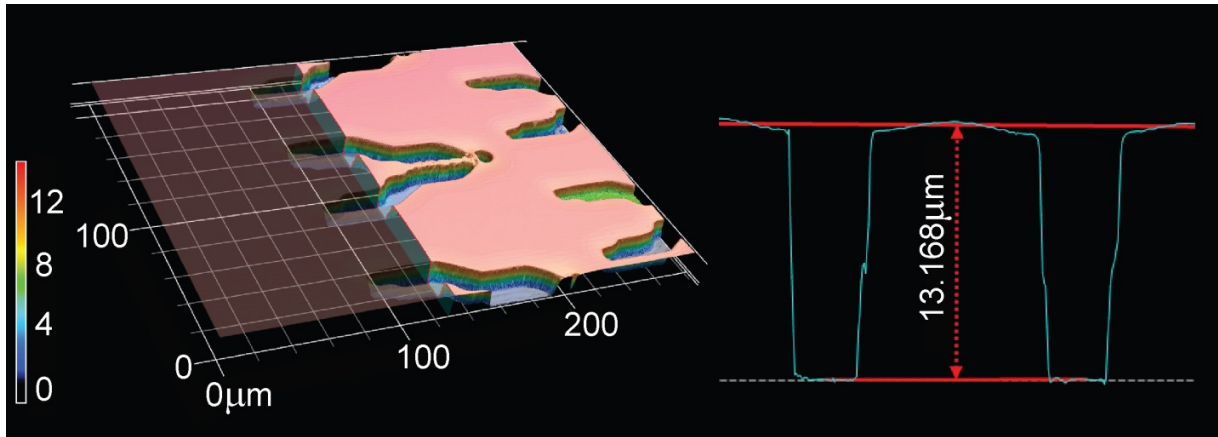
Figure S5. Quality control of final SU8 mold. The exact 3D structure of the final mold (FS814) was determined using laser profilometry (Keyence VKX1100). In the landscape representation (left), the smooth surface on the top and the intended steepness of the shoulders is visible. Height measurements on the 3D dataset can be done at any location (right).

10
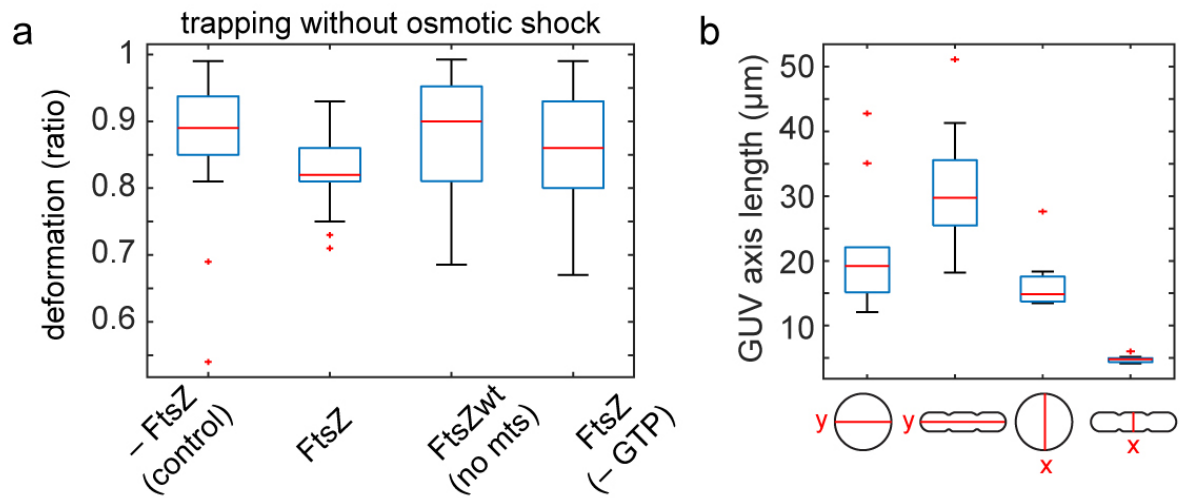
Figure S6 Maximum deformation of FtsZ- or control GUVs before osmotic deflation and determination of GUV aspect ratios after trapping and osmotic shock. a) Deformation of FtsZ- or control GUVs before osmotic deflation. Additional controls for Fig. 1f; data for GUVs with FtsZ-mts and without FtsZ is plotted again for comparison and identical to that of Fig. 1f. Additional controls are FtsZ-wt without membrane targeting sequence (mts) and with FtsZ without GTP in the buffer (no dynamic FtsZ polymerisation). b) The aspect ratio of trapped GUVs was manually determined in ImageJ at GUV mid plane; x and y axis length (input for the y/x ratio plotted in Fig. 1F). Box plot denotes median in red, interquartile range as blue box, the 2.7σ (99.3%) confidence interval as whiskers and outliers as red dots. n(GUVs) = 10.

11
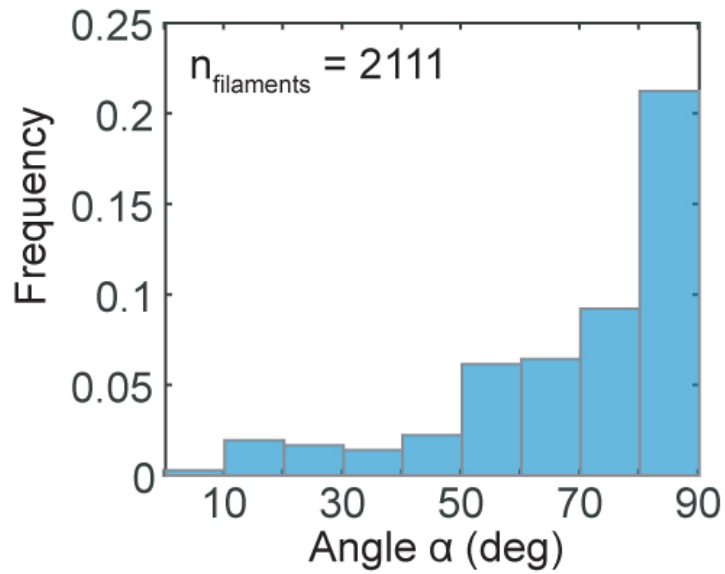
Figure S7 Orthogonal FtsZ filament alignment to the long axis in elongated GUVs. Elongation and indentation of GUVs containing FtsZ filaments leads to filament alignment orthogonal to the long axis at the GUV neck. Distribution of filament angles α for all filaments observed in maximum intensity projections of elongated GUVs. Angles were calculated as described in the methods section.
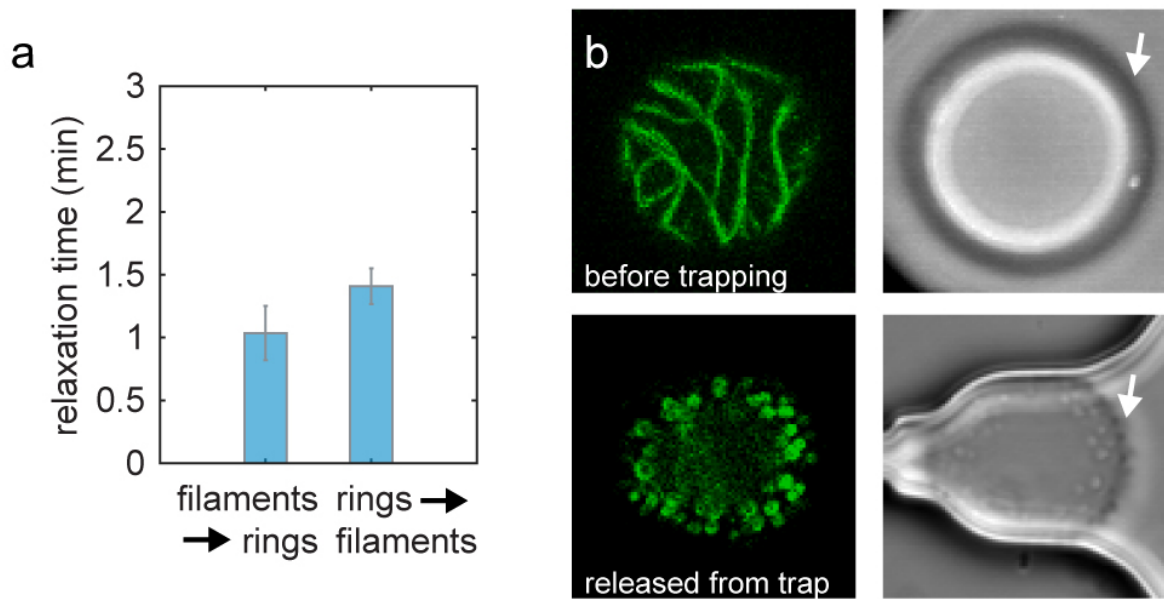
Figure S8 Upon membrane deflation (release from geometric confinement to spherical shape), FtsZ reorganises into dynamic rings that result in membrane protrusions. a) relaxation times for filament to ring transitions as observed by confocal microscopy of GUVs that were pushed out (filament -> rings) or into (rings -> filaments) traps. b) Confocal and corresponding bright field microscopy images of GUVs containing membrane-bound FtsZ filaments (green); example for elongated filaments observed in an untrapped GUV and ring-like filaments observed in a GUV after release from the trap, having assumed a spherical shape again. Note that the membrane shows protrusions after FtsZ filaments have rearranged into dynamic rings (bottom DIC image, white arrow) that are absent in the presence of long filaments (top DIC image, white arrow). Osmolarity was not changed in this experiment.

13
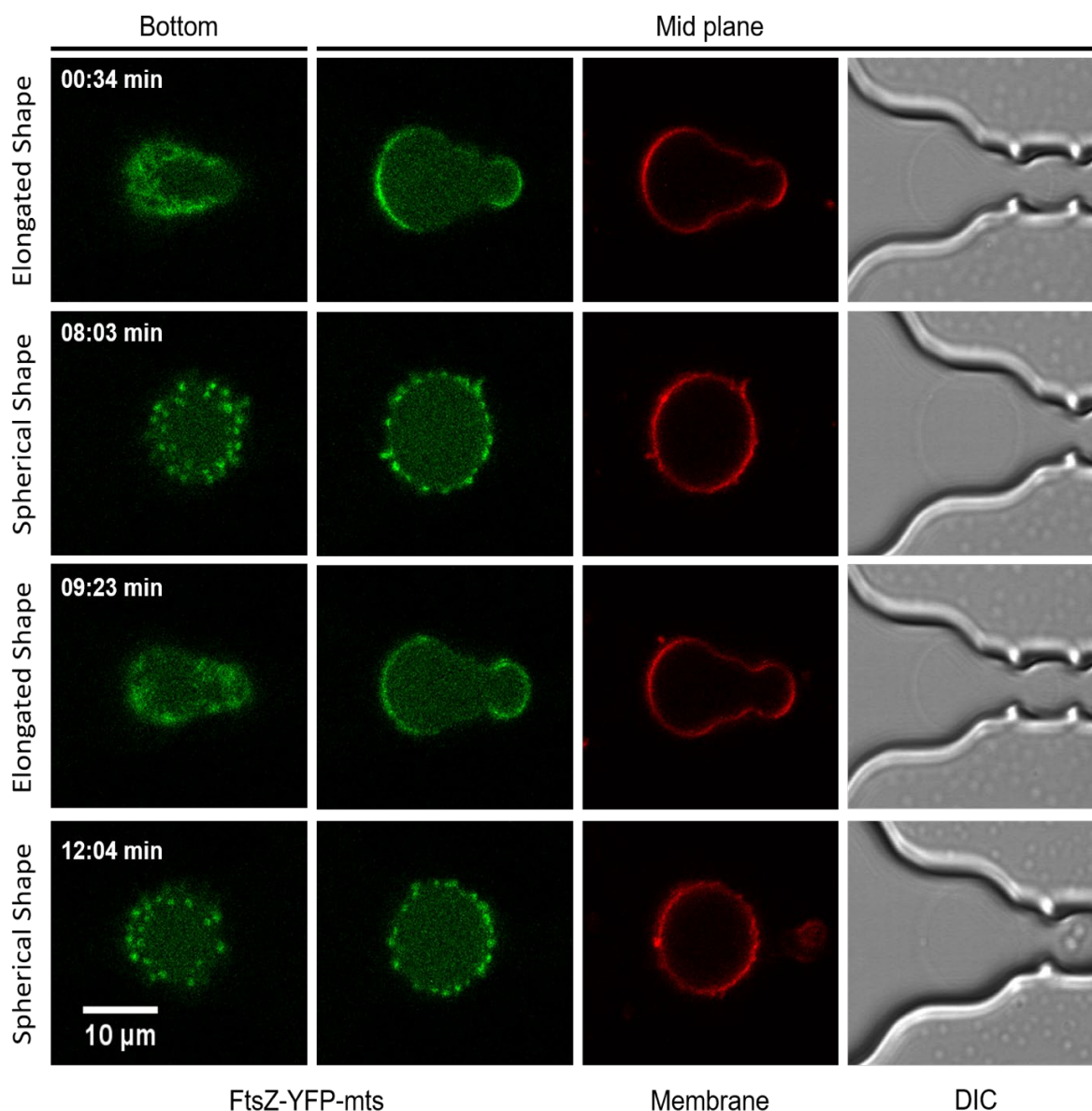
Figure S9 Different buffer conditions does not affect the behaviour of FtsZ. Slightly different buffer and protein conditions previously used in reference [6] were tested, showing that FtsZ is able to form membrane protrusions and filaments under this condition (1.65 µM FtsZ-YFP-mts and 1.4 mM GTP in buffer 125 mM KCl, 25 mM Tris-HCl, 2 mM MgCl$_2$), in agreement with results in our working buffer. Confocal images of a trapped and elongated FtsZ GUV into our microfluidic device. Images of FtsZ-YFP-mts (Green) at the bottom (left), and equatorial plane of the lipid vesicle.

14

Figure S10 Osmotic deflation alone favours FtsZ reorganization into dynamic rings. a) confocal and corresponding bright field microscopy images of non-trapped GUVs in a microtitre plate after an osmotic shock; some GUVs with FtsZ show membrane protrusions (white arrows, bright field image) with ring-like FtsZ filaments (white arrows, green). Scale bar is 10 µm. b) Maximum intensity projection of a GUV with elongated FtsZ filaments (top) and rings (bottom). Scale bars are 5 µm. c) Quantification of GUV populations (FtsZ) showing FtsZ organisation (filaments, rings, undetermined) before or after osmotic deflation. These results show that a mild deflation of FtsZ GUVs is enough to lead FtsZ filament reorganisation into dynamic rings when GUV membranes are not concomitantly tensioned by the microfluidic traps. Box plots denote median in red, interquartile range as blue box, the 2.7σ (99.3%) confidence interval as whiskers and outliers as red dots. d) Quantification of GUV populations showing FtsZ filament organisation (filaments, rings, undetermined) before or after osmotic deflation for GUVs made with our standard buffer conditions and GUVs made with buffers of higher concentrations of buffering components and FtsZ. Note that higher salts/FtsZ concentrations alone do not favour ring formation unless GUVs are osmotically deflated. Data are from >3 independent experiments and >100 GUVs per condition.

15

Figure S11 Membrane attachment of FtsZ is required to shape GUV membranes (into cone-like membrane spikes) upon relaxation from mechanically tensioned shapes or upon osmotic deflation. a) confocal and corresponding bright field microscopy images of non-trapped GUVs in a microtitre plate after an osmotic shock, GUVs with FtsZ-wt without membrane targeting sequence (mts) show no FtsZ-stabilised membrane protrusions after osmotic deflation b) Confocal images of the equatorial plane of an elongated (trapped) GUV (top row) and the same GUV after isosmotic release from the trap (bottom row), having reassumed a spherical shape. GUV contains FtsZ-wt without membrane targeting sequence (left, FtsZ wt-Alexa 488, green; middle, membrane labelled with DOPE-ATTO655; right, corresponding DIC images). Scale bar are 10 µm. Data is representative of GUVs from 12 independent experiments.

16
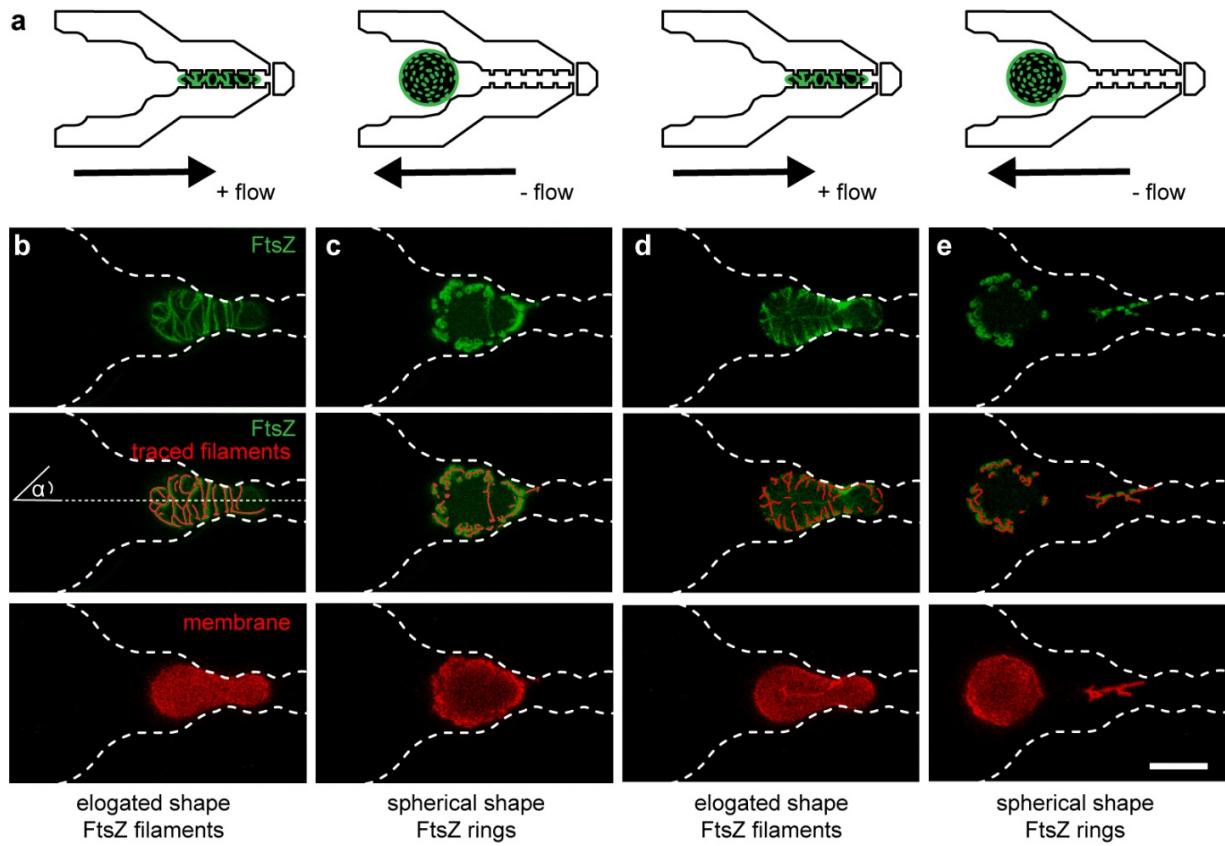
Figure S12 Reversible elongation and relaxation of FtsZ GUVs leads to transitions between FtsZ rings and long filaments. a) Schematic depiction of experiment. FtsZ forms elongated filaments in rod-shaped (tense) vesicles while FtsZ rings are formed when the vesicle is relaxed back to its spherical shape; b) confocal images of the equatorial plane of a trapped and elongated GUV showing FtsZ filaments (top), traced filaments (middle) and GUV membrane (bottom); FtsZ is shown in green. Trap outline is marked (white dotted line). c,d,e) transition of the same GUV between spherical c) and e) and elongated d) shapes purely by manipulation of flow rates and direction. Flow range was -15 to +10 ul/h and osmolarity was kept constant. Data is representative of GUVs from 12 independent experiments. The scale bar is 10 µm

17
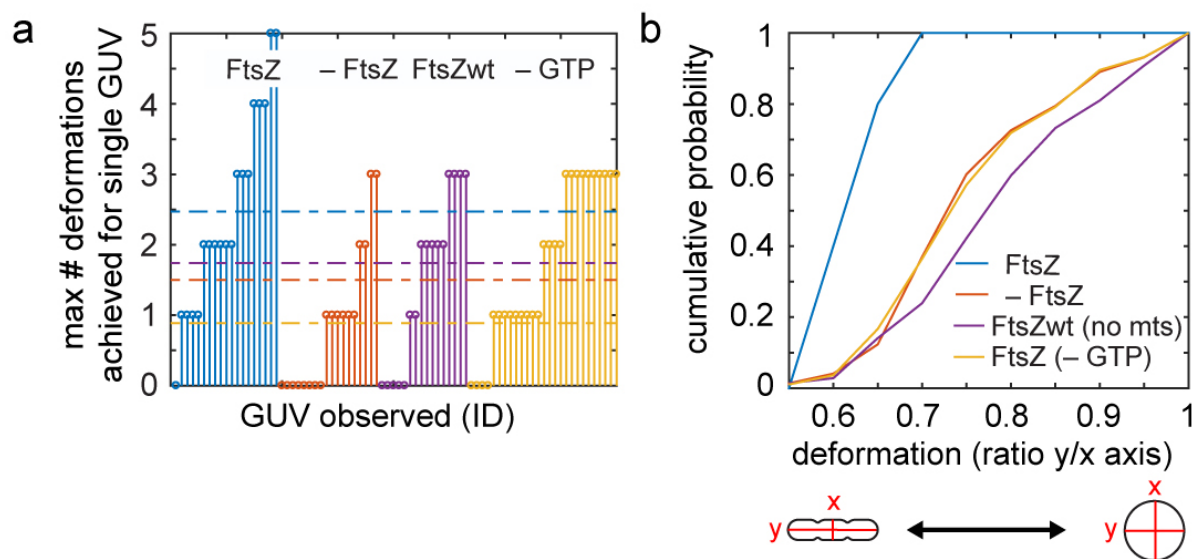
Figure S13 GUVs with a membrane-bound, dynamically polymerising FtsZ cytoskeleton can be deformed more often and more strongly under the same conditions (osmolarities, flow rates). a) Maximum number of deformations achieved for individual GUVs by repeated trapping for GUVs containing FtsZ or control GUVs without FtsZ (red), with FtsZ-wt without membrane targeting sequence (- mts, purple) and with FtsZ without GTP in the buffer (no dynamic FtsZ polymerisation, yellow). Stem plot shows # of deformations achieved for a single GUV; the value for the mean # deformations for each experimental condition is plotted as a horizontal line (colour coded). b) Cumulative probability of GUV deformation ratio achieved by trapping FtsZ or control GUVs without FtsZ (red), with FtsZ-wt without membrane targeting sequence (- mts, purple) and with FtsZ without GTP in the buffer (no dynamic FtsZ polymerisation, yellow). All osmolarities >480 mOsm/kg (internal osmolarity).

18

Movie legends

Movie 1 FtsZ-GUV can be reversibly elongated and relaxed into spherical shape. The movie shows the filament/ring transitions and formation of membrane protrusions generated by FtsZ rings. Osmolarity of the surrounding buffer remains unchanged. Green and red channel correspond to FtsZ-YFP-mts and lipid membrane (DOPE-ATTO 655), respectively. For the video, several confocal movies (played back at 80x) were stitched together. Therefore, time intervals are not constant throughout the entire videos as we do not know the precise time interval between individual videos.

Movie 2 FtsZ-GUV can be deformed into rod- or cigar- shapes using the microfluidic devices. The movie shows reversible squeezing and elongation of a FtsZ-GUV by controlling the flow rate in the device microchannels. Osmolarity of the surrounding buffer remains unchanged. Green channel corresponds to FtsZ-YFP-mts while red channel corresponds to lipid membrane (DOPE-ATTO 655). For the video, several confocal movies (played back at 70x) were stitched together. Therefore, time intervals are not constant throughout the entire videos as we do not know the precise time interval between individual videos.

Movie 3 Continuous time-lapse of reversible FtsZ-GUV deformations in microfluidic devices. The flow rate used in this video varies from -20 µl/h to +5 µl/h to push in and out the vesicle. Reversible transition between FtsZ filaments and rings can be observed. Green and red channel correspond to FtsZ-YFP-mts and lipid membrane (DOPE-ATTO 655), respectively. Two first digits of the time counter represent minutes while the last two correspond to seconds (the movie is played back at 150x).

19

5. Content exchange between protocells

5.1. Introduction and context

In this last chapter we leave the area of protein reconstitution and observations within single vesicles. Instead we look to assemblies of vesicles, or 'populations' as we refer to them in P8. Further, the motivation and context of this study differs. While all previous chapters use bottom-up in vitro reconstitution with the goal of understanding components of currently living organisms (as it is typically the case for biology), the subject of this chapter is the testing of hypotheses for the origins of life. However, knowledge gained from both disciplines can be used for synthetic biology and to understand basic principles in nature. In the same way our observations of Min proteins deforming membranes (which are likely not reproducing actual processes in E.coli) are very interesting for synthetic biology and for our understanding of biological membranes, the observations made in this study can help further our understanding of membranes or basic principles, even if some day proven to not replicate the actual processes at the emergence of life.

While in this work we use a different method, here we use giant unilamellar vesicles made from phospholipids. All living organisms known to date are composed of cells with membranes made of phospholipids. However, phospholipids are typically considered chemically too complex to be candidates for the first protocells. Simpler lipid molecules, like fatty acids,[75] which are generally considered more 'prebiotically plausible'. Nevertheless, we use phospholipids as a good starting point for these bottom-up experiments, as they offer experimental advantages over other lipid molecules. At the same time, phospholipids share many properties with such more simple lipids, and the results in this study can be assumed to be applicable to membranes from possible phospholipid precursors. Further, we can assume that there was a primitive early ancestor common to all current life with membranes made from phospholipids, for which the mechanisms studied in this chapter might also have been relevant.

5.2. Considerations regarding early protocells

Compartmentalization is a prerequisite for life. For protocells (and single-celled organisms in general) lipid-membranes provide confining boundaries and therefore enable the formation of individual entities. By forming these

isolated volumes with genetic information that is distinct from that of others, membrane barriers form the basis of Darwinian evolution.[76,77]

One consideration that is essential for the emergence of life from cellular units is the requirement for certain levels of exchange of matter with the surrounding environment and between organisms. For example, content exchange between individuals enables horizontal gene transfer, an important factor in the evolution of cellular life.[78,79] While modern cells can rely on complicated protein machineries to catalyze these crucial processes, protocells must have accomplished this using more simple mechanisms.

Protocells with membranes made from fatty acids would have been able to exchange small molecules and ions with their environment without any additional factors.[80] These membranes have a relatively high permeability to molecules such as nucleoside triphosphates.[81] Osmotic pressure can also help with passive transport of small molecules across such membranes.[80]

Physicochemical effects have been suggested to trigger conditions under which a transport of larger molecules, such as DNA and RNA, across the membranes of protocells is possible. This is particularly interesting if explained through periodically reoccurring environmental effects, as this enables a rudimentary form of life cycle. In the work presented in this chapter, we explore the transfer of genetic information between simple vesicle compartments by freeze-thaw cycles, however alternative scenarios have been proposed before. For example, it has been shown that electroporation resulting from lightning strikes can enable transport of genetic information.[82] By exposure to a strong electric field across the membrane, the lipid molecules in the membrane shift position, opening up a pore (hole) that acts as a conductive pathway through which hydrophobic molecules like nucleic acids can pass the lipid bilayer.[83]

5.3. Publication 7: Freeze-thaw cycles induce content exchange between cell-sized lipid vesicles

Research paper published in New Journal of Physics.[84]

Litschel T, Ganzinger KA, Movinkel T, Heymann M, Robinson T, Mutschler H, Schwille P. "Freeze-thaw cycles induce content exchange between cell-sized lipid vesicles". *New J Phys* **20** (2018) 055008

https://doi.org/10.1088/1367-2630/aabb96

PAPER · OPEN ACCESS

Freeze-thaw cycles induce content exchange between cell-sized lipid vesicles

View the article online for updates and enhancements.

New Journal of Physics

The open access journal at the forefront of physics

CrossMark

PAPER

Freeze-thaw cycles induce content exchange between cell-sized lipid vesicles

Thomas Litschel[1] , Kristina A Ganzinger[1] , Torgeir Movinkel[1] , Michael Heymann[1] ,
Tom Robinson[2] , Hannes Mutschler[3,4] and Petra Schwille[1,4]

[1]   Department of Cellular and Molecular Biophysics, Max Planck Institute of Biochemistry, D-82152 Martinsried, Germany
[2]   Department of Theory and Bio-Systems, Max Planck Institute of Colloids and Interfaces, D-14424 Potsdam, Germany
[3]   Research Group Biomimetic Systems, Max Planck Institute of Biochemistry, D-82152 Martinsried, Germany
[4]   Authors to whom any correspondence should be addressed.

E-mail: mutschler@biochem.mpg.de and schwille@biochem.mpg.de

Keywords: freeze-thaw, origin of life, protocells, giant unilamellar vesicles, liposomes

Supplementary material for this article is available online

Abstract

Early protocells are commonly assumed to consist of an amphiphilic membrane enclosing an RNA-based self-replicating genetic system and a primitive metabolism without protein enzymes. Thus, protocell evolution must have relied on simple physicochemical self-organization processes within and across such vesicular structures. We investigate freeze-thaw (FT) cycling as a potential environmental driver for the necessary content exchange between vesicles. To this end, we developed a conceptually simple yet statistically powerful high-throughput procedure based on nucleic acid-containing giant unilamellar vesicles (GUVs) as model protocells. GUVs are formed by emulsion transfer in glass bottom microtiter plates and hence can be manipulated and monitored by fluorescence microscopy without additional pipetting and sample handling steps. This new protocol greatly minimizes artefacts, such as unintended GUV rupture or fusion by shear forces. Using DNA-encapsulating phospholipid GUVs fabricated by this method, we quantified the extent of content mixing between GUVs under different FT conditions. We found evidence of nucleic acid exchange in all detected vesicles if *fast* freezing of GUVs at −80 °C is followed by *slow* thawing at room temperature. In contrast, slow freezing and fast thawing both adversely affected content mixing. Surprisingly, and in contrast to previous reports for FT-induced content mixing, we found that the content is not exchanged through vesicle fusion and fission, but that vesicles largely maintain their membrane identity and even large molecules are exchanged via diffusion across the membranes. Our approach supports efficient screening of prebiotically plausible molecules and environmental conditions, to yield universal mechanistic insights into how cellular life may have emerged.

Introduction

Comprehensively defining living matter is difficult [1]. Yet, all living species are capable of decreasing internal entropy and increasing functional complexity at the expense of substances or free energy absorbed from the environment. In order for cellular life to develop this characteristic complexity, even primitive protocells must have compartmentalized their molecular components to separate themselves from each other and the environment, allowing them to maintain and regulate biochemical processes (i.e., develop a metabolism), effectively couple their cellular phenotype to their genotype and prevent takeover by parasitic mutants. This compartment boundary consists of lipid membranes in all known living entities. At the same time, protocells needed to evolve mechanisms to regulate material, energy and information exchange between themselves and their surroundings.

Exchange of material across (sub)cellular compartments is commonly mediated by either proteinaceous membrane channels and transporters, or by compartment fusion and fission events mediated by complex

protein machineries. Similarly, growth and division in modern cells is a tightly regulated process that involves genome replication and partitioning, culminating in the separation of new daughter cells through fission of the mother cell compartment. Given the intricate nature of these complex biological processes, it remains a mystery how the first precursors of our modern cells, doubtlessly much more primitive entities before the advent of proteins, could have exchanged material—itself a prerequisite for the emergence of life.

While numerous compartment systems have been proposed as the first autopoietic units [2], the most prominent protocellular models thought to provide a plausible historic route to modern cells are based on membrane vesicles formed by amphiphiles such as lipids [3], which encapsulate a primitive metabolism and an RNA-based self-replicating genetic system [4]. Typical models for the replication of such primitive vesicles accommodate growth either by uptake of micelles or free amphiphiles, or by vesicle-vesicle fusion events followed by division through vesicle fission [5]. Out of these models, self-reproduction based on micelle feeding has been extensively studied. It typically involves formation, growth, and self-reproduction of buffered, submicrometre vesicles by uptake of alkaline micelles formed by simple fatty acids such as oleic acid [6–13]. In a further expansion of this model, reproduction of multilamellar vesicles composed of prebiotically plausible fatty acid and lipid mixtures was shown to occur through a series of alkaline micelle addition, filamentous growth, and gentle agitation with minimal content leakage of encapsulated RNAs [14]. Primitive replication cycles of vesicles can also be induced by increasing lipid concentration through evaporation and shear-forcing or photochemically induced division [15]. It was hypothesized that RNA replication inside vesicles could lead to an increased osmotic pressure and thus growth at the expense of empty vesicles [16]. Such larger, multilamellar vesicles could then undergo division in environments of gentle shear [14]. However, although isolated aspects of this proposed mechanism have been shown, a combined experimental demonstration of intravesicular RNA replication, growth and division remains elusive. In contrast, proliferation via feeding of a protocell with RNA building blocks by content exchange with 'feedstock' vesicles provides a simple but robust alternative scenario for early protocell replication [17–19]. The required driving force for vesicle encapsulation and content exchange can be provided by environmental conditions such as freeze-thaw (FT) cycling [20–23]. Indeed, repeated FT-induced mixing of vesicle contents by vesicle fusion was recently used to enable sustainable proliferation of liposomes with encapsulated protein expression and protein-catalysed RNA replication [24]. These observations suggest that FT-cycling, among other plausible periodic physicochemical processes such as rehydration and dehydration [25], could have promoted primitive cycles of growth and division of protocells.

An attractive experimental system to study such proliferation scenarios are giant unilamellar vesicles (GUVs), i.e. single bilayer liposomes that are larger than 10 μm. Given their size, GUVs can be directly observed by light microscopy. However, preparation of GUVs encapsulating large biomolecules is experimentally challenging. Commonly used experimental procedures, such as controlled swelling [26, 27] and electroformation [28], complicate handling and content encapsulation.

Here, we present a new high-throughput methodology for homogeneous production of nucleic acid-containing GUV populations by water-in-oil emulsion transfer in a microtiter plate [29]. Our protocol allows for direct exposure of GUVs to different environmental conditions inducing content mixing, without any intermediate sample pipetting steps, and for these processes to be directly monitored by imaging. This reduction of handling steps strongly minimizes potential artefacts introduced by sample manipulation, such as unintended GUV rupture or fusion by shear forces. Using GUVs made of 1-Palmitoyl-2-oleoyl-*sn*-glycero-3-phosphocholine (POPC) as a model system, we have tested different FT-conditions for their potential to drive content exchange across vesicles. We found that fast freezing induced by placing the sample on a metal block at -80 °C, followed by slow thawing at room temperature resulted in efficient nucleic acid exchange in all detected vesicles without any observable vesicle fusion events.

Thus, our results offer an attractive explanation of how intravesicular content, including primitive RNA replicators, could have spread within vesicle populations independently from vesicle fusion and fission events using transient periods of increased membrane permeability.

In the future, our method will allow the rapid exploration of vesicle properties for GUVs made with different amphiphiles and buffer systems, as well as allow the efficient screening of environmental conditions for their potential to induce GUV-based protocell content exchange and propagation.

Methods

GUV preparation
Our method for generating GUVs is based on emulsion transfer in microtiter plates [29, 30]. In contrast to common protocols, we both generated and imaged GUVs in glass bottom microtiter plates, enabling high-throughput parameter optimization. Since the same 96-well plate is used for all experimental steps including GUV generation, freeze-thawing and subsequent imaging, pipetting steps are minimized.

Figure 1. Schematic representation of the GUV generation process. (a) Microtiter plate with wells containing a layer of mineral oil (with POPC lipids) on top of glucose solution. After 30 min of incubation, a lipid monolayer has formed at the water–oil interface. (b) Micro test tubes with the same lipid-in-oil mixture layered over a sucrose solution containing each a differently fluorescently labelled oligonucleotide. (c) Water-in-oil emulsion generated by mechanical agitation. (d) Both emulsions were pipetted in a 1:1 ratio onto the oil phase in microtiter plate wells. (e) GUVS are generated by moving the droplets through the lipid-saturated water–oil interface (emulsion transfer).

First, POPC (1-Palmitoyl-2-oleoyl-*sn*-glycero-3-phosphocholine, Avanti Polar Lipids, Inc.) was dissolved in chloroform at a concentration of 8 mM. The solution (75 μl) was then transferred to a 4 ml glass vial and the chloroform was evaporated under argon flow (15 min), followed by removing residual solvent traces by applying a vacuum (1 h). After addition of 1.5 ml mineral oil (Sigma-Aldrich, M5904), the vial was sonicated for 1 h at 40 °C, and incubated overnight at room temperature to dissolve the lipids in the oil.

The glass bottom microtiter plates (Greiner Bio-One, 96-well glass bottom SensoPlate™) were passivated with Pluronic F-127 (Sigma-Aldrich): after plasma-cleaning the microtiter plate, 50 μl of 20 mg ml^{-1} Pluronic F-127 were added to each well of the plate intended to hold GUVs and incubated for 30 min at room temperature, followed by a wash with 900 mM glucose solution (50 μl). 100 μl of the same glucose solution was then pipetted into each well (outer aqueous phase containing future GUVs) and POPC-mineral oil solution (40 μl) was layered on top, followed by incubation for 30 min at room temperature to form a monolayer at the water–oil interface (figure 1(a)).

To create two distinct fluorescently labelled populations of GUVs, we prepared internal GUV solutions (900 mM sucrose) with DNA oligonucleotides (26 bases (13 repetitions of 5′-CA-3′), IDT) either labelled with a 5′ Cy5 fluorophore (4 μM) or a 5′ 6-FAM fluorophore (8 μM).

To generate the water-in-oil emulsion for the emulsion transfer, 5 μl of each inner phase solution (each containing one of the two oligonucleotides) was added to 250 μl of the POPC-mineral oil solution in a 0.5 ml micro test tube (figure 1(b)). Droplets were formed by shear forces through mechanical agitation (i.e. repeatedly rubbing each tube for about 1 min across the array of cavities on a micro test tube rack) (figure 1(c)), then 40 μl of both emulsions (80 μl in total) were immediately pipetted into each well of the microtiter plate (figure 1(d)). The microtiter plate was subsequently centrifuged for 3 min at 250 g (Eppendorf Centrifuge 5804 R) in a rotor designed to hold microtiter plates (Eppendorf A-2-DWP) to generate GUVs (figure 1(e)).

All steps that involve handling of the hygroscopic mineral oil, except for the last centrifugation step, are carried out in a glove box under nitrogen flow and a humidity of 3%–8% to minimize the amount of water in the organic phase. While this measure generally increased vesicle yields drastically, it proved to be crucial in warm summer months with indoor humidities of more than 50%, when we sometimes did not see any vesicle formation if samples were handled at ambient conditions.

For the experiments in figures 4, S6 and S7 membrane labels were used in the following mole fractions of membrane label to lipids: 0.013 mol% DOPE-ATTO488 (1, 2-dioleoyl-*sn*-glycero-3-phosphoethanolamine labelled with ATTO488) (ATTO-TEC GmbH); 0.017 mol% DiD (DiIC$_{18}$(5)) and DiI (DiIC$_{18}$(3)) (Thermo Fisher Scientific). The labelled dextrans (3000 MW and 40 000 MW) were both used in a concentration of 0.08 mg ml^{-1}.

Freeze-thawing

Three different FT protocols were used, enabling fast freezing and fast thawing (condition A), slow freezing and slow thawing (condition B) and fast freezing followed by slow thawing (condition C). We only observed very few intact vesicles after slow freezing and fast thawing (condition D; figure S3), and therefore did not include this condition in our further investigations and analysis.

3

Figure 2. Comparison of different FT-conditions. (a)–(d) Schematic representations of the freeze-thaw protocols for each condition. (e)–(h) Confocal images of the GUVs, fluorescence intensity of Cy5-DNA is shown in red, fluorescence of 6-FAM-DNA in green. The top image corresponds to an unedited image taken with identical microscope settings and contrast settings across all conditions. The contrast of the images underneath (smaller sections of the top image) has been individually adjusted, shown is both a merged image and each individual channel. (i)–(l) Intensity scatter plots, Cy5 fluorescence intensity (red) is plotted against 6-FAM fluorescence intensity (green) on a logarithmic scale. Each data point represents an individual vesicle. The colour of each point reflects the density of points in the region similar to a heat map, from dark blue (low) to yellow (high). Number of experimental repeats was 5 for (i) and 4 for (j)–(l). (m)–(p) Histograms of the ratio of red intensity over total intensity for each of the respective conditions.

Prior to freezing, the microtiter plates containing GUVs were sealed with a sealing film (Carl Roth Rotilabo®-sealing film for micro test plates) and were positioned at a slight angle for 5–10 min, to allow the GUVs to accumulate on one side of the well.

For condition A, a 10 cm × 6 cm × 6 cm block made of stainless steel was placed in a −80 °C freezer. After the metal block reached the temperature of the freezer, the microtiter plate was placed on top and pressed firmly against it for about 1 min. To allow direct contact with the glass bottom, the metal block must be smaller than the bottom frame of the microtiter plate. After 30 min, the plate and the metal block were taken out of the freezer. The plate was removed from the first metal block and placed onto a second block preheated to 60 °C on a hot plate. After 5 min of thawing at 60 °C, the plate was transferred to the microscope for imaging (see figure 2(b)).

For condition B (figure 2(c)), the microtiter plate was placed into a −20 °C freezer at a slight angle for 30 min, and subsequently into a −80 °C freezer for another 30 min. Afterwards the GUVs were thawed at room temperature for 30 min.

Condition C is a combination of the previous two. The GUVs were frozen for 30 min at −80 °C on a metal block and subsequently thawed for 30 min at room temperature (see figure 2(d)).

Imaging

Imaging was performed with an LSM 780/CC3 confocal microscope (Carl Zeiss, Germany) equipped with a C-Apochromat, 40x/1.2 W objective. We used PMT detectors (integration mode) to detect fluorescence emission (excitation at 488 nm for 6-FAM and 633 nm for Cy5) and record confocal images. To capture many GUVs in high resolution, tile scans were performed by recording a defined number of adjoining single images of the sample (the 'tiles'), moving the sample using motorized stages with high precision. Following the scanning process, the mosaic image is assembled using the stitching algorithms provided by the Zeiss software.

Analysis

Fluorescence images were analysed using custom software written in MATLAB (MATLAB R2014b, The MathWorks, Inc.) adapted from Ranasinghe *et al* [31]. Briefly, vesicles were detected (i.e. regions of interest identified) in each field of view across two images sequentially acquired for each colour channel ('red' and 'green') by converting both images to a binary image (mask) using a threshold intensity set to be the mean single pixel intensity of the bandpass-filtered images plus 0.5–2 times this value. This factor was determined empirically by visual inspection of the binary image obtained and comparison with the original data. In the next step, objects (vesicles) are detected by tracing continuous regions of ones in the binary image. Signals are assumed to correspond to single vesicles if the area of the region is $>10.8~\mu\text{m}^2$ (250 pixel). The mean intensity for the centres of each region/vesicle (i.e. the originally detected region minus a shell of 5 pixel) are then calculated from *both* original images for vesicles detected in either of the two channels. Finally, the intensities are plotted in scatter plots coloured according to data density (figures 2(i)–(l)) and the ratio of red/green intensity was calculated for each vesicle.

MATLAB code for analysing image data is available online.

Results

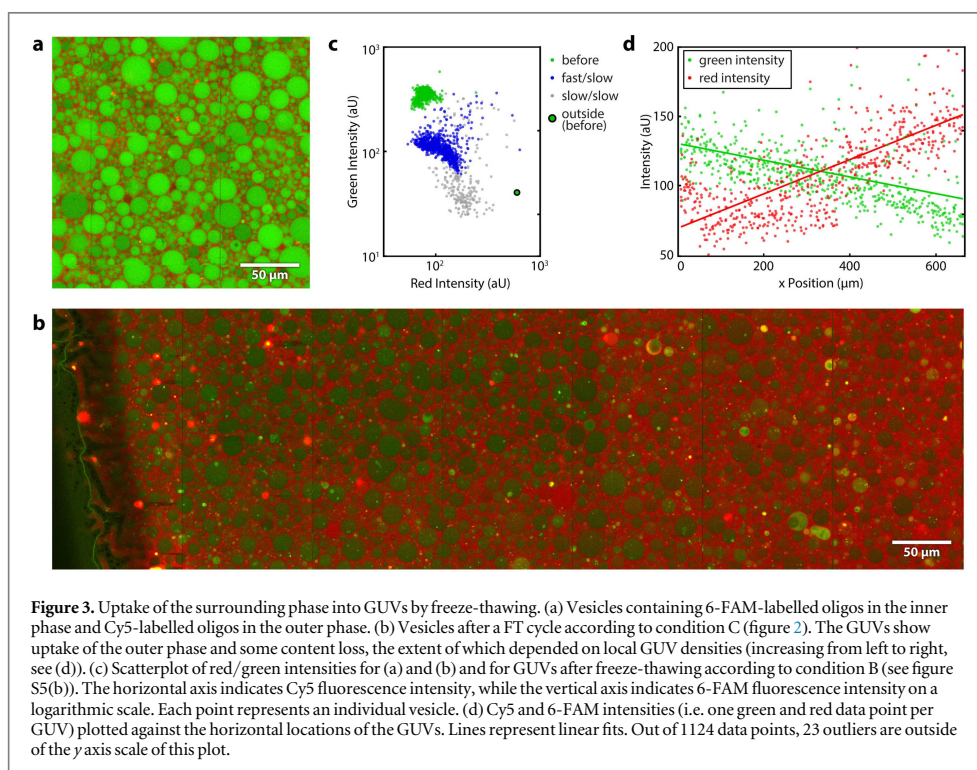### Generating heterogeneous GUV populations by emulsion transfer in microtiter plates

To study the effect of FT-cycling on vesicle content mixing, we first developed a method to simultaneously generate GUVs of differing content via emulsion transfer in microtiter plates, thus greatly improving experimental throughput and parallelizing the screening for optimal conditions. Briefly, two distinct populations of GUVs were obtained by (i) preparing water-in-oil droplets from two solutions, each containing a different fluorescently labelled oligonucleotide. These two emulsions were then (ii) mixed and (iii) passed through a lipid-lined oil–water interface upon which GUVs were formed (figure 1).

We found the surface passivation of the microtiter plate chambers to be a crucial factor in our experiments. We tested β-casein (2 and 5 mg ml^{-1}), PLL-g-PEG (0.5 and 2 mg ml^{-1}) and Pluronic F-127 (1–50 mg ml^{-1}) as passivation agents in combination with various subsequent washing protocols. Vesicle generation in β-casein-passivated chambers was successful, but only very few vesicles remained intact after the FT cycles. PLL-g-PEG seemed promising while working with vesicles that did not contain oligonucleotides, but after incorporating labelled oligonucleotides, the experiments failed. Pluronic F-127 at high concentrations (10–50 mg ml^{-1}) was the only passivating agent to work under relevant conditions. In contrast to the other passivation methods, we also observed the highest overall vesicle yield and no aggregation on the glass surface.

GUV content mixing efficiency depends on both the freezing and thawing rate

With our optimized microtiter plate protocol in hand, we investigated how the yield of content mixing upon freeze-thawing vesicles depended on the heating and cooling rates of the FT process. We tested three different FT protocols with variations in heating and cooling rates. Firstly, the sample was rapidly frozen at $-80~^\circ$C and rapidly thawed at 60 $^\circ$C, in both cases maximizing heat exchange by placing the plate on a metal surface (condition A: fast freezing/fast thawing). Secondly, the sample was cooled slowly to $-20~^\circ$C before cooling it further to $-80~^\circ$C, then slowly thawed at room temperature (condition B: slow freezing/slow thawing). Thirdly, we combined rapid freezing (step 1 from condition A) with slow thawing (step 2 from condition B) such that fast freezing is followed by slow thawing (condition C). The remaining combination (condition D: slow freezing/fast thawing) is not covered in our detailed analysis, since it resulted in almost no vesicles after the FT process (figure S3).

We applied these FT-cycles to microtiter plates containing mixtures of GUVs encapsulating 26 bp DNA oligos either labelled with Cy5 or with 6-FAM, and recorded two-colour images of the GUVs by confocal microscopy, both before (figure 2(e)) and after the FT cycle (figures 2(f)–(h)). We then used an automated, custom image analysis routine to extract the fluorescence intensities for individual GUVs from the image data.

Figure 3. Uptake of the surrounding phase into GUVs by freeze-thawing. (a) Vesicles containing 6-FAM-labelled oligos in the inner phase and Cy5-labelled oligos in the outer phase. (b) Vesicles after a FT cycle according to condition C (figure 2). The GUVs show uptake of the outer phase and some content loss, the extent of which depended on local GUV densities (increasing from left to right, see (d)). (c) Scatterplot of red/green intensities for (a) and (b) and for GUVs after freeze-thawing according to condition B (see figure S5(b)). The horizontal axis indicates Cy5 fluorescence intensity, while the vertical axis indicates 6-FAM fluorescence intensity on a logarithmic scale. Each point represents an individual vesicle. (d) Cy5 and 6-FAM intensities (i.e. one green and red data point per GUV) plotted against the horizontal locations of the GUVs. Lines represent linear fits. Out of 1124 data points, 23 outliers are outside of the *y* axis scale of this plot.

For conditions A–C, we observed that the majority of GUVs contained both DNAs after a FT cycle, whereas before freezing, two distinct populations of vesicles could clearly be distinguished (figures 2(i)–(l)). The efficiency of this mixing of contents varied between the different FT protocols. This content mixing is accompanied by an overall decrease in GUV fluorescence intensity in both colour channels (figures 2(i)–(l), figure S1).

Under condition A (fast/fast), the ratios of green to red intensities were shifted compared to the control for many GUVs, indicating content mixing. However, two populations of GUVs which either contain more Cy5- or 6-FAM-DNA can still be distinguished (figures 2(j) and (n)), indicating that the mixing is incomplete. Only a small population of GUVs shows approximately equal intensities for both dyes, and hence contains approximately equal amounts of oligonucleotides (figures 2(f), (j) and (n)).
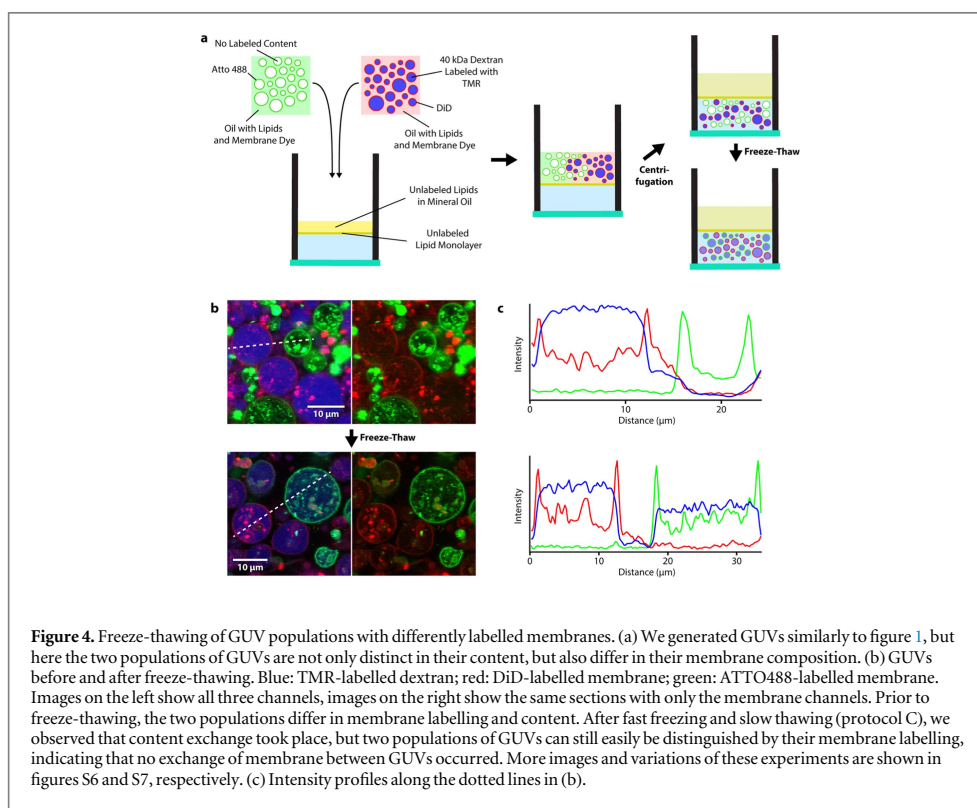
Similarly, condition B (slow/slow) resulted in the majority of GUVs containing a highly uneven ratio of fluorescence signals, and thus an uneven ratio of DNA concentrations (figures 2(k) and (o)). Compared to condition A, however, the overall intensity of these vesicles (and hence the concentration of their contents) was lower (figure S1).

Under condition C (fast/slow), content mixing was by far the most efficient. Most GUVs displayed approximately equal intensity levels for both dye-labelled DNAs (figures 2(l) and (p)), in stark contrast to the first two conditions. In addition, the combined fluorescence intensities from both DNAs contained within the GUVs were similar to those measured for GUVs subjected to condition A (figure S1). Protocol C did not seem to change vesicles numbers noticeably when we visually inspected the data, whereas GUV numbers decreased for protocols A, B and D with almost no intact GUVs remaining for condition D. Thus, condition C not only results in the most complete content mixing but also retains the most GUVs and the most content (labelled oligos) within those GUVs.

We note that after a FT cycle, the GUV size distribution is shifted to slightly smaller vesicle sizes for all tested conditions (figure S2), indicating that the FT cycle induced some degree of vesicle fragmentation.

Inner/outer phase exchange

While fast freezing and slow thawing of vesicles encapsulating differently labelled DNA oligos leads to efficient content mixing, the overall concentration of encapsulated DNA decreased after mixing. We thus investigated whether this noticeable content loss is due to exchange with the surrounding phase during the FT step. To

Figure 4. Freeze-thawing of GUV populations with differently labelled membranes. (a) We generated GUVs similarly to figure 1, but here the two populations of GUVs are not only distinct in their content, but also differ in their membrane composition. (b) GUVs before and after freeze-thawing. Blue: TMR-labelled dextran; red: DiD-labelled membrane; green: ATTO488-labelled membrane. Images on the left show all three channels, images on the right show the same sections with only the membrane channels. Prior to freeze-thawing, the two populations differ in membrane labelling and content. After fast freezing and slow thawing (protocol C), we observed that content exchange took place, but two populations of GUVs can still easily be distinguished by their membrane labelling, indicating that no exchange of membrane between GUVs occurred. More images and variations of these experiments are shown in figures S6 and S7, respectively. (c) Intensity profiles along the dotted lines in (b).

quantify the extent of this exchange, we freeze-thawed GUVs containing 6-FAM-labelled oligos, which were surrounded by an outer phase containing Cy5-labelled oligos (figure 3(a)). While only background-level Cy5 signals were detected inside vesicles before freeze-thawing, the level increases notably after freeze-thawing for the tested conditions (figures 3(b) and (c)). Although this suggests some internalization of the outer phase during the FT process, the intensity of Cy5 measured inside GUVs after FT was still much lower than that measured in the outer phase (on average 18% of outer phase), whereas the average intensity of the encapsulated DNA dropped to ~43% of the initial value for FT condition C (fast freezing, slow thawing) (figure 3(b)). Increased uptake of surrounding fluid is observed for condition B (figure S5(b)), which is consistent with the larger decrease of fluorescence intensity observed for content mixing between GUVs under this condition (figure 2(k)).

If content exchange between GUVs were to happen via content release and uptake (and diffusion of the content through the GUV-surrounding phase), we would expect that content exchange is more efficient at high GUV densities, as dilution of the content would be minimized. Conveniently, our FT-protocol involves tilting of the microtiter plates to an angle of 45° before freeze-thawing, which results in a GUV density gradient across the well (figure S5(a)). In areas with high GUV density, the immediate surrounding phase constitutes only a small fraction of the total volume. We therefore tested whether GUV content composition after freeze-thawing is dependent on the location of the GUVs within the well, and hence the local GUV density. In line with our hypothesis, figures 3(b) and (d) show that vesicles in high-density areas (left) keep more of their original content (6-FAM, green) and encapsulate less of the surrounding phase (Cy5, red) than vesicles in low-density areas (right). Thus, GUV density determines the degree GUV content loss and encapsulation of the surrounding phase.

Freeze-thawing does not induce membrane exchange between GUVs

To gain further insights into the mechanisms responsible for content exchange between vesicles, and to specifically test whether this exchange could, at least partially, be mediated by fusion and subsequent fission of vesicles, we performed our FT-cycling with two populations of GUVs with different membrane labels. The lumen of one GUV population also contained a fluorescently labelled cargo of various molecular sizes to allow for simultaneous monitoring of size-dependent content mixing. We generated the GUVs according to the protocol shown in figure 1, but used different lipid-in-oil solutions in the different steps to generate two GUV

populations: one population with DOPE-ATTO488 in the membrane, but no labelled content; and a second population with DiD-labelled membranes and TMR-labelled 40 kDa dextran cargo (see figure 4(a) for a depiction of the protocol). Importantly, we found that if the time between mixing the two types of emulsions and the centrifugation step is reduced to a minimum, no significant amount of foreign membrane is incorporated into the membrane of the respective other population of GUVs.

When we freeze-thawed the GUVs according to protocol C, surprisingly we observed content mixing, while maintaining two populations of distinctly membrane-labelled vesicles (figure 4(b) and (c)). These data suggest that content exchange is possible even for large molecules up to 40 kDa without a significant number of membrane fusion and fission events. Figure S6 shows more images of the experiment. To validate these findings further, we performed a series of two-colour experiments in which we labelled the membrane of at least one population of GUVs with various membrane dyes (DOPE-ATTO488, DiD and DiI) and also used a variety of labelled cargo molecules (dextran 40 000 MW, dextran 3000 MW and the 6-FAM labelled Oligo from previous experiments). A comparison of confocal images before and after freeze-thawing for these experiments is shown in figure S7. In all cases, we saw a homogenization of contents, but could still distinguish the two populations of vesicles by their distinct membrane labels, or lack thereof.

We conclude from these experiments that GUVs mostly retain their membrane identity during the FT process, and that the cause for content exchange between vesicles is not fusion (and subsequent fission) of vesicles.

To investigate vesicle fate throughout the FT process in more detail, we attempted to follow the GUVs during the thawing process by time-lapse microscopy. Although imaging frozen samples throughout the entire thawing process proved unattainable with our experimental equipment, we were able to follow vesicle shape changes after thawing the sample for 20 min at room temperature. At this stage, the content of the complete sample well was fully thawed. However, numerous elongated vesicles could be observed, as well as their fission into smaller spherical GUVs over the following 5 min (figure S8(a)). While we assume that these events are not required for the content exchange between vesicles, the observations explain the shift to smaller vesicles after freeze-thawing (figure S2). Dynamic shape changes like these can be induced by vesicle deflation through osmotic water extraction. To explore whether changes in osmolarity during the FT process are a possible cause, we analysed the osmolarity in horizontal sections from wells that were frozen according to protocol C. We found a gradient of osmolarity with higher concentrations at the bottom of the well (supplementary figure S8(b)) which could be a cause for the GUV destabilization and subsequent fission.

Discussion

The purpose of this study was to develop and test a convenient but powerful methodology for the exploration of changing environmental conditions, such as FT-cycles, as drivers of content exchange between vesicle compartments. We found that mixing of contents in our POPC-GUV model system proceeded to varying degrees in conditions A–C. Condition C (fast freezing, slow thawing) resulted in the most uniform final state. Final GUVs for both A and B still predominantly contain only one of both DNA oligos, with only a very small fraction of resulting GUVs encapsulating approximately equal amounts of both oligos after FT.

Previously, Tsuji *et al* used a similar FT-protocol to induce content mixing of GUVs and concluded from their findings that content exchange between vesicles is caused by vesicle fusion and fission [24]. In contrast to our work, Tsuji *et al* centrifuged their GUVs at 18 000 g (more than 70× faster than the speed at which we generate our GUVs, 250 g) to 'increase fusion efficiency' and freeze their GUVs using liquid nitrogen in plastic micro reaction tubes with different heat conductivity and surface properties from our glass bottom wells [24]. A well-studied process is the FT-induced collective fusion of small unilamellar vesicles (SUVs) to form large unilamellar vesicles or GUVs [20, 32–34], but the conditions for SUV fusion are unlikely to be identical to those inducing GUV fusion given their different physical properties.

From our findings, we conclude that under our experimental conditions, vesicles exchange their contents independently from fusion and fission. Rather, content exchange occurs via membrane destablization, content leakage and uptake of content from the surrounding phase during the FT process. Three key observations strongly support this conclusion:

(i) If the microtiter plate is handled carefully after thawing, such that the GUVs do not move within the wells, we observe a very homogeneous mixing of content on an intermediate range as figure S4 shows. Fusion of (few) neighbouring vesicles and their subsequent fission would likely lead to a higher local diversity of vesicle contents. Instead, on a small scale, all vesicles have approximately the same ratio of dyes and on a

larger scale, smooth gradients regarding the vesicle content are visible, but rarely sharp contrasts. This indicates a very thorough mixing across tens to hundreds of vesicles.

(ii) As described in figure 3(d) and the respective paragraph, the loss of content and the degree of exchange between GUVs and their surrounding phase seems to be dependent on the local density of GUVs. A model in which GUVs exchange their content via the outer phase explains this phenomenon, because a larger ratio of surrounding phase to GUV volume would dilute GUV content once GUVs become porous upon FT-cycling. Conversely, in regions of high vesicle densities, the surrounding phase contributes only to a small fraction of total volume, and hence only a correspondingly small fraction of GUV content is replaced by surrounding phase, as also observed in out experiments.

(iii) The strongest support for our hypothesis that content exchange is not induced by fusion and fission comes from experiments showing that while mixing of GUV content is highly efficient, GUVs of different membrane compositions do not interchange lipids, and thus remain distinct entities during the process (figures 4, S6 and S7).

It is plausible that the GUVs become more permeable at temperatures slightly below the phase transition temperature of the bilayer lipids ($T_m = -2\,°C$), especially if samples are thawed slowly (conditions B and C). At these temperatures, the GUV outer and inner phases have already thawed, due to the high sugar concentrations that lower the melting temperature. We think that this physicochemical state is restricted to the time when the samples start thawing at the glass bottom of the well (where most GUVs are located). When the upper layers of the well continue to thaw, the layer of GUVs at the glass bottom has already reached a temperature above the phase transition temperature of the lipids, rendering the GUVs impermeable to the DNA oligos or dextran again. A transient increase in membrane permeability during thawing, in combination with diffusion being restricted to the GUV-containing layer close to the glass bottom of the well, could explain how GUVs exchange their content via the surrounding phase without losing most of their content by dilution into the surrounding phase. Only when the entire well thawed, the vesicle content released into the surrounding phase between the vesicles is diluted by exchange with the large volume of outer phase above the GUV-containing layer.

For condition C, an exchange with the outer phase during the freezing step of the protocols is minimized, since freezing of the sample occurs within few seconds. More efficient exchange with the outer phase due to slow freezing explains the increased loss of content and encapsulation of outer phase observed in protocol B (see figures 3(c) and S5(b)). In fact, content loss was so high for condition B that many of the vesicles after freeze-thawing were not detected by our script and were only barely visible by eye.

In summary, we have shown that tightly packed GUVs, if subjected to a FT cycle, can transiently exchange content even in the absence of GUV fusion and fission. In simple protocellular systems based on lipid-encapsulated RNA replicators, such transient periods of content exchange could have facilitated the spread of protocells with functional genomes via direct transfer of replicators. Indeed, cycles of transient compartmentalization and mixing of RNA replicators were previously shown to be sufficient to prevent takeover by parasitic mutants [35]. Moreover, transient increases in membrane permeability could have facilitated uptake of RNA building blocks from other vesicles or the surrounding environment.

Our microtiter plate protocol allows high-throughput *in situ* imaging of many different conditions in parallel, without risking artefacts introduced by vesicle handling. While emulsion transfer allows the encapsulation of a large spectrum of biomolecules, it should be noted that the lipid bilayer of GUVs generated by the emulsion transfer may contain trace amounts of oil, changing their mechanical properties [36]. Therefore, we cannot exclude that results for GUVs generated by a different method might differ from ours.

In the future, our experimental approach will facilitate efficient screening of the vast parameter space of prebiotically plausible molecules and environmental conditions, to eventually derive unifying mechanistic insights into how cellular live may have evolved. It will be interesting to investigate the impact of the lipid phase transition temperature and test if, for example, DOPC (1, 2-dioleoyl-*sn*-glycero-3-phosphocholine), which has a much lower T_m of $-17\,°C$ compared to POPC ($T_m = -2\,°C$), might inhibit content exchange between vesicles. Additionally, our method promises to explore the effect of freeze-thawing on vesicles made from chemically much simpler amphiphiles, such as prebiotically accessible fatty acids and monoacylglycerols [11, 37]. Finally, the microtiter plate layout of our experiments supports convenient future screening experiments e.g. of heterogeneous environments, such as minerals or different buffer conditions, which are compatible with nucleic acid catalysis and formation.

9

Acknowledgments

ORCID iDs

Thomas Litschel ⓘ https://orcid.org/0000-0001-7123-8364
Kristina A Ganzinger ⓘ https://orcid.org/0000-0001-9106-9406
Torgeir Movinkel ⓘ https://orcid.org/0000-0003-3150-2233
Michael Heymann ⓘ https://orcid.org/0000-0002-9278-8207
Tom Robinson ⓘ https://orcid.org/0000-0001-5236-7179
Hannes Mutschler ⓘ https://orcid.org/0000-0001-8005-1657
Petra Schwille ⓘ https://orcid.org/0000-0002-6106-4847

References

[1] Rasmussen S 2009 *Protocells: Bridging Nonliving and Living Matter* (Cambridge, MA: MIT Press) (https://doi.org/10.7551/mitpress/9780262182683.001.0001)
[2] Monnard P-A and Walde P 2015 Current ideas about prebiological compartmentalization *Life* **5** 1239
[3] Hanczyc M M and Monnard P-A 2017 Primordial membranes: more than simple container boundaries *Curr. Opin. Chem. Biol.* **40** (Suppl. C) 78–86
[4] Blain J C and Szostak J W 2014 Progress toward synthetic cells *Annu. Rev. Biochem.* **83** 615–40
[5] Hanczyc M M and Szostak J W 2004 Replicating vesicles as models of primitive cell growth and division *Curr. Opin. Chem. Biol.* **8** 660–4
[6] Blöchliger E, Blocher M, Walde P and Luisi P L 1998 Matrix effect in the size distribution of fatty acid vesicles *J. Phys. Chem.* B **102** 10383–90
[7] Berclaz N, Müller M, Walde P and Luisi P L 2001 Growth and transformation of vesicles studied by ferritin labeling and cryotransmission electron microscopy *J. Phys. Chem.* B **105** 1056–64
[8] Hanczyc M M, Fujikawa S M and Szostak J W 2003 Experimental models of primitive cellular compartments: encapsulation, growth, and division *Science* **302** 618–22
[9] Luisi P L, Stano P, Rasi S and Mavelli F 2004 A possible route to prebiotic vesicle reproduction *Artif. Life* **10** 297–308
[10] Rasi S, Mavelli F and Luisi P L 2004 Matrix effect in oleate micelles-vesicles transformation *Orig. Life Evol. Biosph.* **34** 215–24
[11] Chen I A and Szostak J W 2004 A kinetic study of the growth of fatty acid vesicles *Biophys. J.* **87** 988–98
[12] Stano P, Wehrli E and Luisi P L 2006 Insights into the self-reproduction of oleate vesicles *J. Phys.: Condens. Matter* **18** S2231
[13] Mavelli F and Ruiz-Mirazo K 2007 Stochastic simulations of minimal self-reproducing cellular systems *Phil. Trans. R. Soc.* B **362** 1789–802
[14] Zhu T F and Szostak J W 2009 Coupled growth and division of model protocell membranes *J. Am. Chem. Soc.* **131** 5705–13
[15] Budin I, Debnath A and Szostak J W 2012 Concentration-driven growth of model protocell membranes *J. Am. Chem. Soc.* **134** 20812–9
[16] Chen I A, Roberts R W and Szostak J W 2004 The emergence of competition between model protocells *Science* **305** 1474–6
[17] Caschera F, Sunami T, Matsuura T, Suzuki H, Hanczyc M M and Yomo T 2011 Programmed vesicle fusion triggers gene expression *Langmuir* **27** 13082–90
[18] Saito A C, Ogura T, Fujiwara K and Murata S 2014 Nomura S-iM. introducing micrometer-sized artificial objects into live cells: a method for cell–giant unilamellar vesicle electrofusion *PLoS One* **9** e106853
[19] Kurihara K, Okura Y, Matsuo M, Toyota T, Suzuki K and Sugawara T 2015 A recursive vesicle-based model protocell with a primitive model cell cycle *Nat. Commun.* **6** 8352
[20] Anzai K, Yoshida M and Kirino Y 1990 Change in intravesicular volume of liposomes by freeze-thaw treatment as studied by the ESR stopped-flow technique *Biochim. Biophys. Acta (BBA)—Biomembr.* **1021** 21–6
[21] Monnard P-A, Oberholzer T and Luisi P 1997 Entrapment of nucleic acids in liposomes *Biochim. Biophys. Acta (BBA)—Biomembr.* **1329** 39–50
[22] MacDonald R C, Jones F D and Qui R 1994 Fragmentation into small vesicles of dioleoylphosphatidylcholine bilayers during freezing and thawing *Biochim. Biophys. Acta (BBA)—Biomembr.* **1191** 362–70
[23] Costa A P, Xu X and Burgess D J 2014 Freeze-anneal-thaw cycling of unilamellar liposomes: effect on encapsulation efficiency *Pharm. Res.* **31** 97–103
[24] Tsuji G, Fujii S, Sunami T and Yomo T 2016 Sustainable proliferation of liposomes compatible with inner RNA replication *Proc. Natl Acad. Sci.* **113** 590–5
[25] Damer B and Deamer D 2015 Coupled phases and combinatorial selection in fluctuating hydrothermal pools: a scenario to guide experimental approaches to the origin of cellular life *Life* **5** 872
[26] Akashi K, Miyata H, Itoh H and Kinosita K 1996 Preparation of giant liposomes in physiological conditions and their characterization under an optical microscope *Biophys. J.* **71** 3242–50
[27] Magome N, Takemura T and Yoshikawa K 1997 Spontaneous formation of giant liposomes from neutral phospholipids *Chem. Lett.* **26** 205–6
[28] Angelova M I and Dimitrov D S 1986 Liposome electroformation *Faraday Discuss. Chem. Soc.* **81** 303–11
[29] Pautot S, Frisken B J and Weitz D A 2003 Production of unilamellar vesicles using an inverted emulsion *Langmuir* **19** 2870–9
[30] Hadorn M, Boenzli E, Eggenberger Hotz P and Hanczyc M M 2012 Hierarchical unilamellar vesicles of controlled compositional heterogeneity *PLoS One* **7** e50156

[31] Ranasinghe R T *et al* 2018 Detecting RNA base methylations in single cells by *in situ* hybridization *Nat. Commun.* **9** 655

[32] Kasahara M and Hinkle P C 1977 Reconstitution and purification of the D-glucose transporter from human erythrocytes *J. Biol. Chem.* **252** 7384–90

[33] Pick U 1981 Liposomes with a large trapping capacity prepared by freezing and thawing of sonicated phospholipid mixtures *Arch. Biochem. Biophys.* **212** 186–94

[34] Gibson S M and Strauss G 1984 Reaction characteristics and mechanisms of lipid bilayer vesicle fusion *Biochim. Biophys. Acta (BBA)—Biomembr.* **769** 531–42

[35] Matsumura S *et al* 2016 Transient compartmentalization of RNA replicators prevents extinction due to parasites *Science* **354** 1293–6

[36] Campillo C *et al* 2013 Unexpected membrane dynamics unveiled by membrane nanotube extrusion *Biophys. J.* **104** 1248–56

[37] Chen I A, Salehi-Ashtiani K and Szostak J W 2005 RNA catalysis in model protocell vesicles *J. Am. Chem. Soc.* **127** 13213–9
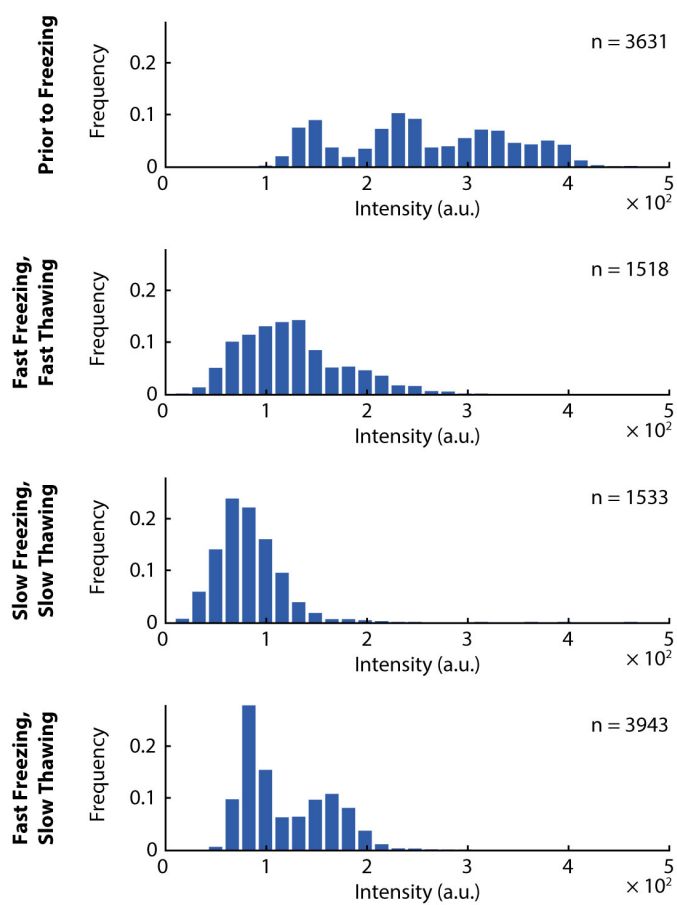
Figure S1. GUV intensity distribution. Histograms showing the intensity distribution of GUVs for the control before freezing and each FT condition. Number of GUVs n is given for each condition; the intensity (x-axis) is the combined intensity for both fluorescent signals (Cy5 and 6-FAM).

1
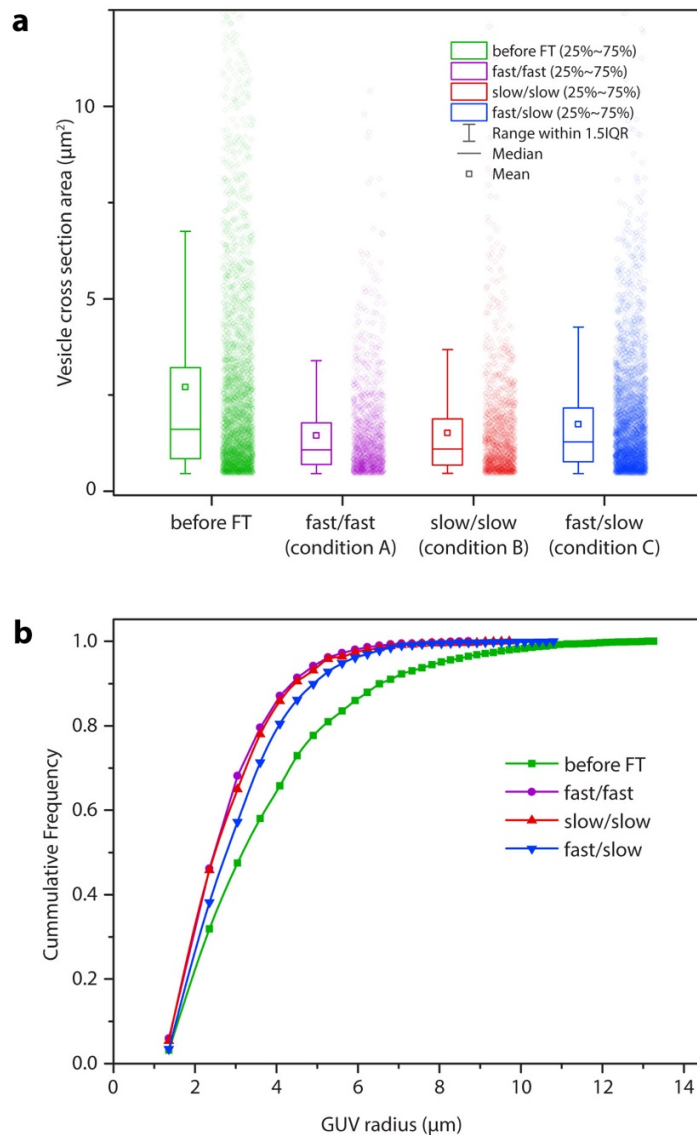
Figure S2. Size Distribution of GUVs prior to freeze-thawing and for each condition shown in figure 2. (a) Box plots and 1-D scatter plots show the cross-section area of the vesicles. Each data point in the scatter plot represents an individual GUV. A description of the box plot elements can be found in the legend of the plot. **(b)** A cumulative plot of the GUV radii shows that after freeze-thawing the fraction of large GUVs is reduced.

2
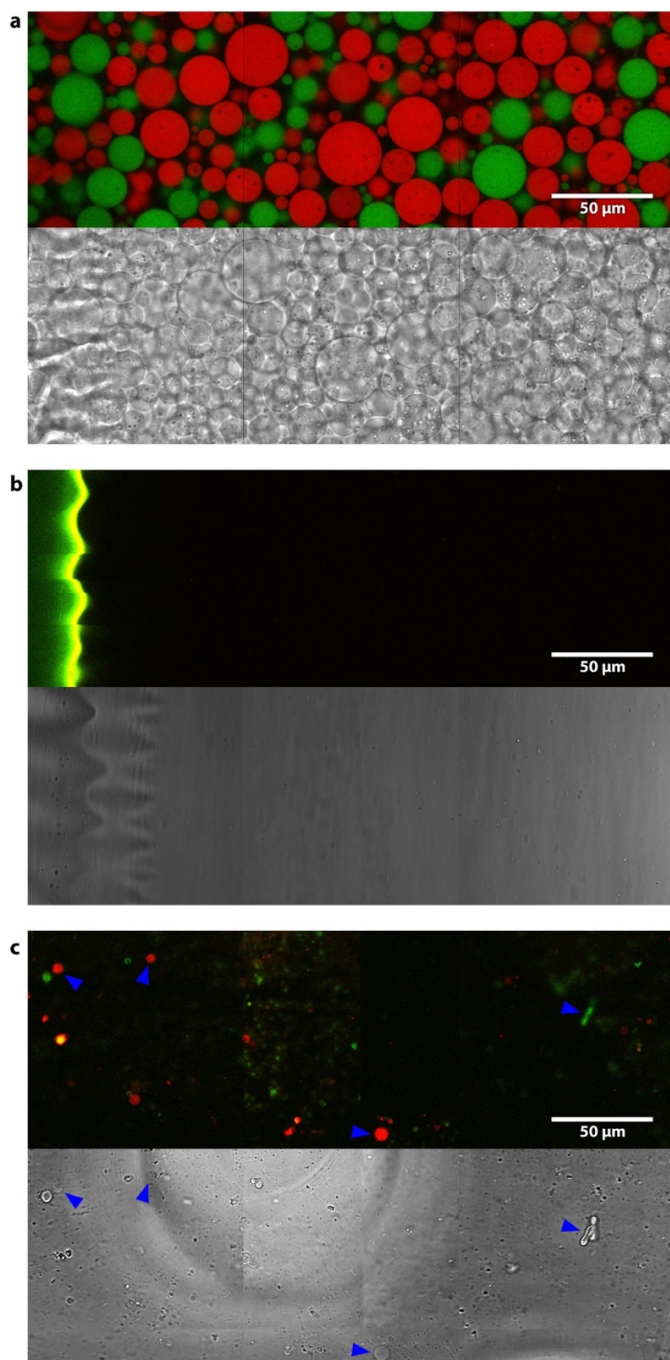
Figure S3. Effect of slow freezing and subsequent fast thawing (condition D) on GUVs. (**a**) GUVs prior to freezing and thawing. Top: Fluorescence intensity of Cy5-oligos is shown in red, fluorescence of 6-FAM-oligos in green as shown in figure 2(e). Bottom: Differential interference contrast (DIC) images of the same field of view. (b) After slow freezing and fast thawing (condition D), no vesicles were observed. The DIC image, which would show vesicles that are outside of the focal plane within a certain range, confirms this. (c) In some instances, very small vesicles that do not show signs of content mixing can be observed.

3
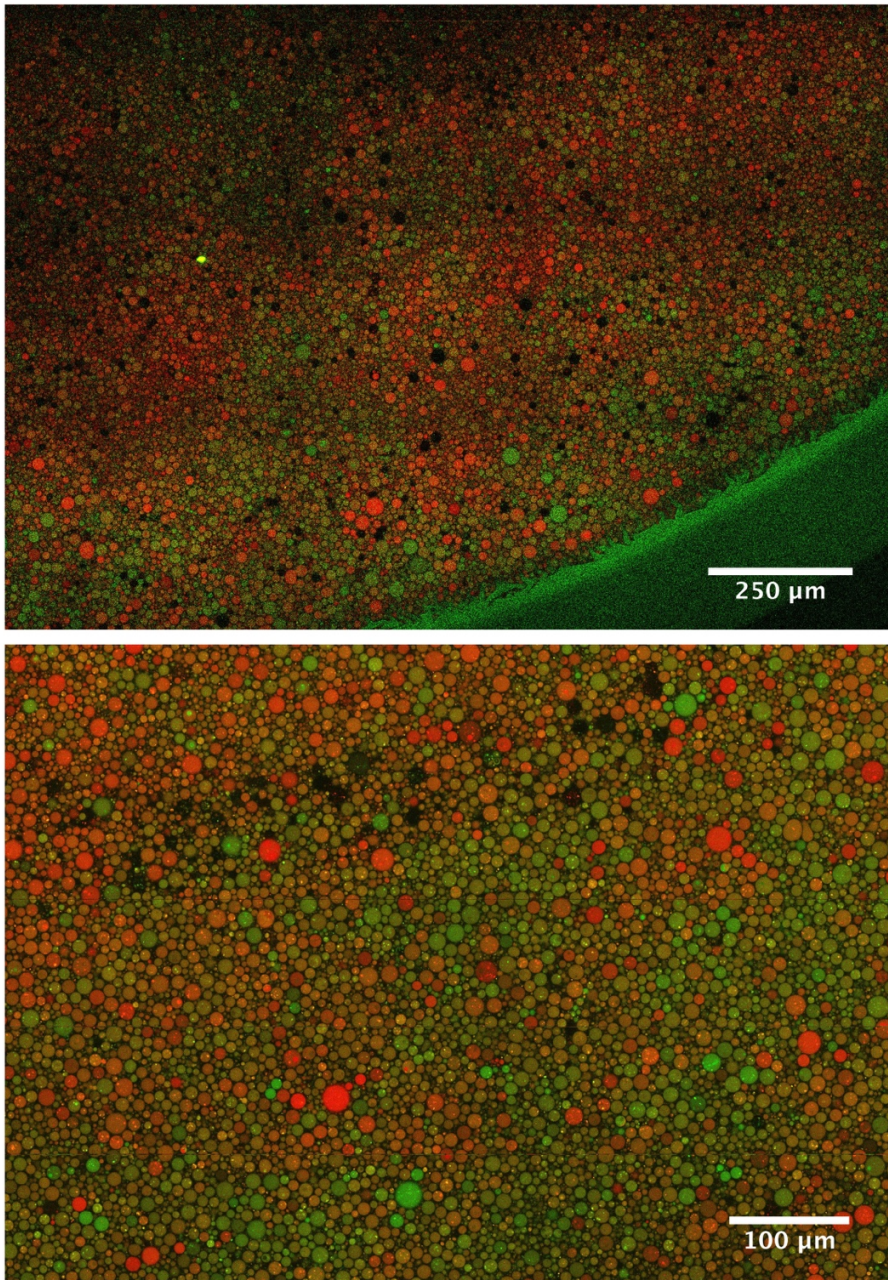
Figure S4. Confocal microscopic images of GUVs after a FT cycle. Experiment like in figure 2(h), according to protocol C (fast freezing, slow thawing). Some samples show a large variety of ratios of the two labelled DNA oligos. In some sectors Cy5 (red) predominates while in others 6-FAM (green) labelled DNA is the dominant conjugate. We assume this phenomenon arises from regions that contain predominantly one population of vesicles before freezing. This inhomogeneity is a large-scale phenomenon, spanning over tens to hundreds of vesicles. We see that these red or green areas fade smoothly into each other, indicating that content mixing is very efficient.
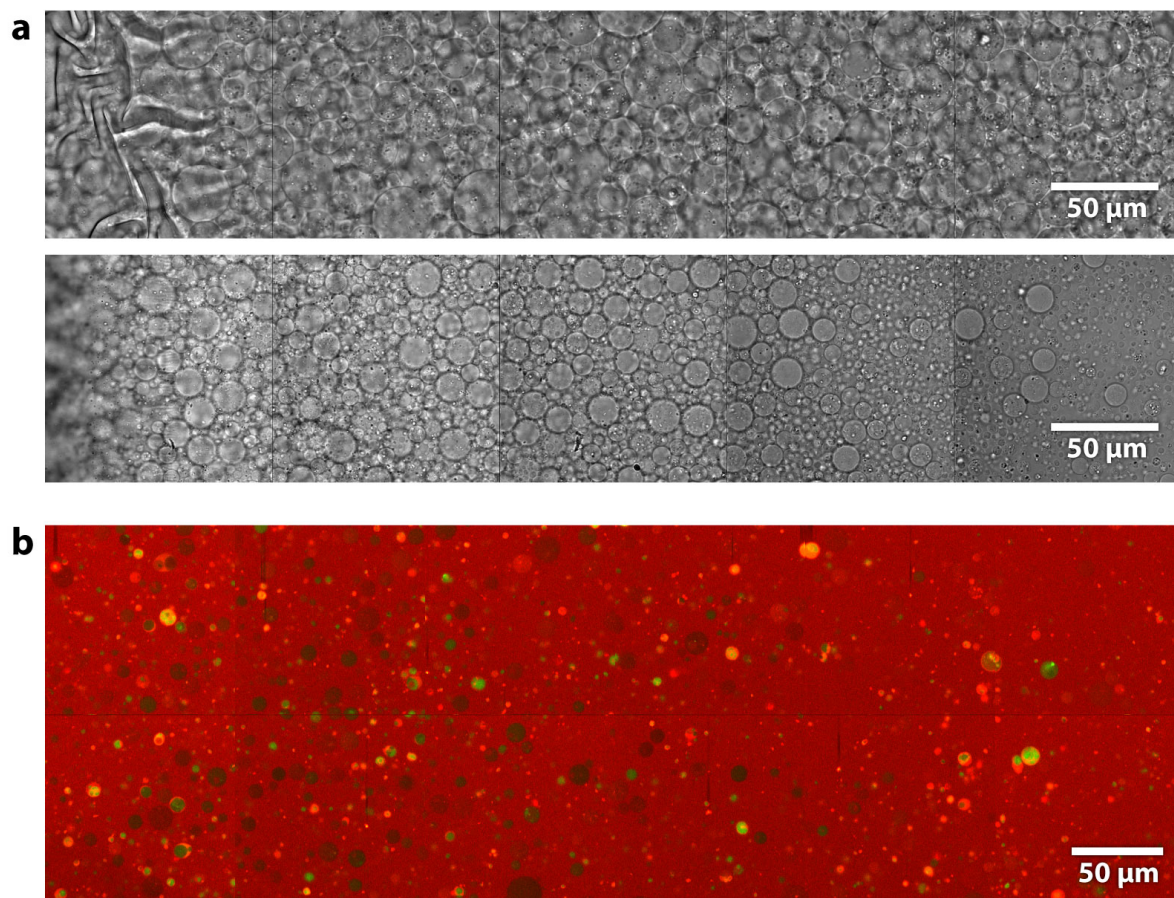
Figure S5. (**a**) DIC images of GUVs (prior to freeze-thawing) show several layers of GUVs in z-dimension (orthogonally to the glass bottom). Before freeze-thawing we incubate the microtiter plate at a 45° angle, to accumulate GUVs on one side of the chamber (here on the left). The density of GUVs is the highest on the left and decrease towards the right side. The bottom image shows an experiment with a lower vesicle yield, showing the gradient more clearly. On the left side GUVs are densely packed with several layers stacked on top of each other, towards the centre of the image GUVs are still dense in the x and y dimension, but with only one layer in the z-direction and on the right, only few small vesicles can be seen. (**b**) Image data (condition B) for the data analysed quantitatively in the scatter plot of figure 3(c) (grey). Vesicles containing DNA-oligos labelled with 6-FAM are generated in an outer phase containing DNA-Oligos labelled with Cy5 (see figure 3(a)). Compared to fast freezing and slow thawing (figure 3(b)), the GUVs lose more of their original content, and on average encapsulate more of the outer phase.

5
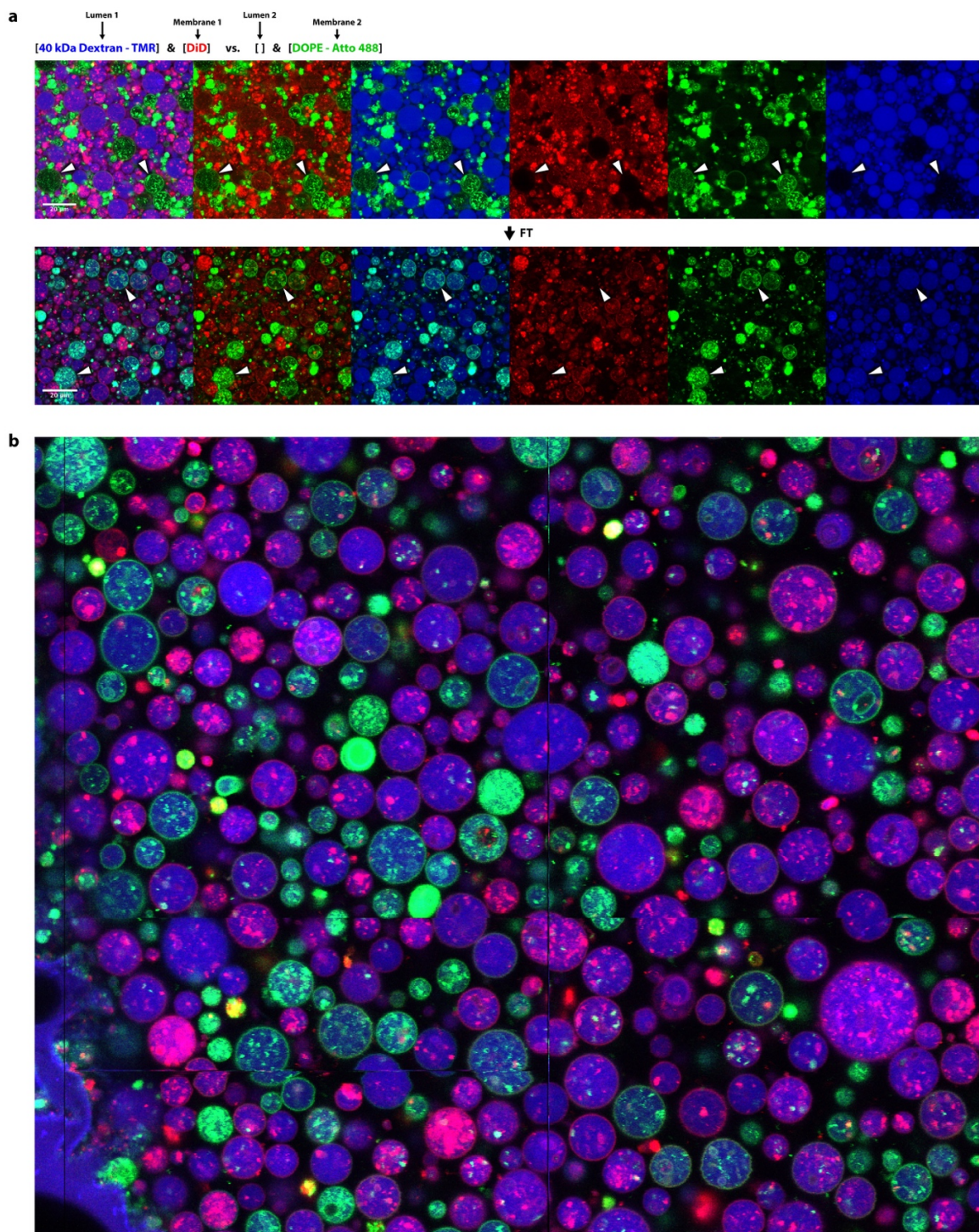
Figure S6. Freeze-thawing of GUV populations with differently labelled membranes and exchange of Dextran (40 kDa) between GUVs. (FT condition C). (a) Sample before and after freeze-thawing. Montages show all channels and different combinations of channels. Red: DiD, green: DOPE labelled with ATTO 488, blue: Dextran labelled with TMR. Arrows mark examples for GUVs with membranes labelled with ATTO 488 (green); before freeze-thawing, these

6

GUVs do not contain 40 kDa Dextran (blue). After freeze-thawing the blue channel shows a TMR signal in those GUVs. (**b**) Additional image of the sample after freeze-thawing.

7
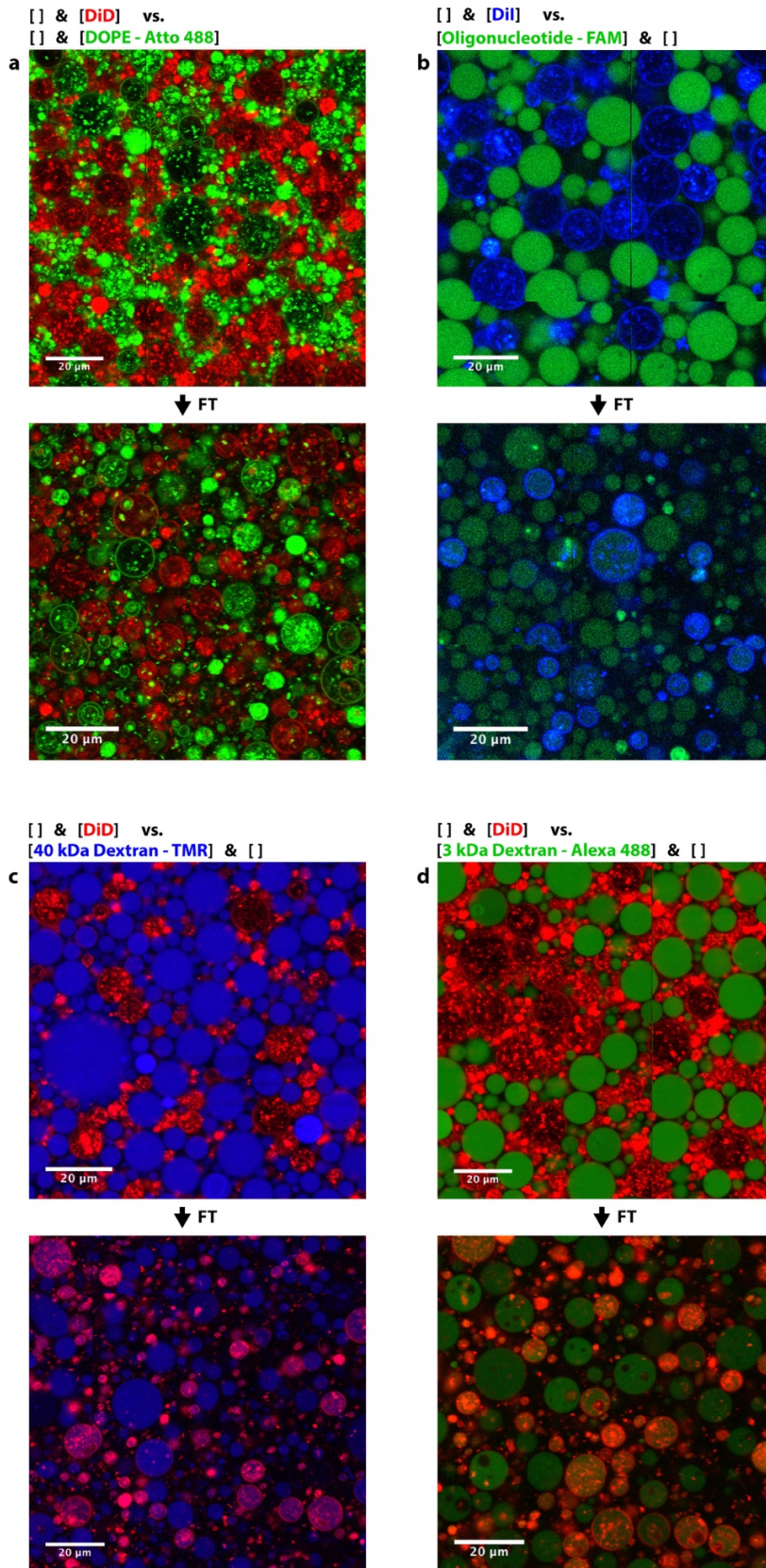
Figure S7. Additional experiments to test for membrane exchange between GUVs through freeze-thawing. (**a**) Experiments in which only the membranes, but not the content of GUVs were fluorescently labelled. Membranes were labelled with DiD and DOPE – ATTO 488. GUVs after freeze-thawing clearly show two populations of vesicles with no indications of mixing of membrane labels. (**b**) One population of GUVs contains labelled Oligonucleotides from the experiment in figure 1 to 3, the other population has membranes labelled with DiI. After freeze-thawing there still are two distinct types of GUVs with only one group showing labelled membranes. But both groups contain labelled oligonucleotides. (**c**) Similar experiment to (b), but with different membrane label and labelled dextran instead of the oligoes. (**d**) Like (c), but with a smaller dextran molecule labelled with Alexa 488.

8
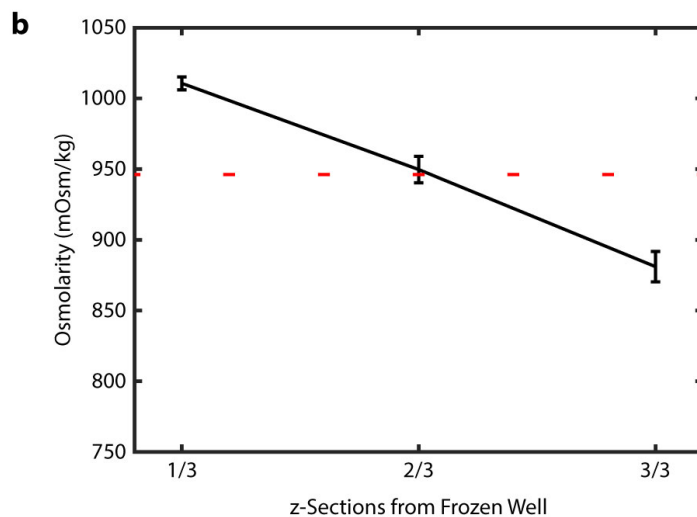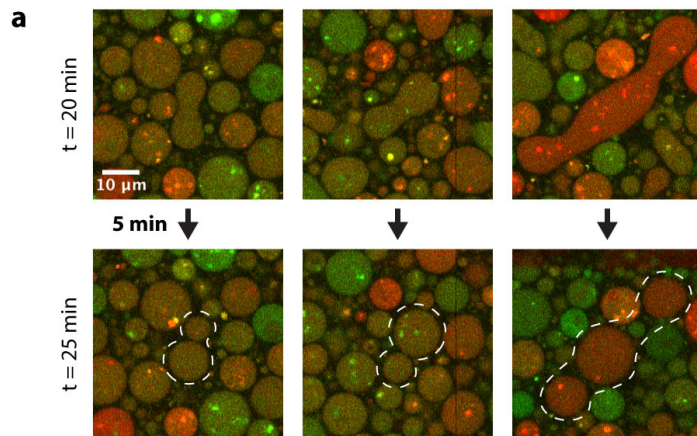
Figure S8. (**a**) Confocal microscopic images of GUVs captured after 20 and 25 minutes incubation (thawing) at room temperature. Top images show the same regions as bottom images; dotted lines indicate previously elongated/merged GUVs. (**b**) Glucose gradient in frozen microtiter well. GUVs are in the bottom 1/3 section (left). The red dotted line indicates the osmolarity of the glucose solution prior to freezing. To acquire the measurements, 200 µl glucose solution was dispensed into a microtiter plate well and then frozen at -80°C on a metal block, as in condition A and C. We then retrieved the frozen cylinder from the well and, while still frozen, cut it with a scalpel into three approximately equally sized vertical sections (~66 µl each). After thawing, we determined the osmolality of each section with a micro-sample osmometer (Fiske® Model 210). Three repetitions of this experiment are included in the plot.

9

6. Discussion

In this thesis, I present my contributions to the field of bottom-up synthetic biology by using of giant unilamellar vesicles as model membrane systems. I have encapsulated a diverse array of biological components in GUVs to achieve biomimetic behavior and function. In each case, I made use of the properties of the GUVs to achieve behaviors or make observations that would have not been possible with other approaches like by using alternative model membrane systems.

While we argue that GUVs are the natural choice in the field of bottom-up cell biology in the pursuit of increasingly cell-like behavior, there are still many challenges ahead. The extremely flexible and deformable membranes discussed in this thesis still have very little in common with the complex membranes of actual biological cells, particularly those of single celled organisms. This becomes particularly evident with our encapsulation of the Min system (chapter 3). Our observation of striking, large scale deformations through the binding and unbinding of Min proteins was an exciting observation, as such dynamic vesicle behavior was unprecedented in the field of synthetic biology. However, in live E. coli cells, the binding and unbinding of Min proteins has not been observed to directly deform the cell membrane in any way. In a way, the rigid PDMS compartments of Zieske et al.[47,61] and Caspi et al.[50] imitate the processes in E. coli much better than our GUV-approach. Of course, at the same time these approaches are a 'dead-end' toward the actual reconstitution of cell-division, as these rigid compartments are not dividable by any protein machinery. These above mentioned discrepancies between GUVs and actual cells are of course not a drawback of the system, but just a testament to the complexity of living cells and how much work lies ahead in the field.

In chapter 4 we show a hybrid approach by combining microfabricated chambers/channels with protein-encapsulating vesicles. These squeezed vesicles can take on a non-spherical form, while still maintaining their membrane tension (or even increasing membrane tension as in Publication 5), which would not be possible without the microfabricated structural determinant. This approach does and will allow the investigation of geometry dependence of protein systems in combination with the free standing bilayers of GUVs. Allowing for a non-spherical compartment shape might even facilitate the bottom-up reconstitution of a vesicle division mechanism. However, towards the reconstitution of synthetic cells, these approaches remain workarounds, as they aren't compatible with the long-term goal of

independent and potentially proliferating artificial cells. The results shown in chapter 2 demonstrate a step towards a more cell-like approach by reconstituting a synthetic cell cortex. We show in figure 6 of Publication 2 that such a cortex can even prevent the vesicle from collapsing upon drying and freezing. While this was quite exciting, our approach is not the most cell-like, as in vivo, the cell cortex consists of more of branched actin rather than bundled. This makes it even more surprising, however, that even these relatively 'heterogeneous' cortices can prevent the vesicles from collapse.

A core theme of this thesis was the bottom-up reconstitution of processes related to cell division and proliferation – a truly exciting topic, as it is directly linked to the pillars of life. Division of membrane compartments has been a persistent goal in synthetic biology[85-88] and actually a few systems exist that achieve some way of division through mechanical or physicochemical processes[89-91] or other factors not from within the vesicles[92,93]. In the sense of creating biomimetic behavior, it seems that a criteria for this goal of division should be an energy-consuming mechanism that acts from within. Arguably the dumbbell-oscillations we observe in Publication 3 fulfill these criteria and represent a periodic splitting of a vesicle, as the vesicle compartment is truly divided into two compartments. It should also be noted, that (i) while maybe somewhat counterintuitive, the unbinding of MinDE from the membrane – the step that causes the division – is the step that consumes ATP and (ii) after some time of oscillating, the system usually "gets stuck" in the divided state. This divided state represents a division into individual volumes/units, which, from a biological perspective, is all that matters. Also experimentally this divided state is not far off from truly separated vesicles - we assume that by just agitating the sample, the two connected compartments could easily split into two intact but fully disconnected vesicles. It should also be pointed out that, besides this rather synthetic approach (the division through forces exerted directly by the Min proteins is a rather synthetic approach), we also successfully reconstituted MinDE pole-to-pole oscillations in vesicles, which represents a crucial stepping stone for the in vitro, bottom-up reconstitution of bacterial cell division.

In Publication 2 we achieve a similar stepping stone, however for eukaryotic cell division. We assemble a number of features within vesicles that are crucial for a potential vesicle division: membrane bound actin bundles, ring formation, and constriction thereof. Unfortunately these reconstituted features seem insufficient for the division of vesicles, as long as the positional stability of the contracting ring on the membrane cannot be ensured.

However, toward the bottom-up design of a minimal division machinery, this system was an ideal starting point for identifying the additional components required.

Through the research presented in this thesis, I demonstrated not only the versatility of GUVs as model membrane systems, but the potential of encapsulation as a method to reconstitute cell-like features and processes of biological systems. The ability to combine confinement, biomimetic membranes, and purified protein could be used to investigate endless functional protein systems. While I have shown the successful application to a few key systems here, this field is likely to grow rapidly, resulting in the reconstitution of increasingly complex systems, and helping us toward the goal of understanding biological organization, complexity, and dynamics on the scale of an entire cell.

7. Bibliography

The following bibliography does not concern citations within the reprinted publications of this thesis. For citations within these publication refer to the "References" section at the end of each publication.

1   Loose, M., Fischer-Friedrich, E., Ries, J., Kruse, K. & Schwille, P. Spatial regulators for bacterial cell division self-organize into surface waves in vitro. *Science* **320**, 789-792, doi:10.1126/science.1154413 (2008).

2   Litschel, T. & Schwille, P. Protein Reconstitution Inside Giant Unilamellar Vesicles. *Annu Rev Biophys*, doi:10.1146/annurev-biophys-100620-114132 (2021).

3   Pollard, T. D. Cytoplasmic contractile proteins. *J Cell Biol* **91**, 156s-165s, doi:10.1083/jcb.91.3.156s (1981).

4   Ganzinger, K. A. & Schwille, P. More from less - bottom-up reconstitution of cell biology. *J Cell Sci* **132**, doi:10.1242/jcs.227488 (2019).

5   Liu, A. P. & Fletcher, D. A. Biology under construction: in vitro reconstitution of cellular function. *Nat Rev Mol Cell Biol* **10**, 644-650, doi:10.1038/nrm2746 (2009).

6   Kuhne, W. *Untersuchungen uber das Protoplasma und die Contractilitat.* (W. Engelmann, 1864).

7   Straub, F. Studies of the Inst. of Med. Chem. Univ. Szeged edit., by Szent-Györgyi, vol. II. *Basel and New York: S. Karger*, 3 (1942).

8   Szent-Györgyi, A. G. The Early History of the Biochemistry of Muscle Contraction. *The Journal of General Physiology* **123**, 631-641, doi:10.1085/jgp.200409091 (2004).

9   Mullins, R. D. & Hansen, S. D. In vitro studies of actin filament and network dynamics. *Curr Opin Cell Biol* **25**, 6-13, doi:10.1016/j.ceb.2012.11.007 (2013).

10   Smith, B. A., Gelles, J. & Goode, B. L. Single-molecule studies of actin assembly and disassembly factors. *Methods Enzymol* **540**, 95-117, doi:10.1016/B978-0-12-397924-7.00006-6 (2014).

11   Pollard, T. D. Actin and Actin-Binding Proteins. *Cold Spring Harb Perspect Biol* **8**, doi:10.1101/cshperspect.a018226 (2016).

12   Dogterom, M. & Koenderink, G. H. Actin-microtubule crosstalk in cell biology. *Nat Rev Mol Cell Biol* **20**, 38-54, doi:10.1038/s41580-018-0067-1 (2019).

13   Lappalainen, P. Actin-binding proteins: the long road to understanding the dynamic landscape of cellular actin networks. *Molecular Biology of the Cell* **27**, 2519-2522, doi:10.1091/mbc.e15-10-0728 (2016).

14   Backouche, F., Haviv, L., Groswasser, D. & Bernheim-Groswasser, A. Active gels: dynamics of patterning and self-organization. *Physical Biology* **3**, 264-273, doi:10.1088/1478-3975/3/4/004 (2006).

15   Koenderink, G. H. *et al.* An active biopolymer network controlled by molecular motors. *Proceedings of the National Academy of Sciences* **106**, 15192-15197, doi:10.1073/pnas.0903974106 (2009).

16   Köhler, S., Schaller, V. & Bausch, A. R. Structure formation in active networks. *Nature Materials* **10**, 462-468, doi:10.1038/nmat3009 (2011).

17   Murrell, M. P. & Gardel, M. L. F-actin buckling coordinates contractility and severing in a biomimetic actomyosin cortex. *Proceedings of the National Academy of Sciences* **109**, 20820-20825, doi:10.1073/pnas.1214753109 (2012).

18   Stam, S. *et al.* Filament rigidity and connectivity tune the deformation modes of active biopolymer networks. *Proceedings of the National Academy of Sciences* **114**, E10037-E10045, doi:10.1073/pnas.1708625114 (2017).

19   Schaller, V., Weber, C., Semmrich, C., Frey, E. & Bausch, A. R. Polar patterns of driven filaments. *Nature* **467**, 73-77, doi:10.1038/nature09312 (2010).

20   Vogel, S. K., Petrasek, Z., Heinemann, F. & Schwille, P. Myosin motors fragment and compact membrane-bound actin filaments. *eLife* **2**, e00116, doi:10.7554/eLife.00116 (2013).

21   Sonal *et al.* Myosin-II activity generates a dynamic steady state with continuous actin turnover in a minimal actin cortex. *Journal of Cell Science* **132**, jcs219899, doi:10.1242/jcs.219899 (2019).

22   Murrell, M. & Gardel, M. L. Actomyosin sliding is attenuated in contractile biomimetic cortices. *Molecular Biology of the Cell* **25**, 1845-1853, doi:10.1091/mbc.e13-08-0450 (2014).

23   Doherty, G. J. & McMahon, H. T. Mediation, modulation, and consequences of membrane-cytoskeleton interactions. *Annu Rev Biophys* **37**, 65-95, doi:10.1146/annurev.biophys.37.032807.125912 (2008).

24   Lagny, T. J. & Bassereau, P. Bioinspired membrane-based systems for a physical approach of cell organization and dynamics: usefulness and limitations. *Interface Focus* **5**, 20150038, doi:doi:10.1098/rsfs.2015.0038 (2015).

25   Sonnleitner, A., Schütz, G. J. & Schmidt, T. Free Brownian Motion of Individual Lipid Molecules in Biomembranes. *Biophysical Journal* **77**, 2638-2642, doi:https://doi.org/10.1016/S0006-3495(99)77097-9 (1999).

26   Przybylo, M. *et al.* Lipid Diffusion in Giant Unilamellar Vesicles Is More than 2 Times Faster than in Supported Phospholipid Bilayers under Identical Conditions. *Langmuir* **22**, 9096-9099, doi:10.1021/la061934p (2006).

27   Cortese, J. D., Schwab, B., Frieden, C. & Elson, E. L. Actin polymerization induces a shape change in actin-containing vesicles.

Proceedings of the National Academy of Sciences **86**, 5773-5777, doi:10.1073/pnas.86.15.5773 (1989).

28   Miyata, H. & Hotanif, H. Morphological changes in liposomes caused by polymerization of encapsulated actin and spontaneous formation of actin bundles. *Proc. Nad. Acad. Sci. USA* **89**, 11547-11551 (1992).

29   Lipowsky, R., Richter, D. & Kremer, K. in *The Structure and Conformation of Amphiphilic Membranes.* (eds Reinhard Lipowsky, Dieter Richter, & Kurt Kremer) 1-6 (Springer Berlin Heidelberg).

30   Miyata, H., Nishiyama, S., Akashi, K.-i. & Kinosita, K. Protrusive growth from giant liposomes driven by actin polymerization. *Proceedings of the National Academy of Sciences* **96**, 2048-2053, doi:10.1073/pnas.96.5.2048 (1999).

31   Furukawa, R., Kundra, R. & Fechheimer, M. Formation of liquid crystals from actin filaments. *Biochemistry* **32**, 12346-12352, doi:10.1021/bi00097a010 (1993).

32   Tanaka, S., Takiguchi, K. & Hayashi, M. Repetitive stretching of giant liposomes utilizing the nematic alignment of confined actin. *Communications Physics* **1**, 18, doi:10.1038/s42005-018-0019-2 (2018).

33   Honda, M., Takiguchi, K., Ishikawa, S. & Hotani, H. Morphogenesis of liposomes encapsulating actin depends on the type of actin-crosslinking. *J Mol Biol* **287**, 293-300, doi:10.1006/jmbi.1999.2592 (1999).

34   Tsai, F. C. & Koenderink, G. H. Shape control of lipid bilayer membranes by confined actin bundles. *Soft Matter* **11**, 8834-8847, doi:10.1039/c5sm01583a (2015).

35   Limozin, L. & Sackmann, E. Polymorphism of Cross-Linked Actin Networks in Giant Vesicles. *Physical Review Letters* **89**, doi:10.1103/PhysRevLett.89.168103 (2002).

36   Litschel, T. *et al.* Reconstitution of contractile actomyosin rings in vesicles. *Nature Communications*, doi:10.1038/s41467-021-22422-7 (2021).

37   Turing, A. M. The Chemical Basis of Morphogenesis. *Philosophical Transactions of the Royal Society of London. Series B, Biological Sciences* **237**, 37-72 (1952).

38   Zhabotinsky, A. M. Periodic Liquid Phase Reactions. *Proc. Acad. Sci. USSR* **157**, 392 (1964).

39   Loose, M., Fischer-Friedrich, E., Herold, C., Kruse, K. & Schwille, P. Min protein patterns emerge from rapid rebinding and membrane interaction of MinE. *Nat Struct Mol Biol* **18**, 577-583, doi:10.1038/nsmb.2037 (2011).

40   Miyagi, A., Ramm, B., Schwille, P. & Scheuring, S. High-Speed Atomic Force Microscopy Reveals the Inner Workings of the MinDE Protein Oscillator. *Nano Letters* **18**, 288-296, doi:10.1021/acs.nanolett.7b04128 (2018).

41   Kretschmer, S., Zieske, K. & Schwille, P. Large-scale modulation of reconstituted Min protein patterns and gradients by defined mutations in MinE's membrane targeting sequence. *PLoS One* **12**, e0179582, doi:10.1371/journal.pone.0179582 (2017).

42   Glock, P., Brauns, F., Halatek, J., Frey, E. & Schwille, P. Design of biochemical pattern forming systems from minimal motifs. *eLife* **8**, e48646, doi:10.7554/eLife.48646 (2019).

43   Glock, P. *et al.* Stationary Patterns in a Two-Protein Reaction-Diffusion System. *ACS Synthetic Biology* **8**, 148-157, doi:10.1021/acssynbio.8b00415 (2019).

44   Denk, J. *et al.* MinE conformational switching confers robustness on self-organized Min protein patterns. *Proceedings of the National Academy of Sciences* **115**, 4553, doi:10.1073/pnas.1719801115 (2018).

45   Vecchiarelli, A. G., Li, M., Mizuuchi, M. & Mizuuchi, K. Differential affinities of MinD and MinE to anionic phospholipid influence Min

patterning dynamics in vitro. *Mol Microbiol* **93**, 453-463, doi:10.1111/mmi.12669 (2014).

46   Schweizer, J. *et al.* Geometry sensing by self-organized protein patterns. *Proc Natl Acad Sci U S A* **109**, 15283-15288, doi:10.1073/pnas.1206953109 (2012).

47   Zieske, K. & Schwille, P. Reconstitution of self-organizing protein gradients as spatial cues in cell-free systems. *Elife* **3**, doi:10.7554/eLife.03949 (2014).

48   Zieske, K., Schweizer, J. & Schwille, P. Surface topology assisted alignment of Min protein waves. *FEBS Lett* **588**, 2545-2549, doi:10.1016/j.febslet.2014.06.026 (2014).

49   Zieske, K., Chwastek, G. & Schwille, P. Protein Patterns and Oscillations on Lipid Monolayers and in Microdroplets. *Angew Chem Int Ed Engl* **55**, 13455-13459, doi:10.1002/anie.201606069 (2016).

50   Caspi, Y. & Dekker, C. Mapping out Min protein patterns in fully confined fluidic chambers. *Elife* **5**, doi:10.7554/eLife.19271 (2016).

51   de Boer, P. A., Crossley, R. E. & Rothfield, L. I. A division inhibitor and a topological specificity factor coded for by the minicell locus determine proper placement of the division septum in E. coli. *Cell* **56**, 641-649, doi:10.1016/0092-8674(89)90586-2 (1989).

52   Hu, Z., Mukherjee, A., Pichoff, S. & Lutkenhaus, J. The MinC component of the division site selection system in Escherichia coli interacts with FtsZ to prevent polymerization. *Proceedings of the National Academy of Sciences* **96**, 14819-14824, doi:10.1073/pnas.96.26.14819 (1999).

53   Bassereau, P. *et al.* The 2018 biomembrane curvature and remodeling roadmap. *J Phys D Appl Phys* **51**, doi:10.1088/1361-6463/aacb98 (2018).

54   Litschel, T., Ramm, B., Maas, R., Heymann, M. & Schwille, P. Beating Vesicles: Encapsulated Protein Oscillations Cause Dynamic

Membrane Deformations. *Angew Chem Int Ed Engl* **57**, 16286-16290, doi:10.1002/anie.201808750 (2018).

55   Christ, S., Litschel, T., Schwille, P. & Lipowsky, R. Active shape oscillations of giant vesicles with cyclic closure and opening of membrane necks. *Soft Matter* **17**, 319-330, doi:10.1039/d0sm00790k (2021).

56   Soares e Silva, M. *et al.* Self-organized patterns of actin filaments in cell-sized confinement. *Soft Matter* **7**, doi:10.1039/c1sm06060k (2011).

57   Deshpande, S. & Pfohl, T. Real-time dynamics of emerging actin networks in cell-mimicking compartments. *PLoS One* **10**, e0116521, doi:10.1371/journal.pone.0116521 (2015).

58   Faivre-Moskalenko, C. & Dogterom, M. Dynamics of microtubule asters in microfabricated chambers: The role of catastrophes. *Proceedings of the National Academy of Sciences* **99**, 16788-16793, doi:10.1073/pnas.252407099 (2002).

59   Opathalage, A. *et al.* Self-organized dynamics and the transition to turbulence of confined active nematics. *Proceedings of the National Academy of Sciences* **116**, 4788-4797, doi:10.1073/pnas.1816733116 (2019).

60   Mellouli, S. *et al.* Self-organization of the bacterial cell-division protein FtsZ in confined environments. *Soft Matter* **9**, 10493-10500, doi:10.1039/C3SM51163D (2013).

61   Zieske, K. & Schwille, P. Reconstitution of pole-to-pole oscillations of min proteins in microengineered polydimethylsiloxane compartments. *Angew Chem Int Ed Engl* **52**, 459-462, doi:10.1002/anie.201207078 (2013).

62   Minc, N., Burgess, D. & Chang, F. Influence of cell geometry on division-plane positioning. *Cell* **144**, 414-426, doi:10.1016/j.cell.2011.01.016 (2011).

63   Wu, F., van Schie, B. G. C., Keymer, J. E. & Dekker, C. Symmetry and scale orient Min protein patterns in shaped bacterial sculptures. *Nature Nanotechnology* **10**, 719-726, doi:10.1038/nnano.2015.126 (2015).

64   Söderström, B., Badrutdinov, A., Chan, H. & Skoglund, U. Cell shape-independent FtsZ dynamics in synthetically remodeled bacterial cells. *Nature Communications* **9**, 4323, doi:10.1038/s41467-018-06887-7 (2018).

65   Stachowiak, M. R. *et al.* Mechanism of cytokinetic contractile ring constriction in fission yeast. *Dev Cell* **29**, 547-561, doi:10.1016/j.devcel.2014.04.021 (2014).

66   Ganzinger, K. A. *et al.* Microfluidic trapping of vesicles reveals membrane-tension dependent FtsZ cytoskeletal re-organisation. *bioRxiv*, 791459, doi:10.1101/791459 (2019).

67   Whitesides, G. M., Ostuni, E., Takayama, S., Jiang, X. & Ingber, D. E. Soft lithography in biology and biochemistry. *Annu Rev Biomed Eng* **3**, 335-373, doi:10.1146/annurev.bioeng.3.1.335 (2001).

68   Whitesides, G. M. The origins and the future of microfluidics. *Nature* **442**, 368-373, doi:10.1038/nature05058 (2006).

69   Volpatti, L. R. & Yetisen, A. K. Commercialization of microfluidic devices. *Trends Biotechnol* **32**, 347-350, doi:10.1016/j.tibtech.2014.04.010 (2014).

70   He, Y., Wu, Y., Fu, J.-z., Gao, Q. & Qiu, J.-j. Developments of 3D Printing Microfluidics and Applications in Chemistry and Biology: a Review. *Electroanalysis* **28**, 1658-1678, doi:https://doi.org/10.1002/elan.201600043 (2016).

71   Nielsen, A. V., Beauchamp, M. J., Nordin, G. P. & Woolley, A. T. 3D Printed Microfluidics. *Annual Review of Analytical Chemistry* **13**, 45-65, doi:10.1146/annurev-anchem-091619-102649 (2020).

72   Glick, C. C. *et al.* Rapid assembly of multilayer microfluidic structures via 3D-printed transfer molding and bonding. *Microsystems & Nanoengineering* **2**, 16063, doi:10.1038/micronano.2016.63 (2016).

73   Jia, H. *et al.* Shaping Giant Membrane Vesicles in 3D-Printed Protein Hydrogel Cages. *Small* **16**, e1906259, doi:10.1002/smll.201906259 (2020).

74   Ganzinger, K. A. *et al.* FtsZ Reorganization Facilitates Deformation of Giant Vesicles in Microfluidic Traps*. *Angew Chem Int Ed Engl* **59**, 21372-21376, doi:10.1002/anie.202001928 (2020).

75   Muller, U. F. Re-creating an RNA world. *Cell Mol Life Sci* **63**, 1278-1293, doi:10.1007/s00018-006-6047-1 (2006).

76   Deamer, D., Dworkin, J. P., Sandford, S. A., Bernstein, M. P. & Allamandola, L. J. The First Cell Membranes. *Astrobiology* **2**, 371-381, doi:10.1089/153110702762470482 (2002).

77   Szathmáry, E., Santos, M. & Fernando, C. in *Prebiotic Chemistry* (ed Peter Walde) 167-211 (Springer Berlin Heidelberg, 2005).

78   Gyles, C. & Boerlin, P. Horizontally transferred genetic elements and their role in pathogenesis of bacterial disease. *Vet Pathol* **51**, 328-340, doi:10.1177/0300985813511131 (2014).

79   Kamimura, A., Matsubara, Y. J., Kaneko, K. & Takeuchi, N. Horizontal transfer between loose compartments stabilizes replication of fragmented ribozymes. *PLOS Computational Biology* **15**, e1007094, doi:10.1371/journal.pcbi.1007094 (2019).

80   Chen, I. A. & Walde, P. From self-assembled vesicles to protocells. *Cold Spring Harb Perspect Biol* **2**, a002170, doi:10.1101/cshperspect.a002170 (2010).

81   Ma, W., Yu, C., Zhang, W. & Hu, J. Nucleotide synthetase ribozymes may have emerged first in the RNA world. *RNA* **13**, 2012-2019, doi:10.1261/rna.658507 (2007).

82   Demaneche, S. *et al.* Laboratory-scale evidence for lightning-mediated gene transfer in soil. *Appl Environ Microbiol* **67**, 3440-3444, doi:10.1128/AEM.67.8.3440-3444.2001 (2001).

83   Neumann, E., Schaefer-Ridder, M., Wang, Y. & Hofschneider, P. H. Gene transfer into mouse lyoma cells by electroporation in high electric fields. *EMBO J* **1**, 841-845 (1982).

84   Litschel, T. *et al.* Freeze-thaw cycles induce content exchange between cell-sized lipid vesicles. *New Journal of Physics* **20**, doi:10.1088/1367-2630/aabb96 (2018).

85   Hürtgen, D., Härtel, T., Murray, S. M., Sourjik, V. & Schwille, P. Functional Modules of Minimal Cell Division for Synthetic Biology. *Advanced Biosystems* **3**, 1800315, doi:10.1002/adbi.201800315 (2019).

86   Kretschmer, S., Ganzinger, K. A., Franquelim, H. G. & Schwille, P. Synthetic cell division via membrane-transforming molecular assemblies. *BMC Biol* **17**, 43, doi:10.1186/s12915-019-0665-1 (2019).

87   Exterkate, M. & Driessen, A. J. M. Synthetic Minimal Cell: Self-Reproduction of the Boundary Layer. *ACS Omega* **4**, 5293-5303, doi:10.1021/acsomega.8b02955 (2019).

88   Schwille, P. Division in synthetic cells. *Emerging Topics in Life Sciences*, doi:10.1042/etls20190023 (2019).

89   Kas, J. & Sackmann, E. Shape transitions and shape stability of giant phospholipid vesicles in pure water induced by area-to-volume changes. *Biophys J* **60**, 825-844, doi:10.1016/S0006-3495(91)82117-8 (1991).

90   Farge, E. & Devaux, P. F. Shape changes of giant liposomes induced by an asymmetric transmembrane distribution of phospholipids. *Biophys J* **61**, 347-357, doi:10.1016/S0006-3495(92)81841-6 (1992).

91   Deshpande, S., Spoelstra, W. K., van Doorn, M., Kerssemakers, J. & Dekker, C. Mechanical Division of Cell-Sized Liposomes. *ACS Nano* **12**, 2560-2568, doi:10.1021/acsnano.7b08411 (2018).

92   Steinkuhler, J. *et al.* Controlled division of cell-sized vesicles by low densities of membrane-bound proteins. *Nat Commun* **11**, 905, doi:10.1038/s41467-020-14696-0 (2020).

93   Dreher, Y., Jahnke, K., Bobkova, E., Spatz, J. P. & Gopfrich, K. Division and Regrowth of Phase-Separated Giant Unilamellar Vesicles*. *Angew Chem Int Ed Engl*, doi:10.1002/anie.202014174 (2020).

Acknowledgements

First and foremost I want to thank Charlotte, my favorite person and favorite collaborator, for supporting me in so many different ways. You've made the past four years of my life a wonderful experience. I can even say that about the very last year – a year dominated by the current pandemic – which would have been a horrible experience without you. We've spent literally all our time together and I don't think there is any other person on planet earth I could have done that with.

I would like to thank my family, who has supported me throughout my life with every decision I've made.

I would like to thank Petra for taking me as a PhD student and for offering me the perfect amount of freedom for my work. I appreciate all the different topics and directions I was able to explore. I appreciate all the advice you gave me and it was always fun working with you. I don't think I could have made a better decision four and a half years ago than joining the Schwille lab.

I'd like to thank the entirety of the current and former Schwille lab. Almost every one of you had a part in this work in one way or another.

I would like to thank all external collaborators during my doctoral studies: Tabea Kirchhofer, Tina Seemann, Tom Robinson, Hannes Mutschler, Naoko Mizuno, Danielle Holz, Dimitris Vavylonis, Allen Liu, Simon Christ, Reinhard Lipowsky, Wenxin Zhang, Judita Mascarenhas and Victor Sourjik.

I would like to thank the MPI core facilities, particularly Giovanni Cardone and Martin Spitaler from the Image Facility and Daniel Bollschweiler from the EM facility.

I would also like to thank the master, bachelor and school students I worked with over the years for the many fun hours we had in the lab: Torgeir Movinkel, Julian Penzinger, Nelson Butterfield, Gunnar Goetz and Lars Hansen.